MICROWAVE LENS DESIGNS: OPTIMIZATION, FAST SIMULATION ALGORITHMS, AND 360-DEGREE SCANNING TECHNIQUES

Junwei Dong

Dissertation submitted to the faculty of the Virginia Polytechnic Institute and State University in partial fulfillment of the requirements for the degree of

Doctor of Philosophy
In
Electrical Engineering

Dr. Amir I. Zaghloul (Chair)
Dr. William A. Davis
Dr. Yong Xu
Dr. JoAnn Paul
Dr. Chang-Tien Lu
Dr. Steven Weiss

September 11, 2009

Falls Church, VA

Keywords: microwave lens, rotman lens, printed lens, beam-forming network, minimum phase error, fast simulation, 360-degree scanning, multifunctional array

MICROWAVE LENS DESIGNS: OPTIMIZATION, FAST SIMULATION ALGORITHMS, AND 360-DEGREE SCANNING TECHNIQUES

Junwei Dong

ABSTRACT

Microwave lenses support low-phase error, wideband, wide-angle scanning, and true-time delay (TTD) beam forming. They provide ideal performance for applications such as satellites, remote-piloted vehicles, collision-avoidance radars and ultra-wideband communications systems. The emerging printed lenses in recent years have facilitated the advancement of designing high performance but low-profile, light-weight, and small-size beam-forming networks (BFNs). The microwave lens adopts a few beam ports to illuminate the prescribed receiving ports that feed energy into radiating antennas. Multi-beam patterns can be achieved by exciting multiple beam ports at a time. The design process starts with path-length equations from a limited number of beam-port foci assumptions. This constraint does not take into account the amplitude information; however, it allows an initial lens geometry to be solved. The resulted scanning angle of microwave lens is limited by the beam port contour, as such ± 90 degrees.

In this dissertation, three contributions are made from the aspects of minimized phase errors, accurate and efficient simulation algorithms, and 360-degree scanning range extension. First, a minimum-phase-error, non-focal lens design method is proposed. It does not require a specific number of foci along the beam contour; however, minimum phase errors for all beam ports are able to be achieved. The proposed method takes into account flexible prescribed geometrical design parameters, and adopts numerical optimization algorithms to perform phase error minimization. Numerical results compared with the published tri-focal and quadru-focal lenses demonstrate the merits of the proposed method. Second, an accurate and fast simulation method for the microwave lens has been developed to predict the phase, amplitude, array factor, and power efficiency performance. The proposed method is compared to both full-wave simulation

and measurement. Comparable results have been achieved. Third, a novel method for a 360-degree scanning microwave lens is proposed. This concept uses the beam ports and the receive ports in an interleaving sequence such that adjacent ports alternate beam and receive functions. The result is a lens that produces scanned beams on opposite sides of the structure resulting in a 360-degree scanning range. The structure can use multiple opposing facets or continuous circular-port and radiating-element contours. To prove the concept, a four-facet microstrip lens has been designed, simulated, fabricated, and tested. The comparison between full-wave simulation and measurement has demonstrated good agreement.

ACKNOWLEDGEMENTS

Foremost, my gratitude is to my advisor, Dr. Amir I. Zaghloul, without whom this dissertation was made not possible. Amir has been a very good mentor and collaborator to me since my research started at Virginia Tech in 2006. As a mentor, he has provided me the freedom to explore on my own, and at the same time guidance to recover when my steps faltered. As a collaborator, he has dedicated countless hours to discuss, criticize and explore new solutions together with me in many aspects of several research topics. It was a great pleasure to research together with him, and certainly, it will be in future, too.

I would like to thank the Ohio State University and IAI Elta Electronics Industries for partially funding this research. Some of the measurement data in this dissertation was obtained from them and the US Army Research Laboratory. Dr. Mona Zaghloul at the George Washington University allowed me to use their network analyzer, and I also received help from her student Mr. Hsu-Cheng Ou. All of you are sincerely thanked for your general support. This three-year research was made possible through a continuous devotion, and using several right tools. I am greatly indebted to two distinguish companies and their colleagues. In 2008 summer, I was provided internship in EM Software & Systems (USA) in Hampton, VA to explore the accurate microwave lens simulation method using FEKO. Collaboration with Dr. C. J. Reddy and Dr. Rensheng(Ray) Sun has given me a very valuable experience. In the summer of 2009, I was employed by the Microwave Engineering Corporation (MEC) in North Andover, MA as a Research Engineer to continuously research on the microwave lens. Dr. Rudy Cheung has provided many practical advices, which help me understand more and enrich my ideas. Thank EMSS and MEC also for the simulation software and other toolkits.

My extended appreciation is to the members of my advisory committee –Dr. William A. Davis, Dr. Yong Xu, Dr. Chang-Tien Lu, Dr. JoAnn Paul and Dr. Steven J. Weiss – for the advice and assistance provided throughout my research. Dr. Davis deserves special thanks owning to the three EM courses teaching me over two years, and the numerous thought-provoking comments on EM modeling, antenna etching, programming and professional documentations, etc. Besides, certain individual chapter of this dissertation

was reviewed and commented by my friends: Nassissie Fekadu at Noblis, Dr. Mark Dorsey at U.S. Naval Research Laboratory, Zuduo Zheng at Arizona State University, Dongcai Su at Jilin University, Ying Huang at Syracuse University, and Taeyoung Yang at Virginia Tech. Thank you all for your time and thoughtful advice.

I would like to express my heart-felt gratitude to the special and wonderful persons around me: Dr. Wael Abulshohoud, Karen Tripp and Fifi O'Connor. Wael is a dear friend, mentor and grandpa to me. My academic pursuit has been closely guided and assisted by him since six years ago when I started my undergraduate research in China. My life has also been helped and enriched by him, in so many aspects. Karen is thanked for her enormous encouragement, support and utmost confidence in me throughout my Bachelor, Master and Doctoral study. Thank you also for driving all the way from Canada to join my defense. Fifi is thanked for providing a cozy 'home' for both my wife and me in DC. We have been treated as daughter and son since the first day we walked in that house. At Fifi's, we build things from scratch and grow our own vegetables and flowers in the little farm. I am also thankful to her for offering me a wonderful real-life education.

It is a good opportunity to dedicate my thanks to those who – knowingly or not – provided valuable help in one way or another during my graduate study at the Northern Virginia Center. They are Dr. Lamine Mili, Dr. Gary Brown, Dr. Tim Pratt, Barbara Barrell, Jim Murphy, Karen Akers, Marija Telbis-Forster, Cynthia Roberson, Hasan Amdir, Tony, Ibrahima Diagne, Hua Lin, Xiao Wang, Dr. Qiuzhan Zhou, Dr. Xiangning Lin, and Dr. Yifan Zhu, Jian Liu, Feng Chen, Jing (David) Dai, Yufeng Kou, Chen Wang, Li Chen, and Bin Zhou.

My deepest appreciation is to my beloved mother Feng'e Dong and father Xuxian Dong. They will probably never figure out what their son wrote here in such a magic language to themselves. But I know how easily the happiness could break the boundary and allow love being exchanged between ourselves. Here, I just want to note it down, again, you son feels so proud of you! I am so obliged to gain endless courage, strength and

enthusiasm from both of you! To my little sister Lijuan Dong: thank you for always standing on my side and giving me your utmost support. I am so happy you and Hongyao Wang got engaged recently. May the best future be with both of you.

Finally, but most specially, my thanks go to one high school classmate - my lovely wife, Sumin Li. Thank you for being with me over the years, bringing so much magic and happiness into our little world. During my Ph.D. study, she has provided me countless ideas – either the good or the bad, and numerous advices – either the workable or the un-workable. Thanks for that and also for finding the right etchant materials and fabricate several prototype lenses for my research. Thanks for being my secretary for so many times during my three-year graduate study. At the end, I wish you best luck to your Ph.D. study in Chemistry at the George Washington University. I promise I will be a free, fully armed, and dedicated secretary for you in the rest of your study.

Table of Contents

NOMENCLATURE

$\mathscr{E}$	Electric field intensity (volts/meter)
$\mathscr{D}$	Electric flux density (coulombs/meter^2)
$\mathscr{H}$	Magnetic field intensity (amperes/meter)
$\mathscr{B}$	Magnetic flux density (webers/meter^2)
$\mathscr{J}_c$	Electric conducting current density (amperes/meter^2)
$\mathscr{J}_i$	Electric impressed current density (amperes/meter^2)
$\mathscr{q}_v$	Electric charge density (coulombs/meter^2)
$\nabla\times$	Curl vector operator that describes the rotation of a vector field
$\nabla\cdot$	Divergence operator that measures the magnitude of a vector field's source
ε	Permittivity of the medium (farad/meter)
μ	Permeability of the medium (henry/meter)
σ	Conductivity of the medium (siemens/meter)
$\vec{r}$, $\bar{r}_0$	Spatial vector, observation coordinate, local source coordinate
t	Time (second)
ω	Angular velocity (radians/second)
$\overline{E}$	Frequency-domain electrical vector field intensity (volts/meter)
$\overline{H}$	Frequency-domain magnetic vector field intensity (amperes/meter)
ϕ_e	Phase quantity (radian)
$\mathrm{Re}\{*\}$	Real part of a complex number
$\mathrm{Im}\{*\}$	Imaginary part of a complex number
$\overline{J}_i$	Frequency domain electric impressed current density (amperes/meter^2)
k	Wave number, $k = k' - jk''$, k'(radians/meter): k''(nepers/meter)
E_0	Amplitude of the prescribed electrical field intensity (volts/meter)
E_x, $\mathscr{E}_x$	Depolarized electrical field intensity along x direction (volts/meter)
H_x, $\mathscr{H}_x$	Depolarized magnetic field intensity along x direction (volts/meter)
η	Wave impedance (Ohm)

S	Poynting vector
$H_y^+,\ H_y^-$	Magnetic field traveling along + and – y directions
$\tan\delta$	Loss Tangent
V	Voltage (volts)
I	Current (amperes/meter^2)
R	Resister (ohms)
L	Inductor (henry)
C	Capacitor (farad)
Q	Charge (coulomb)
Φ	Magnetic flux (webber)
$\overline{B}$	Magnetic flux density (webber/meter^2)
Z_0, Z_L	Impedance
Γ	Reflection coefficient
i, j	Index numbers
S_{ij}	Scatter matrix coefficient between port i and port j
$\overline{A}$	Magnetic vector potential
Φ	Electrical Scalar potential
$\delta(x_0)$	Delta function
$\hat{k}$	Unit vector, wave propagation direction
$\overline{J}_\perp(\overline{r}_0)$	Normal component of the vector current
$\widetilde{\overline{J}}_\perp(\overline{k})$	Spatial Fourier transform operator
$\overline{f}(\theta,\varphi)$	Vector pattern in spherical coordinate
a_i	Array feeding amplitude for the ith element (volts)
φ_i	Array feeding phase for the ith element (radian)
$\Delta\phi$	Phase shift between the adjacent array elements (radian)
d	Array spacing (meter)
λ	Wave length (meter)
α	Off center focal angle (degree)

β	Focal ratio, $\beta = OF_2 / OF_1$, $\beta = f_2 / f_1$ =1/g in short
ψ	Array scan angle (degree)
θ	Subtended angle for beam port phase centers (degree)
γ	Ray to beam angle ratio $\gamma = \sin(\psi_\alpha) / \sin(\alpha)$
Y_3	The distance of any array point from the x axis (meter)
y_3	The normalized distance of any array point from the x axis
ζ	Intermediate parameter, $\zeta = Y_3\gamma / f_1$
OF_2:	Side focal length, or f_2 in short
OF_1	is the center focal length, or f_1 in short
T	Transmission line length (meter)
e	The eccentricity of the beam contour
w	The normalized relative transmission line length, $w = (W - W_0) / f_1$
ε_r, ε_e, ε_i	The dielectric constants for cavity region, transmission line and environment
X,Y	The undetermined coordinates of inner receiving port phase centers (meter)
F/D	Ratio between the focal length and aperture dimension
ΔW	Reference transmission line length (meter)
N, M	Number of beam ports, number of receiving elements
(x_i, y_i)	The normalized coordinates of the i^{th} beam port
(x_j, y_j)	The normalized j^{th} receiving port position
Y_j	The j^{th} phased array element height (meter)
D	Dimension of array aperture (meter); Region of the independent variables
Δ_d	Phase error (degree)
Δ_F	Phase error normalized to F
f_0	Center frequency (Hertz)
$\boldsymbol{B}$	Testing Band (Hertz)
N_b	Beam Port #
N_r	Receive Port #
h	Substrate Thickness

t	Copper thickness (meter)
l_1	Direct coupling factor
l_i	Indirect coupling factor (meter)
W	Transmission line length (meter); The width of the taper (meter)
d_B , d_C	The tapered port size (meter)
θ_{BC}	Angle difference between the normal of taper B and C (radian)
Θ	Maximum subtended beam angle, the angle refers to the beam port (degree)
∇A	The gradient of A
$f(\vec{x})$	A general objective function for minimization
x, y	Normalized undetermined coordinates of inner receiving port phase centers
x_{pi}	The solution coordinate along the i^{th} dimension
D_k^x	Sub-region for search
prob(*)	The probability of event *

TABLE OF FIGURES

LIST OF TABLES

CHAPTER 1. INTRODUCTION

As the field of wireless techniques pervasively grows in space-based platforms, radar, wireless communications and personal electronics, the frequency of operation for the electronic devices keeps increasing. As the frequency increases, the signal carrying large bandwidth information becomes more and more directional. To reliably transmit/receive the information in/from certain direction, a beam-forming device that produces true-time delay, wideband, wide-angle, steerable beams is desirable. The narrow beam produces good isolation between adjacent radiation elements; hence multiple beams are possible to be simultaneously obtained by reusing the antenna structure. In doing so, multiple functionalities can be incorporated in a single electronic system. This device, implementable using a printed circuit board (PCB), is attractive in terms of low-profile and mechanical properties such as light weight and strong resiliency.

A phased array is the essential device that utilizes the beam-forming network to radiate energy into free space. Since the 1950s, it has been widely adopted in many radar and satellite systems to perform electronically-controlled beam scanning. For decades, array systems have been restricted for military applications due to high cost and complexity. In recent years, low cost high performance array and its supporting devices have been realized using printed circuit technology, thus array-based commercial applications such as wireless point-to-point communications and auto-collision avoidance radar have emerged. Besides, since the Federal Communications Commission (FCC) issued new bands for commercial ultra-wideband (UWB) [1] and Extremely High Frequency (EHF) applications [2], low-profile high performance arrays have been under investigation. The low-cost high-performance beam-forming networks would facilitate new application development.

The research performed in this dissertation aims at designing microwave lens-based beam-forming networks and optimizing their performance. Traditional design theory will be improved in terms of minimized phase errors and scanning capabilities. Microwave lens for PCB implementation is emphasized. Accurate simulation and analysis method

based on electromagnetics full-wave simulation will be explored. Further improved method based on hybrid ray tracing technique is developed to accelerate the simulation. The latter is suitable for lens optimization or handling extremely large structures. Besides, a novel technique that enables single lens to perform 360-degree scanning is proposed. A couple of microwave lenses have been designed, fabricated and tested, and they are covered throughout these topics. Their simulation and measurement data are primarily used to support the proposals in this dissertation.

It is necessary to review some basic concepts before presenting the specific design subjects, as the aforementioned designs are abided by the laws of electromagnetic theories. The fundamentals of the antenna and array theory serve as one of the key components to form the objective of the beam-forming network. Thus, in the remainder of the session (1.1-1.3), we first review the basic knowledge on waves, antenna and array that have extensively been used during the lens design and analysis process. Besides, understanding the BFNs and previous researchers' works have provided invaluable basis for this dissertation to propose new formulations, simulation method and optimization strategies. The basis of BFNs and some existing models are introduced in section 1.3. Furthermore, because several existing EM simulation toolkits have been involved to conduct performance evaluation and concept validation prior to the implementation, the basic EM simulation methods are reviewed in section 1.4. Section 1.5 enlists the contributions of this dissertation and the presentation of outlines for the rest of the chapters.

1.1 Review of Basic Electromagnetics and Waves Concepts

Electronic devices operating at high frequencies usually have physical size comparable to the wavelength, thus classical circuit theory hardly applies. It is the Maxwell equations that provide the fundamental theories for many engineers to perform predictive design and pursue solid explanation. In this section, we first review the Maxwell equations and their time-domain and frequency-domain representations. Then focus is put on behaviors of electrical magnetic fields and their relationship to energy. Furthermore, the waves in real medium will be addressed with emphasis on their amplitude and phase characteristics

during propagation. Finally, it is worthwhile reviewing a few circuit model parameters that intrinsically link to the behavior of the electronic designs. Note concepts covered in this section primarily serve for understanding the microwave lens designs in this dissertation rather than providing comprehensive electromagnetics basis. A detailed derivation of the equations presented in this chapter can be found in Appendix A.

1. Maxwell Equations

The time-domain Maxwell equations in differential form are shown in (1-1)-(1-5), and they are written in the MKS (meter, kilogram, second) unit system. This set of equations consists of the classical Faraday law, Ampere law and Gauss law. Faraday law states that the time varying magnetic flux produces electrical field, while the Ampere law originally described that time varying electrical current produces rotational magnetic fields. Maxwell proved that for these equations to be consistent there must be a displacement current term $\partial \mathscr{D} / \partial t$ present, hence we presently call the ampere law as Maxwell-Ampere law. A current source produces fields, and the Gauss law describes the relationship between field and its enclosed source quantity. Because there is no magnetic charge found in nature, the right hand of equation (1-4) is zero. Equation (1-5) states that moving electrical charges produce electrical current.

$$\nabla \times \mathscr{E} = -\frac{\partial \mathscr{B}}{\partial t} \qquad \text{(Faraday law)} \qquad (1\text{-}1)$$

$$\nabla \times \mathscr{H} = \frac{\partial \mathscr{D}}{\partial t} + \mathscr{J}_c + \mathscr{J}_i \qquad \text{(Maxwell-Ampere law)} \qquad (1\text{-}2)$$

$$\nabla \cdot \mathscr{D} = \rho_v \qquad \text{(Gauss law)} \qquad (1\text{-}3)$$

$$\nabla \cdot \mathscr{B} = 0 \qquad \text{(Gauss law – magnetic form)} \qquad (1\text{-}4)$$

$$\mathscr{J} = \frac{\partial \rho_v}{\partial t} \qquad \text{(Current continuity equation)} \qquad (1\text{-}5)$$

where,

$\mathscr{E}$: electric field intensity (volts/meter)

$\mathscr{D}$: electric flux density (coulombs/meter^2)

$\mathscr{H}$: magnetic field intensity (amperes/meter)

$\mathscr{B}$: magnetic flux density (webers/meter^2)

$\mathscr{J}_c$: electric conducting current density (amperes/meter^2)

$\mathscr{J}_i$: electric impressed current density (amperes/meter^2)

$\mathscr{q}_v$: electric charge density (coulombs/meter^2)

$\nabla\times$: curl vector operator that describes the rotation of a vector field

$\nabla\cdot$: divergence operator that measures the magnitude of a vector field's source

The electric and magnetic flux densities are defined regardless of the material properties; so that the source produces these quantities can be easily found by Gaussian integration without mentioning the materials. The material properties appear in the constitutive relations with the electrical and magnetic fields, as shown in (1-6)-(1-8).

$$\mathscr{D} = \varepsilon \mathscr{E} \tag{1-6}$$

$$\mathscr{B} = \mu \mathscr{H} \tag{1-7}$$

$$\mathscr{J}_c = \sigma \mathscr{E} \tag{1-8}$$

where, ε is called permittivity of the medium, μ is the permeability, and σ refers to the conductivity. According to [3], above relationships hold true if $\mathscr{E}$, $\mathscr{H}$ and their time derivatives are not very large.

It is noted that the vector quantities in the Maxwell equations are functions of both time and space. If we express the field in a form of $\mathscr{E} = \mathscr{E}(\vec{r},t)$, where $\vec{r}$ represents the spatial vector. It is found that the vector quantities in the Maxwell equations can be expressed in a single frequency harmonic form shown in (1-9). If we substitute this as well as the constitutive relationships into the Maxwell equations, the frequency-domain expression of (1-10)-(1-11) is yielded. The frequency-domain representation of waves is adopted through out this dissertation.

$$\begin{aligned}\mathscr{E}(\vec{r},t) &= |\overline{E}(\vec{r})|\cos[\omega t + \phi_e(\vec{r})] \\ &= \mathrm{Re}\{|\overline{E}(\vec{r})| e^{j[\omega t+\phi_e(\vec{r})]}\} \\ &= \mathrm{Re}\{|\overline{E}(\vec{r})| e^{j\phi_e(\vec{r})} e^{j\omega t}\} \\ &= \mathrm{Re}\{\overline{E}(\vec{r}) e^{j\omega t}\}\end{aligned} \tag{1-9}$$

$$\nabla\times\overline{E} = -j\omega\mu\overline{H} \tag{1-10}$$

$$\nabla\times\overline{H} = j\omega\in\overline{E} + \sigma\overline{E} + \overline{J}_i \tag{1-11}$$

2. Electrical, Magnetic Fields and Energy

The Maxwell equations (1-10)-(1-11) provide the governing laws for electrical, magnetic fields and current behaviors in medium with properties of ε, μ and σ. Any of the quantity within the equations might be considered as unknowns depending on different real life applications. Generally, for beam-forming network design, a typical problem dealt with is that given impressed current $\overline{J}_i$ excitations within a known geometry to solve for the field performance. Similarly, when a beam former feeds array, conducting current on the antenna would produce travelling fields in free space. The latter is a typical radiation problem, which will be exclusively discussed in the section 1.2. In this section, we focus on deriving the solution of planar waves from Maxwell functions and illustrate their relationships with energy storage and propagations.

Assuming fields exist in a source-free region, then they must satisfy the Maxwell equations of (1-10) and (1-11) providing $\overline{J}_i = 0$. Substitute one to the other, and it gives electric vector wave equation (1-12) and magnetic vector wave equation (1-13).

$$\nabla \times \nabla \times \overline{E} + (\omega^2 \varepsilon\mu + j\omega\mu\sigma)\overline{E} = 0 \tag{1-12}$$

$$\nabla \times \nabla \times \overline{H} + (\omega^2 \varepsilon\mu - j\omega\mu\sigma)\overline{H} = 0 \tag{1-13}$$

Applying the vector identity of (1-14), equations (1-12) and (1-13) can be written as (1-15) and (1-16).

$$\nabla \times \nabla \times \overline{A} = \nabla(\nabla \cdot \overline{A}) - \nabla^2 \overline{A} \tag{1-14}$$

$$\nabla^2 \overline{E} + (\omega^2 \varepsilon\mu - j\omega\mu\sigma)\overline{E} = 0 \tag{1-15}$$

$$\nabla^2 \overline{H} + (\omega^2 \varepsilon\mu - j\omega\mu\sigma)\overline{H} = 0 \tag{1-16}$$

In convention, $\omega^2 \varepsilon\mu - j\omega\mu\sigma$ is defined as the wave number quantity, k^2. Thus (1-15) and (1-16) have arrived at a form with linear operators on the electrical and magnetic fields. These results of the rectangular components of the fields satisfy the Helmholtz equations of (1-17).

$$\nabla^2 \psi + k^2 \psi = 0 \tag{1-17}$$

Let us take the depolarized component of E_x for example, and assume it is independent of x and y. Thus E_x satisfies (1-18).

$$\frac{d^2E_x}{dz^2} + k^2 E_x = 0 \tag{1-18}$$

Details on solving this equation and the wave equations with forcing term $\bar{J}_i$, are attached in Appendix A. Here we list the result in (1-19) without proof.

$$E_x = E_0 e^{-jkz} \tag{1-19}$$

The associated magnetic field is found by substituting (1-19) into (1-10).

$$H_y = \sqrt{\frac{\epsilon}{\mu}} E_0 e^{-jkz} = \frac{E_0}{\eta} e^{-jkz} \tag{1-20}$$

where the ratio between the E field and H field is defined as the wave impedance. Now if we apply relationship (1-9), the instantaneous fields are found as

$$\mathscr{E}_x(\vec{r},t) = \mathrm{Re}\{E_x e^{j\omega t}\} = E_0 \cos(\omega t - kz) \tag{1-21}$$

$$\mathscr{H}_y(\vec{r},t) = \mathrm{Re}\{H_y e^{j\omega t}\} = \frac{E_0}{\eta} \cos(\omega t - kz) \tag{1-22}$$

These are waves traveling along +z direction, as shown in Figure 1- 1, the magnetic field is in phase to the electrical field, both normal to the direction of propagation. The power density of the fields can be found by calculating the Poynting vector, **S**. In frequency domain, **S** for the fields in (1-21) and (1-22) is shown in (1-23).

$$\mathrm{S}=\mathrm{E}\times\mathrm{H}^* = \hat{z}\frac{E_0^{\,2}}{\eta} \tag{1-23}$$

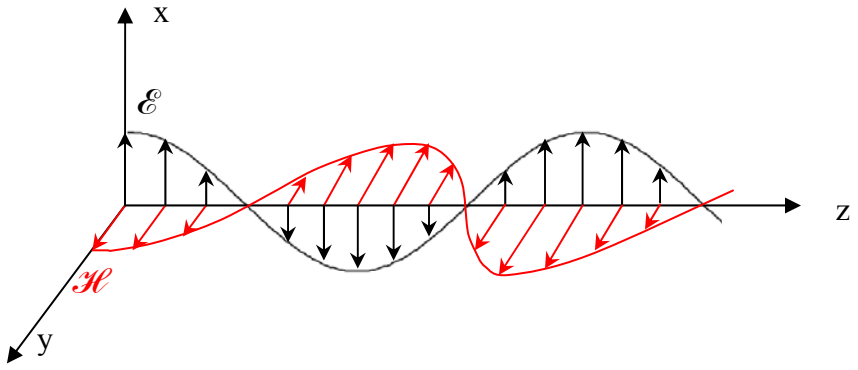

Figure 1- 1. Linearly Polarized Uniform Traveling Wave along z Direction

Result in (1-23) indicates that real power flows along z direction with power density value of E_0^2/η. In many electronic designs such as transmission line and antenna, it is always desirable to have real **S**. However, in reality, when the electrical or magnetic fields encounter discontinuities, in order to satisfy the boundary conditions, reflections may occur. The reflected fields may combine with the original field forming an imaginary portion of Poynting vector **S**. The imaginary power density represents the reactive powers stored, which eventually generate heat in the devices. The following paragraph illustrates how the other form of fields called standing waves can be formed.

Suppose the field of (1-19) travels in a bounded medium, due to discontinuity, it gets total reflection and forms a 180^o phase shift from the original incident wave. The total field at the region is the superposition of both fields as below:

$$\begin{aligned} E_x^{total} &= E_x^+ + E_x^- \\ &= E_0 e^{-jkz} + E_0 e^{jkz+j\pi} \\ &= E_0[\cos(kz) - j\sin(kz)] + E_0[\cos(kz+\pi) + j\sin(kz+\pi)] \\ &= E_0[\cos(kz) - j\sin(kz)] + E_0[-\cos(kz) - j\sin(kz)] \\ &= -j2E_0\sin(kz) \end{aligned} \tag{1-24}$$

$$\begin{aligned} H_y^{total} &= H_y^+ + H_y^- \\ &= \frac{E_0}{\eta} e^{-jkz} - \frac{E_0}{\eta} e^{jkz+j\pi} \\ &= \frac{E_0}{\eta}[\cos(kz) - j\sin(kz)] - \frac{E_0}{\eta}[\cos(kz+\pi) + j\sin(kz+\pi)] \\ &= \frac{E_0}{\eta}[\cos(kz) - j\sin(kz)] + \frac{E_0}{\eta}[\cos(kz) + j\sin(kz)] \\ &= \frac{2E_0}{\eta}\cos(kz) \end{aligned} \tag{1-25}$$

These co-existing waves are out of phase to each other, the phases in the time domain do not depends on z, hence they are no longer traveling waves. Consequently, the Poynting vector in (1-26) is an imaginary number, as shown in (1-26). The energy goes back and forth between the E and H fields with respect to time. These more or less represent their standing wave behaviors.

$$S=E\times H^{*}=-\hat{z}\frac{j2E_0^{\,2}}{\eta}\sin(2kz) \qquad (1\text{-}26)$$

We emphasized the fields' behavior and their relationships by reactive and real powers, because these concepts are frequently met in many electronic devices design process. Take the microwave tapered horn in Figure 1- 2 as an example, which is typical geometry of the radiation port in microwave lens design, because of the tapering, fields' reflection happens within the taper. As what we have seen above, part of the energy is stored due to the standing waves within the tapers. Note the tapering geometry, it plays essential rule to minimize the amount of stored powers. Understanding these basic concepts help construct improved designs. It is also worth pointing out that there is another form of evanescent waves that can steal power from the electronic devices. We shall review that in section 1.2 when discussing the near field of an antenna.

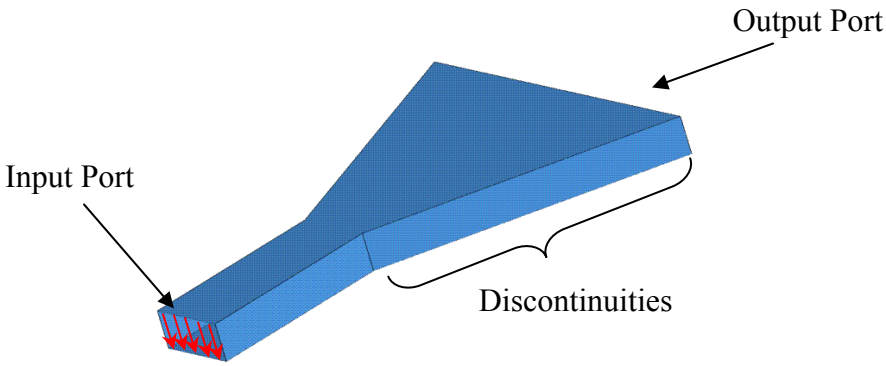

Figure 1- 2. Microwave Tapered Horn Example

3. Waves in Real Medium

In this dissertation, the microwave lens is designed on printed circuit board that has certain dielectric material filled layer. High dielectric constant material leads to size reduction, but the loss tangent of the medium tends to grow too. In this section, we discuss the waves' amplitude and phase variations in medium filled with lossy dielectric.

The general expression of the planar wave is (1-27). Assume it travels in a medium with ε value of (1-28), and σ =0.

$$E(\bar{r})=E_0 e^{-j\bar{k}\cdot\bar{r}} \qquad (1\text{-}27)$$

$$\varepsilon = \varepsilon_r + j\varepsilon_r \tan\delta \tag{1-28}$$

where $\tan\delta$ is the loss tangent of the medium. From the definition of wave number in (1-16), it is found

$$k = \omega\sqrt{(\varepsilon_r + j\varepsilon_r \tan\delta)\mu} \approx \omega\sqrt{\varepsilon_r\mu}(1 - \frac{j\tan\delta}{2}) \tag{1-29}$$

Assume $\hat{k} = \hat{r}$,and substitute (1-29) into (1-27), this gives

$$E(\bar{r}) = E_0 e^{-r\omega\sqrt{\varepsilon_r\mu}\tan\delta/2} e^{-jr\omega\sqrt{\varepsilon_r\mu}} \tag{1-30}$$

This is still planar wave traveling in the r direction, but with amplitude decaying ratio of $e^{-r\omega\sqrt{\varepsilon_r\mu}\tan\delta/2}$ due to the loss tangent. The phase variation follows the relation of the real portion of ε. In Figure 1- 3, the amplitude decaying trend at different frequencies for Rogers 3006 is illustrated. As the frequency increases, more attenuation occurs. Figure 1- 4 shows the phase variation along r direction for different materials. The solid reference line in Figure 1- 4 represents the phase constant planes in the free space. The difference between the two curves demonstrates that waves travelling in higher ε_r medium can receive the same phase variation but travel much shorter distance. This enables the size of the printed lenses to be decreased by a factor of $\sqrt{\varepsilon_r}$ from the ones in free space.

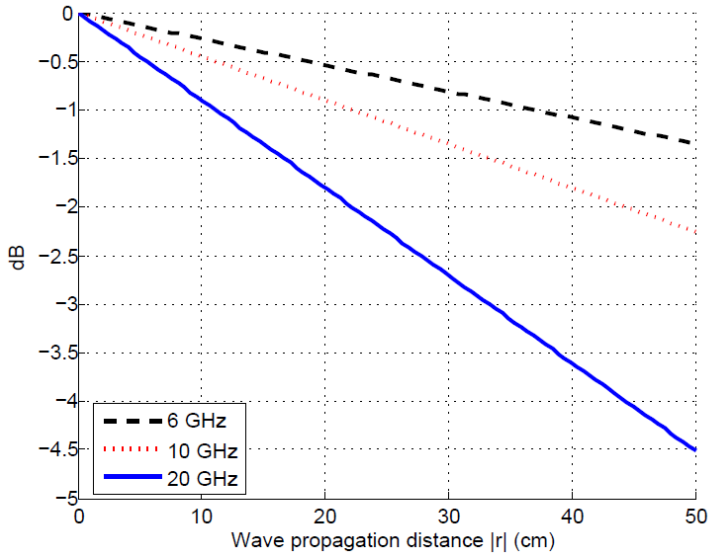

Figure 1- 3. Field Amplitude versus Traveling Distance in Rogers 3006 (ε_r =6.15, $\tan\delta$ =0.002) at Frequency of 6, 10 and 20 GHz

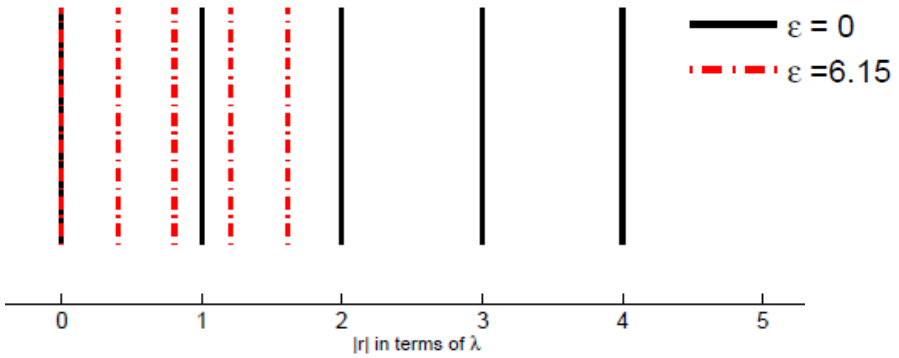

Figure 1- 4. Phase Front versus Traveling Distance for Different ε

So far we have dealt with the planar wave representation in the form of (1-27). Beside of the loss tangent of the material, the amplitude of the waves may decay in certain order of |r|. Two typical cases are the spherical and cylindrical waves, as shown in (1-31) and (1-32), which form circular phase fronts in the propagation domain.

$$E(\bar{r}) = \frac{E_0}{|\bar{r}|} e^{-j\bar{k}\cdot\bar{r}} \tag{1-31}$$

$$E(\bar{r}) = \frac{E_0}{\sqrt{|\bar{r}|}} e^{-j\bar{k}\cdot\bar{r}} \tag{1-32}$$

4. Some Parameters for Circuit Analysis

The electric and magnetic fields contain energy, and the real power of the Poynting vector leads to its propagation. This energy can be guided and travel along constrained structures. When the dimension of the structure is much smaller than the wavelength, circuit elements are usually derived from the Maxwell equations to facilitate the design.

Voltage **V**, occurs between two parts of the circuit elements and it is defined by line integration of the E field, as shown in (1-33). Current **I**, standards for the amount of Coulombs passed per second, relates to the conducting current density by (1-34), where A is the cross-sectional area of the conductor. Resistance **R**, measures the opposition to the passage of the current, and it determines the amount of current through the object for

a given potential difference of V, hence **I=V/R**. Capacitance **C**, defined by (1-35) depicts the ability of storing charges (or electrical fields), where Q is the amount of charges. An inductor **L**, which stores currents (or magnetic fields due to these currents), is defined by the ratio between the magnetic flux over the current producing these fields, (1-36).

$$V = \int_l \overline{E} \cdot d\overline{l} \tag{1-33}$$

$$I = \overline{J}_c A \tag{1-34}$$

$$C = \frac{Q}{V} \tag{1-35}$$

$$L = \frac{\Phi}{I} \tag{1-36}$$

where

$$\Phi = \int_s \overline{B} \cdot d\overline{A} \tag{1-37}$$

Now let us consider a transmission line with characteristic impedance of Z_0 connecting to load Z_{in}, as shown in Figure 1- 5. For instant, in this dissertation, typically transmission line is designed at Z_0=50Ω. The load Z_L might represent any port that attaches to the transmission lines, e.g. horn antenna, terminal load, etc. At the discontinuity point, voltage and current exist in both directions, here we expressed them as

$$V_L = V^+ + V^- \tag{1-38A}$$

$$I_L = I^+ + I^- \tag{1-38B}$$

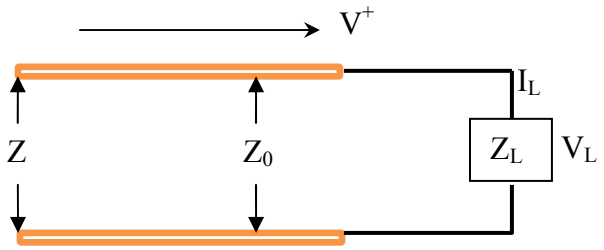

Figure 1- 5. A Transmission Line with Impedance Z_0 Terminated by Load Z_L

It is not hard to find that equation (1-39) holds after applying the Ohm's law. By substituting (1-38) in (1-39), the *reflection coefficient* between the backward and forward voltages is calculated as (1-40). This is an important design parameter, as it tells how much field (and power) is reflected from the load component of Z_L. We will shortly see that Z_L normally is a function of frequency, given constant transmission line Z_0, and Γ is

used to characterize the bandwidth of the microwave devices. Besides, the real and imaginary parts of the total system impedance Z can also be used to evaluate the power efficiency.

$$\frac{V_L}{Z_L} = \frac{V^+}{Z_0} - \frac{V^-}{Z_0} \tag{1-39}$$

$$\Gamma = \frac{Z_L - Z_0}{Z_L + Z_0} \tag{1-40}$$

A beam-forming network typically has multiple inputs and outputs. Figure 1- 6 illustrates the typical problem we will deal with in the following chapters. The N ports network behavior is described by the scatter coefficient matrix of (1-41). S_{ij} represents the coupling between port i and j when all other ports are terminated. We shall keep in mind that the matrix shown below only captures the network behavior at single frequency. Should the frequency responds are required, SNP matrix at multiple frequencies have to be calculated. The SNP file is a standard touchstone format that is used to describe N-Scatter-Parameters.

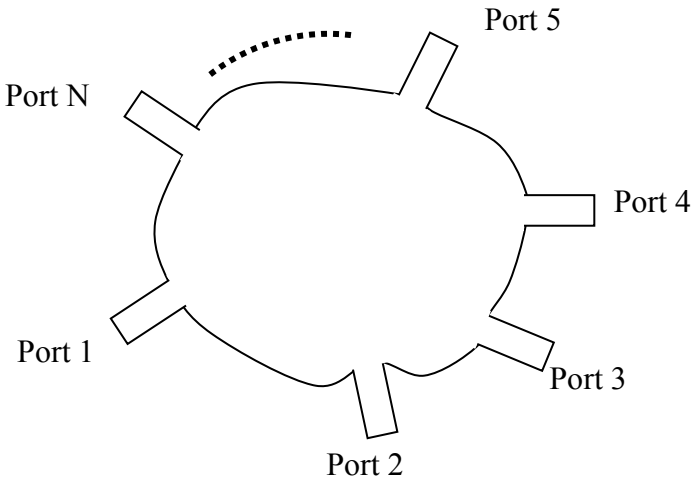

Figure 1- 6. Typical N Port Network Structure

$$SNP = \begin{bmatrix} S_{11} & S_{21} & S_{31} & \cdots & S_{N1} \\ & S_{22} & S_{32} & \cdots & S_{N2} \\ & & S_{33} & \cdots & S_{N3} \\ & & & \ddots & \vdots \\ & & & & S_{NN} \end{bmatrix} \tag{1-41}$$

1.2 Review of Antenna and Array Fundamentals

Typical microwave lens design involves topics on radiation component, wave propagation in lossy medium, transmission line and array. Thus it is necessary to review some of the fundamentals on antenna and array theories. The purpose of the following paragraphs is to describe how antenna and array work. Two examples are used, one elemental dipole and one regular dipole. The former is used to describe how the near field and far field of the antenna behave, as well as the representation of pattern and gain. The latter is adopted to illustrate how the Fourier theory relates to the far field of a real antenna, and how it governs the behavior of an array. We will cover both topics to the extent that helps understand the microwave lens design in this dissertation.

1. Antenna

The excitation of a real antenna is impressed electric current, as shown in equation (1-11). Sometimes it might be easy to consider the current as magnetic current, because a looped electric current can be regarded as magnetic dipole, and vise versa. We stay with the electric current representation in this dissertation.

Let us assume a current $\overline{J}_i(\bar{r}_0)$, where $\bar{r}_0$ implies the current distribution coordinate. Now the fields at observation coordinate of $\bar{r}$ become function of $\overline{J}_i$. Typical method for solving equation (1-10)-(1-11) is the potential theory. Because the divergence of H field is zero, from vector identity, H can be expressed as $\overline{H} = \nabla \times \overline{A}$, where $\overline{A}$ is called the magnetic potential vector. If we substitute it back into (1-10), equation (1-42) is yielded, due to which the electrical scalar potential can also be defined based on $\nabla\Phi = \overline{E} + j\omega\mu\overline{A}$. Reorganizing equations (1-10)-(1-11) and using potentials and vector identity, equation (1-43) can be found.

$$\nabla \times (\overline{E} + j\omega\mu\overline{A}) = 0 \tag{1-42}$$

$$\nabla(\nabla \cdot \overline{A}) - \nabla^2\overline{A} = (j\omega\varepsilon + \sigma)\nabla\Phi + (\omega^2\varepsilon\mu - j\omega\mu\sigma)\overline{A} + \overline{J}_i \tag{1-43}$$

Lorentz Gauge assumes that $\nabla(\nabla \cdot \overline{A}) = (j\omega\varepsilon + \sigma)\nabla\Phi$, after applying this condition. (1-43) becomes an inhomogeneous equation of (1-44).

$$\nabla^2\overline{A} + k^2\overline{A} = -\overline{J}_i \tag{1-44}$$

$\overline{A}$ can be solved from equation (1-44), the result is shown in (1-45). Note the solution of $\overline{A}$, it is in the observation coordinate, while the integration is over source coordinate.

$$\overline{A}(\bar{r}) = \frac{1}{4\pi}\iiint_{r_0} \frac{\overline{J}_i(\bar{r}_0)e^{-jk|\bar{r}-\bar{r}_0|}}{|\bar{r}-\bar{r}_0|}dv_0 \tag{1-45}$$

After obtaining the magnetic potential, the electrical and magnetic fields can be found from the detailed derivation in Appendix A. The results are given in (1-46)-(1-47).

$$\overline{E} = -j\omega\mu\overline{A} + \frac{1}{j\omega\varepsilon - \sigma}\nabla(\nabla\cdot\overline{A}) \tag{1-46}$$

$$\overline{H} = \nabla\times\overline{A} \tag{1-47}$$

It is observable that given any current distributions, the electrical and magnetic fields at observation point $\bar{r}$ can be solved by two steps. 1) solve the potential by integration of the current over its supporting structure; 2) solve the fields by relationships given in (1-46)-(1-47). This seems straight forward, however, in reality, to sense the exact current distribution on the supporting structure itself can be extremely hard. A typical way of solving the current distribution $\overline{J}_i(\bar{r}_0)$ is assuming it has a format governed by linear combinations of basis functions weighted by unknown coefficients. By substituting it into (1-45), the fields can be solved. After applying boundary conditions, equations can be yielded to solve these unknowns. We will discuss the concepts of solving $\overline{J}_i(\bar{r}_0)$ and the fields using numerical simulations in section 1.4.

To address more antenna basics, we use an elemental dipole that has been explicitly solved in Appendix A as an example. The infinitesimal dipole lies along the z axis, as shown in Figure 1-7. Assume the current on it is $\overline{J} = \hat{z}J_0\delta(x_0)\delta(y_0)\delta(z_0)$. According to Appendix A, $\overline{A}(\bar{r})$, $\overline{E}(\bar{r})$ and $\overline{H}(\bar{r})$ are solved as shown in (1-48)-(1-50).

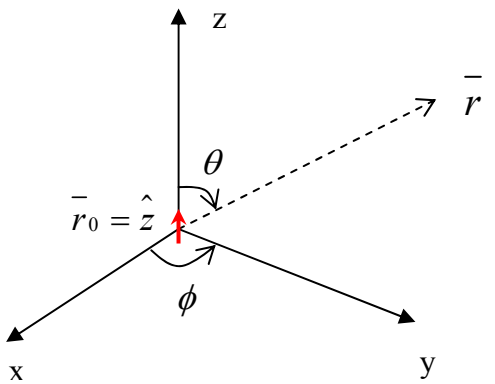

Figure 1- 7. Elemental Dipole along z Axis

$$\overline{A}(\bar{r}) = \hat{z}J_0 \frac{e^{-jkr}}{4\pi r} = \hat{r}J_0 \cos\theta \frac{e^{-jkr}}{4\pi r} - \hat{\theta}J_0 \sin\theta \frac{e^{-jkr}}{4\pi r} \tag{1-48}$$

$$\overline{H}(\bar{r}) = \hat{\phi}J_0 \sin\theta \frac{e^{-jkr}}{4\pi r}(jk + \frac{1}{r}) \tag{1-49}$$

$$\overline{E}(\bar{r}) = -\hat{r}\frac{j2J_0\eta}{k}\cos\theta \frac{e^{-jkr}}{4\pi r}(\frac{jk}{r} + \frac{1}{r^2}) + \hat{\theta}\frac{jJ_0\eta}{k}\sin\theta \frac{e^{-jkr}}{4\pi r}(k^2 - \frac{jk}{r} + \frac{1}{r^2}) \tag{1-50}$$

From (1-49)-(1-50), a couple of things are observed. First, the fields produced by infinitesimal dipole along z direction travel along radial direction. Second, it produces E field polarized waves along $\hat{r}$ and $\hat{\theta}$, and H field polarized waves along $\hat{\phi}$. Third, both E and H have components attenuating in the order(s) of $1/r$. High order fields decay much faster than that of the low order fields. In the far field, the fields can be approximated by the lowest order term, resulting in equations (1-51) and (1-52). It is noticed that in the far field E=ηH, and the cross product of the unit vector between $\widehat{E}$ and $\widehat{H}$ gives the wave propagation direction.

$$\overline{H}_f(\bar{r}) = \hat{\phi}jkJ_0 \sin\theta \frac{e^{-jkr}}{4\pi r} \tag{1-51}$$

$$\overline{E}_f(\bar{r}) = \hat{\theta}jkJ_0\eta \sin\theta \frac{e^{-jkr}}{4\pi r} \tag{1-52}$$

High order fields exist at the near field of the elemental dipole, and this applies to most of the real antennas. Different from the standing wave mentioned in section 1.1, the high order fields behave like evanescent waves that die down shortly after increasing r. If we look at the Poynting vector of the fields in (1-53), there are both reactive power, stored along $\hat{\theta}$ and $\hat{r}$, and real power that only travels along $\hat{r}$ direction. Figure 1- 8 shows the radiated power density versus θ in a linear scale. This type of pattern information is very important to evaluate the beam width of the port design in microwave lens. If a radiation element is designed to send signal into certain direction, the beam pattern is critical information to calculate the amount of power delivered into a given receiving aperture.

$$S = \overline{E} \times \overline{H}^* = \hat{\theta}\frac{J_0^2\eta \sin 2\theta}{k}\frac{1}{(4\pi r)^2}(\frac{j}{r^3} + \frac{jk^2}{r}) + \hat{r}\frac{J_0^2\eta \sin^2\theta}{k}\frac{1}{(4\pi r)^2}(\frac{j}{r^3} + \frac{2k}{r^2} + k^3) \tag{1-53}$$

2. Array

Identical antennas operating close to each other are considered as an array. In doing so, electronic steerable beams can be produced by simply varying the phase of the antennas. This section covers the basis of array concepts by reviewing its relationship to spatial Fourier transforms. The amplitude and phase tapering will be discussed by examples of uniform spacing linear dipole array.

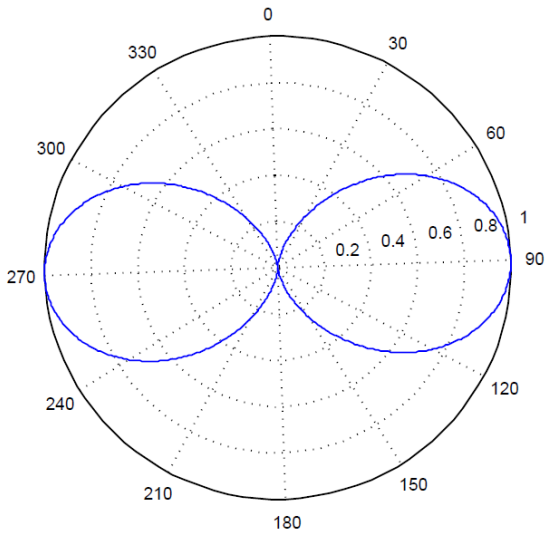

Figure 1- 8. Elemental Dipole Linear Scale Power Density Pattern versus θ

In practical design, as far as radiation concerns, the far field is more of an interest. Thus we can apply the far field approximation of $r \gg r_0$ before calculating the Green's function integration. As it is shown in the Appendix A, after applying Taylor expansion of $|\bar{r}-\bar{r}_0|$, the Green's function term in equation (1-45) becomes (1-54).

$$\frac{e^{-jk|\bar{r}-\bar{r}_0|}}{|\bar{r}-\bar{r}_0|} \simeq \frac{e^{-jk[r-r_0\cos\psi_0+\frac{r_0^2\sin^2\psi_0}{2r}+o(\frac{r_0^3}{r^2})]}}{r-r_0\cos\psi_0+\frac{r_0^2\sin^2\psi_0}{2r}+o(\frac{r_0^3}{r^2})} \tag{1-54}$$

where $\psi_0 = \hat{r}_0 \cdot \hat{r}$. When $r \gg r_0$, the denominator of (1-54) approaches r, and the high order term in the phase can be dropped out too. (1-54) becomes

$$\frac{e^{-jk|\bar{r}-\bar{r}_0|}}{|\bar{r}-\bar{r}_0|} \simeq \frac{e^{-jkr}}{r}(e^{jkr_0\cos\psi_0 - \frac{jkr_0^2\sin^2\psi_0}{2r}}) \tag{1-55}$$

Assume D_{max} is the maximum dimension of the antenna. It has been proved in the literature that as long as $r > (D_{\max})^2 / \lambda$, the r_0^2 / r phase term can be ignored. Hence:

$$\frac{e^{-jk|\bar{r}-\bar{r}_0|}}{4\pi|\bar{r}-\bar{r}_0|} \simeq \frac{e^{-jkr}}{4\pi r} e^{jkr_0\cos\psi_0} = \frac{e^{-jkr}}{4\pi r} e^{j\bar{k}\cdot\bar{r}_0} \tag{1-56}$$

Substitute the above result into equations (1-45)-(1-47), the H and E far fields are solved as shown in (1-57)-(1-58).

$$\bar{H}_f = -jk\frac{e^{-jkr}}{4\pi r}\iiint_{r_0}[\hat{k}\times\bar{J}(\bar{r}_0)]e^{j\bar{k}\cdot\bar{r}_0}dv_0 \tag{1-57}$$

$$\bar{E}_f = -jk\eta\frac{e^{-jkr}}{4\pi r}\iiint_{r_0}[(\hat{k}\cdot\bar{J}_0)\hat{k}-\bar{J}(\bar{r}_0)]e^{j\bar{k}\cdot\bar{r}_0}dv_0 \tag{1-58}$$

These equations apply to all types of real antennas. Interestingly, the integration parts of both equations have a format of Fourier transforms between $\bar{k}$ and $\bar{r}_0$ domains. Let us take (1-58) as an example, assume the effective current is named as $\bar{J}_\perp(\bar{r}_0)$, pattern is denoted by $\bar{f}(\theta,\varphi)$. The field pattern term (the integral portion) is actually the Fourier transform of the current along the directions that are normal to propagation direction $\hat{k}$, as shown depicted by (1-59). The inverse transform is (1-60).

$$\bar{f}(\theta,\varphi) = \widetilde{\bar{J}_\perp}(\bar{k}) = \iiint_{r_0}\bar{J}_\perp(\bar{r}_0)e^{j\bar{k}\cdot\bar{r}_0}dv_0 \tag{1-59}$$

$$\bar{J}_\perp(\bar{r}_0) = \frac{1}{(2\pi)^3}\iiint\widetilde{\bar{J}_\perp}(\bar{k})e^{-j\bar{k}\cdot\bar{r}_0}d\bar{k} \tag{1-60}$$

Suppose another identical antenna is located at $\bar{r}_1+\bar{r}_0$, as illustrated by Figure 1- 9, we now want to estimate the total radiation fields at observation point $\bar{r}$. The solution is approached in this way: first solve the field for the position translated antenna, and then use superposition to estimate the total fields. Note this ignores the mutual couplings between the two elements, however; in practical design, it has led to a reasonable estimation.

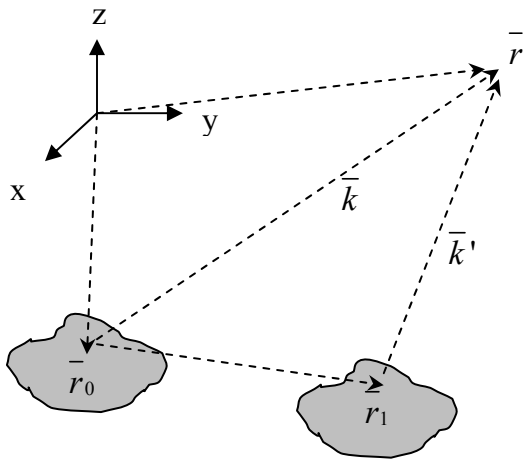

Figure 1- 9. Shifted Current Source in Free Space

The current source at $\bar{r}_1 + \bar{r}_0$ can be written as

$$\begin{aligned} \bar{J}_\perp(\bar{r}_1 + \bar{r}_0) &= \frac{1}{(2\pi)^3} \iiint \widetilde{\bar{J}}_\perp(\bar{k}_1) e^{-j\bar{k}_1 \cdot (\bar{r}_1 + \bar{r}_0)} d\bar{k}_1 \\ &= \frac{1}{(2\pi)^3} \iiint [\widetilde{\bar{J}}_\perp(\bar{k}_1) e^{-j\bar{k}_1 \cdot \bar{r}_1}] e^{-j\bar{k}_1 \cdot \bar{r}_0} d\bar{k}_1 \end{aligned} \tag{1-61}$$

The forward transform gives

$$\begin{aligned} \widetilde{\bar{J}}_\perp(\bar{r}_1 + \bar{r}_0) &= \frac{1}{(2\pi)^3} \iiint_{r_0} \{\iiint \widetilde{\bar{J}}_\perp(\bar{k}_1) e^{-j\bar{k}_1 \cdot (\bar{r}_1 + \bar{r}_0)} d\bar{k}_1\} e^{j\bar{k} \cdot \bar{r}_0} dv_0 \\ &= \frac{1}{(2\pi)^3} \iiint_{r_0} \widetilde{\bar{J}}_\perp(\bar{k}_1) \{\iiint e^{-j\bar{k}_1 \cdot (\bar{r}_1 + \bar{r}_0)} e^{j\bar{k} \cdot \bar{r}_0}\} d\bar{k}_1 dv_0 \end{aligned} \tag{1-62}$$

Apply the relationship (1-63) in (1-62), we get (1-64).

$$\iiint e^{j\bar{k} \cdot (\bar{r} - \bar{r}_0)} d\bar{k} = (2\pi)^3 \delta(\bar{r} - \bar{r}_0) \tag{1-63}$$

$$\widetilde{\bar{J}}_\perp(\bar{r}_1 + \bar{r}_0) = \frac{1}{(2\pi)^3} \iiint_{r_0} \widetilde{\bar{J}}_\perp(\bar{k}_1) (2\pi)^3 \delta(\bar{r}_1 + \bar{r}_0) e^{j\bar{k} \cdot \bar{r}_0} dv_0 = \widetilde{\bar{J}}_\perp(\bar{k}_1) e^{-j\bar{k} \cdot \bar{r}_1} \tag{1-64}$$

Thus the pattern of a shifted antenna is a product between its original pattern and a phase shift term.

$$\bar{f}_{\bar{r}_1 + \bar{r}_0}(\theta, \varphi) = \bar{f}_{\bar{r}_0}(\theta, \varphi) e^{-j\bar{k} \cdot \bar{r}_1} \tag{1-65}$$

The total pattern for the two elements is

$$\overline{f}_T(\theta,\varphi) = \overline{f}(\theta,\varphi)(1+e^{-j\bar{k}\cdot\bar{r}_1}) \tag{1-66}$$

It is easy to extend the concepts to N identical antennas with relative position of $\bar{r}_i + \bar{r}_0$. The total pattern is equal to the elemental pattern times the phase term due to the array factor, as shown below

$$\overline{f}_N(\theta,\varphi) = \overline{f}(\theta,\varphi)(1+\sum_{i=1}^{N} e^{-j\bar{k}\cdot\bar{r}_i}) \tag{1-67}$$

In reality, the array elements are not necessarily to be fed by the same amplitude and phase as each other. As shown below, we develop the pattern expression for linear, uniform spacing array, which is a typical feeding scheme for the microwave lens design.

Suppose each antenna of the linear array is fed by amplitude a_i and phase φ_i, as indicated in Figure 1- 10, the current distribution in (1-59) will be weighted by factor of $a_i e^{-jk\varphi_i}$. This constant factor will eventually be translated into the array factor of equation (1-67). This leads to the particular result shown in (1-68).

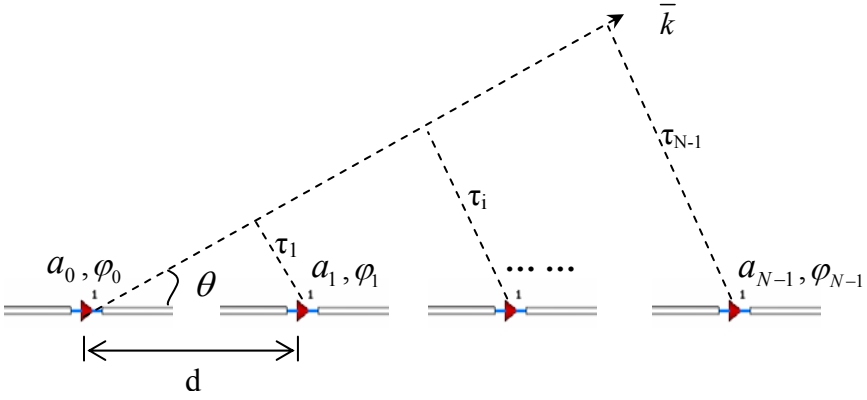

Figure 1- 10. Uniform Spacing Linear Dipole Array

$$\begin{aligned}\overline{f}_N(\theta,\varphi) &= \overline{f}(\theta,\varphi)(a_0 e^{j\varphi_0} + \sum_{i=1}^{N-1} a_i e^{j\varphi_i} e^{-j\bar{k}\cdot\bar{r}_i}) \\ &= \overline{f}(\theta,\varphi)[a_0 e^{j\varphi_0} + \sum_{i=1}^{N-1} a_i e^{j(\varphi_i - idk\cos\theta)}] \\ &= \overline{f}(\theta,\varphi)\sum_{i=0}^{N-1} a_i e^{j(\varphi_i - idk\cos\theta)}\end{aligned} \tag{1-68}$$

The array factor (AF) of linear array with uniform spacing d is

$$AF(\theta) = \sum_{i=0}^{N-1} a_i e^{j(\varphi_i - idk\cos\theta)} \tag{1-69}$$

For the given array spacing d, and feeding information, the array factor of linear array is a function of θ. The angle refereeing to the maximum value of AF is called beam angle; the difference between the first and the secondary maxima is called the side lobe level (SLL). Typical scheme of achieving scanning beams is to vary the feeding phase information. Typical method for reducing the SLL is to use tapered feeding amplitudes. For now assume each element is fed with the same amplitude $a_i = 1$, but using linearly increasing phases $\varphi_i = i\Delta\phi$. As an example, two cases of $\Delta\phi = 0$ and $\Delta\phi = \pi/2$ for $N = 6$, $d = \lambda/2$ are plotted in Figure 1- 11. It is observed that $\Delta\phi = \pi/2$ case gives beam angle of 30°, while beam stays at broadside for the no-phase-shift scenario. In case the elements are fed with tapered amplitudes, SLL can be greatly reduced, as shown in Figure 1- 12, nevertheless, it also evidently leads to a larger beam width.

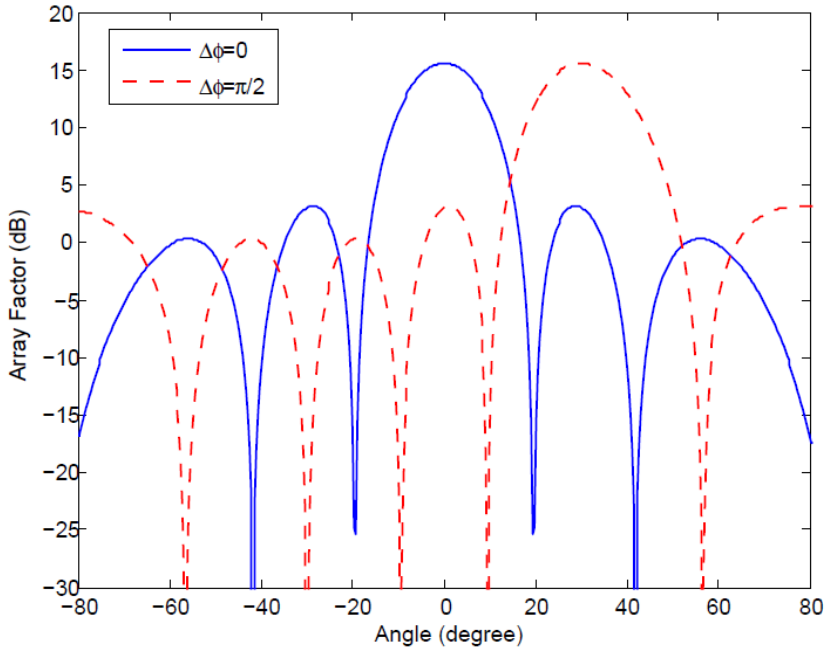

Figure 1- 11. Array Factors of 6 Uniform Spacing Linear Array with Uniform Amplitude Excitation and Linear Phase Shift of $\Delta\phi = 0$ and $\Delta\phi = \pi/2$

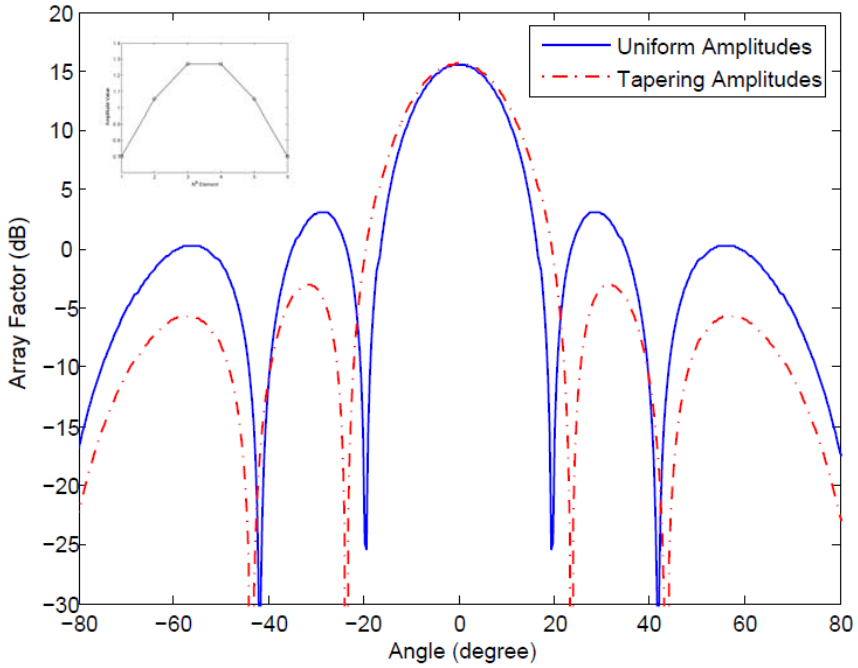

Figure 1- 12. Array Factors of 6 Uniform Spacing Linear Array with Uniform and Tapered Amplitude Excitations for $\Delta\phi = 0$

The pattern of the array is the product of the single element pattern and the array factor, as depicted by equation (1-68). In practical design, the beam width of the single element limits the scanning capability, because a large scanning angle in the array factor can only be supported by good radiation efficacy of a single antenna along that direction. Array does not produce beam of good quality at angles larger than a few dB beam width of a single element. In the following, we show some results for dipole phased array. According to Appendix A, the electric far field has the form of (1-70), resulting of pattern (1-71). Assume the dipole antenna has length L=0.4λ, the array is formed by 6 linear half-wavelength spacing elements along z direction (similar to Figure 1- 10). Comparison between single element pattern and the total pattern by applying the feeding schemes of Figure 1- 10 is demonstrated in Figure 1- 13. It is found that the array has achieved narrower beams that are steerable by controlling the phase shift angles. Besides, as the beam scans into large angle, the SLL increases and highest gain decreases accordingly. This is due to the fact that aperture efficiency is reduced in calculating the AF and the lower gain occurs at higher angles of the single element pattern.

$$\overline{E}_f = \hat{\theta} jk\eta J_0 L \frac{e^{-jkr}}{4\pi r} \frac{\sin(k\cos\theta L/2)}{k\cos\theta L/2} \sin\theta \tag{1-70}$$

$$\overline{f}_{dipole}(\theta,\varphi) = \hat{\theta} \frac{\sin(k\cos\theta L/2)}{k\cos\theta L/2} \sin\theta \tag{1-71}$$

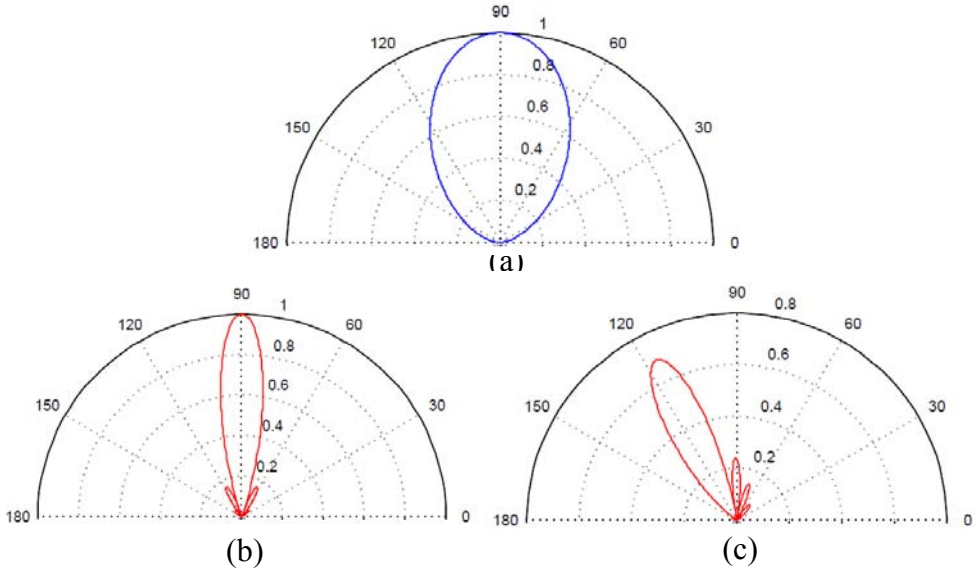

Figure 1- 13. Array Pattern of (a) Single Dipole L=0.4λ; (b) 6 Uniform Spacing Elements with $\Delta\phi = 0$; (c) 6 Uniform Spacing Elements with $\Delta\phi = \pi/2$

1.3 Introduction to Beam-forming Network

From previous sections, we learnt that antenna is a device that converts the impressed current into free space displacement current (or fields). The current information explicitly described the behavior of the radiated fields, as shown in equations (1-45)-(1-47). The same principle applies to an array too, but with the fed currents whose amplitudes and phases are adjustable to the designers. In doing so, it meets the needs of controllable beam shapes. In general, both single antenna and array can be considered as radiation aperture. As the aperture size increases (array case), energy can be squeezed into narrow beam; while the aperture current information determines the direction and pattern of its propagation. In reality, there are many applications such as satellite systems desirable to send one or multiple squeezed beams into steerable angles. The device that produces

dynamic feeding information for an aperture is critical; typically, it refers to the beam-forming network (BFN).

The BFN usually consists of M input ports and N-output ports that are subjected to feed N array elements. Typical layout is shown in Figure 1- 14. A BFN produces desirable amplitude and phase distributions across the aperture for each input port so that quality beams can be sent into different angles. A beam-forming network can be planar or 3 dimension, depending on the aperture requirement. Usually, 2D BFN produces 2D steerable fan beams, while 3D BFN generates 3D steerable pencil beams.

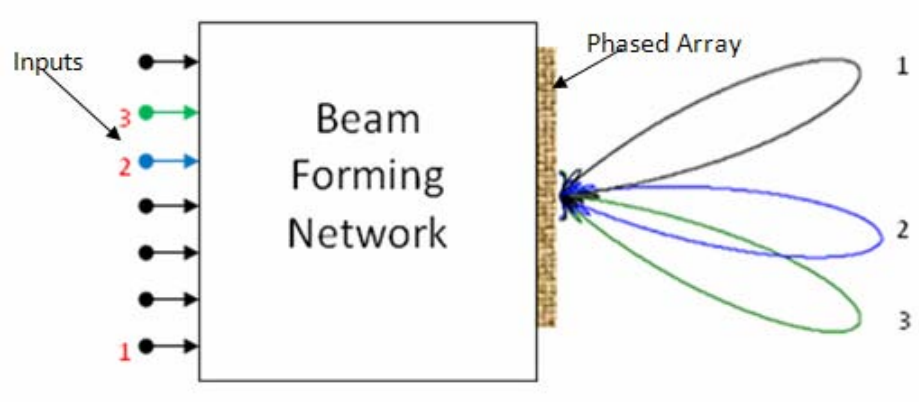

Figure 1- 14. Beam-forming Network

There are several ways of designing and categorizing the BFNs. In the following paragraphs, we are limited to describe several popular implementation schemes. They are the digital BFNs, network BFNs and microwave lens BFNs. The proposed design in this dissertation falls in the regime of lens BFNs. Advantages and drawbacks of different BFNs compared, are discussed here.

1. Digital Beam Forming Networks

Digital Beam Forming Networks use a computer or chip processor to control electronic components forming exact amplitude and phase for different channels of the array elements, as indicated in Figure 1- 15. The advantages of digital BFNs are that zero phase error, flexible amplitude tapering and infinite number of scanning steps. However, digital BFNs are limited to low-microwave frequencies due to low bit-bandwidth of current A/D

devices [4]. It may also require fast processors in order to form a coherence receiver. In case of large processing information, the computation speed becomes difficult.

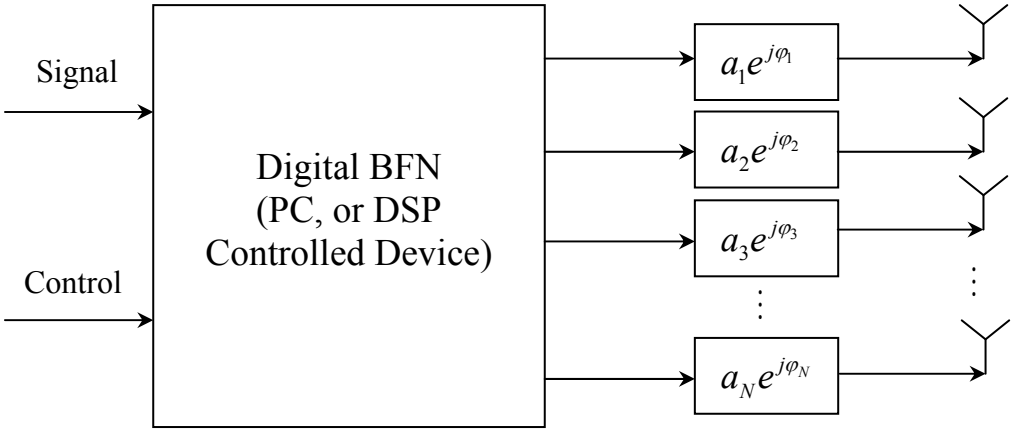

Figure 1- 15. Digital Beam-forming Network

2. Network Beam Forming Networks

Probably one of the earliest BFNs originated from the Butler matrix Beam Forming Networks. It consists of alternate rows of hybrid junctions and fixed phase shifters. Figure 1- 16 is a typical diagram for an 8x8 Butler matrix. The advantages of a Butler matrix are that it is easy to construct and it is also implementable using printed circuit boards. However, it requires crossovers on the lines as indicated in Figure 1- 16. The produced beams are dependent on frequency. The beam shift occurs as the frequency varies, which is not desirable in most communications links, as certain bandwidth information is expected to be sent to the same location.

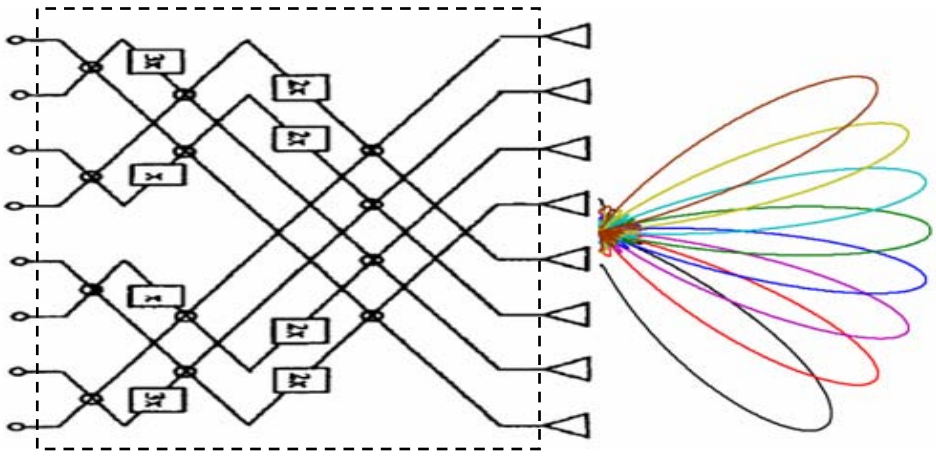

Figure 1- 16. Butler Matrix BFN

There are also other types of network BFNs such as Blass and Nolen matrices. The Blass matrix uses a set of array element transmission lines which intersect a set of beam port lines, with a directional coupler at each intersection [4]. However this type of BFN is hard to construct. The Nolen matrix is a modified design of Blass and Butler matrices, but is seldom used owing to the high parts count and difficulties connected with the networks [4].

3. Microwave lens Beam Forming Networks

The microwave lens is another type of Beam Forming Networks that apply path delay mechanism to form the desired phase front at the array input. A general diagram is shown in Figure 1-16. Each of the input connects to a beam port that radiates semi-circular phase front within the lens cavity. Array of receiving elements functioning as receivers then guide the energy into the output array. Because of the properly designed beam, receiving port positions and transmission line length, correct phase and acceptable amplitude distributions, can be achieved across the aperture.

There are several theories to initialize the lens geometries. In general, if the cavity is homogenous, the focal lens design approaches can be applied, e.g. Rotman lens. If the cavity is filled with inhomogeous medium, ray path equation as function of refraction index are adopted, e.g. Luneberg's lens. In this paper, we only deal with homogeneous medium. The path-length design mechanism in the microwave lens is independent of frequency, thus it is typically considered as true-time delay device. The homogenous lenses can be implemented using waveguide, striplines and microstrip materials, hence high power, wide bandwidth, and low profile can be achieved respectively.

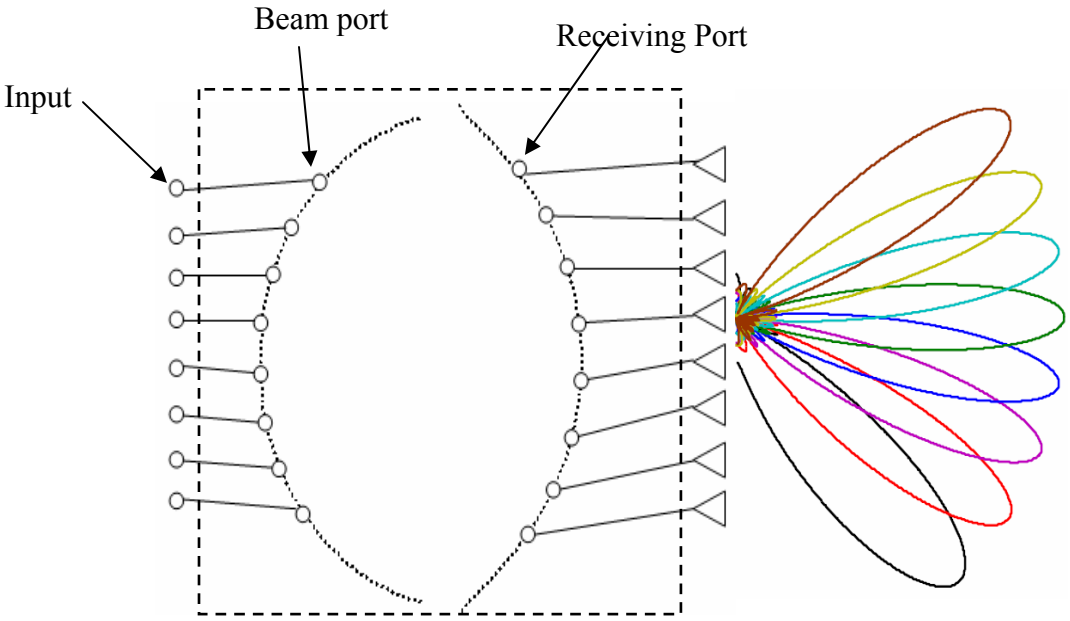

Figure 1- 17. Microwave Lens BFN

1.4 Introduction to Electromagnetics (EM) Simulation Methods

The performance of the electronic devices can be predicted by solving Maxwell equations. Given a number of parameters in (1-1)-(1-5) and solving for the others is typical EM analyzing task. As the boundary and problem itself get complicated, it is usually not possible to find solutions by hand as what we did for the dipoles in Appendix A. Numerically solving the Maxwell equations has been invaluable and attractive approach for decades. The advancement of various simulation methods has enabled and optimized many designs of complex electronic structures.

Solving Maxwell equations accurately is generally considered as full-wave simulation. Because Maxwell equations can be expressed in either time domain as in (1-1)-(1-5) or in frequency domain as in (1-10)-(1-11), the full time simulation methods are typically divided into time-domain (TD) and frequency-domain (FD) solvers. Furthermore, based on solving either integral equations or differential equations, the simulation methods are further classified into integral solvers and differential solvers. The time-domain integral solver is called Finite Integral Technique, which is the principle solver in CST Microwave Studio [5]; the time-domain differential solver is referred to the Finite

Difference-Time Domain (FD-TD), which is the principle solver in commercial software XFDTD [6] and GEMS [7]. Time-domain solvers usually require the problem structure being meshed by squares and cubes (cell), where the unknown E fields and H fields are assigned on the edges and centers. An example of time domain using Maxwell equations is shown in (1-72)-(1-73). The equations can be discretized by using the relationship in (1-74), resulting in the expressions presented in (1-75)-(1-76). As it shows, the coupled fields along both space and time are yielded as i and n propagate. The excitations of these solvers are typical time-domain signals such as a Gaussian pulse that contains the frequency bandwidth of interest. The frequency response can be calculated from Fourier transform of the time domain results afterwards.

$$\frac{\partial H_y}{\partial t} = \frac{1}{\mu}\left(\frac{\partial E_z}{\partial x} - \sigma_m H_y\right) \tag{1-72}$$

$$\frac{\partial E_z}{\partial t} = \frac{1}{\in}\left(\frac{\partial H_y}{\partial x} - \sigma E_z\right) \tag{1-73}$$

$$\left.\frac{\partial f}{\partial x}\right|_{x,t} = \frac{f(x+\Delta x,t) - f(x-\Delta x,t)}{2\Delta x} + o[(\Delta x)^3] \tag{1-74}$$

$$H_y\,|_{i+0.5}^{n+0.5} = D_a H_y\,|_{i+0.5}^{n-0.5} + D_b(E_z\,|_{i+1}^{n} - E_z\,|_{i}^{n}) \tag{1-75}$$

$$E_z\,|_{i}^{n+1} = C_a E_z\,|_{i}^{n} - C_b(H_y\,|_{i+0.5}^{n+0.5} - H_y\,|_{i-0.5}^{n+0.5}) \tag{1-76}$$

The frequency-domain integral solver is referred to as the Method of Moment (MoM), and it is the principle solver in commercial software FEKO; while the frequency-domain differential solver is referred to as the Finite Element Method (FEM), and it is the principle solver of software Ansoft HFSS. MoM generally considers currents as the unknowns, thus the volume mesh is not required as the current only flows on the surface of the geometry. FEM regards E and H fields as the typical unknowns, and it requires a 3D volume mesh. Similar to FDTD and FIT, fields based solvers sometimes require an artificial solving box where certain boundary conditions have to be complied with. FEM volume mesh is intrinsically suitable for problems with inhomogeous medium, as material property can be stored in each tetrahedral element upon creating the mesh. The MoM is very efficient for radiation problems, since the current distribution can be directly transformed to fields by applying the relationship of (1-45)-(1-47). Given the

request on far field only, the Fourier transform of (1-59)-(1-60) yields accurate and efficient calculations. The basic principle of frequency solvers is assuming the unknown identity has a format of linear combination of basis functions weighted by the unknown coefficients, as shown in (1-77). After enforcing the boundary conditions (e.g. (1-78)-(1-79) for PEC boundary), the problem can be translated into matrix equation to solve for the unknowns. This kind of technique is considered important to solve the differential (as well as integral) equations, because the solution of these equations is unique as long as the functions defining it are reasonably smooth and bounded [8]; if you find a solution, then that is the solution.

$$I(x) = \sum \alpha_i \Psi_i(x) \tag{1-77}$$

$$\hat{n} \times \overline{E} = 0 \tag{1-78}$$

$$\hat{n} \times (\overline{H}^{+} - \overline{H}^{-}) = J_s \tag{1-79}$$

When the objects get too large to be handled by the full-wave simulation, approximation has to be made. These types of solvers are considered as hybrid or asymptotic simulations. In Figure 1- 18, different types of computational EM methods are listed. Microwave lens structure in this dissertation is electronically large in two dimensions, with the third dimension much smaller than a wave length. It is generally considered as 2.5D problem. It may be too large to be handled by the full-wave simulation, and too small for applying simple asymptotic models.

In this dissertation, we adopt the planar Green's function MoM in FEKO to conduct the full-wave simulation for the lens design. And then devise a hybrid model for accelerating the simulation. Both methods will be validated by measurement. We further use MoM in FEKO to predict the performance of a couple of improved designs prior to their fabrication. CST was used to perform some initial assessment on the proposed lens simulation method, whose further results are compared with FEKO as well. Besides, the radiation components and tapered ports assisting the microwave lens design are investigated by aids of both FEKO and HFSS.

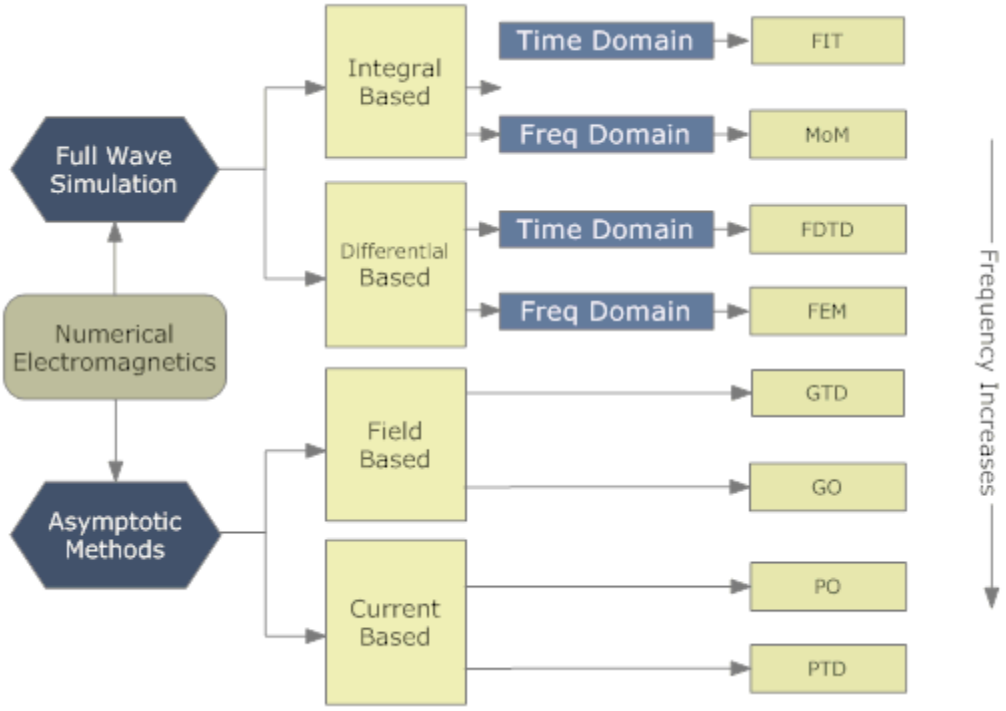

Figure 1- 18. Simulation Methods for Computational Electromagnetics

1.5 Scope of This Dissertation

In this dissertation, several improved designs of Microwave lens BFNs are presented. The electrical performance of microwave lens is classified by phase errors, amplitude errors, maximum scanning angle, tolerance angle of true-time delay, return loss, bandwidth, power efficiency, maximum power sustained etc; the mechanical performance have size, weight, etching/milling tolerance etc. Since 1970s, there have been two research mainstreams on microwave lens. First, seek more design parameters and freedoms in the lens initial geometrical optics formulation, at the same time improve phase-error performance. Second, explore computational simulation methods to estimate phase and amplitude performance across the aperture (typically for waveguide and microstrip lenses).

In this dissertation, initial efforts were put to explore new microwave lens design theories that can possibly take into account more design variables/freedoms but offering the minimum phase errors. The existing lens design theories are all based on focal lens schemes, which presumably achieve zero phase errors for limited number of given focal beam ports, thus the non-focal ports have relatively high phase errors. The initial discovery is that the classical lens design theories can be remedied by taking into account more design parameters which offer great flexibility in formulating the lens geometry, and at the same time phase errors can be minimized by adopting a non-focal lens design scheme.

The exploration of microstrip lenses and non-focal lenses leads to a method for designing 360-degree scanning microwave lenses. Because of the constraints on focal equations, the existing lens theory can only design an asymmetric contour lens, which results of a maximum scanning angle of $\pm 90^0$ (in reality, the limit might be only $\pm 60^0$). The 360-degree lens proposed in this dissertation adopts the non-focal lens design concept, allowing using interleaving beam and receiving ports to reoccupy a symmetric lens contour, scanning an azimuth region of 360^0. It possesses most of the classical lens design advantages. Both simulation and measurement of the prototype lens have demonstrated very good results.

The two concepts above fall into the first mainstream of the microwave lens designs. To accurately predict the microwave lens performance, the second mainstream (simulation methods) is still in great need. Accurate simulation strategies mean that new designs can be evaluated and improved before the physical implementation. New performance factors such as amplitude, efficiently, tolerance angle of true-time delay, return loss and so on can be captured as well. In this dissertation, planar Green's function served as accurate simulation method is firstly investigated. It is then used to assess the design of the hybrid ray tracing methods. Existing full-wave software is not suitable for complete lens iterative optimization process because of the high computational cost. The ray tracing techniques proposed achieves thousand times accelerations and can reasonably approach both full-wave and measurement results.

The remainder chapters of the dissertation detail the design and analysis of microwave lens optimization, simulation, and 360-degree scanning techniques. Chapter 2 starts with reviewing the history, applications and general procedures of the microwave lens design. Chapter 3 covers the detail analysis of microwave lens design theory and the improved non-focal lens design scheme. The comparison with existing design methods are investigated by numerical simulations. Because the full-wave simulation serves as toolkits to assess the new design of 360-degree lenses, they are first presented in Chapter 4. Both simulation and measurement data are used in the analysis of Chapter 4. Chapter 5 describes the theory of 360-degree microwave lenses, the prototype designed, fabricated, and tested, and both the simulation and the measurement used to prove the concepts. Finally, the dissertation is closed by conclusions and future perspectives in Chapter 6.

CHAPTER 2. MICROWAVE LENS AS BEAM-FORMING NETWORK

Microwave lens emerged as a beam-forming network (BFN) in the 1950s, and it subsequently was invoked in numerous cutting edge applications. Advancements in materials science and fabrication technologies led to new implementations of the microwave lenses using waveguide, striplines and microstrip. In recent years, wireless communications supporting multi-beams and smart/adaptive antenna arrays have become more and more prevailing. Many applications including automobile collision-avoidance, remotely piloted radars, and remote satellite sensor all require compact, lightweigh antenna systems capable of providing wide-angle scanning over a broad frequency bandwidth. The development of printed microwave lenses has offered potential solutions for those emerging technologies. Figure 2- 1 shows general characteristics of the printed microwave lens.

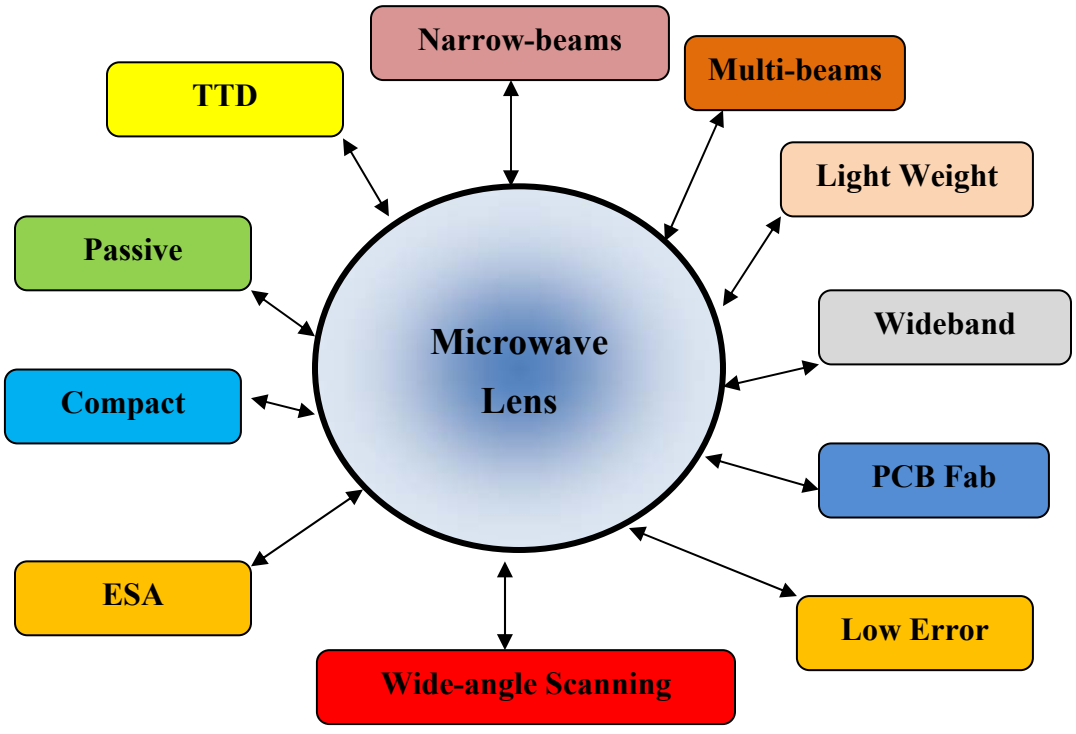

Figure 2- 1. Characteristics of Microwave Lens

It is not possible to propose a new design concept that is useful in practical sense without looking at the history of its development, real life applications and general design procedures. This chapter serves for such purpose. The history of microwave lens design familiarizes us with how previous researchers improved the design of microwave lenses and their visions upon the development. Furthermore, to review the past and emerging applications of microwave lens helps form and assess the usefulness of the newly proposed designs. The microwave lens design procedures demonstrate how a lens model can be formulated, simulated and eventually fabricated. This is intended to build a large picture where we can allocate the contributions of this dissertation. Therefore the objectives of the research can be reasonably outlined in section 2.4.

2.1 Brief History of Microwave Lens Development

Microwave lens is a structure capable of focusing the electromagnetic energy into a point. The microwave region defines the region with the electromagnetic spectrum with wavelength between 1mm and 300mm. During its development in 1950s, metallic plate and constrained line techniques were originally adopted in designing the Ruze Lens [9] and the R-2R microwave lens [10-12]. The array shape was designed to be circular with confined dimensions in the R-2R lens, which has ultimately limited its usefulness in practice. In 1957, a general theory of improved constrained lens was invented by Gent [13], and it was named bootlace lens because of its general structure shown in Figure 2-2.

According to [14] and [15], the Gent lens was adopted to design the precision aircraft landing system in Australia and the United States in 1970s. At the mean time, group of researchers in MIT funded by the Army Research Lab (ARL) carried research on the improvement of microwave lens design too. In 1960, Rotman and Tuner applied Gent general lens design schemes in their early warning radar systems [16]; in 1962 they reported a 3 perfect focal point microwave lens, which has greatly improved the phase error and design freedoms of the original Ruze Lens [17]. After this, systems based on the Rotman lens design was applied in Raytheon in 1967 [18] and further tested in the leading-edge of an F-4 aircraft in 1972 [16]. After Archer [19, 20] and recent researchers

proposed idea of designing printed Rotman Lens, more and more applications based on the microstrip and stripline designs are booming up [21-25].

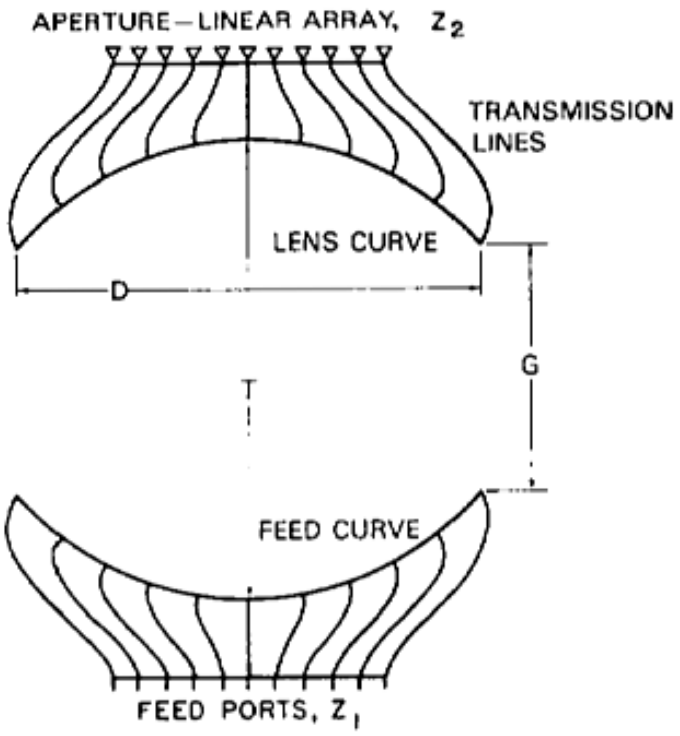

Figure 2- 2. The Gent Bootlace Lens Configuration [13]

Although the microwave lenses are dominated by the Rotman lens designs (RLD) since then, with the insight visions of model's fundamental limits, researchers have developed modified 3 focal lenses [26-29], methods of designing the 4 focal [30] and non-focal lens [31]. The conventional models and their development are briefly addressed in the following sections.

1. The Rotman Lens Design

The lens design models in this dissertation starts with reviewing the conventional Rotman Lens Design (RLD) [17]. The original RLD consists of a parallel conducting plate, fed by horn antennas along the beam contour, and transmission lines that connect the inner receiver contour and the outer phased arrays, as shown in Figure 2- 3. The lens was

designed for feeding linear arrays. There are 3 focal points located on the beam contour, which generate zero theoretical phase errors along the phase front of the linear array elements. In the original model the parallel plate was assumed air filled. The beam contour was restricted to be circular and the scan angle produced by linear array is constrained to be the same value as the subtended beam port angle.

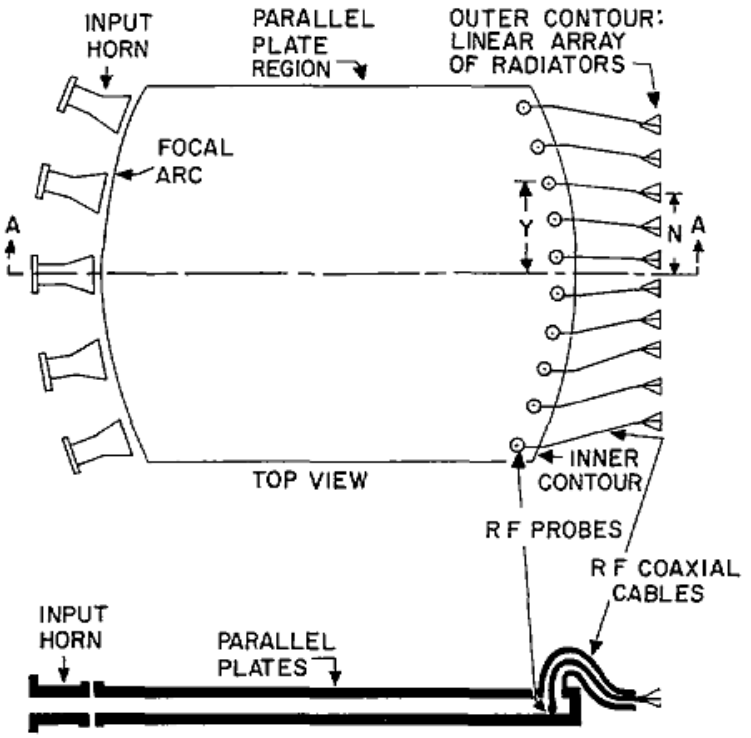

Figure 2- 3. The Original Rotman Lens Configuration [17]

2. Katagi's Refocus Lens Design

Based on the concept of Rotman lens design, Katagi proposed an improved design in 1983 [27]. By applying a refocus method, the modified equations theoretically demonstrated that changing the circular contour and altering the radiation angles yield lower phase errors than the original design. The phase error reduction across the aperture was proven to be very important, especially when designing lenses larger than 100 wavelengths. The path-length equations can be approximated by expanding the trigonomial terms using power series. In this way, the phase error can be expressed in terms of linear combination of power of the path lengths. As discussed in [32, 33], such

refocus method can correct the lower order phase errors but cannot compensate the higher order errors.

3. Hansen's Design Trade for Rotman Lens

The general design equations and parameters are reformulated in R. C. Hansen's work [29]. In this design trade, the elliptical beam contour was introduced, and the relation between the scan angle and the beam subtended angle is captured by the parameter defined as $\gamma=\sin\Psi/\sin\alpha$, which are discussed in Section 3.1.1. Relation between the phase errors and typical design parameters are studied, the optimization factor β is finalized. In Hansen's work, the lens is still assumed air filled and beams are scanned into free space. The gain is discussed but inner reflections and mutual coupling have not been considered for the amplitude analysis.

4. Smith's Trifocal Lens Designs

M. S. Smith [28] emphasized the flexibility of designing large scan angle Rotman Lens by applying small subtended beam regions. The path-length equation was firstly expressed in a power series and the importance of focal length R factor was studied. In later work [34], the Snell's equations and 1D aperture theory were first time used to predict the amplitude performance of the Rotman Lens. A prototype of waveguide lens, designed based on conventional 3 focal method, without side wall assumptions, was conducted. Both simulation and measurement [34] demonstrated cosine shape tapered amplitude distributions.

5. Planar Quadrufocal Lens Designs

The Quadrufocal bootlace lenses were first proposed to design 3 dimensional lens beams forming networks by Rao [35, 36]. The lens consists of four perfect focal points along a linear feeding line and a non planar output phased array. Rappaport and Zaghloul [30] applied this technique to design a circular feeding contour and linear output 2 dimensional lens. Different from the RLD, the planar lens allows 4 symmetric perfect focal points allocated along the beam contour, and this arrangement can still feed the same number of phased array elements at the output. Beam contour perturbation was the

technique adopted in [30] to improve the phase performance of the quadrufocal planar lens. It is noted that the lens equations only support designs of air filled lens and the scan angle is also restricted to be the same with the subtended angle.

6. Non-focal Lens Design and 360-degree Scanning Lens

The conventional Rotman Lens phase error could be reduced by adapting a non focal design strategy, proposed by Dong, Zaghloul and Rotman [31] in 2008. The proposed method allows designing a Rotman Lens phase center contour without passing any ideal foci. The original Rotman lens [17] was designed to have 3 ideal focal points, which yields a deterministic inner receiving contour that gives zero path-length error for the beams emitted from these 3 focal points. However, in the realistic design, more beam elements are expected to occupy the beam contour, which leads to phase errors for the non-focal beams. The non-focal lens can be designed to achieve minimum average phase errors for all the elements rather than achieving best matches for only selected beams. This idea later leads Dong and Zaghloul to propose a 360-degree scanning lens [37-39] in 2009. The proposed lens have symmetric beam and inner receiving contours, whose beam ports and receiving ports are interleaved. Beam port and receiving ports can maintain different modes of operations; it is possible to reuse the receiving port as beam port if circulators are adopted. Both of the non-focal and 360-degree lenses are topics in this dissertation, which are detailed in Chapter 3 and Chapter 5 respectively.

2.2 Microwave Lens Applications

Several historical applications of microwave lenses have been mentioned during reviewing the history of their development in section 2.1. The primary military applications of microwave lenses are airborne and marine radars. For example, the AN/ALQ-184 self protect ECM system for the air force tactical aircraft, and the AN/SQL32 electronic countermeasures system (Figure 2- 4) built by Raytheon company adopt microwave lens structure to perform the advanced beam forming [40].

Applications requiring multi-beams in either azimuth or elevation directions can apply single 2D planar microwave lens. As the theory predicted and experiment demonstrated,

the scanning capability of single microwave lens reaches $\pm 60^0$ off the broadside. Many lens prototypes published [41-44] have demonstrated so. John Toon [45] at Georgia Institute of Technology discussed the recent development of the low-profile printed Rotman Lens could lead to many civilian applications as well.

(a) AN/ALQ-184 (b) AN/SQL32

Figure 2- 4. Examples of Microwave Lens Used for Airborne and Marine Radars [40]

As discussed in Chapter 1, the Butler matrix is a planar beamforming device with N input and N corresponding outputs. Stacked Butler BFNs are often used to facilitate three dimensional beam scanning. Microwave lenses can be stacked to feed planar arrays and provide simialr scanning performance.The pencil beam former has applications in space communications and imaging systems. Sketch of pencil beam BFNs based on Buler matrix for studying the cosmic noise absorption[46] and 3D microwave lens from [47] is illustrated in Figure 2- 5A.

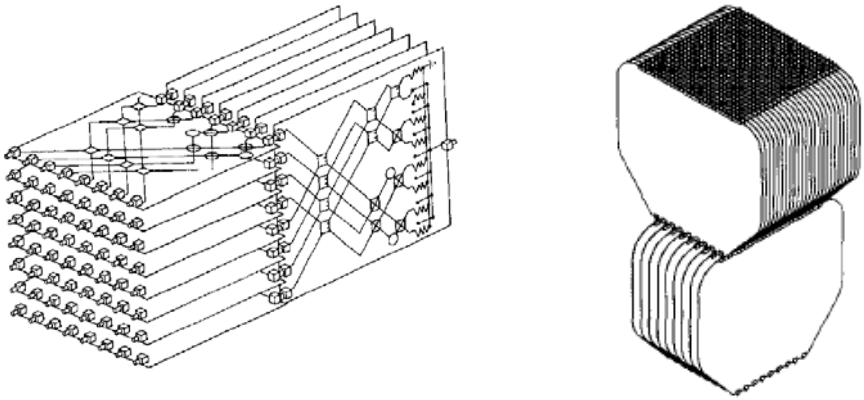

Figure 2- 5A. Butler Matrix for Radio Wave Images for Study of Cosmic Noise Absorption [46]; Right: Stacked Rotman Lens Shown Capable of Producing Pencil Beams [47]

Options of photonic beam forming using microwave lens were proposed by Hans Steyskal [48] and Ruth Rotman [49]. Because the microwave lens is passive, TTD and wide scan angle, it is good candidate for designing the photonic imaging system. One of the passive imaging systems was released in [50]. The lens was designed across the band of 75.5-93.5 GHz, as shown in Figure 2-5B. In the example, the subject on the right hand wearing a shirt over a concealed pistol was successfully detected [50].

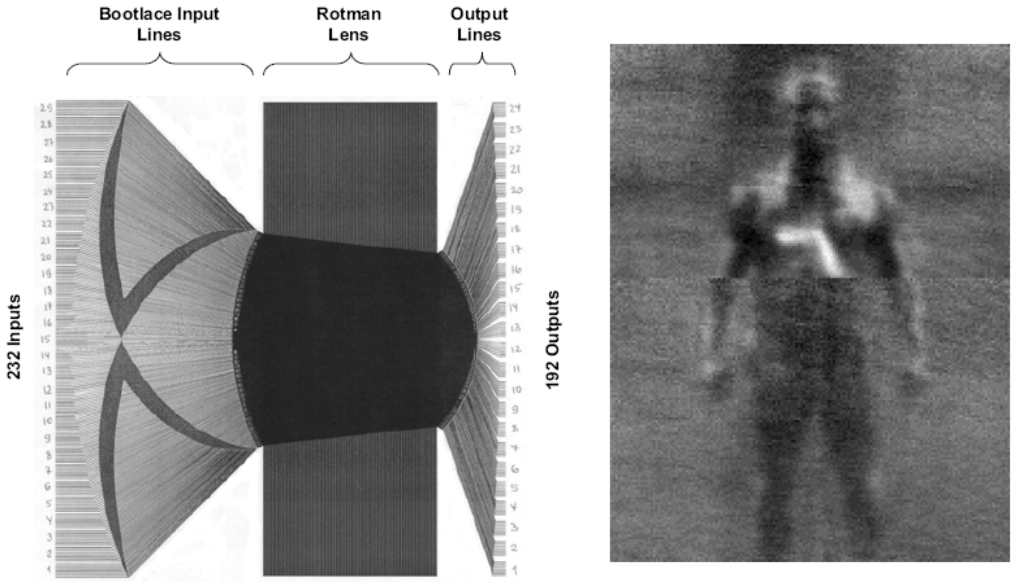

Figure 2-5B Photonic Rotman lens BFNs in Passive Imaging Systems [50]

As discussed in the background section of Chapter 1, the microwave lens beam-forming techniques possess more advantages than the conventional Butler matrix. With the advancement of recent material and fabrication technologies, BFNs of microwave lenses can be low-profile, compact, light-weighted, and maintain wide band, wide-angle scanning capabilities. The narrow, multi-beams, TTD and electrically scanning antennas (ESA) properties shown in Figure 2- 1 allow designing radar systems operating in multi-modes and multi-functionalities. This might lead to new applications such as compact and smart sensing systems on the unmanned aircraft or future robot. These systems are especially desired to integrate functions of active/passive target acquisition, secure point to point (P2P) communications, situational awardable sensors all in one body. An

example of vehicular sensor design using microwave lens has been approached in [51, 52]. Further improvement might allow the vehicular sensors performing collision avoidance, imaging, ad-hoc communications at a time in future.

2.3 Microwave Lens Design Procedures

A successful microwave lens must follow systematic design procedures. The standard design procedures have been enhanced by the recent development of full-wave and asymptotic simulation methods. Research has been carried at different steps of these procedures over the years. The following paragraphs outline a general case that is adopted by most scholars. It consists of five steps: 1) Microwave lens specifications, 2) Geometry optical (GO) lens parameters, 3) port, transmission line implementation, 4) performance estimation of complete lens, and 5) Fabrication and measurement.

1. Microwave lens specifications

Electronic devices are designed to meet certain specifications. The microwave lens electrical specifications include phase errors, amplitude errors, maximum scanning angle, tolerance angle of true-time delay, return loss, bandwidth, power efficiency, maximum power sustained etc; its mechanical specifications include: size, weight, etching/milling tolerance etc (Table 2-1). Not all design requirements can be met at the same time, for example, the efficiency, bandwidth and size of the lens usually trade off each others. However, reasonable design specifications can usually be fulfilled in one or more designing steps.

Table 2- 1. The Microwave Lens Design Specifications

Microwave Lens Electrical Specifications	Microwave Lens Mechanical Specifications
Phase Errors	Size
Amplitude errors	Weight
Maximum Scanning Angle	Etching/milling tolerance
Tolerance Angle of True-time Delay	Temperature range
Return Loss, Bandwidth	Robustness
Power Efficiency	Resilience
Maximum Sustainable Power	Sustainability

2. Geometry optical lens parameters formulation

The lens geometry optical parameters contain the positions of the beam, receiving ports and the transmission line lengths. These parameters are results of many other inter-dependant design parameters that affect the phase error performance. Conventionally, the lens design theories are classified in terms of how these initial GO parameters are formed. Existing methods include tri-focal, quadru-focal and non-focal design methods, as discussed previously. The key differences between these theories are generally the number of design freedoms and the theoretical phase error performance across the aperture. Figure 2- 6 indicates various parameters of a trifocal lenses, whose contour and transmission lines are typical functions of other parameters as marked on the figure. Figure 2- 7 implies that the corresponding shape of a lens varies when different parameter is applied. There are no definite good or bad models, which depends on the geometrical constraints and their optimization methods. A final result of satisfactory is usually based on the balance between the size, shape and the phase errors.

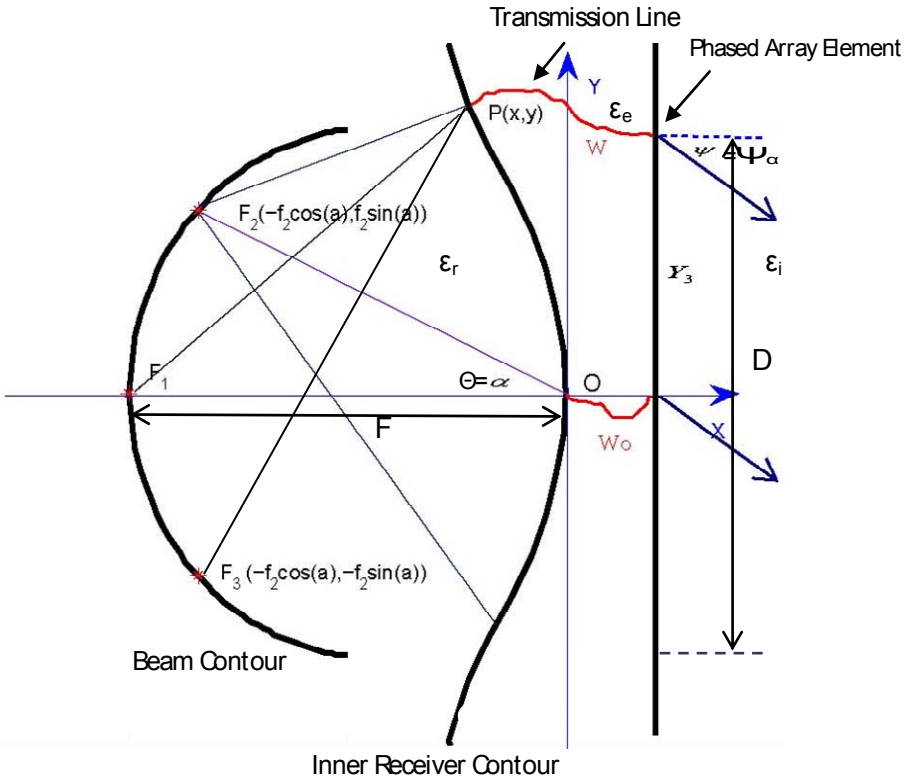

Figure 2- 6. Parameters of a Trifocal Lens

A few performance/design factors are worthwhile considering during the geometry optical lens parameters formulation. They are the maximum scanning angles, number of scanning steps, dielectric materials filled, overall dimension of the lens, and all GO parameters that determined the phase errors across the aperture (for example, F/D, $g=f_2/F$).

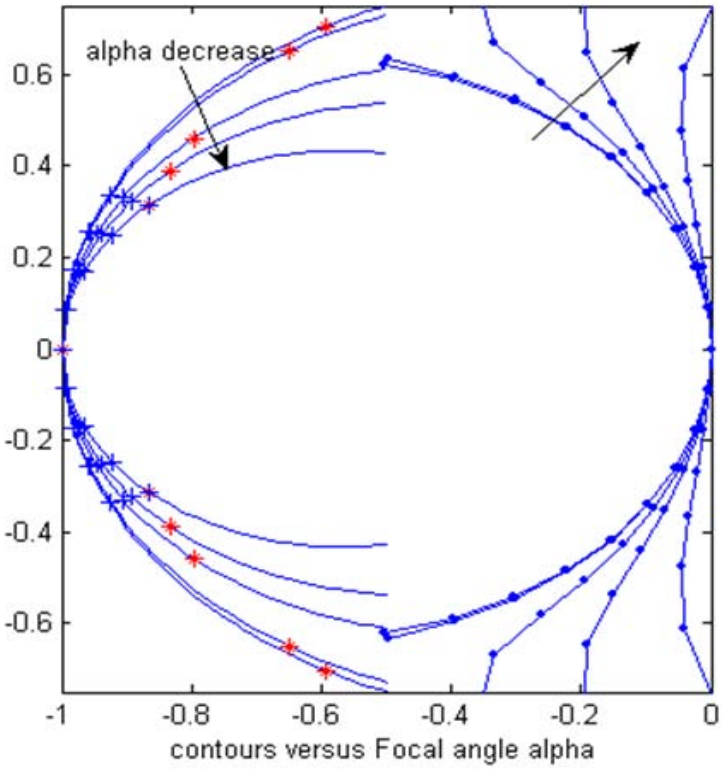

Figure 2- 7. Lens Geometry Variation for Different Alpha Values

3. Ports and transmission line implementations

Upon having the phase centers and transmission line lengths of the lens, the materials for implementing the structures and transmission lines have to be carefully selected. Typical lens ports are realized by open end waveguide, striplines and microstrip tapered horns, as shown in Figure 2- 8. The transmission lines can be implemented by built-on strip lines or stand-alone coaxial cables, as shown in Figure 2- 9.

During this step, the performance parameters of bandwidth, return loss have to be considered, because the port size, tapering and length play great roles on them. Besides, it is also noted that the pointing direction of the ports and the way of implementing the side wall ports can affect the final amplitude performance.

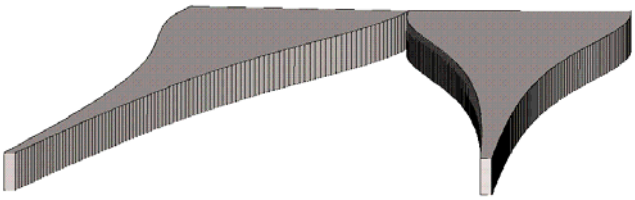

(a)

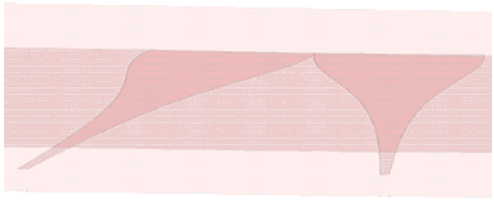

(b)

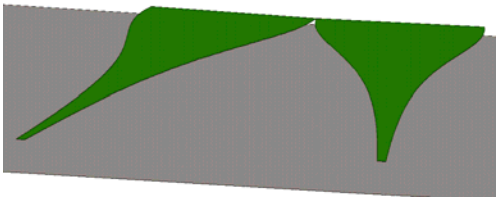

(c)

Figure 2- 8. Port Implementation Methods (a) Waveguide, (b) Stripline, (c) Microstrip

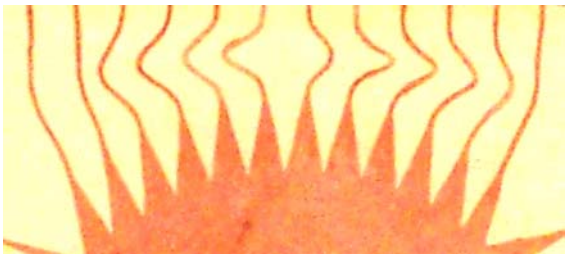

(a)

(b)

Figure 2- 9. The Transmission Lines Implemented Using (a) Built on Strip Lines, (b) Coaxial Cables

4. Performance evaluation of the complete lens

After the structure is formulated, performance of the complete lens is estimated using either full-wave simulations or asymptotic methods depending on the size of the lens and available toolkits. An accurate simulation method can estimate most of the electrical performance in Table 2-1. For example, Figure 2- 10 illustrates the simulated surface current in FEKO. And Figure 2- 11 is its array factor (gain for isotropic elements) that validated by the measurement result. We will detail this process in Chapter 4. We shall note that the accurate simulation of the electronic large lens is still in its early age. As soon as efficient and accurate methods get available, simulation is not only used to

estimate or validate the lens performance, but also to conduct optimizations. The optimization process involves repetitive interaction between the GO structure and the simulation.

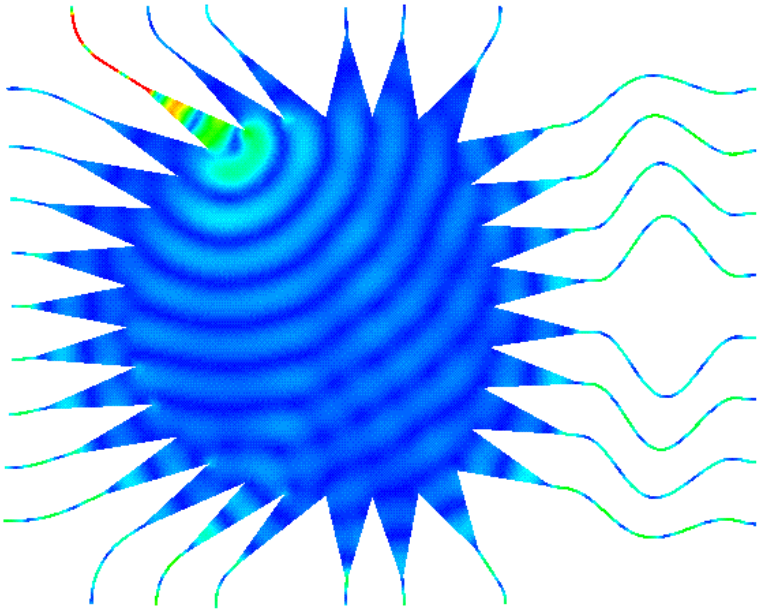

Figure 2- 10. Simulated Surface Current

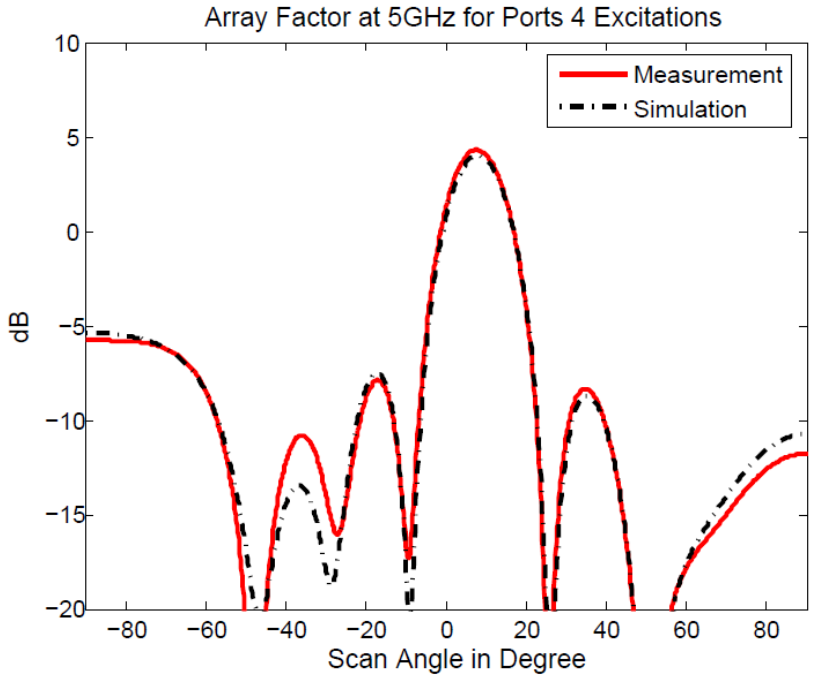

Figure 2- 11. Simulated Array factor (gain for isotropic elements) Compared to Measurement

5. Fabrication and measurement

Based on the materials, a microwave lens can be fabricated using different methods. Usually the waveguide lens is built for low loss and high power handling. A printed circuit board (PCB) realization is the focus of this dissertation owing to its inherent benefits of low-profile, light weight, low cost, and convenient integration with printed circuit antenna designs. PCB designs can be fabricated using chemical etching or milling machines. In this dissertation, prototypes are fabricated using etching. As an example, Figure 2- 12 indicates the etching process of the 360-degree scanning lens presented in Chapter 5. In most cases, the lenses are implemented with input and output ports of typical 50Ω coaxial connectors. Sometimes the array elements are formulated on the same microstrip laminate such as [51], resulting of a lens with ports directly integrated into the array ports, and the lens ports have an impedance equal to the input impedance of the given element. The former case is measured using 2-port network analyzer with all un-test ports terminated by loads, while the latter's pattern can be measured in a chamber. The fabricated lenses in this dissertation are all measured using the network analyzer, as shown in Figure 2- 13.

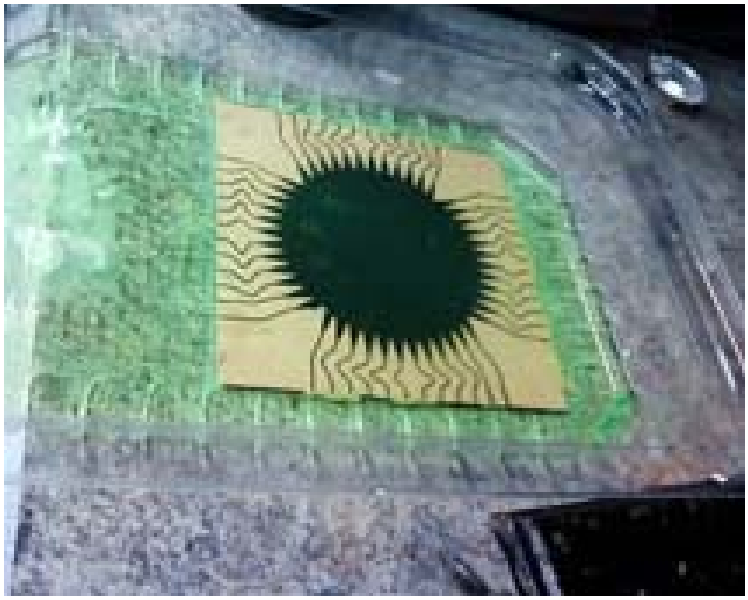

Figure 2- 12. Microstrip Lens Etching Example

Figure 2- 13. Microwave Lens Measurement Example

2.4 Research Objectives

The research detailed in this dissertation traverses many aspects of microwave lens theory, design, and implementation with significant results being published in a wide range of technical articles [31, 37, 38, 51, 53-56]. The primary focus of this dissertation can be divided into three main objectives: 1) minimizing phase errors in non-focal microwave lenses, 2) design and validate simulation algorithms suitable for electrically large lens structures, and 3) design a single lens structure capable of providing 360-degree scanning.

The first objective is to design the non-focal microwave lens method that has less phase errors than the traditional focal lens designs. Various parameters relating to the classical focal lenses and enhanced new formulation methods will be addressed. As we described before, the method for calculating the GO initial parameters are primarily validated by comparing the phase error performance. Thus the proposed approach is evaluated by

comparing with the published results of the traditional tri-focal and quadru-focal lenses. Array factors are investigated as well.

The second objective is to design and validate efficient simulation algorithms that are suitable for electronically large microwave lens performance estimation. Simulation results of a moderate size lens are compared to certified full-wave simulation results. The lens should be fabricated and measured. The measured data will be used to validate both the full-wave simulator and proposed algorithms. As discussed in Chapter 2.1, lens design using accurate simulations is relatively new area of study, thus improved design examples based on accurate simulation methods will be demonstrated.

The third objective is to devise a microwave lens that utilizes single lens structure to produce 360-degree scanning capability. The new proposed lens should possess good performance such as TTD and wideband etc. Prototype lens will be designed, simulated, fabricated and tested. Its phase, amplitude and beam scanning properties will be validated by both full-wave simulation and measurement.

CHAPTER 3. MICROWAVE LENS FORMULATION AND NON-FOCAL LENS PHASE ERROR MINIMIZATION

The microwave lens as BFN is designed for feeding either linear array that produces azimuth scanning beams or planar array that generates 3 dimensional scanning pencil beams, as indicated in Section 2.2. Because the 3D array BFN as shown in Figure 2- 5 is essentially formed using 2D microwave lens, lens theories are conventionally formulated in 2 dimensional coordinates. According to the array theory in Section 1.2, to enable a linear array to produce scanning beams, a typical linear phase shift and acceptable amplitude distributions across the aperture are required, as illustrated in Figure 3- 1.

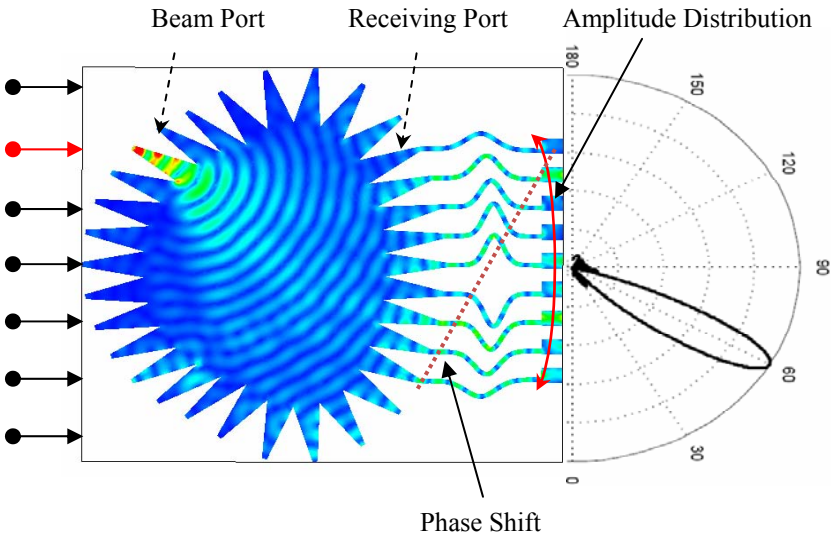

Figure 3- 1. Linear Array Fed by BFN

The microwave lens design starts with theoretical geometry optical parameters. From Section 1.1, we learnt that planar, spherical and cylindrical wave maintain the same phase variations along the radial direction in the same medium. The far field of a radiation element approaches to plane wave, as depicted by equations (1-51)-(1-52) and (1-70). Given the homogeneous and low loss medium filled in the microwave lens, within limited path length, the electromagnetic wave' phase varies more dramatically than the amplitude. Thus the amplitude across the aperture does not greatly affect the direction of

scanning beams but only the SLL. Consequently, the lens theory is able to be formulated using the path delay concepts.

Several existing theories of microwave lens have been briefly reviewed in Chapter 2. As it shows, the original Rotman lens formulation has been modified and improved over the years. The forthcoming sections 3.1 and 3.2 cover the basis of traditional focal lenses and the optimization methods. Because this dissertation is orientated to designing microstrip based printed lenses, new parameters such as material properties have been incorporated. Besides, there is no comprehensive lens equations that have combined different geometry freedoms as proposed in [52]. Thus, the derivation in this chapter is not necessary to duplicate the existing equations but rather to provide the optimal design strategy. Section 3.3 proposes and validates the non-focal design method that allows lens' beam contour possessing no focal point but yielding minimum phase error across the aperture. The non-focal lens will be compared to the published results of traditional trifocal and quadru-focal lenses.

3.1 Tri-focal Rotman Lens Formulation

3.1.1 Printed 2-D Trifocal Rotman Lens

Figure 3- 2 represents a general structure similar to the conventional tri-focal Rotman lens [17]. The inputs of the beam-forming network shown in Figure 3- 1 connect to the beam contour in Figure 3- 2, where the beam port phase centers lie. Similarly, the inner-receiver contour stands for the locus of phase centers of the inner receiving ports. Between the inner-receiver ports and the phased array elements (point sources assumed here) are the constrained transmission lines with physical lengths W. The microwave lens works in a way that each point on the beam contour is assumed to produce a cylindrical wave toward the inner-receiver direction. Tapered phases and amplitudes are produced at the inner-receiver points, which then direct the energy to the transmission line and generate proper feeding for the radiating array elements. In the design procedure, we consider the inner-receiver contour of P(X,Y) and transmission line length of W as the unknowns. In other words, we assume the beam port positions and array element positions are given parameters. Given the coordinate system shown in Figure 3- 2, we

also define that each beam port phase center refers to one subtended angle θ and each radiation beam refers to one radiation angle Ψ. It is noted that the medium of the beam-to-receiver 'cavity', transmission lines and the radiation environment can be different as the lens can be dielectric filled and the transmission lines can be implemented using coaxial cables in practice. Hence the three regions in the lens are marked as having different relative permittivity factors of ε_r, ε_e and ε_i. The parameters for deriving the general design equations are listed below:

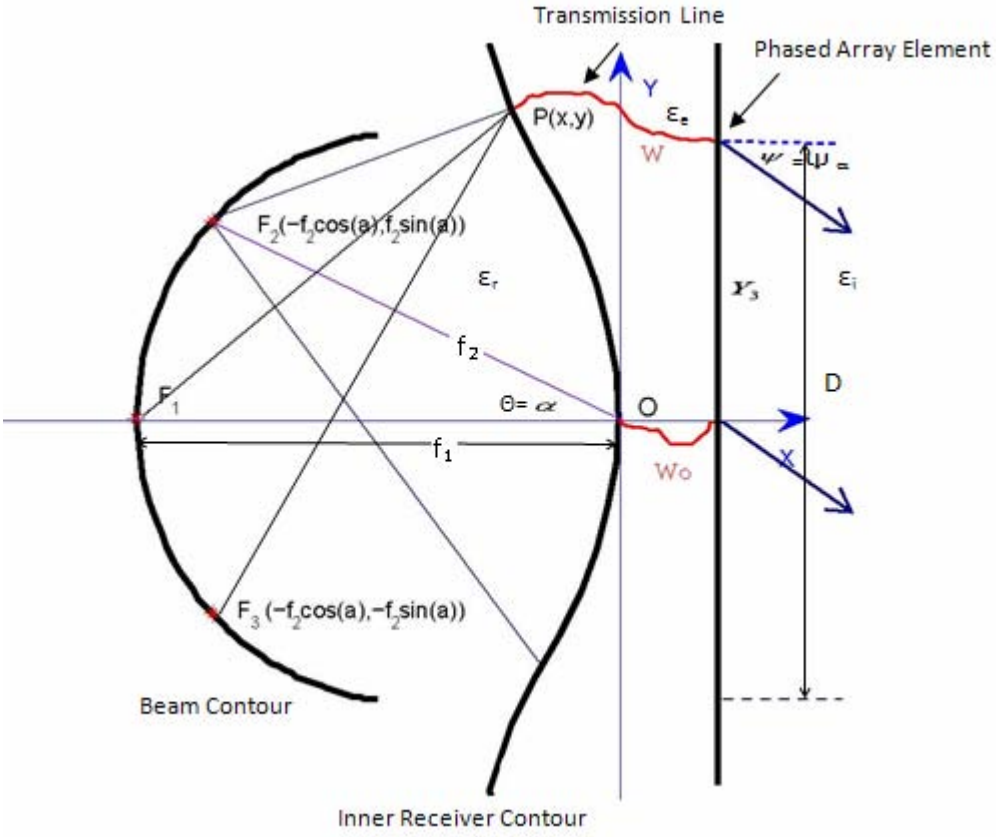

Figure 3- 2. Trifocal Lens Design Scheme

α : Off center focal angle;

β : Focal ratio, $\beta = OF_2 / OF_1$, $\beta = f_2 / f_1$ in short;

ψ : Array scan angle;

θ : Subtended angle for beam port phase centers;

γ : Ray to beam angle ratio, $\gamma = \sin(\psi_\alpha) / \sin(\alpha)$;

ζ : Intermediate parameter, $\zeta = Y_3\gamma / f_1$, Y_3 is the distance of any array point from the x axis;

OF_2: Side focal length, f_2 in short; OF_1 is the center focal length, f_1 in short;

W: Transmission line length;

e: The eccentricity of the beam contour;

w: The normalized relative transmission line length, $w = (W - W_0) / f_1$;

ε_r, ε_e, ε_i: the dielectric constants for cavity region, transmission line and environment;

X,Y: the undetermined coordinates of inner receiving port phase centers, normalized as x,y.

Now we address design methods of solving P(X, Y) and W. Note there are three parameters that need three equations to explicitly solve for them. This is achieved by postulating that there are three ideal focal points (F_1, F_2, F_3) along the beam contour, and each of them produces exact linear phase shift for the array to scan into certain known direction. If we assume that the ideal focal points are located at $\theta = \pm \alpha$ and 0, and their corresponding radiation angles are $\Psi = \pm \Psi_\alpha$ and $\Psi = 0$, given Ψ_α is a known angle, simultaneous equations in (3-1)-(3-3) are satisfied:

$$\begin{cases} F_2 P\sqrt{\epsilon_r} + W\sqrt{\epsilon_e} + Y_3\sqrt{\epsilon_i}\sin(\psi_\alpha) = f_2\sqrt{\epsilon_r} + W_0\sqrt{\epsilon_e} & (3\text{-}1) \\ F_3 P\sqrt{\epsilon_r} + W\sqrt{\epsilon_e} - Y_3\sqrt{\epsilon_i}\sin(\psi_\alpha) = f_2\sqrt{\epsilon_r} + W_0\sqrt{\epsilon_e} & (3\text{-}2) \\ F_1 P\sqrt{\epsilon_r} + W\sqrt{\epsilon_e} = f_1\sqrt{\epsilon_r} + W_0\sqrt{\epsilon_e} & (3\text{-}3) \end{cases}$$

where Y_3 is the y coordinate of the array element, F_iP is the physical distance from focal point F_i to P, and f_i is the focal length between F_i and O.

When the subtended focal angle α is equal to the scan angle Ψ_α, and all medium are assumed air filled, equations in (3-1)-(3-3) become the standard Rotman lens formulations [17]. Researchers in [27-29] proved that the subtended angle θ can be different from the scan angle Ψ, by applying which, it achieves a flexibility of designing

more compacting beam region to feed the same scan region when $\Psi > \theta$. Furthermore, when designing stripline and microstrip lenses, using different dielectric constant cables seem practical. Thus we shall seek solutions from the generalized equations in (3-1)-(3-3).

Normalizing (3-1) by the electrical length of the central focal length $\sqrt{\in_r} f_1$, results in (3-4)-(3-6):

$$\begin{cases} \dfrac{F_2P}{f_1} = \dfrac{f_2}{f_1} - \dfrac{W-W_0}{f_1}\dfrac{\sqrt{\in_e}}{\sqrt{\in_r}} - \dfrac{Y_3\sin\psi_\alpha}{f_1}\dfrac{\sqrt{\in_i}}{\sqrt{\in_r}} = \beta - w\dfrac{\sqrt{\in_e}}{\sqrt{\in_r}} - \dfrac{Y_3\sin\psi_\alpha}{f_1}\dfrac{\sqrt{\in_i}}{\sqrt{\in_r}} & (3\text{-}4) \\ \dfrac{F_3P}{f_1} = \dfrac{f_2}{f_1} - \dfrac{W-W_0}{f_1}\dfrac{\sqrt{\in_e}}{\sqrt{\in_r}} + \dfrac{Y_3\sin\psi_\alpha}{f_1}\dfrac{\sqrt{\in_i}}{\sqrt{\in_r}} = \beta - w\dfrac{\sqrt{\in_e}}{\sqrt{\in_r}} + \dfrac{Y_3\sin\psi_\alpha}{f_1}\dfrac{\sqrt{\in_i}}{\sqrt{\in_r}} & (3\text{-}5) \\ \dfrac{F_1P}{f_1} = 1 - \dfrac{W-W_0}{f_1}\dfrac{\sqrt{\in_e}}{\sqrt{\in_r}} = 1 - w\dfrac{\sqrt{\in_e}}{\sqrt{\in_r}} & (3\text{-}6) \end{cases}$$

where β is the ratio between the off and central focal lengths, and the lower case lettering w stands for the normalized transmission lengths referred to the center line length. From Figure 3- 2 we know the following equations hold true.

$$\begin{cases} F_3P^2 = (-f_2\cos\alpha - X)^2 + (-f_2\sin\alpha + Y)^2 = f_2^2 + X^2 + Y^2 + 2f_2X\cos\alpha - 2f_2Y\sin\alpha & (3\text{-}7) \\ F_3P^2 = (-f_2\cos\alpha - X)^2 + (-f_2\sin\alpha - Y)^2 = f_2^2 + X^2 + Y^2 + 2f_2X\cos\alpha + 2f_2Y\sin\alpha & (3\text{-}8) \\ F_1P^2 = (f_1 + X)^2 + Y^2 & (3\text{-}9) \end{cases}$$

Normalizing (3-7)-(3-9) by f_1, we have:

$$\begin{cases} \dfrac{F_2P^2}{f_1^2} = \dfrac{f_2^2}{f_1^2} + \dfrac{X^2}{f_1^2} + \dfrac{Y^2}{f_1^2} + 2\dfrac{f_2X\cos\alpha}{f_1^2} - 2\dfrac{f_2Y\sin\alpha}{f_1^2} = \beta^2 + x^2 + y^2 + 2\beta x\cos\alpha - 2\beta y\sin\alpha & (3\text{-}10) \\ \dfrac{F_3P^2}{f_1^2} = \dfrac{f_2^2}{f_1^2} + \dfrac{X^2}{f_1^2} + \dfrac{Y^2}{f_1^2} + 2\dfrac{f_2X\cos\alpha}{f_1^2} + 2\dfrac{f_2Y\sin\alpha}{f_1^2} = \beta^2 + x^2 + y^2 + 2\beta x\cos\alpha + 2\beta y\sin\alpha & (3\text{-}11) \\ \dfrac{F_3P^2}{f_1^2} = \dfrac{(f_1+X)^2}{f_1^2} + \dfrac{Y^2}{f_1^2} = (1+x)^2 + y^2 & (3\text{-}12) \end{cases}$$

Square (3-4)-(3-6) and equate with (3-10)-(3-12):

$$\begin{cases} (\beta - w\dfrac{\sqrt{\in_e}}{\sqrt{\in_r}} - \dfrac{Y_3 \sin\psi_\alpha}{f_1}\dfrac{\sqrt{\in_i}}{\sqrt{\in_r}})^2 \\ = \beta^2 + w^2\dfrac{\in_e}{\in_r} + (\dfrac{Y_3 \sin\psi_\alpha}{f_1})^2\dfrac{\in_i}{\in_r} - 2\dfrac{\beta Y_3 \sin\psi_\alpha}{f_1}\dfrac{\sqrt{\in_i}}{\sqrt{\in_r}} + 2\dfrac{wY_3 \sin\psi_\alpha}{f_1}\dfrac{\sqrt{\in_e \in_i}}{\in_r} - 2\beta w\dfrac{\sqrt{\in_e}}{\sqrt{\in_r}} \\ = \beta^2 + x^2 + y^2 + 2\beta x\cos\alpha - 2\beta y\sin\alpha \qquad (3\text{-}13) \\ (\beta - w\dfrac{\sqrt{\in_e}}{\sqrt{\in_r}} + \dfrac{Y_3 \sin\psi_\alpha}{f_1}\dfrac{\sqrt{\in_i}}{\sqrt{\in_r}})^2 \\ = \beta^2 + w^2\dfrac{\in_e}{\in_r} + (\dfrac{Y_3 \sin\psi_\alpha}{f_1})^2\dfrac{\in_i}{\in_r} + 2\dfrac{\beta Y_3 \sin\psi_\alpha}{f_1}\dfrac{\sqrt{\in_i}}{\sqrt{\in_r}} - 2\dfrac{wY_3 \sin\psi_\alpha}{f_1}\dfrac{\sqrt{\in_e \in_i}}{\in_r} - 2\beta w\dfrac{\sqrt{\in_e}}{\sqrt{\in_r}} \qquad (3\text{-}14) \\ = \beta^2 + x^2 + y^2 + 2\beta x\cos\alpha + 2\beta y\sin\alpha \\ (1+x)^2 + y^2 = \left(1 - w\dfrac{\sqrt{\in_e}}{\sqrt{\in_r}}\right)^2 \qquad (3\text{-}15) \end{cases}$$

Sum and subtract equation (3-14) from (3-13), the simplified simultaneous equations are shown below:

$$\begin{cases} w^2\dfrac{\in_e}{\in_r} + (\dfrac{Y_3 \sin\psi_\alpha}{f_1})^2\dfrac{\in_i}{\in_r} - 2\beta w\dfrac{\sqrt{\in_e \in_i}}{\in_r} = x^2 + y^2 + 2\beta x\cos\alpha \qquad (3\text{-}16) \\ \dfrac{\beta Y_3 \sin\psi_\alpha}{f_1}\dfrac{\sqrt{\in_i}}{\sqrt{\in_r}} - \dfrac{wY_3 \sin\psi_\alpha}{f_1}\dfrac{\sqrt{\in_e \in_i}}{\in_r} = \beta y\sin\alpha \qquad (3\text{-}17) \\ 2x + x^2 + y^2 = w^2\dfrac{\in_e}{\in_r} - 2w\dfrac{\sqrt{\in_e}}{\sqrt{\in_r}} \qquad (3\text{-}18) \end{cases}$$

Note we are looking for the locus of point P(X, Y), which actually forms the receiving element port contour, shown in Figure 3- 2. In these equations (3-16)-(3-18), x, y, and w are the variables. From equation (3-17), we have:

$$y = \frac{Y_3 \sin\psi_\alpha}{f_1 \sin\alpha}\frac{\sqrt{\in_i}}{\sqrt{\in_r}} - \frac{wY_3 \sin\psi_\alpha}{\beta f_1 \sin\alpha}\frac{\sqrt{\in_e \in_i}}{\in_r} = \frac{Y_3 \sin\psi_\alpha}{f_1 \sin\alpha}\frac{\sqrt{\in_i}}{\sqrt{\in_r}}(1 - \frac{w}{\beta}\frac{\sqrt{\in_e}}{\sqrt{\in_r}}) = \zeta\frac{\sqrt{\in_i}}{\sqrt{\in_r}}(1 - \frac{w}{\beta}\frac{\sqrt{\in_e}}{\sqrt{\in_r}}) \quad (3\text{-}19)$$

x can be calculated from (3-16)+(3-18), shown in (3-20):

$$x = \frac{\in_i {y_3}^2 \sin^2\psi}{2\in_r(\beta\cos\alpha - 1)} + \frac{(1-\beta)w}{\beta\cos\alpha - 1}\sqrt{\frac{\in_e}{\in_r}} \qquad (3\text{-}20)$$

w is formulated from (3-16)-(3-18) into an standard equation shown in (3-21),

$$\frac{a \in_r}{\in_e} w^2 + b\sqrt{\frac{\in_r}{\in_e}} w + c = 0 \tag{3-21}$$

To sum up, the unknowns X, Y and W-W_0 are solved from the above equations, as given in (3-22)-(3-24):

$$\begin{cases} w_{12} = \dfrac{\sqrt{\in_e}}{\sqrt{\in_r}} \dfrac{-b \pm \sqrt{b^2 - 4ac}}{2a} & (3\text{-}22) \\ x = \dfrac{\in_i y_3^{\,2} \sin^2 \psi}{2 \in_r (\beta \cos\alpha - 1)} + \dfrac{(1-\beta)w}{\beta \cos\alpha - 1}\sqrt{\dfrac{\in_e}{\in_r}} & (3\text{-}23) \\ y = \sqrt{\dfrac{\in_i}{\in_r}} \dfrac{Y_3 \sin\psi_\alpha}{f_1 \sin\alpha}\left(1 - \dfrac{w}{\beta}\sqrt{\dfrac{\in_e}{\in_r}}\right) & (3\text{-}24) \end{cases}$$

where,

$$\begin{cases} a = 1 - \left(\dfrac{1-\beta}{1-\beta C}\right)^2 - \dfrac{\zeta^2}{\beta^2}\dfrac{\in_i}{\in_r} & (3\text{-}25) \\ b = -2 + \dfrac{2\zeta^2}{\beta}\dfrac{\in_i}{\in_r} + \dfrac{2(1-\beta)}{1-\beta C} - \dfrac{\zeta^2 S^2 (1-\beta)}{(1-\beta C)^2}\dfrac{\in_i}{\in_r} & (3\text{-}26) \\ c = \left(-\zeta^2 + \dfrac{\zeta^2 S^2}{1-\beta C} - \dfrac{\zeta^2 S^4}{4(1-\beta C)}\right)\dfrac{\in_i}{\in_r} & (3\text{-}27) \\ \beta = f_2 / f_1; & (3\text{-}28) \\ \zeta = \dfrac{Y_3 \sin\psi_\alpha}{f_1 \sin\alpha} & (3\text{-}29) \end{cases}$$

Here x, y are the X, Y values normalized to f_1, and w is the path-length difference W-W_0 normalized to f_1, and $S = \sin\alpha; C = \cos\alpha$.

Now equations (3-22)-(3-24) have determined the inner receiving contour and the transmission lines. Note there are only three focal ports applied so far along the beam contour, where in the realistic design, more than 3 ports are usually applied. To determine their locations, we assume the beam contour has an ellipse shape that has all the three focal points passed, and the eccentricity can be a design parameter controlling the shape of the beam contour. As shown in Figure 3- 3, the eccentricity is defined as (3-30) [57]:

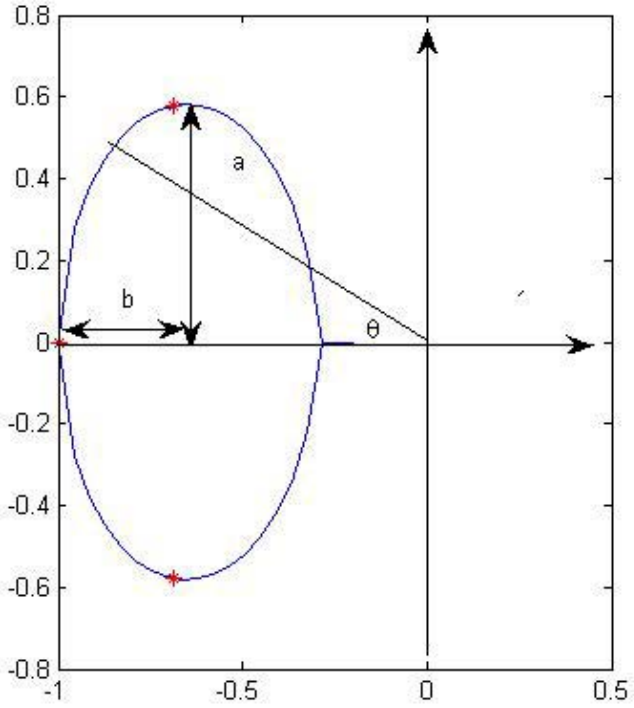

Figure 3- 3. Beam Contour Formulations

$$e = \sqrt{\frac{a^2 - b^2}{a^2}} \tag{3-30}$$

The ellipse function shown in Figure 3- 3 can be defined as (3-31),

$$\frac{(x+1-b)^2}{b^2} + \frac{y^2}{a^2} = 1 \tag{3-31}$$

The parameters a can be determined by substituting the known off-axis foci that pass the ellipse. Equation (3-32) below gives the result.

$$a = \frac{1}{2}\frac{-\beta^2 \cos^2\alpha + 2\beta\cos\alpha + \beta^2 \sin^2\alpha(e^2 - 1) - 1}{\sqrt{1-e^2}(\beta\cos\alpha - 1)} \tag{3-32}$$

Thus, the contour of the beam port is a function of α, β and e. Now to determine the beam port positions, the line function passing the beam port and origin is defined as:

$$y_b = -\tan\theta * x_b \tag{3-33}$$

where θ is the beam subtended angle and x_b and y_b are the undetermined beam port coordinates. Equate (3-33) with (3-31), the coordinate can be determined, as shown in (3-34).

$$x_b = \frac{1}{2}\frac{a[-2a + 2ab + 2\sqrt{b^2a^2 - b^2\tan^2\theta + 2b^3\tan^2\theta}]}{a^2 + b^2\tan^2\theta} \tag{3-34}$$

3.1.2 Phase Errors and Their Interpretations

The intuition of microwave lens design is to use different beam ports to produce different desired phases and amplitudes for the phased arrays, which then generate the scanned beams into the free space. As shown in Figure 3- 4, in order to produce multi-beams, more than 3 ports usually occupy the lens beam contour. Consequently, the ports allocated at the non-focal points produce phase errors, in other words, they are not able to form the path-length equalities, as equations shown in (3-1)-(3-3).

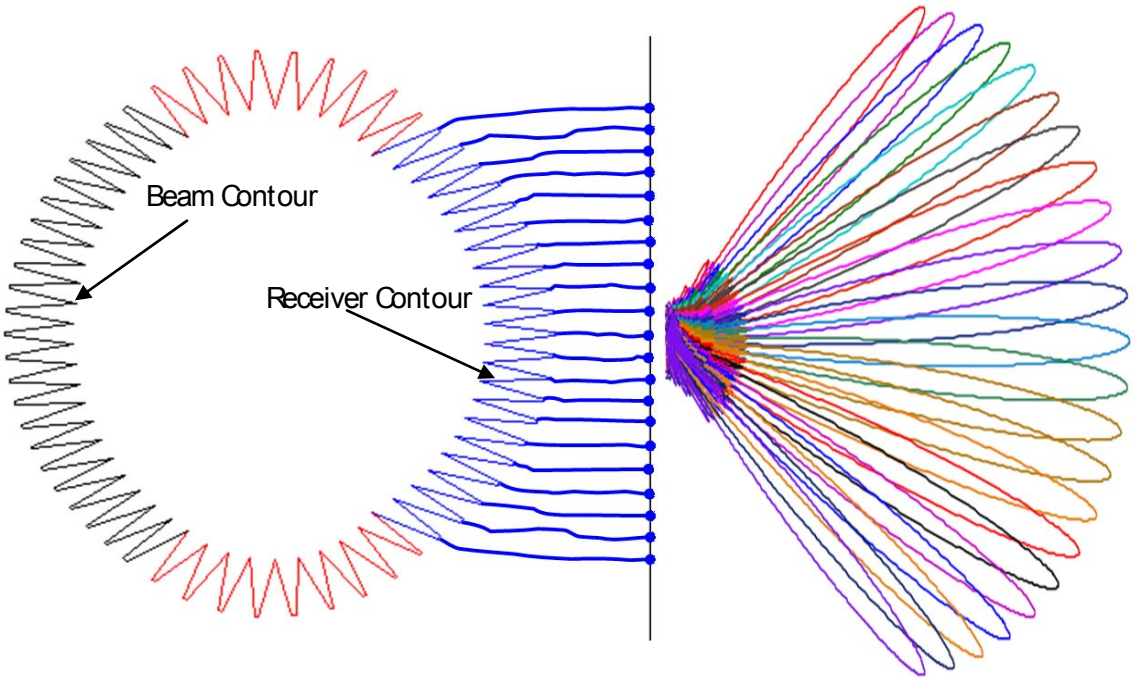

Figure 3- 4. The Microwave lens BFN Uses Each Beam Port to Produce Phase and Amplitude Tapers for the Linear Array, Which Generate the Consequent Scan Beam in the Free Space.

There are two alternative ways of viewing the phase errors. One is the phase error for each beam port produced across the phase front of the aperture; the other is the maximum phase error across the aperture for all beams ports. The former expression reflects the detailed phase contents for each beam, while the later generally stands for the phase performance for all beam ports. Take a lens design with $\alpha=30^0$ for example, when θ is equal to 20^0 and 40^0, the phase error appears, as indicated in Figure 3- 5. In Figure 3- 6, the maximum phase errors for each θ are expressed. The former format puts more emphasis on the detailed phase errors for a single beam across the aperture, while the latter depicts the general performance of the phase errors for all beams. Note that references [17, 28, 29] used the first type expression to evaluate the performance of the lens design, while [30, 36] adopted the second one. In this dissertation, we use the latter to describe and evaluate the phase performance of non-focal lens designs. It could be seen that the area enclosed by the curve or the average phase error level of the curve in the Figure 3- 6 stands for the objective function of the minimization. The less the area or average level is, the better phase performance the lens achieves.

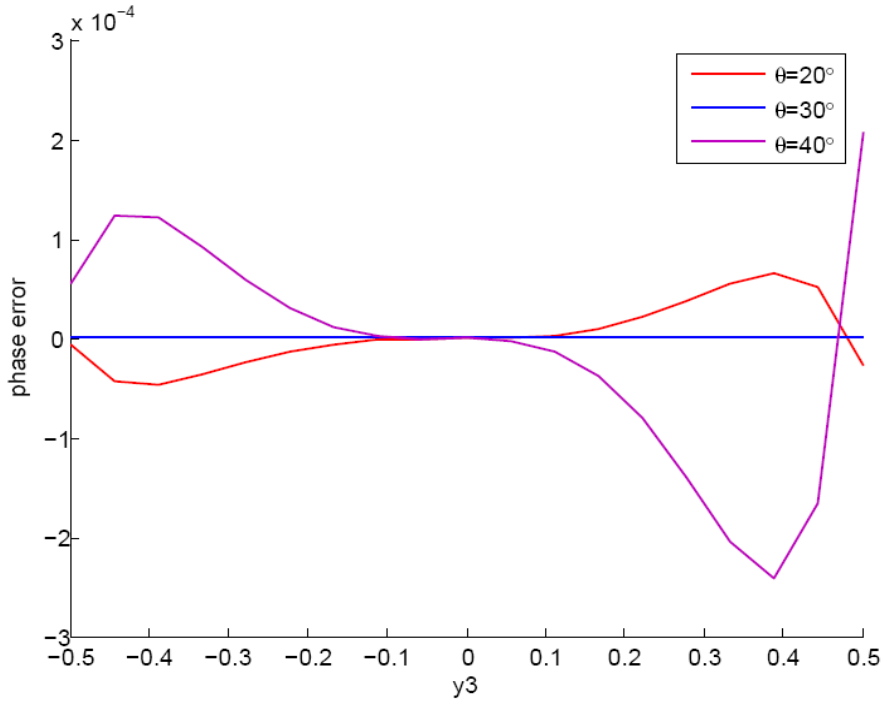

Figure 3- 5. Phase Errors Normalized to F across the Aperture for Single Port, $\alpha=30^0$, g=1.130, F/D=1

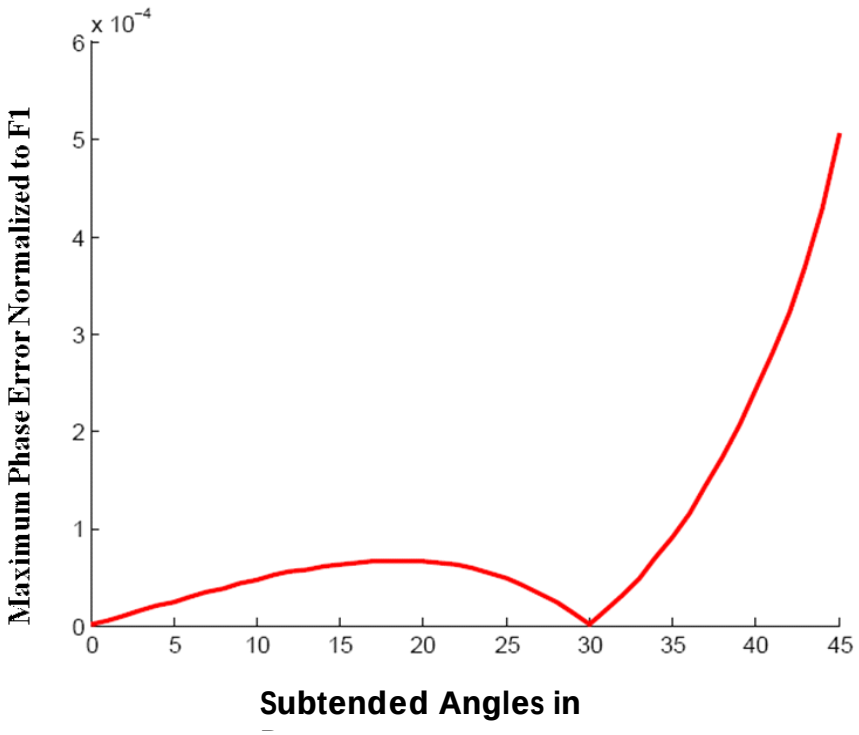

Figure 3- 6. Maximum Phase Errors across the Aperture for All Beam Ports, $\alpha=30^0$, g=1.130, F/D=1

3.1.3 Phase Error Optimization Methods for Tri-focal Lenses

The design parameters affect the structure of the microwave lens, as well as the phase error performance. The phase center locations are finalized by proper designed geometric parameters and some optimization factors. In this section, the effects of focal angle α, maximum subtended angle θ_m , focal ratio β (or g factor), eccentricity e and F/D ratio are studied.

Figure 3- 7 and Figure 3- 8 show the results of beam and receiving contours variation as a function of focal angle α and maximum subtended angle θ_m. Figure 3- 7 indicates that as the focal angle decreases, the beam contour shrinks toward the center, and the receiving contour gets much flatter. Figure 3- 8 shows that the maximum subtended angle only affect the positions of the beam ports, both beam and receiving ports do not vary. Note

for a given maximum scan angle, one can adjust either θ_m or ray to beam angle ratio γ to meet the requirement.

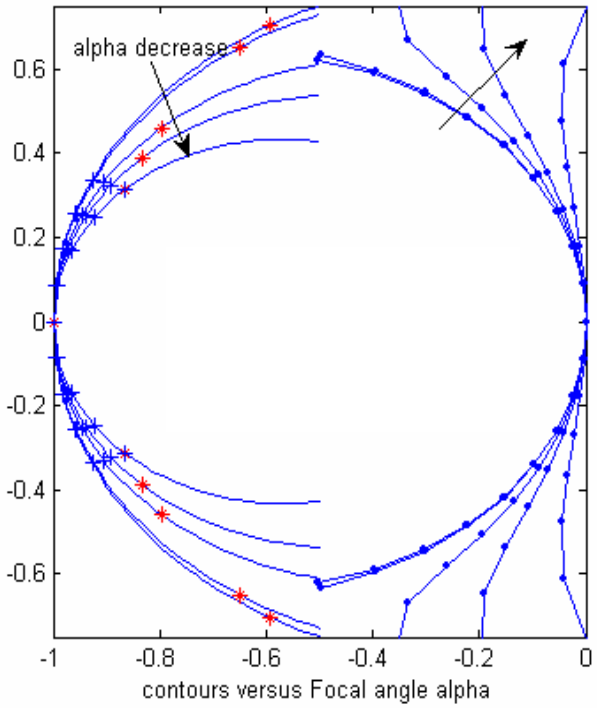

Figure 3- 7. Lens Beam and Receiving Contours versus Focal Angle α

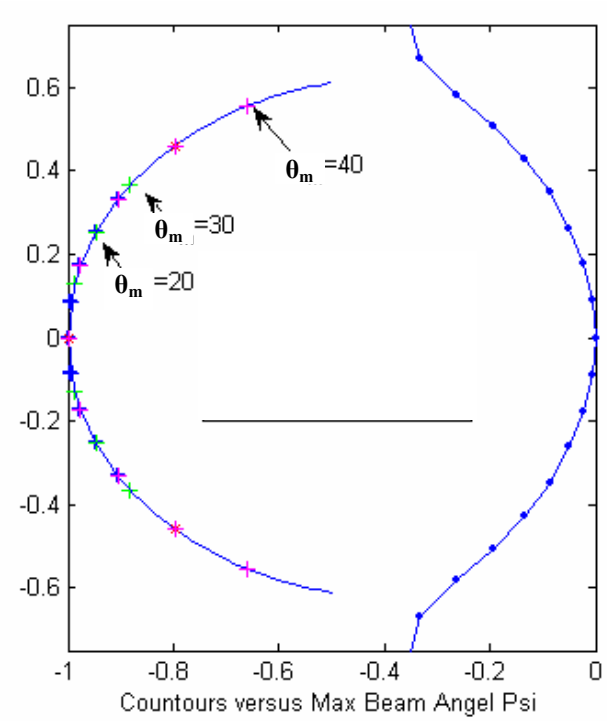

Figure 3- 8. Lens Structure versus Maximum Subtended Angle θ_m

The β parameter is considered as the phase optimization factor in [29], and this is inverse ratio of the original proposed factor g [17]. Following the examples conducted in Figure 3- 5 and Figure 3- 6, it is found that different g=1/β values give different phase performance shown in Figure 3- 9. In the original model [17], g=1.137 was found the best value for F/D=1, $\alpha=30^0$ lens design. After using the second type of phase error expression, it is found that g=1.130 is actually more optimal. Beside of the phase errors, the β also changes the lens contours. Given the constant focal angle $\alpha=30^0$, F/D=1, Figure 3- 10 shows that beam contour outspreads and receiving contour shrinks as β increases.

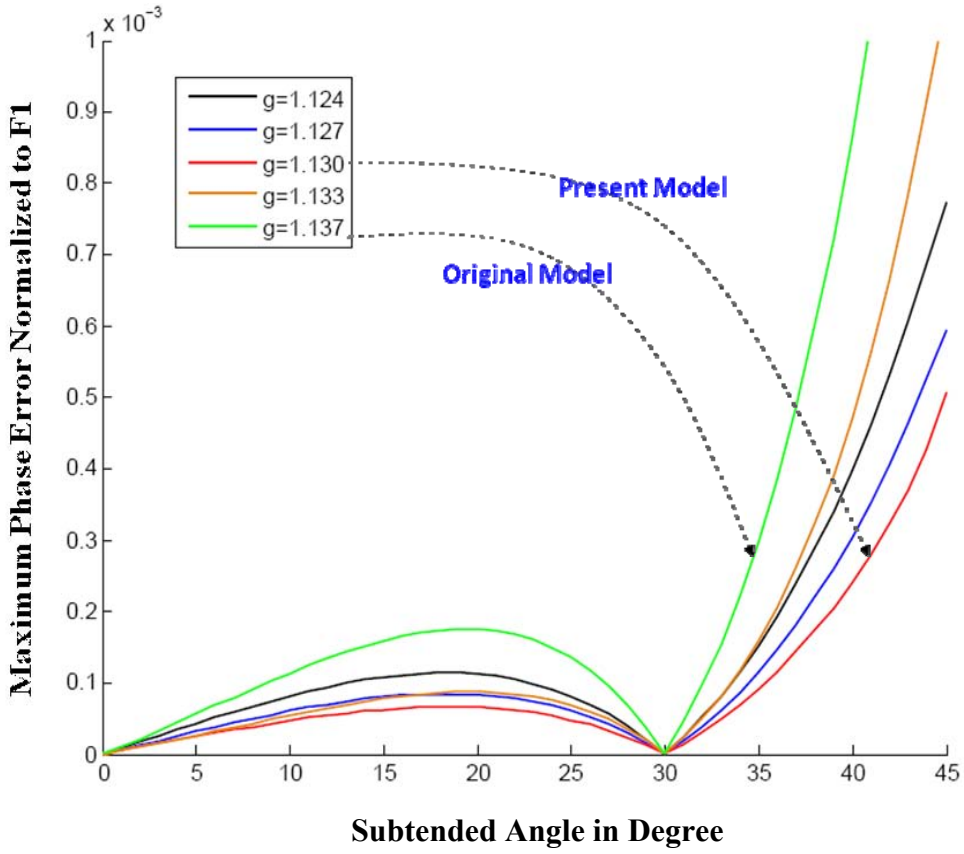

Figure 3- 9. Use g=1/β Parameter to Conduct Lens Optimization, $\alpha=30^0$, F/D=1

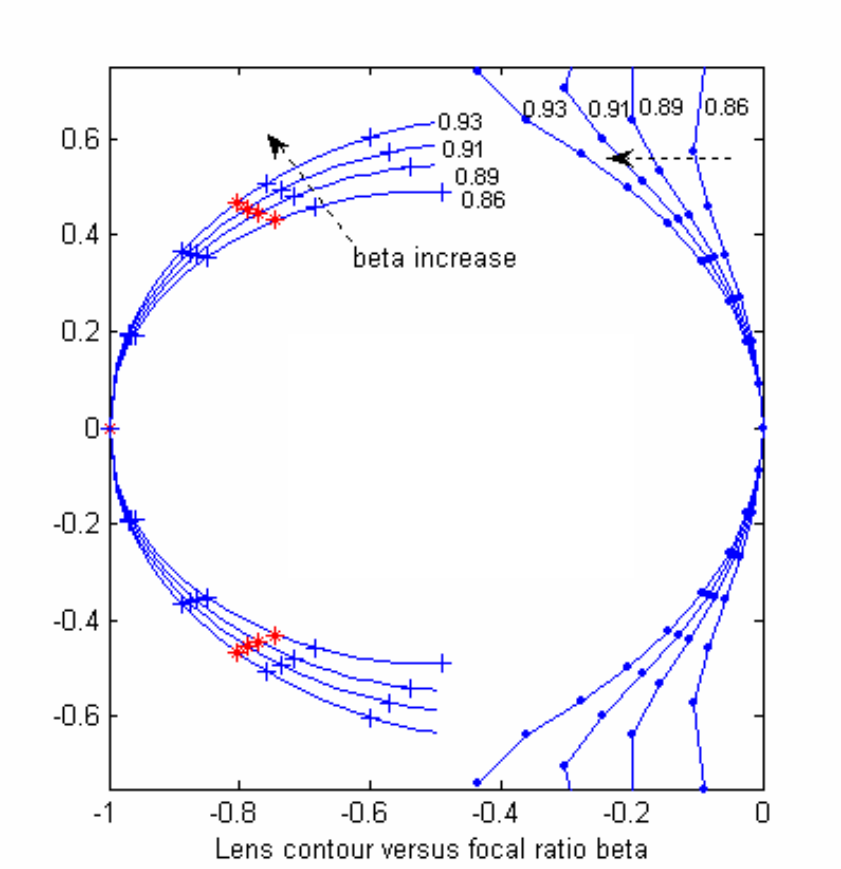

Figure 3- 10. Lens Beam and Receiving Contours versus Parameter β

According to numerical investigations, the eccentricity of the beam curve is not a significant improvement factor for the g-optimized Rotman lens. Figure 3- 11 shows typical optimization results by varying e.

The F/D ratio is an important factor during the phase error optimization process. Different F/D values yield different levels of phase errors, given all other parameters are not varied (Figure 3- 12). It is noted that previous simulations maintain a constant F/D ratio of 1. This is because the typical case is to follow equation $g = 1 + \alpha^2 / 2$ proposed in [17] to approach the optima. This equation only approximates the best g value for r=1 case. More comprehensive results are shown in Table 3-1. The results demonstrated in Figure 3- 12 and Table 3-1 provide important information that lenses based on different methods could only be compared to each other under the equivalent value of r condition.

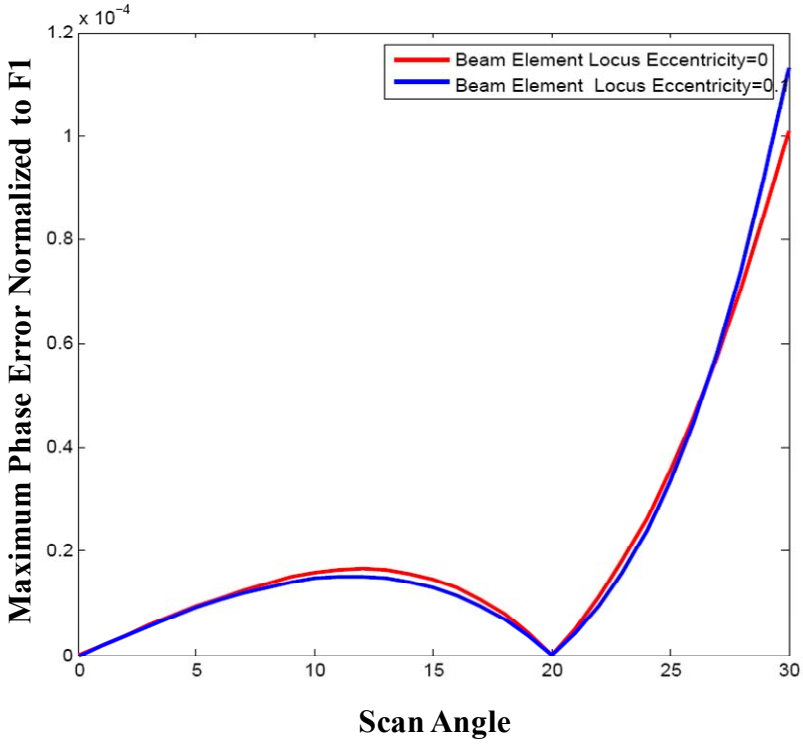

Figure 3- 11. Phase Error versus Eccentricity of the Beam Counter

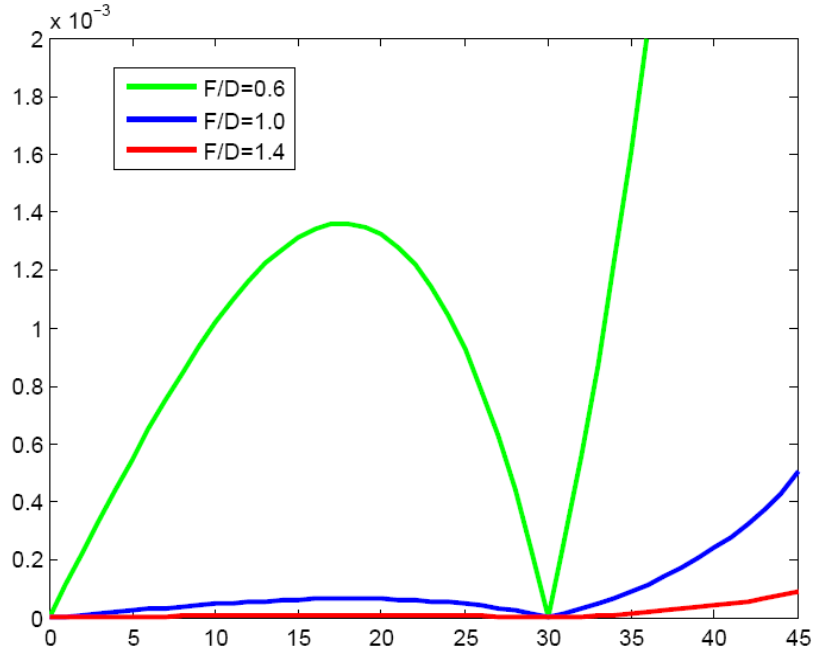

Figure 3- 12. Different F/D Reflects Different Levels of Phase Errors

Table 3- 1. Best g Value for Different Focal Angles at Different F/D Ratio

Best g	F/D=0.6	F/D=1	F/D=1.4
$\alpha = 10^0$	1.009	1.013	1.014
$\alpha = 20^0$	1.034	1.055	1.060
$\alpha = 30^0$	1.073	1.130	1.143
$\alpha = 40^0$	1.120	1.161	1.278
Phase Error	High	Medium	Low

3.2 Quadra-focal Lens Formulation

3.2.1 Printed Quadrufocal Lens

The quadrufocal lens first appeared in the three dimensional lens designs [36]. As shown in Figure 3- 13, beam contour in the plane of x=0 feeds a concaved receiving plane where the receiving ports are allocated. What follows each of the receiving port (X,Y,Z) is the transmission line W, which connects the radiating array element. Considering the x=0 plane, the 2D qudrufocal lens was formed in [30], as shown in Figure 3- 14. In contrast to the trifocal lens, four equations are formed due to the path-length equality, shown in (3-33)-(3-36).

$$\begin{cases} F_1P\sqrt{\epsilon_r} + W\sqrt{\epsilon_e} + Y_3 \sin\alpha\sqrt{\epsilon_i} = F_1O\sqrt{\epsilon_r} + W_0\sqrt{\epsilon_e} & (3\text{-}33) \\ F_2P\sqrt{\epsilon_r} + W\sqrt{\epsilon_e} + Y_3 \sin\beta\sqrt{\epsilon_i} = F_2O\sqrt{\epsilon_r} + W_0\sqrt{\epsilon_e} & (3\text{-}34) \\ F_3P\sqrt{\epsilon_r} + W\sqrt{\epsilon_e} - Y_3 \sin\alpha\sqrt{\epsilon_i} = F_3O\sqrt{\epsilon_r} + W_0\sqrt{\epsilon_e} & (3\text{-}35) \\ F_4P\sqrt{\epsilon_r} + W\sqrt{\epsilon_e} - Y_3 \sin\beta\sqrt{\epsilon_i} = F_4O\sqrt{\epsilon_r} + W_0\sqrt{\epsilon_e} & (3\text{-}36) \end{cases}$$

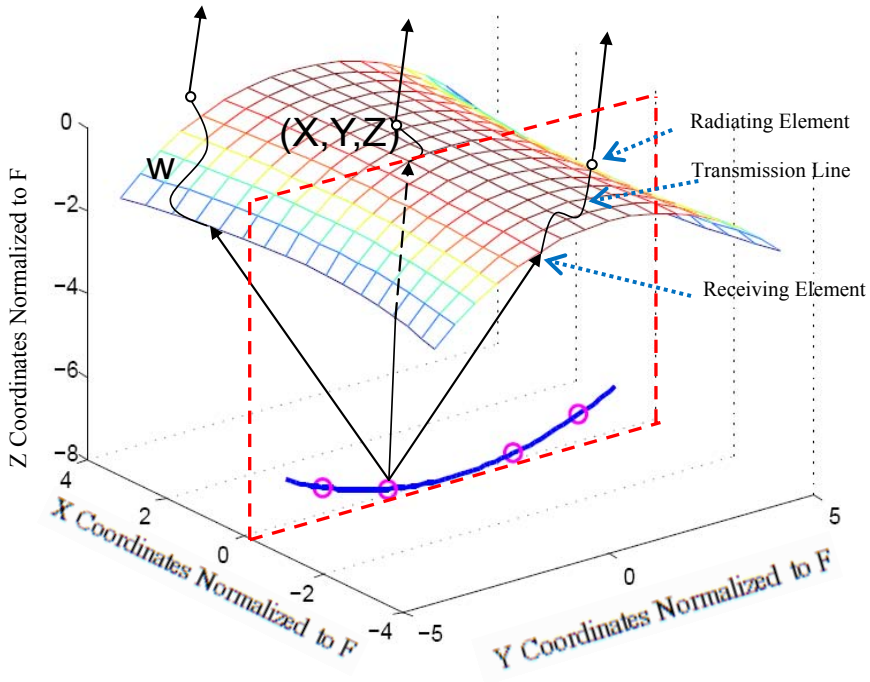

Figure 3- 13.3D Quadrufocal Lens Design

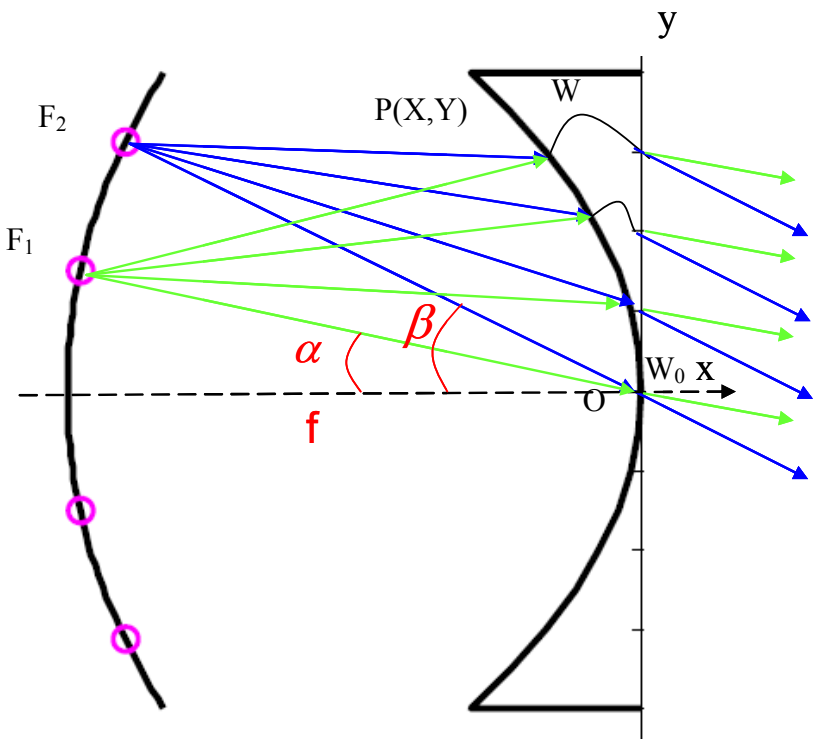

Figure 3- 14.Planar Quadrufocal Lens Design Scheme

where α β are absolute values for the four focal subtended angles, F_iP is a function of X and Y, Y_3 is the outer array element height, W is the transmission line length, and $FO = GO = f$. The permittivities of the cavity region, transmission lines and environmental space are ε_λ, ε_e and ε_i. The three unknowns X, Y, $\Delta W=W-W_0$ can be solved by following the calculation method done in [30], a general result shown in (3-37)-(3-40).

$$\begin{cases} X = -Y_3^2 \in_i \dfrac{\cos\alpha + \cos\beta}{2f \in_r} & (3\text{-}37) \\ Y = Y_3\sqrt{\dfrac{T \in_i}{\in_r}} & (3\text{-}38) \\ \Delta W = f(1-\sqrt{T})\sqrt{\dfrac{\in_r}{\in_e}} & (3\text{-}39) \end{cases}$$

where

$$T = 1 + \frac{1}{\in_r f^2 - \in_i Y_3^2}\left[\frac{\in_i^2 Y_3^4}{\in_r}\left(\frac{\cos\alpha + \cos\beta}{2f}\right)^2 - \in_i Y_3^2 \cos\alpha\cos\beta\right] \quad (3\text{-}40)$$

3.2.2 Phase Errors and Optimization Methods for Quadrufocal Lenses

The planar 4 focal lens contour could be optimized by perturbing the beam contour, firstly adopted in [30]. The same scheme was investigated here; however, the beam port perturbation is along the direction of the subtended angle. Figure 3- 15 shows the maximum phase error normalized to f across the aperture for these two cases, where $\varepsilon_\lambda = \varepsilon_e = \varepsilon_i = 1$, r=1, $\alpha = 11^0$ and $\beta = 25^0$.

When the radiation angle gets different from the subtended angle, further phase error reduction can be achieved. The example shown in Figure 3-16 applied the technique originally adopted to optimize the trifocal Rotman Lens in [27]. It is also possible to operate more investigations on the focal angles versus geometry change, F/D ration versus phase errors. Because they more or less possess the same trend as the tri-focal lens, they are not cover in this report.

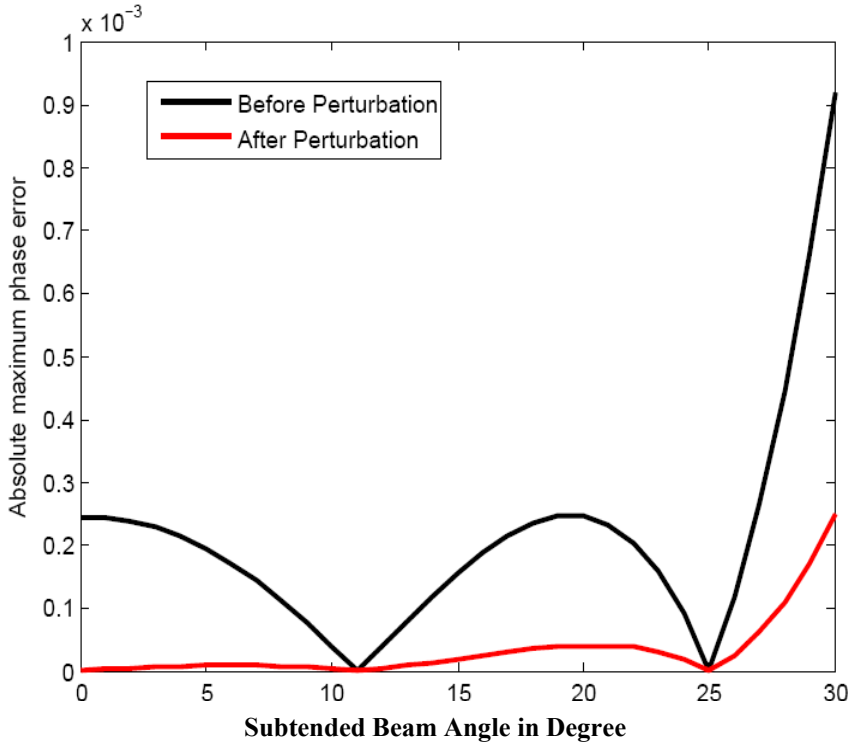

Figure 3- 15. Beam Port Perturbation is Applied to Minimize the Quadrufocal Lens Phase Errors

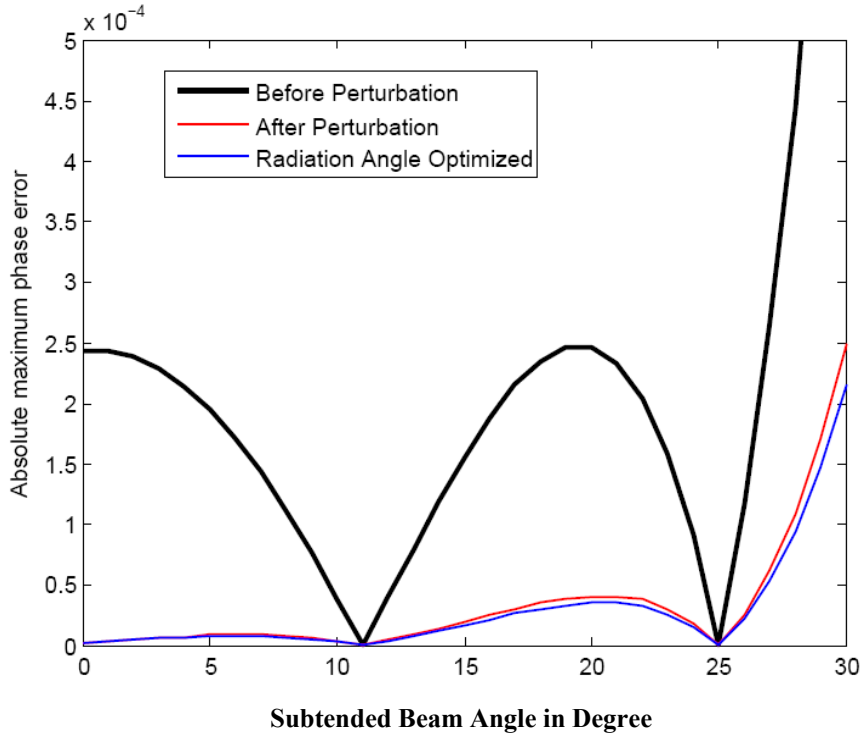

Figure 3- 16. Radiation Angle Optimization Could Further Reduce the Phase Errors

3.3 Non-focal Lens Phase Error Minimization

3.3.1 2-D Non-focal Microwave Lens Formulation

As described in previous sections, the phase errors have become intrinsic characteristics in the bootlace lens design. In realistic environments, to produce multiple beams, more ports in the focal region are expected to lie on the beam contour, as indicated in Figure 3-17. In the previous sections' tri and quadrufocal lens designs, the inner receiver contour and transmission lines are totally determined by the initial focal points parameters, as depicted by equations (3-1)-(3-3) and (3-33)-(3-36). Beams produced by these focal ports are theoretically perfect. However, phase errors occur on the non-focal port beams, and optimizing these errors becomes a prime target. As indicated in the previous section, the focal lens optimization methods are limited in altering non-focal port position, e.g. by changing the eccentricity of the ellipse [29] or beam port perturbation [30], and changing the non-focal port scan angle, e.g. phase error reduction method in [27]. There is no unified phase error reduction method. Besides, each of the aforementioned methods involves complicated lens re-formulations. To choose the best solution, one usually solves trifocal and quadrufocal equations and conduct complicated and separate simulations based on different methods. It is realized that, since the final objective in practice is to minimize the phase errors for all beam ports, instead of constraining limited number of ideal focal points, why not allow introducing perturbations to both beam and inner receiving port contours, transmission lines and even scan angles at the same time. In this sense, conditions for perfect focal points are no longer enforced, and the phase error performance essentially becomes a function of design variables, with phase error minimization achieved in a single optimization process, as indicated in Figure 3- 18.

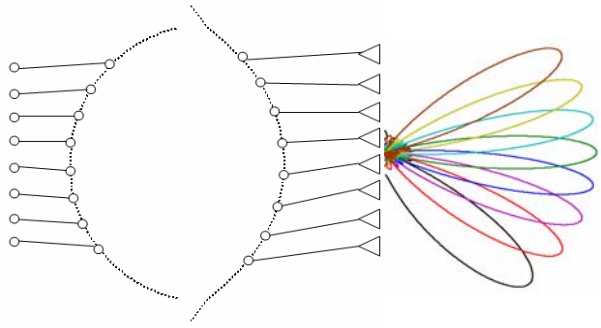

Figure 3- 17. More than Focal Points of Beam Ports are Usually Expected to Occupy the Beam Contour in Realistic Design

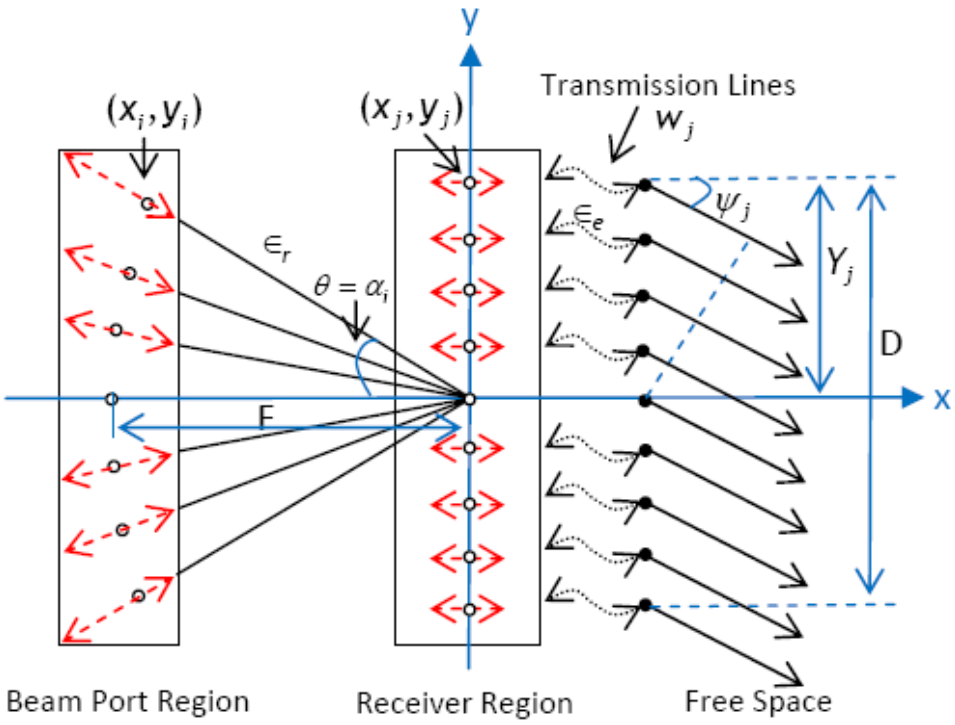

Figure 3- 18. Non-focal Lens Optimization Scheme [58]

Two tasks are considered in order to design the non-focal lens, one is to build reasonable objective function that describes the general performance of the phase errors for all beam ports, and the other is to seek correct and applicable numerical toolset in optimizing the objective function.

Suppose there are N beam ports, and M inner receiving ports, as shown in Figure 3- 18. Define (x_i, y_i) as the coordinates of the i^{th} beam port with subtended angle at the receiving array center of α_i, and (x_j,y_j) as the j^{th} receiving port position, with w_j as the transmission line length reference to transmission line length of the center receiving port. Y_j is the j^{th} phased array element height, and Ψ_i is the radiation angle resulting from the i^{th} beam port excitation. The lens region and transmission line have dielectric constants of ε_r and ε_e respectively. Given maximum scan angle $\pm\Psi_m$, and the maximum subtended angle is α_m, without losing generality, we can solve:

subtended angle increment:

$$|\alpha_{i+1} - \alpha_i| = 2\alpha_m/N \qquad (1<=i<N) \qquad (3\text{-}41)$$

scan angle increment:

$| \Psi_{i+1} - \Psi_i | = 2\Psi_m / M \qquad (1 <= j < M)$ (3-42)

array element spacing:

$| Y_{j+1} - Y_j | = D/M \qquad (1 <= j < M)$ (3-43)

Other determined parameters include:

y_j: y coordinate of j^{th} receiving port, with typical value of Y_j;

y_i: y coordinate of i^{th} beam port, which is equal to (x_i *tan α_i);

Electrical path length of the i^{th} beam port to the middle array element phase front is:

$$L1 = \sqrt{\in_r}\sqrt{x_i^2 + y_i^2} \tag{3-44}$$

As shown in Figure 4, the i^{th} beam port phase center to the j^{th} array element phase front electrical length is:

$$L2 = \sqrt{\in_r}\sqrt{(x_i - x_j)^2 + (x_i \tan\alpha_i - y_j)^2} + \sqrt{\in_e} w_j + Y_j \sin(\psi_i) \tag{3-45}$$

The difference between (3-44) and (3-45) gives the theoretical phase error for the i^{th} beam port excitation. A function relating all phase errors for all beam ports reflects the phase performance, which is defined in (3-46) as:

$$f(x_i, x_j, \alpha_i, \psi_i, \in_r, \in_e, w_j) = \sum_{i=1}^{N}\sum_{j=1}^{M} | L2 - L1 | \tag{3-46}$$

Defining F/D for lens design is important, because optimizations based on different F/D values are basically saturated at different phase error levels, as shown in Figure 3- 12. This implies that lens designed using different methods should only compare with one another under the scenario of the same F/D value. In non-focal lens design, it is suggested to fix center beam port and middle inner receiver port positions. In this way, F is constant value and r=F/D still holds. The total number of each variable, such as x_i and x_j, in equation (8) is N-1 and M-1, respectively.

Parameters α_i, Ψ_i are usually assigned by relations (3-41)-(3-43), ε_r and ε_e can be chosen according to model requirement and material availability. As a result, the optimization of

lens phase performance has been transferred to the function (3-46) minimization in terms of variables x_i, x_j and w_j, as given in (3-47):

$$\min(f) \propto \{x_i, x_j, w_j\} \tag{3-47}$$

Equation (3-47) is an N+2M-3 dimension global minimization problem. The objective function f is addressed in equation (3-46). Numerical methods such as genetic algorithms (GA) [59] and DSZ algorithms (DSZA) [60] can be adopted to treat such functions. Both algorithms randomly generate finite number of solutions in a form of $\{x_i, x_j, w_j\}$ and have them weighted by their objective functions, the inferior solutions can be evolved by operations such as mutation or regeneration, etc. In this way, each new loop always passes superior solutions into the next evolution until stable optimum results are produced. The flow chart of such algorithms is shown in Figure 3- 19, and it is noticed that both methods apply stochastic evolutionary search techniques in optimizing the functions. The GA will be described in detail in the next section, because the forthcoming validation section 3.3.3 applies this method. And the DSZ algorithms will be addressed in Chapter 5 for the 360-degree lens design.

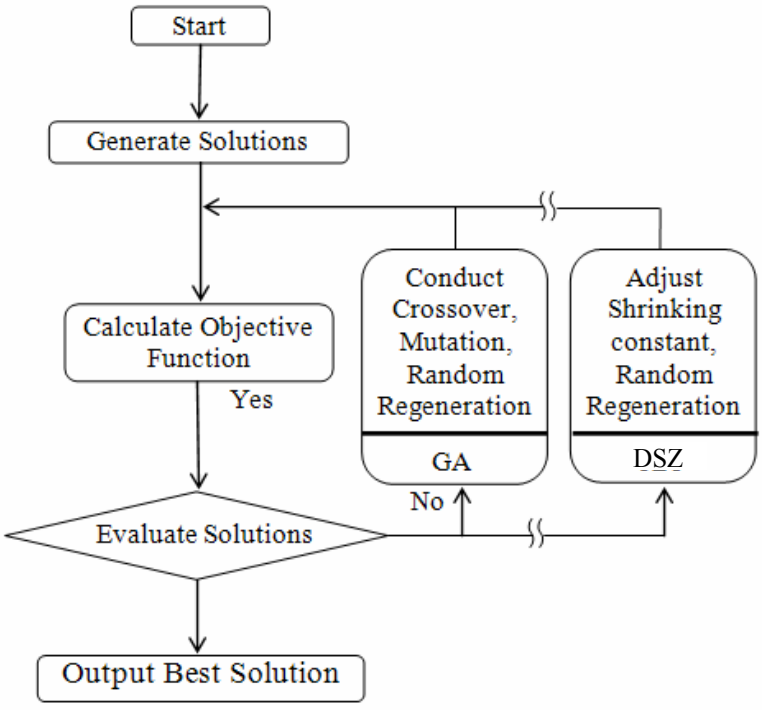

Figure 3- 19. GA and DSZ Optimization Algorithms Flow Chart

3.3.2 Global Optimization Algorithms – Genetic Algorithms

A general objective function is denoted as $f(\vec{x})$, $\vec{x}:[x_1,\cdots,x_i,\cdots,x_n]$ where $x_i(1\le i\le n)$ is real number. D is the region of the independent variables, where D: $l\le x\le u$, $(l_i\le x_i\le u_i, 1\le i\le n)$. Without losing generality, the optimization task is assumed to look for the minimum value of $f(\vec{x})$. The corresponding solution for the global minimum is denoted by $p:[x_{p1},\cdots,x_{pi,}\cdots,x_{pn}],(1\le i\le n)$.

In this section, solving the above problem using the genetic algorithm (GA) is discussed. Table 3-2 provides typical nomenclatures used to describe this algorithm. The GA starts with coding the unknown variables into chromosome, then randomly generate N number of solutions $\overline{X}=[\overrightarrow{x_1};...;\overrightarrow{x_j};...;\overrightarrow{x_N}]$ (population), as shown in the diagram shown in Figure 3- 20. The solutions (chromosome) are weighted based on their fitness function values, the inferior ones will be updated by the 'selection', 'crossover' and 'mutation' operations. GA is an iterative solver; the optimization is terminated by either meeting criteria or reaching the maximum number of iterations. The evolution process and its related parameters will be described below.

Table 3- 2. Nomenclatures in Genetic Algorithms

Genetic Terms in Nature	**Operations in Algorithms**
Chromosome	A series of coded variables
Gene	The 'bit' in Chromosome
Allele	Characteristics value
Locus	Position in the series
Genetype	Candidate solution
Individual	The solution
Fitness	Evaluation criteria
Population	Array of solutions
Reproduction	Reproduce new solution based on fitness value
Crossover	Process of producing new solution from crossover principle
Mutation	Change of values within the coded series (Chromosome)

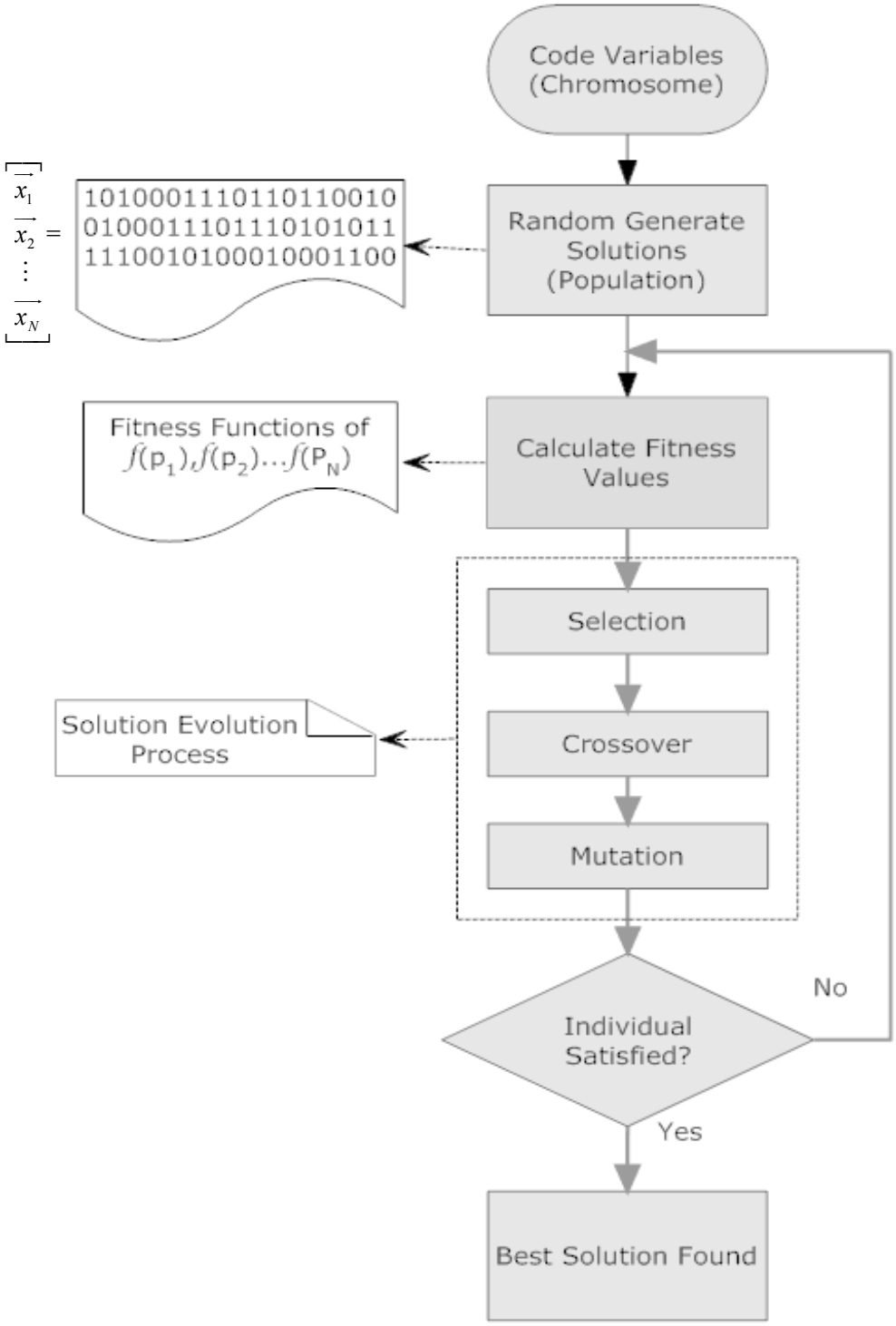

Figure 3- 20. The Genetic Algorithm Diagram

1. Coding in Chromosome

A series of unknown variables such as $\vec{x}:[x_1,\cdots,x_i,\cdots,x_n]$ expressed in certain data structure is considered as chromosome in the GA. In practical applications, the variables are not necessary numbers, thus forming a chromosome probably is easy for the computer to handle. Typical encoding formats are:

- Binary encoding;
- Real number encoding;
- Integer/string array encoding;

For example, given three integer numbers of x_1, x_2, x_3, satisfying $0< x_1<6$, $0< x_2<15$, $0< x_3<30$, the chromosomes encoded by binary and integer codes are indicated in Figure 3-21.

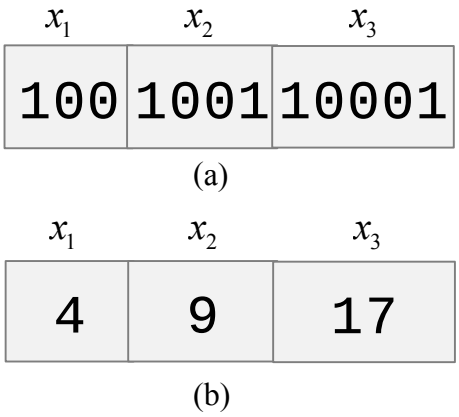

Figure 3- 21. Binary and Integer Encoded Chromosomes

2. Construction of fitness function

The objective function $f(\vec{x})$ is also called fitness function. The chromosomes in the randomly generated populations can be weighed and ranked based on their fitness function values. Many scientific problems can be converted into optimization problems; there are fundamental theories that address how different engineering problems can be transformed into GA minimization. The typical task of the transformation process is to build the proper fitness function. In the non-focal lens design, the fitness function is the average phase errors across the aperture for all beam port excitations, as shown in equation (3-46).

3. Evolution model

When population $\overline{X} = [\overrightarrow{x_1}; \ldots; \overrightarrow{x_j}; \ldots; \overrightarrow{x_N}]$ is weighted by their fitness function of $[\overrightarrow{f_1}; \ldots; \overrightarrow{f_j}; \ldots; \overrightarrow{f_N}]$, the superior solutions could be selected in a given percentage such as $f_k / \sum_{i=1}^{N} f_i$. Inferior solutions (individuals) are eliminated and new ones are reproduced by the 'crossover' and 'mutation' shown in Figure 3- 20. The crossover reflects the data structure variation shown in Figure 3- 22, where whole sets of genes can be truncated and translated. The mutation indicates the single data variation as shown in Figure 3- 23, which provides the possibility of the gene evolutions.

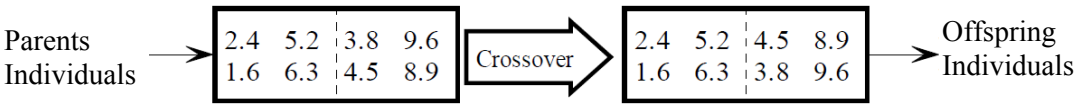

Figure 3- 22. Single Locus Crossover

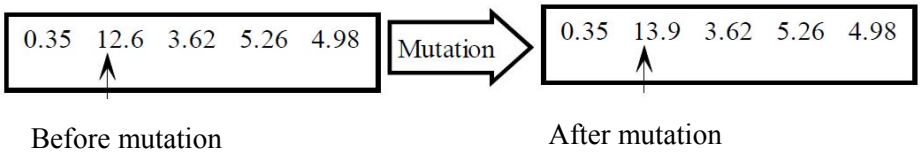

Figure 3- 23. Single Gene Mutation

To sum up, the typical procedure of the GA can be expressed in program codes as:

```
begin
    t=0;
        initialize Fit(t);
        evaluate Fit(t);
        while not finished do
        begin
            t=t+1;
            select Fit(t) from Fit(t-1);
            reproduce pairs in Fit(t);
            evaluate Fit(t);
        end
end
```

The detailed codes for optimizing the non-focal lens are attached in Appendix B.

3.3.3 Non-focal Lens Numerical Results Compared to Focal Lenses

We now present a design example of a non-focal Rotman lens that minimizes the phase error over the array aperture by using the genetic algorithms. The lens parameters are based on the ones in quadrufocal lens design [30], and F/D for each lens is 1. Maximum phase errors normalized to F versus the half plane subtended/scan angles are compared to the trifocal and quadrufocal lens designs, as shown in Figure 3- 24. It is noticeable that there are ideal focal points at 0^0 and 23^0 for the trifocal lens and at 11^0 and 25^0 for the quadrufocal lens. Although the proposed GA result does not have any perfect focal points, the maximum phase errors for most ports are lower than tri and quadrufocal lenses, demonstrating that a relatively optimal phase performance is achieved.

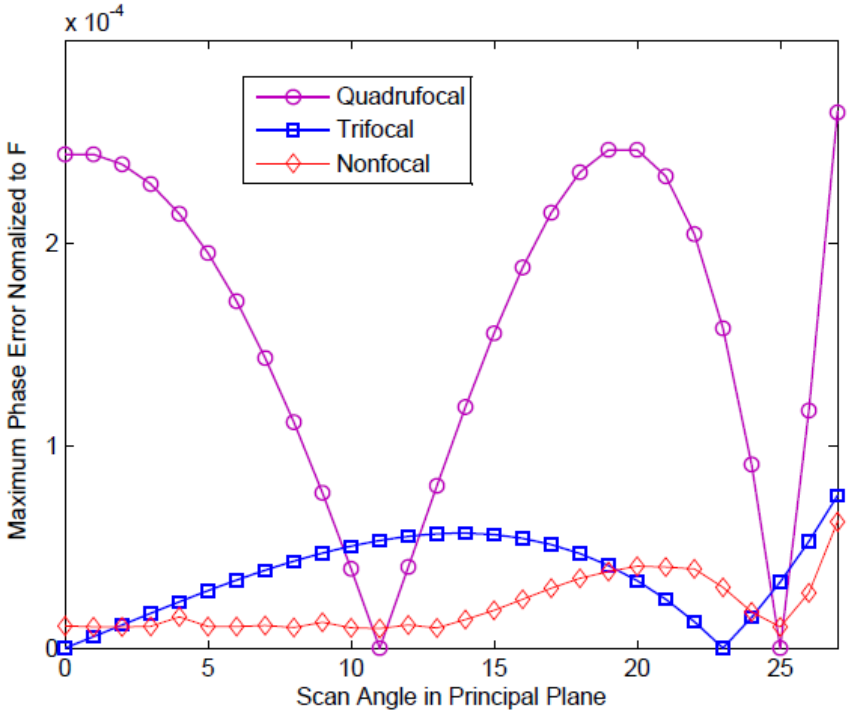

Figure 3- 24. Comparison between Non-focal Lens and Focal Rotman Lenses, r=1

The maximum phase error over all scan angles is chosen as the optimization parameter to be minimized using the genetic algorithm as depicted in the results in Figure 3- 24. To evaluate the phase performance across the aperture, Figure 3- 25 and Figure 3- 26 represent the typical phase distributions across the array aperture that consists of 21 uniform spaced elements for the trifocal lens and the non-focal lens at beam port

excitations of $\alpha_i=10^0$ and 25^0. It is observable that the highest phase errors of the trifocal lens occur at the edge receiving ports, while the ones of the non-focal lens take place at relatively center ports. Although the non-focal lens exhibits higher errors along a few center ports, averagely low-phase errors have been well maintained across the array aperture.

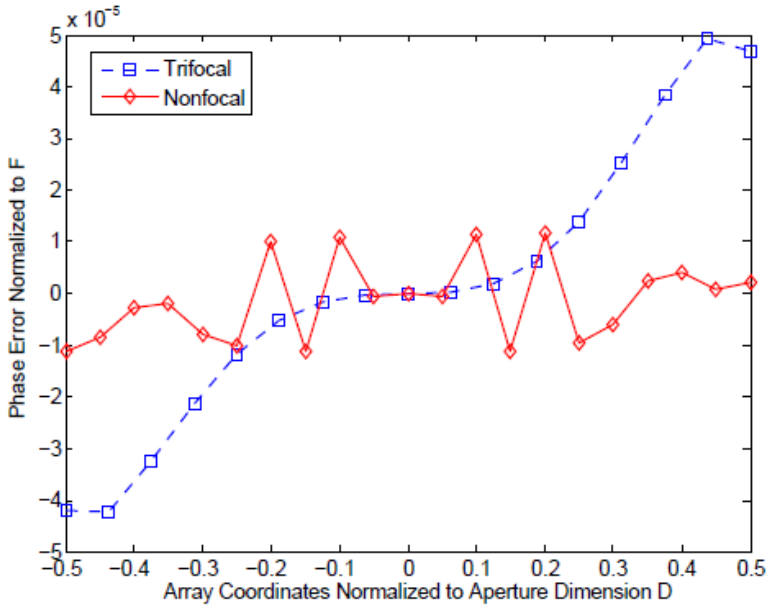

Figure 3- 25. Phase Errors across Array Aperture of Trifocal and Non-focal Lenses for Beam Excitation at $\alpha i=10^0$

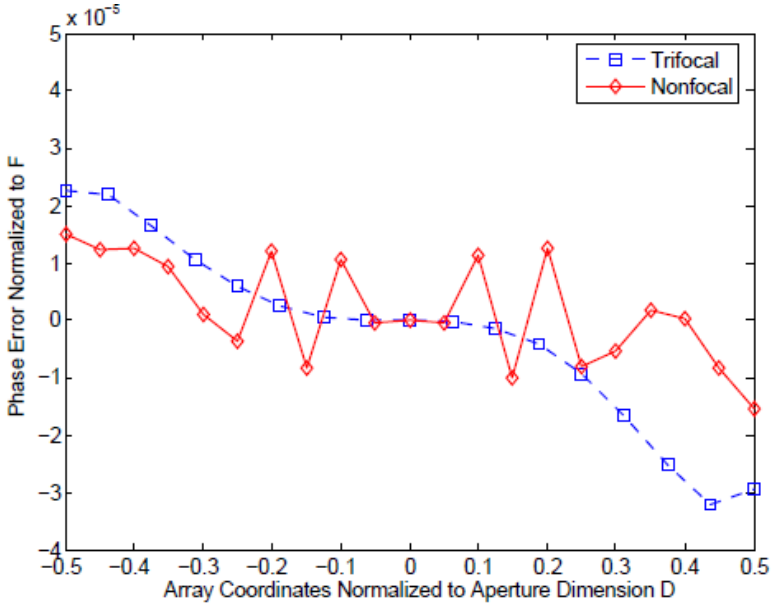

Figure 3- 26. Phase Errors across Array Aperture of Trifocal and Non-focal Lenses for Beam Excitation at $\alpha i=25^0$

The microwave lens is considered a true-time delay structure; hence the phase factors are conventionally normalized to certain geometry dimension on the lens, such as 'center focal length' F. This scheme has been adopted in [17, 29]. In practical design, for different array aperture size and frequency, the phase error in degree is generally preferred representation. The phase error in degree denoted by Δ_d can be readily calculated from equation (10), where Δ_F stands for the phase error normalized to F, λ is wavelength and D is the array aperture size.

$$\Delta_d = \frac{360F\Delta_F}{\lambda} = 360r\Delta_F \frac{D}{\lambda} \qquad (10)$$

Take Figure 6 for example, the maximum phase error normalized to F for Quadrufocal and Non-focal lenses are $\Delta\varphi_F$ = 2.7E-4 and $\Delta\varphi_F$ = 0.7E-4 respectively. Given r=1, their phase errors in degree varies linearly in terms of the aperture size over wavelength, as shown in Figure 3- 27. It is noticeable that for a given phase error normalized to F, as the aperture size in wavelength increases, the effective phase errors in degrees increase as well.

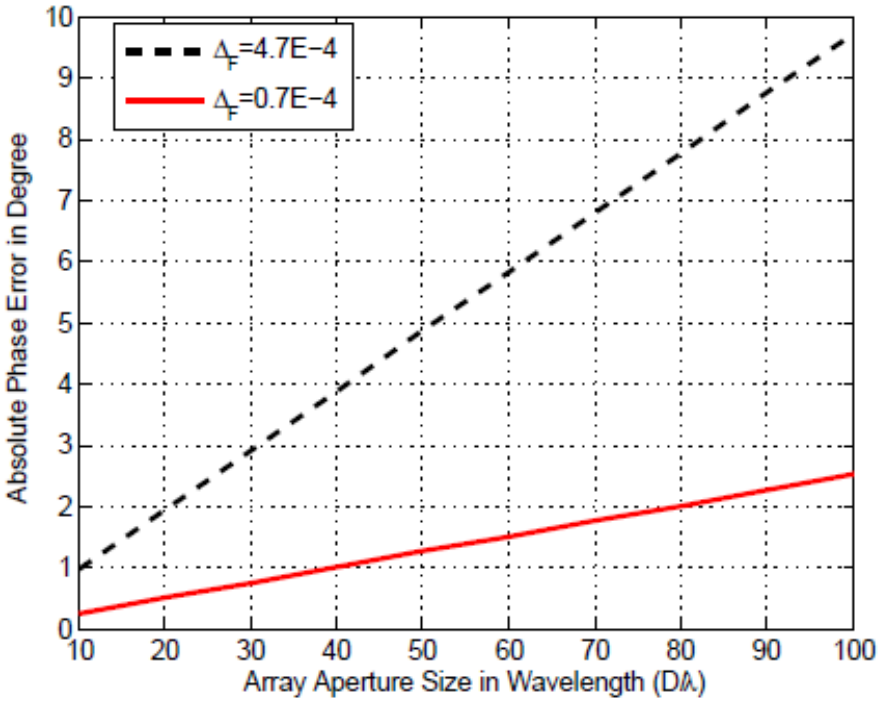

Figure 3- 27. Phase Errors in Degree versus Array Aperture Size for Phase Errors of Δ_F=4.7E-4 and Δ_F=0.7E-4

3.3.4 Array Factor Analysis

The non-focal lens phase error reduction becomes significant when feeding large aperture array. This can get practically important by viewing the Rotman lens development trend. In recent years, such device has been proposed in photonic beam forming [61] and extremely high frequency (EHF) sensor designs [51]. As the frequency increases, the applications may require extremely narrow beams. The required number of array elements may reach hundreds, e.g. in [50], the number of elements for the imaging system is 130. To illustrate the pattern difference between non-focal and focal lenses for large aperture array, we take the maximum phase errors achieved in Figure 3- 24 as phase deviations. Given aperture size of 75λ, the array factors with uniform illumination for quadrufocal and non-focal lens of zero-degree-beam-port excitations are demonstrated in Figure 3- 28. The non-focal lens has resulted in lower side lobes than the quadrufocal lens due to its low-phase error property possessed.

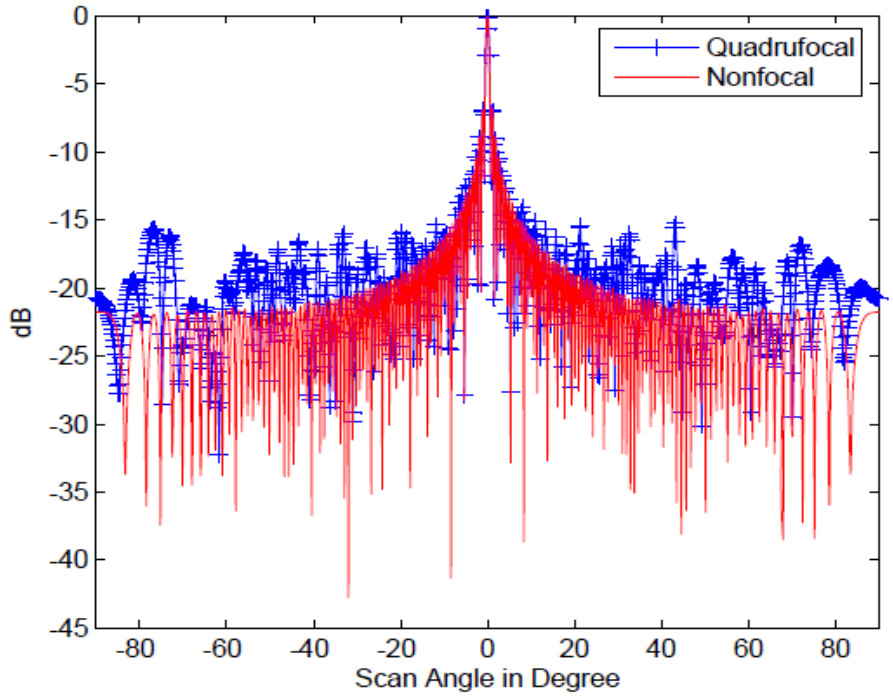

Figure 3- 28. Array Factor Comparison for Quadrufocal and Non-focal Lenses at $\alpha_i=0^0$ for 75λ Aperture

It is worthwhile pointing out that in most practical Rotman lens design, the structure initialization always starts with one or more low-phase error models. After having these initial phase centers, different implementation methods, based on either microstrip, stripline or waveguide, follow different mechanism to allocate the physical beam and receiving ports. Work proposed in this section serves for the first purpose. Extensive codes that produce the microstrip lens geometries in this dissertation have been released in Appendix C. The consequent research in latter scope as well as the rigorous mutual coupling analysis can be answered by more rigorous simulation method in the next chapter.

CHAPTER 4. MICROWAVE LENS EFFICIENT SIMULATION METHODS AND MEASUREMENT VALIDATIONS

Microwave lenses such as the Bootlace/Rotman lenses are designed by implementing physical ports on the predetermined theoretical phase centers. These phase center positions are calculated using geometry optical methods described in the previous chapter under the assumptions of perfect cylindrical waves and true-time delay. A real physical lens does not satisfy these conditions due to different port implementation approaches and mutual coupling effects. Both full-wave investigation and measurement have indicated strong variations at the phase and amplitude couplings between the input and output ports. Efficient models predicting both phase and amplitude performance are still in great demand in order to perform advanced lens evaluation and optimization.

In this chapter, more accurate simulation methods that are capable of predicting both the amplitude and phase information are investigated. Section 4.1 starts with seeking efficient approaches in the full-wave simulation regime. The two dimensional Green's function MoM in FEKO is a potential solver. We will demonstrate its accuracy by comparing the results with measurement. Simulations as tools of assessing various performance of the microwave lens are discussed in this section, too. Considering the high computational cost, we found that the current method is still not convenient to be adopted in the lens optimization iterations or handle large lens structures. A more efficient simulation method is still needed. Hence, in Section 4.2, we propose an alternative simulation method based on the ray tracing concept. A microwave lens is systematically treated by hybrid of a flexible tapered port model and multiple-ray-path coupling approach. The proposed method leads to designing the minimum return loss tapering port and fast lens simulation of acceptable accuracy. We will formulate the ray tracing method for typical microstrip lenses. The predicted results of amplitude, phase couplings, array factors are validated by both using full-wave simulation and measurement.

4.1 Microwave Lens Full-wave Analysis

From the previous chapters, we have learnt that to design a microwave lens, one can follow geometry optical models [17] to formulate initial phase centers of the input and output ports. Then physical implementations are applied by following waveguide, stripline or microstrip mechanisms. We also noticed that the mutual couplings between the adjacent ports as well as the multi-reflections are not predictable by the initial direct ray formulation. Consequently, to draw reasonable estimation of the phase and amplitude information, accurate analysis tools such as full-wave solvers are desired. In recent years, researchers have analyzed Rotman Lens using different numerical techniques, including [62] with finite different time domain (FDTD) in XFDTD, [63] with finite element method (FEM) in HFSS and [54] with finite integration technique (FIT) in CST Microwave Studio. However, to conduct lens optimization, more efficient and accurate methods are still in demand. In this section, we analyze one printed microstrip lens. Given the nature of the printed structure of this Lens, the method of moments (MoM) with planar Green's Function seems more suitable in terms of both accuracy and computation efficiency.

The Rotman Lens under consideration is 8x8 microstrip lens (8 scanning beams, 8 fed array elements). To capture its general performance, we evaluate the phase and amplitude coupling between each beam port and receiving port across a frequency band, as well as the single port to aperture phase and amplitude couplings. Pattern performance is achieved by calculating the array factor using the simulated and measured amplitude and phase information. The errors occurred at the phase, amplitude and pattern are emphasized through post processing. This process assumes a linear phase shift, uniform amplitude tapering and true-time delay design objectives. Simulation results were compared with the measurement across the frequency band of 4-5GHz throughout the evaluation.

4.1.1 Lens Model under Test

The Rotman Lens presented in this section is built on the microstrip laminate Rogers 5870. Lens layout is shown in Figure 4- 1, whose beam ports are marked as 1, receiving

ports are marked as 2, and dummy ports are marked as 0. Note that the dummy ports in lens design are sometimes necessary in order to reduce the side wall reflections as well as to increase the adjacent beam port isolations. In the current lens, all ports are implemented by physical triangular tapered mictorstrip horns, and the transmission line is build on the same layer using traditional 50 Ohm microstrip lines. Port numbers are included in Figure 4-1 as well to facilitate the analysis in forthcoming sections.

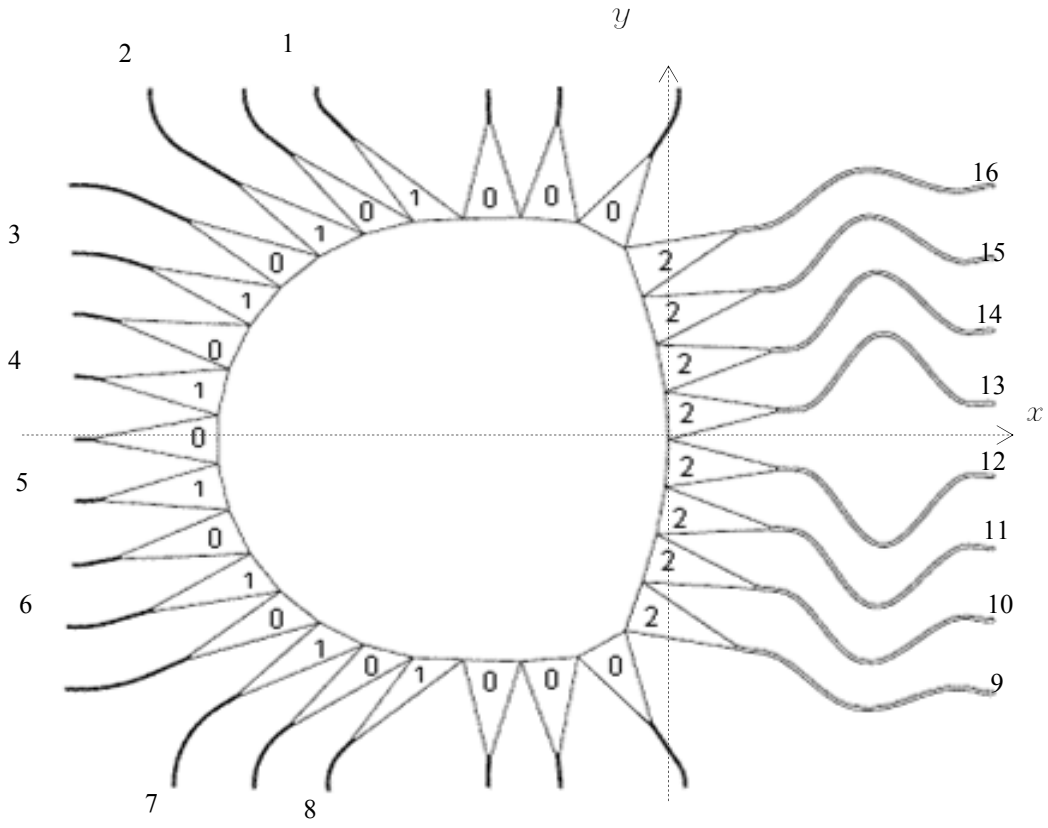

Figure 4- 1. Rotman Lens Layout

Figure 4- 2 is the Rotman lens prototype of Figure 4- 1. It was fabricated by the US Army Research Lab (ARL) in Adelphi, MD. This lens was designed at the center frequency 4.6 GHz, and extensive S-parameter measurements were taken and the results were published in [64]. These results will be used in this paper for validating the FEKO model as well as evaluating the lens performance. Some technical parameters used to construct the lens are listed in Table 4- 1.

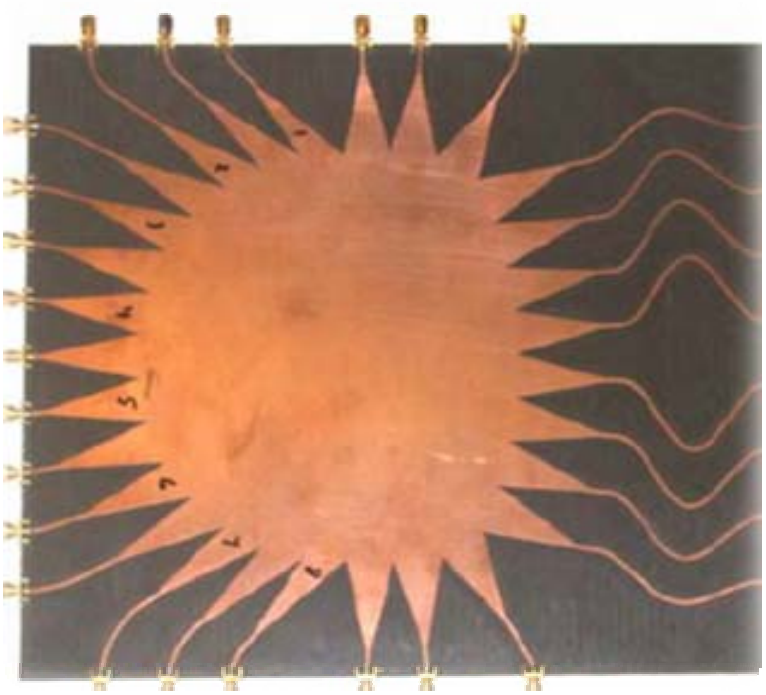

Figure 4- 2. Fabricated Rotman Lens Prototype

Table 4- 1. Rotman Lens Parameters

Symbol	Quantity	Value
f_0	Center Frequency	4.6 GHz
$\boldsymbol{B}$	Testing Band	4-5 GHz
N_b	Beam Port #	8
N_r	Receive Port #	8
ε_r	Relative Permittivity	2.3
tanδ	Loss tangent	0.0012
d	Array Spacing	31.9mm
σ	Conductivity	5.7 e+7
h	Substrate Thickness	31.9 mm
t	Copper thickness	0.07 mm

*Terminal impedance is 50Ω, so the width of the transmission line is designed approximately 1.526 mm. The lens shown in Figure 4- 1 has 13 dummy ports.

4.1.2 FEKO Simulation and Measurement Results

In this section, we focus on the full-wave simulation in FEKO and its validation. We shall keep in mind that the Rotman lens is multiple-port-network structure. While conducting comparisons, either the port to port coupling across frequency or the port to aperture coupling tapering at a single frequency, in both amplitude and phase is important.

The simulation was based on the Planar Green's Function solver in FEKO by assuming an infinite ground plane. Each input/output is modeled as microstrip port. Each port is assigned 50Ohm load so that when any beam port is excited, all others can be terminated. The S parameters between the beam ports and the receiving ports are requested. Eleven discrete frequency steps from 4 to 5 GHz were simulated. The entire simulation took 8.965 hours in a 64-bit workstation, using 4-core Intel(R) Xeon(R) 3.0GHz CPUs. The peak memory consumption of all processes was 2.136 GByte. Detailed lens construction process and simulation configurations in FEKO are attached in Appendix D.

For performance across the aperture, it is suggested to study the amplitude and phase couplings when single ports are excited at a single frequency; for performance across the frequency band, we can study the port to port couplings in their amplitude and phase, respectively. Due to the symmetric structure of a Rotman lens, it is not necessary to compare the results for all ports. Typical ports and comparison strategies standing for the lens performance are listed in Table 4- 2. In this section, we stress on comprehensive comparison between FEKO and Measurement. In the next section, we will focus on the performance analysis based on these data by post processing.

Table 4- 2. Comparison Objects between FEKO and Measurement

	1. Couplings across aperture at 4.6 GHz				2. Couplings Across 4-5 GHz			
Feed Port	1	2	3	4	5	6	7	8
Receiving Port	9–16	9–16	9–16	9–16	13	14	15	16
Amplitude	√	√	√	√	√	√	√	√
Phase	√	√	√	√	√	√	√	√
Figures	Figure 4- 4, Figure 4- 5				Figure 4- 6, Figure 4-7			

1. Couplings across aperture at 4.6 GHz

In both simulation and measurement, the raw data received is more or less the single port to port S-parameters with the amplitude and phase information. For lens design, we first need to examine if the single port excitation is able to produce reasonable amplitude and phase information across the array aperture at the desired frequency, as indicated in Figure 4- 3.

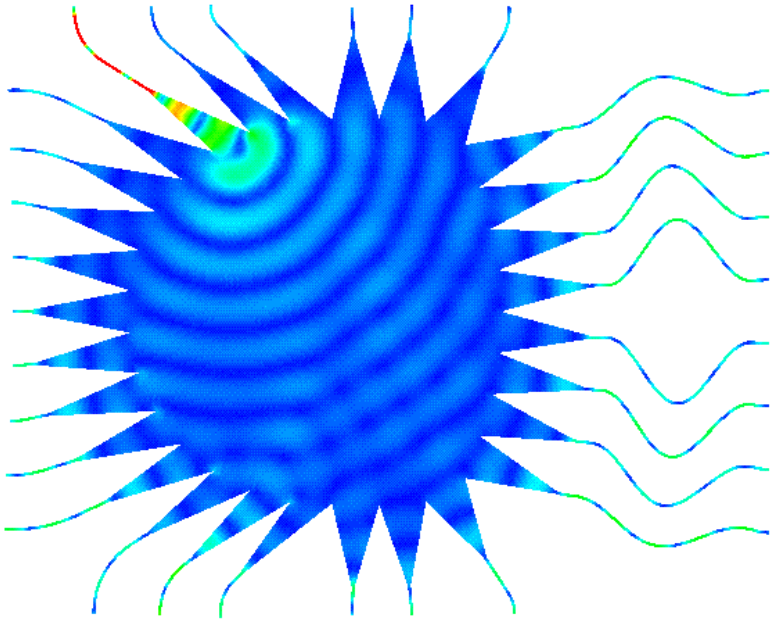

Figure 4- 3. Surface Current for Single Port Excitation

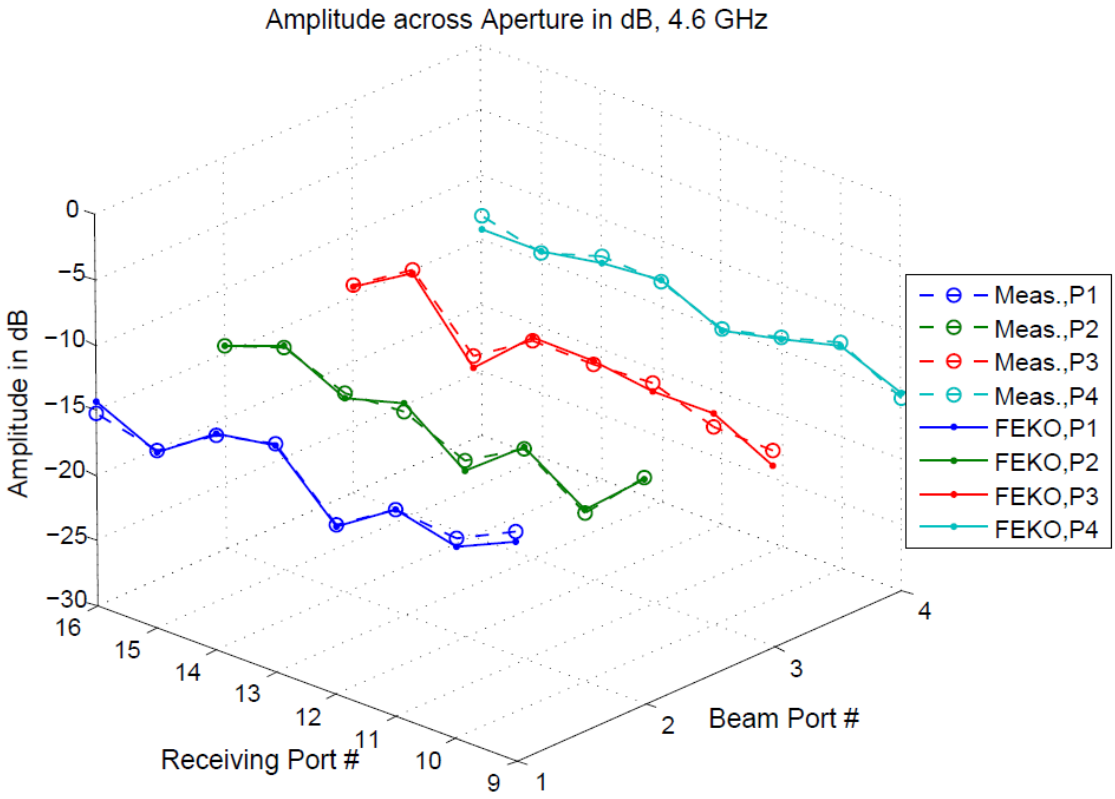

Figure 4- 4. FEKO and Measurement Comparison for Amplitude Taper across the Aperture at 4.6 GHz

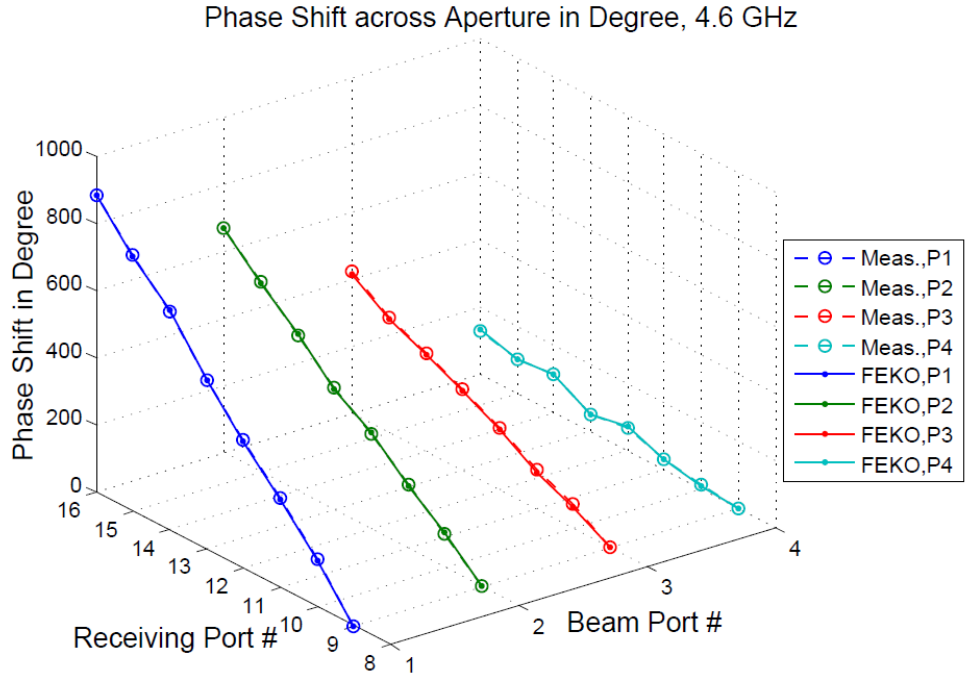

Figure 4- 5. FEKO and Measurement Comparison for Phase Shift across the Aperture at 4.6 GHz

In Figure 4- 4 and Figure 4- 5 we arrange the amplitude coupling and phase shift between beam ports (1-4) and all receiving ports (9-16) in the 3-D plots. It is observed that the amplitude varies along -15dB for all four port excitations. However, as the beam port moves into the center (from 1 to 4), there is a trend that the amplitude fluctuations saturate. From the phase shift perspective, both simulation and measurement show a good agreement. It has achieved a linear phase shift across the aperture. The phase shift for the large angle beam port (e.g. port 1) has a higher slope than the center port (e.g. port 4), which guarantees a large angle scanning beam can be generated. The lens is desired to have uniform amplitude tapering and perfect linear phase shift, the errors occurred over the ideal case is considered as error analysis, which will be explained in the next section.

2. Couplings across aperture across 4-5 GHz

The insertion loss across frequency for single port to port is another important factor, as from the communications system design point of view, this reflects how much gain variation tolerance over the frequency the device possesses. Besides, the phase variations across the frequencies may get significant to answer if the medium is dispersive.

To illustrate the performance across 4-5GHz, according to Table 2, we plot the amplitude and phase couplings between the chosen single ports (5, 6, 7, 8) and receiving ports (13, 14, 15, 16) in Figure 4- 6 and Figure 4- 7. These figures reveal the consistency between the simulation results and the measurement with one exception that the amplitudes encounter higher attenuation at certain frequencies for different port couplings. This exception is probably due to the reflection within the cavity and the different beam port frequency response.

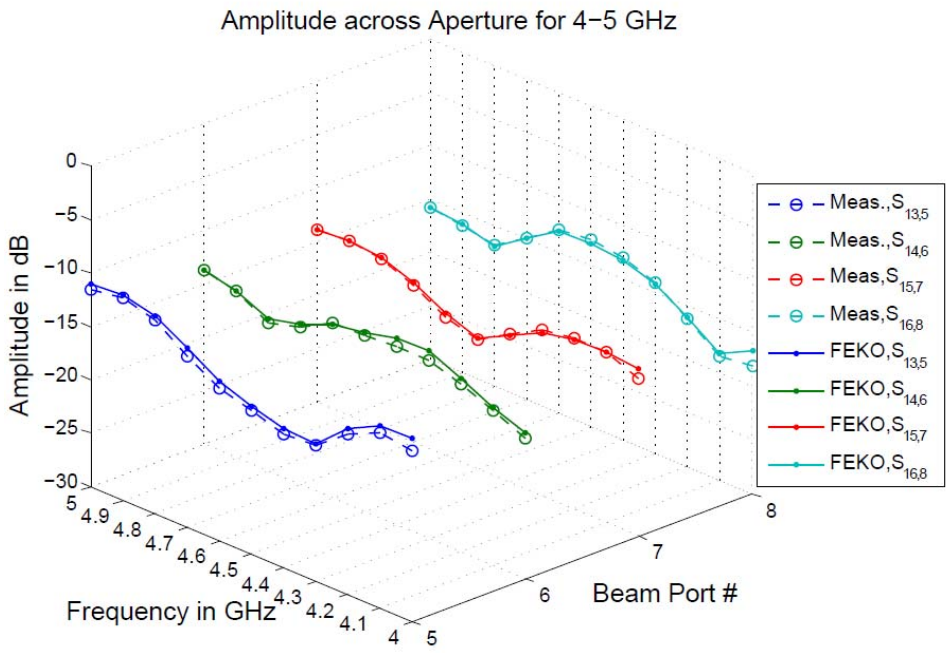

Figure 4- 6. Port to Port Amplitude Coupling Comparison between FEKO and Measurement for 4-5 GHz

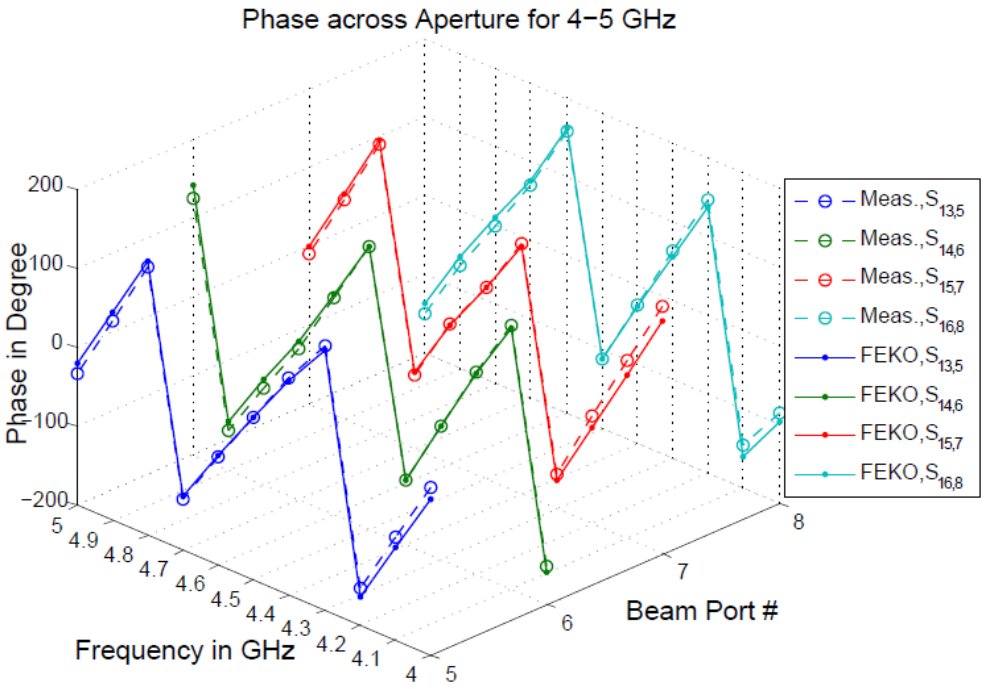

Figure 4- 7. Port to Port Phase Coupling Comparison between FEKO and Measurement for 4-5 GHz

4.1.2 More Post processing Analysis

So far we have been able to accurately compare between FEKO and measurement, but we have not interpolated the results in a way of assisting the lens optimizations. To conduct lens optimization, it is necessary to know how much the results are deviated from the objectives. Although the goal of this section is not to conduct lens optimization, we focus on the error analysis for general lens design from the perspectives of phase, amplitude and pattern, which are essential components of lens optimization in future. Some of the full-wave lens optimization strategies are discussed in the next section.

The general objective of the lens design is to achieve uniform amplitude tapering so as to yield maximum gain, and perfect linear phase shift across the aperture so as to produce stable beams. Resulting from both factors, the true-time delay is also the objective of lens design, meaning, the scanning pointing direction should not change as the frequency varies. In this section, we analyze the amplitude, phase and the scanning direction errors.

1. Amplitude Error Analysis

In Figure 4- 4 we showed the amplitude tapering across the aperture for different beam port excitations. For each beam port, there are corresponding amplitude errors. Figure 4- 8 shows the amplitude errors across the aperture for beam port 4 at 4.6GHz. It is straight forward to use the standard deviation to evaluate the variation of the amplitude errors. Hence, the amplitude errors for all beam ports can be calculated. Figure 4- 9 illustrates the amplitude variations for all the beam ports at 4.6GHz. It is observed that the amplitude errors are not symmetric despite the symmetric design of the lens geometry in Figure 4- 1. In simulation, this may be due to the non symmetric meshes, and in measurement, this is probably due to the fabrication error.

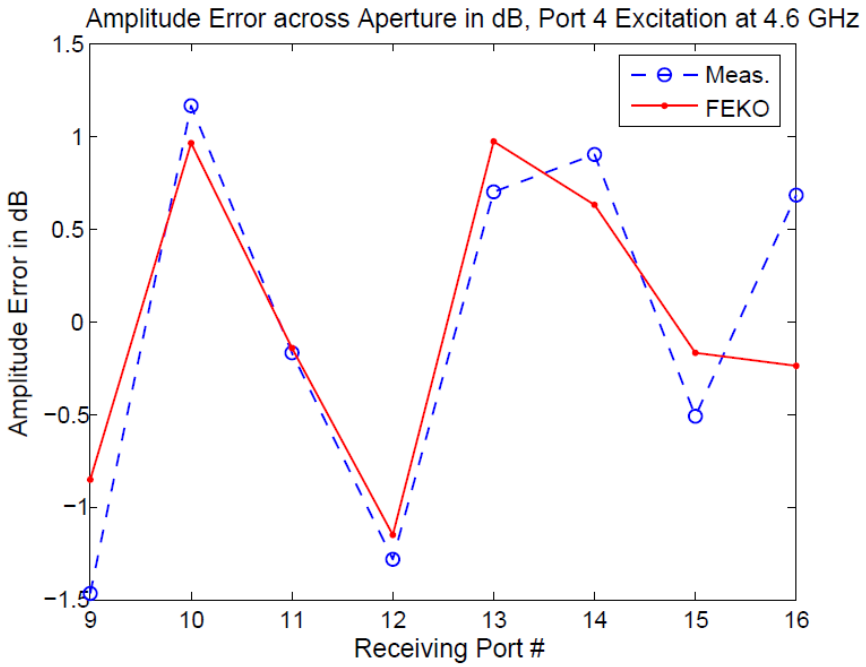

Figure 4- 8. Amplitude Errors across the Output Ports for Port 4 Excitations at 4.6GHz

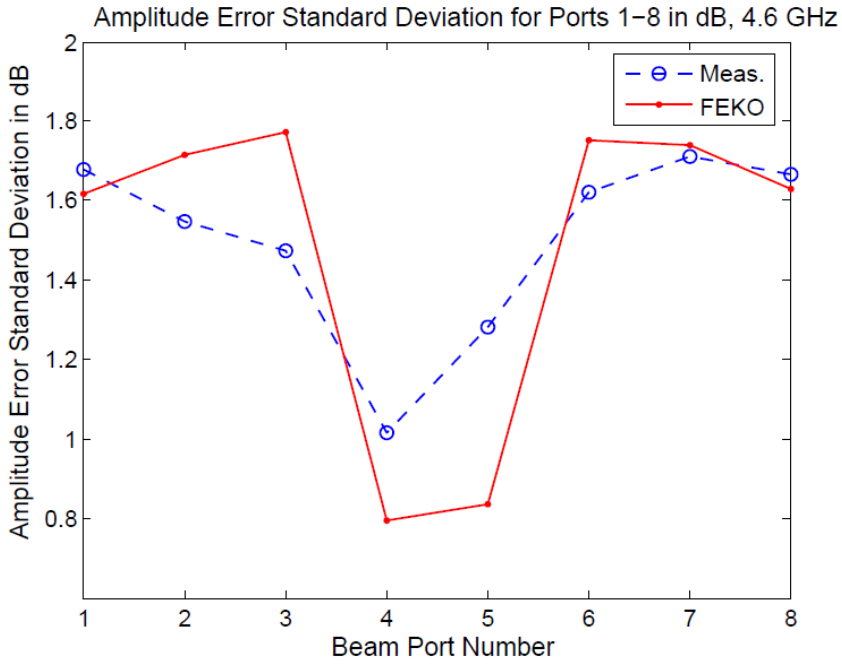

Figure 4- 9. Amplitude Error Standard Deviation for All Beam Ports across Aperture at 4.6GHz

Figure 4- 10 plots the error deviations for all beam ports at various frequencies. It is found that the lens under test maintains average amplitude error of about 1.5dB for all beam ports across the entire frequencies of interest. As the frequency increases, both measurement and FEKO indicate increased amplitude variations.

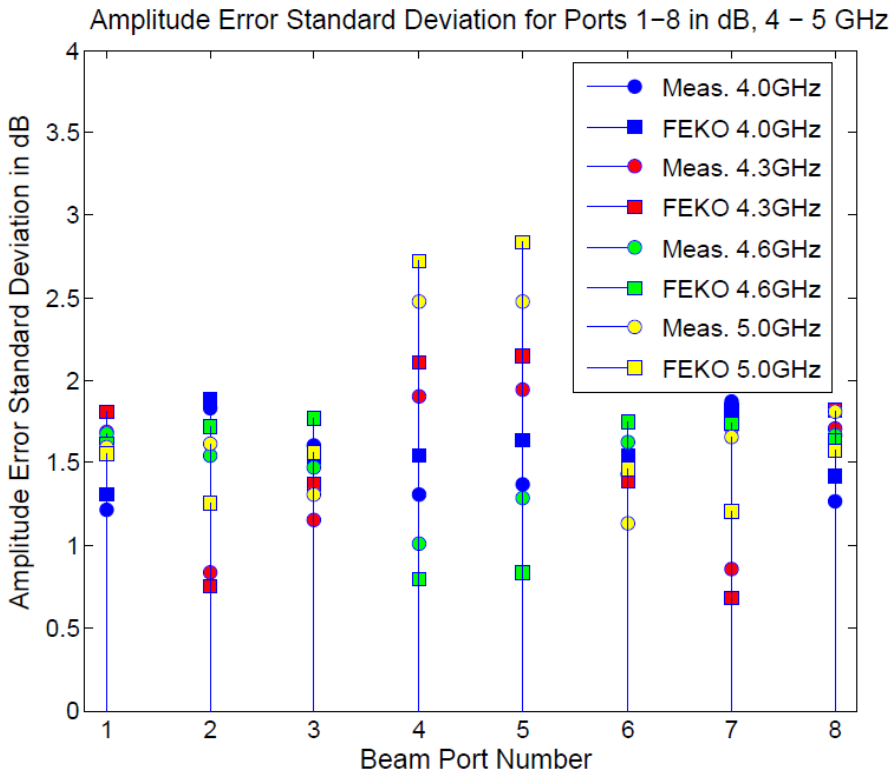

Figure 4- 10. Amplitude Error Standard Deviation for All Beam Ports across Aperture at 4-5GHz

2. Phase Error Analysis

The phase shift representation at single frequency was shown in Figure 4- 5. The phase error occurs when phase shift is not linear any more. Similar to amplitude errors, phase error across aperture takes place for each beam port excitation. Example for Port 4 excitation at 4.6 GHz is shown in Figure 4- 11. The phase error standard deviation extracted from Figure 4- 11 is chosen as the criteria of the single beam port phase performance. The phase error standard deviations for all beam ports at 4.6 GHz are shown in Figure 4- 12. Note that the center beam ports 4 and 5 have exhibited high phase errors up to 15 degrees for the given lens.

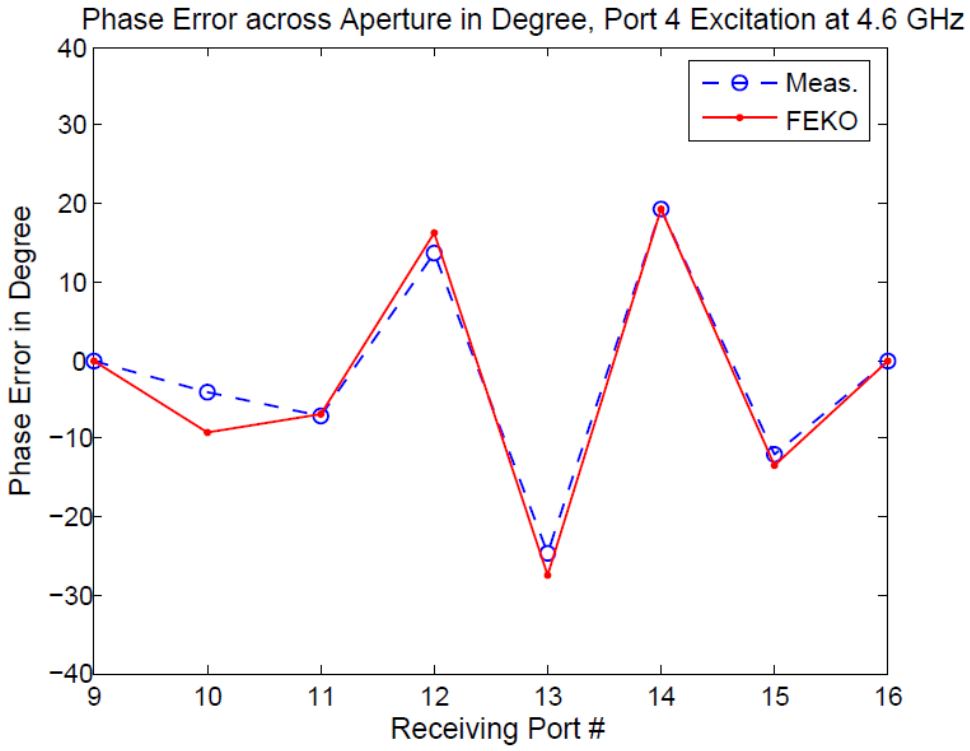

Figure 4- 11. Phase Errors across the Output Ports for Port 4 Excitation at 4.6GHz

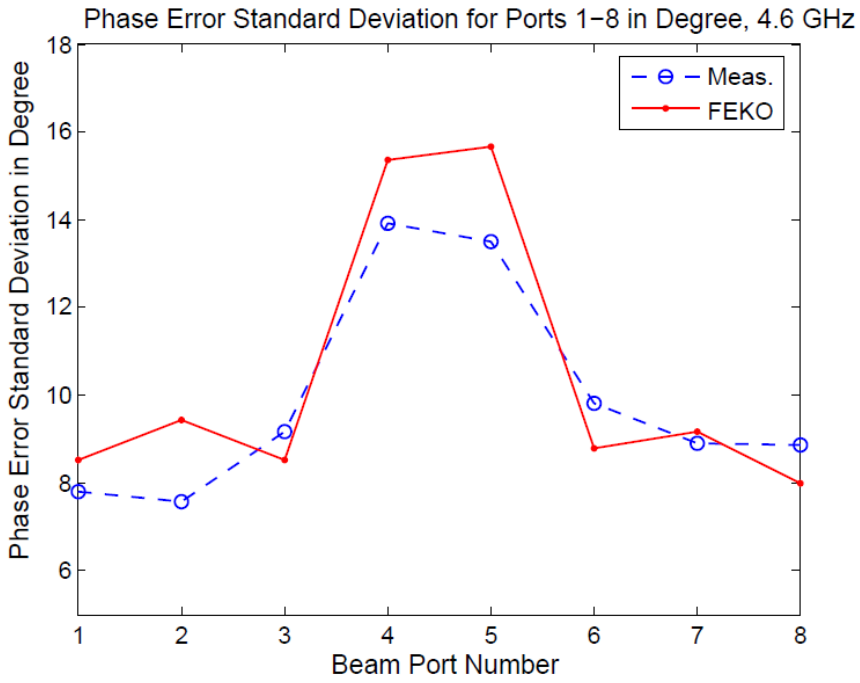

Figure 4- 12. Phase Error Standard Deviation for All Beam Ports across Aperture at 4.6GHz

Figure 4- 13 plots the phase error deviations for all beam ports at 4-5 GHz. It is found that the lens under test has average phase error of about 12 degrees for all beam ports across the entire frequencies of interest. As the frequency increases, the variation in phases increases as well, indicating that more attention should be paid on the high frequency operation during the initial formulation.

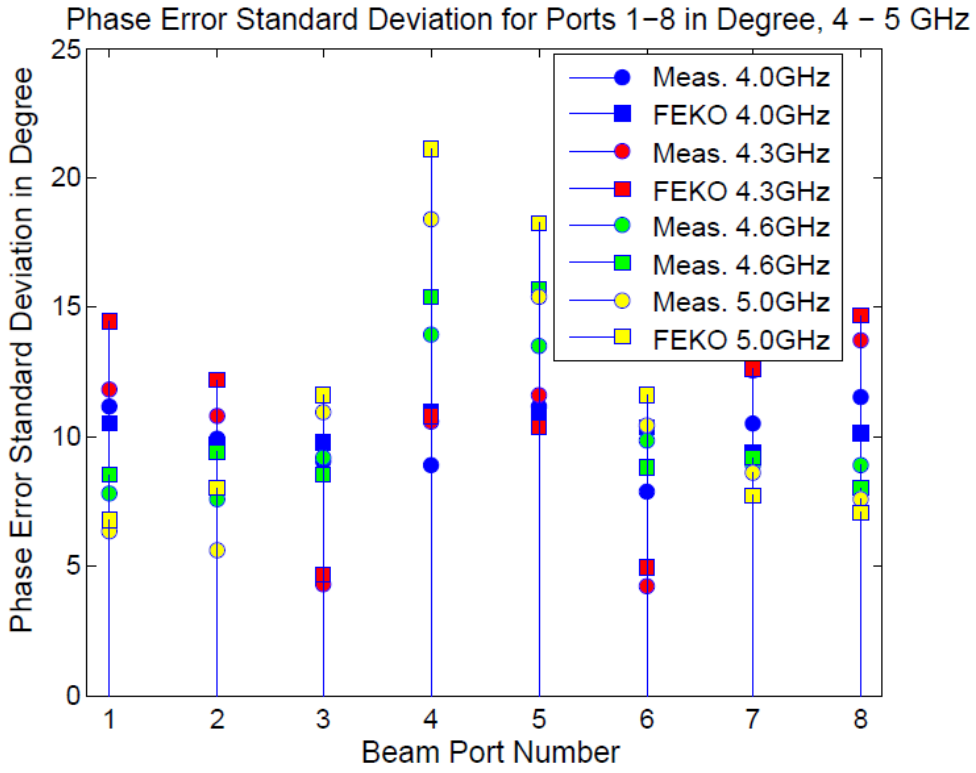

Figure 4- 13. Phase Error Standard Deviation for All Beam Ports across Aperture at 4.6GHz

3. Array Factor Analysis

Whether the amplitude variations in Figure 4- 9 and the phase variations in Figure 4- 13 are acceptable or not depends on the operational array's performance. Typically, amplitude and phase affect the side lobe levels, and the scanning directions. These parameters can be estimated by calculating the array factors, in other words, solving the pattern for isotropic radiation elements.

We investigated the pattern performance by calculating the array factor at lowest frequency 4GHz and highest frequency 5GHz. The following plots assume a linear array

with uniform spacing of 31.9mm. Both measurement and simulation data are plotted in Figure 4- 14 and Figure 4- 15. For single frequency operation, the lens scan up to $\pm 45^{o}$ by eight discrete steps, which is actually resulted from the eight beam port excitations; as the scanning angle increases, gain decreases and the beam width increases because the array aperture efficiency gets lower for large scan angles. Comparison between Figure 4- 14 and Figure 4- 15 indicates that the beam width decreases and highest gain increases as the frequency increases. Besides, as implied by the high variations in both phase and amplitude tapering at higher frequency, patterns at 5GHz reflect much higher gain variation than that at 4GHz.

We also investigated the true-time delay behavior for the given Rotman lens. As it shows in Figure 4- 16, the scanning angle between 4GHz and 5GHz varies between 0.54^{o} and 1.45^{o}. The beam pointing directing has slightly higher errors at the large scanning angles. Note that both measurement and FEKO have predicted asymmetric patterns between 1-4 port excitations and 5-8 port excitations due to their implementation errors.

In general, we processed the phase errors in terms of linear phase shift, calculated amplitude errors based on uniform tapering objective and estimated the pattern performance based on true-time delay property. FEKO simulation and measurement have demonstrated consistent results. The fabricated lens can be characterized by average amplitude error of 1.5 dB, phase errors of 12 degrees, true-time delay with tolerance less than 1.5 degrees across 4-5 GHz.

There are several strategies for improving the microwave lens design using the full-wave analysis. The next section will articulate some of these perspectives.

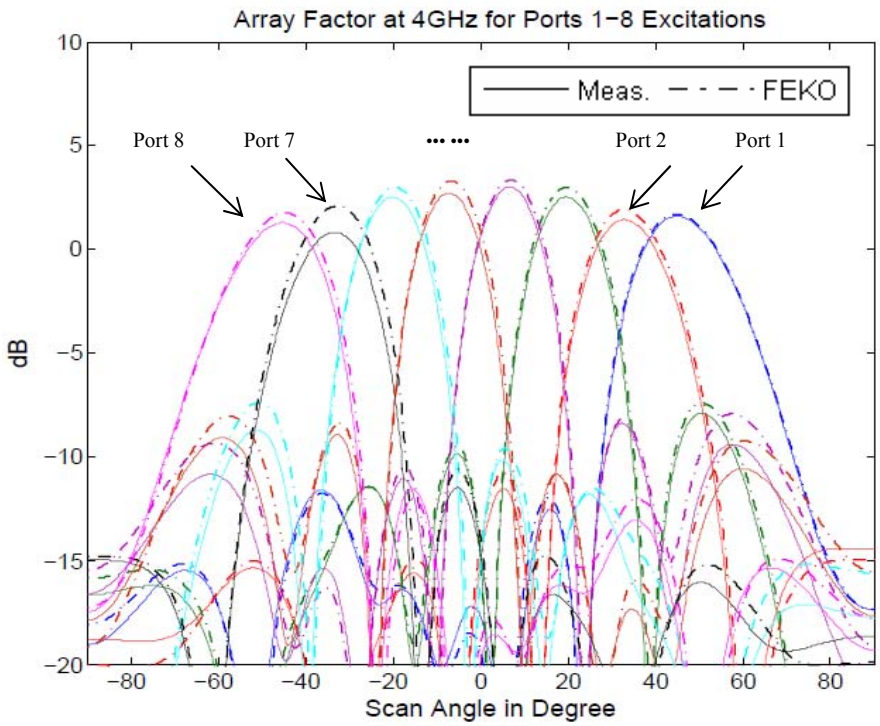

Figure 4- 14. Array Factor for All Beam Port Excitations at 4GHz Based on Measurement and Simulation

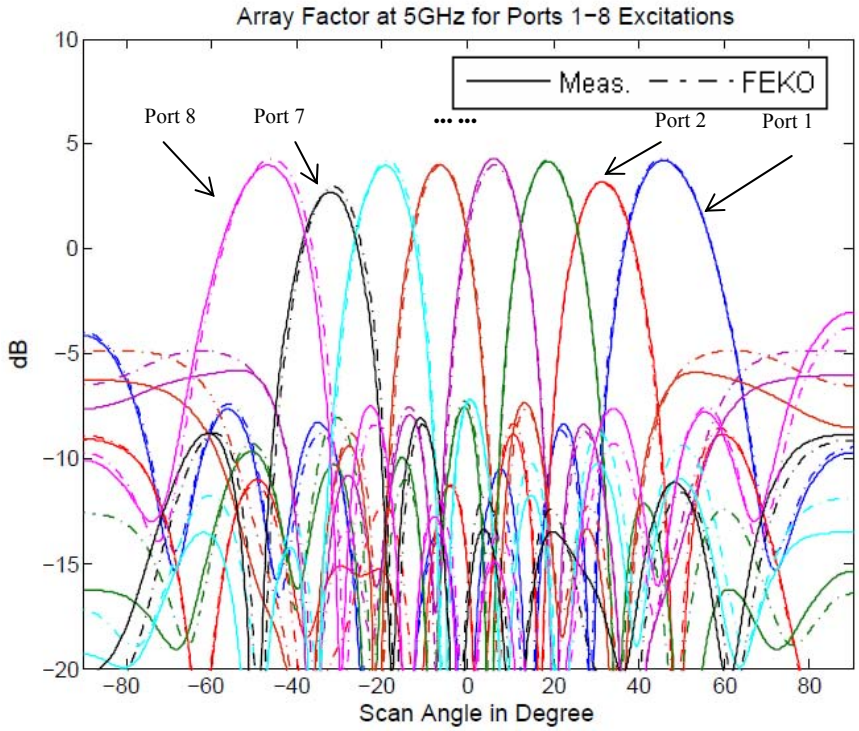

Figure 4- 15. Array Factor for All Beam Port Excitations at 5GHz Based on Measurement and Simulation

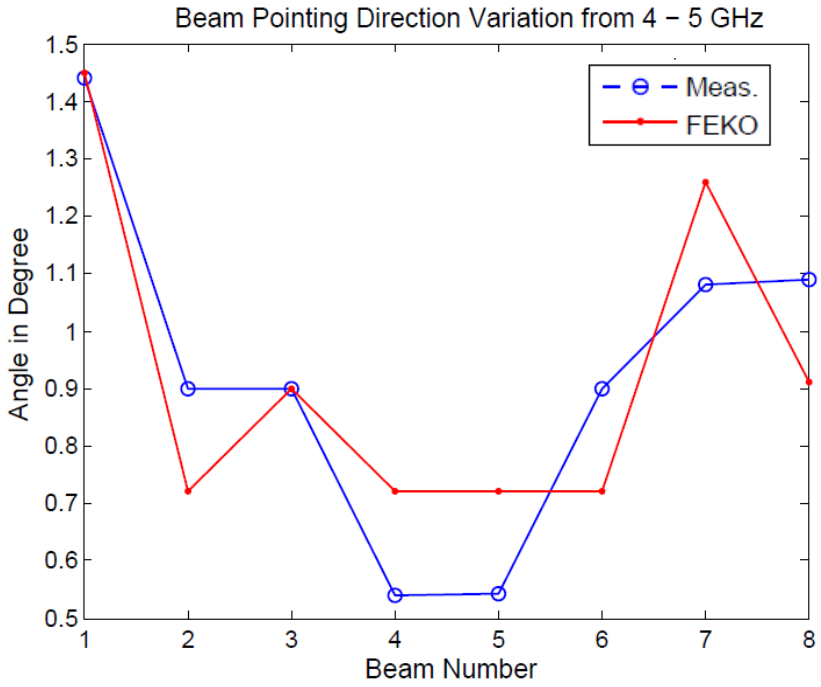

Figure 4- 16. Scanning Angle Variation between Results at 4GHz and 5GHz

4.1.3 Summary and Future Aspects

In previous sections, we have shown that the amplitude and phase errors can be accurately estimated by the measurement and full-wave simulations. The former is more or less considered as secure way of validations, while the latter is preferred to conduct lens optimization in future. It is suspected that the amplitude errors are caused mainly due to the unbalanced energy propagation directions as well as the reflections within the cavity, the phase errors are particularly caused by the phase center shift as well as the reflections within the cavity. We list several several potential ways to improve their performance below.

1. Beam Port Pointing Direction

The beam port pointing direction, shown in Figure 4- 17, affects the gain pattern of each port excitation. To approach the uniform amplitude, typical lens is designed as pointing to the origin. However, for different subtended angle beams, they may have different best pointing angles yielding the desired amplitude distributions along the aperture.

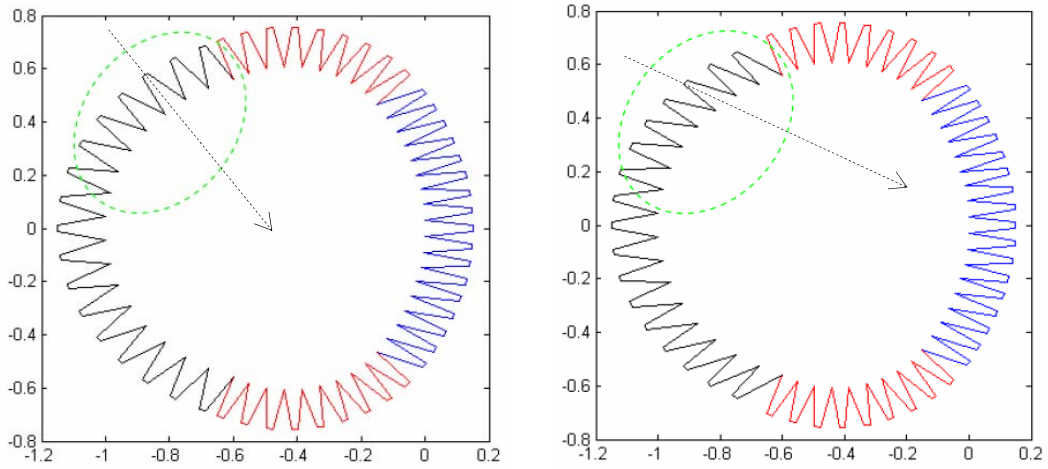

Figure 4- 17. Beam Port Porting Direction Layout

2. Sidewall Freedom of Designs

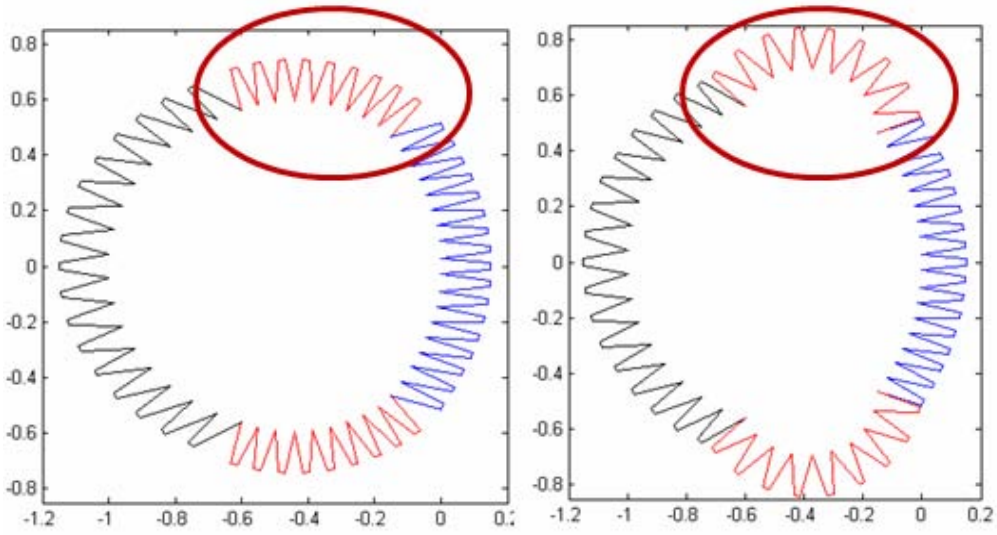

Figure 4- 18. Lens Layout with Different Sidewalls

As it demonstrated in [56], the sidewall dummy port terminations play important rule in reducing the reflections in the cavities. To maximize the absorbing ratio or minimize the reflection at certain direction, the sidewall curvature (Figure 4- 18) and the port sizes are essential parameters. The parametric studies of sidewall optimization have not been reported by full-wave analysis so far.

3. Tapered Horn Optimization

When single beam port is in operation, all dummy ports and other beam ports are expected to be loaded. The geometries of the tapered lines greatly affect their reflection coefficients. It also affects the operational bandwidth of the lens. So far, most of printed Rotman lenses have adopted triangular shape taper horn thanks to its simplicity. However, it has been found that such tapered line is not optimized, hence has high return loss. Several alternative tapered horns as it indicates in Figure 4- 19 are worth investigating for the optimal frequency response. Detailed work on analyzing the tapering port will be presented in the next section.

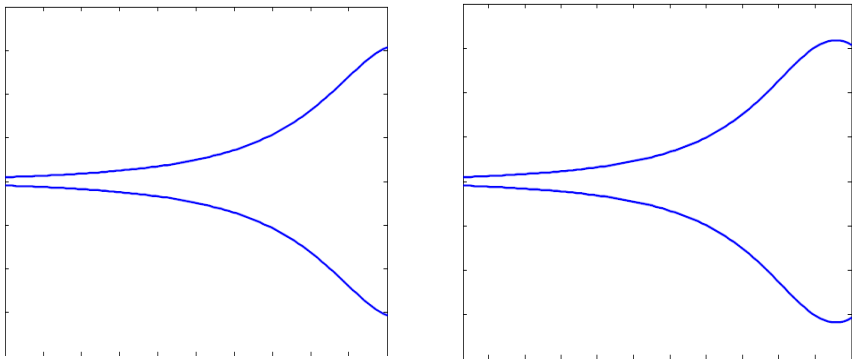

Figure 4- 19. Tapered Horn with Different Geometries

Using full-wave simulation to optimize lens design is a relatively new topic. There are more design freedoms to improve its performance, such as phase center variations versus frequency and mismatch between the cavity and the tapered port junctions, etc. The only drawback of the current full-wave solvers is its high computation cost, which will lead to either very time consuming process, or advanced hardware configuration requirement. Therefor, it is still valuable to devise asymptotic simulation methods that are fast and reasonably accurate to perform the entire lens simulation. Hence, we will address such hybrid method in the next section.

4.2 Fast Ray Tracing Techniques for Microwave Lens Design

Microwave lens models based on geometry optical methods in [17, 29-31] produce theoretical phase centers and transmission line length for the lens initial geometry formulation. However, they capture neither the amplitude behavior across the array aperture or the multiple reflections within the lens cavity. The initial investigation on amplitude couplings in the microwave lens regime was carried in [34], some further research was presented in [28] and [65]. These models adopt two apertures coupling theory with no assumption on either the adjacent elements or profiles of tapered ports. As discussed previously, very accurate full-wave simulation methods such as FDTD [62], FIT [54], FEM [66] and MoM [55] have been applied to predict both phase and amplitude performance of the microwave lens in recent years. Because of the high computation cost, the full-wave methods are hardly adopted to perform lens optimization. Currently, the full-wave solvers are primarily investigated as validation tools for the existing designs [54, 55, 62, 66]. Thus, to develop a simulation method that is fast and accurate is still valuable for the microwave lens design currently.

This section investigates a ray tracing method that is capable to simulate the entire lens structure and conceptually reflect the mutual coupling effect within the lens cavity. By hybridizing with a sophisticated tapered port model, it is appropriately accurate to conduct both phase and amplitude predictions. The presentation in Section 4.2.1 will start with the ray tracing concept for whole lens structure, and then discuss in detail the sub-models of tapered port, two ports couplings, model combination and the ray tracing process. The validation will be addressed in Section 4.2.2 and Section 4.2.3, which proceeds from two points of view: 1) apply ray tracing simulation to predict performance of single port excitation, which leads to the amplitude and phase shift across the aperture performance evaluations; 2) use ray tracing simulation to evaluate lens performance across the frequency. Two fabricated lenses are used in each individual subject. The full-wave simulation and measurement results will be used to assess the proposed design concept.

4.2.1 Ray Tracing Method for Microwave Lens

1. Ray Tracing Concept for Microwave Lens Design

Figure 4- 20 shows a general Rotman lens structure, without the transmission lines connected to the tapered ends on both sides of the lens. The ports on the left hand (in black) indicates the beam ports, the ones on the right hand (in blue) illustrate the receiving ports, while the ones in between (in red) stand for the sidewall dummy ports. To estimate the coupling between any two ports, e.g. points A and D, we need to consider at least three contributors, 1) the return loss due to the tapered beam port, denoted by AB, 2) the direct line of sight coupling between B and C, 3) the reflection due to the receiving port taper CD. The three contributors are combined into a direct coupling factor l_1 between A and D. Beside of the direct coupling, there are reflections off other ports that result in signals in the direction of the receiving port, e.g. reflections off ports QZ and TN represented by coupling factors l_i and l_j, respectively. The reradiated or reflected rays couple with all ports causing secondary couplings. The ultimate coupling result between A and D is the sum of the direct coupling and all secondary couplings.

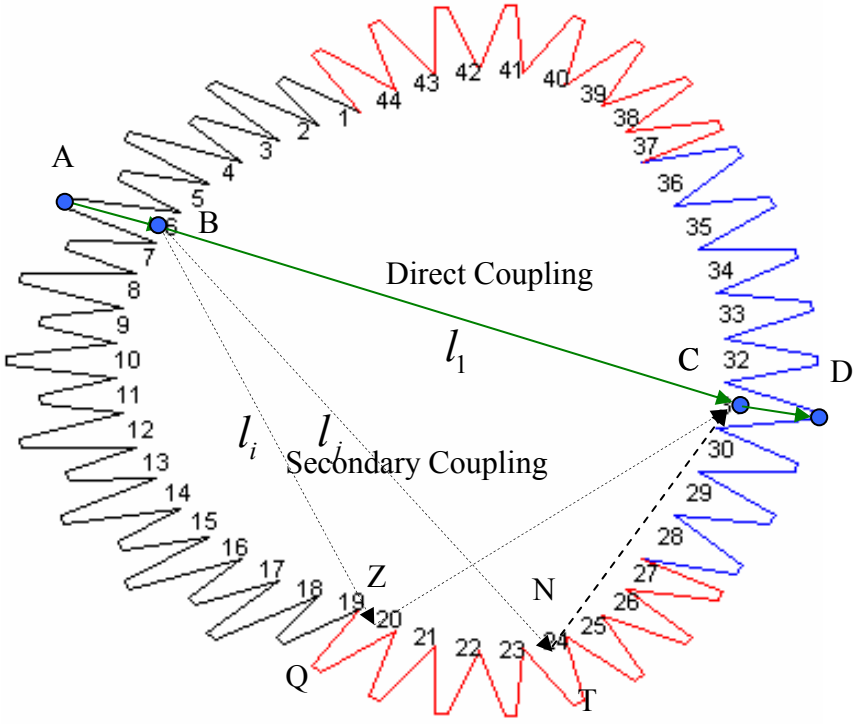

Figure 4- 20. The Basic Idea of Ray Tracing in Microwave Lens

We will first device a method for modeling the tapered port, and further discuss the aperture to aperture coupling models. Direct coupling and secondary coupling expressions are derived and combined in the ray tracing process. The transmission lines will be readily taken into account afterwards. The tapered port models are emphasized here, not only because it is important for the ray tracing simulation, but also it provides significant information for the return loss of the beam port, which actually determines the lens' lowest operation frequency.

2. Tapered Port Models

The tapered port is an essential transmitting and receiving element in the printed microwave lens design, as shown in Figure 4- 20. The port is necessary to be tapered for two reasons. 1) The transmission line that guides energy in/out the lens usually has characteristic impedance of 50Ω, which more or less constraints the width of the port input/output given the specific microstrip material. The cavity junction usually have lower impedance due to the large surface area, hence the tapered line functioning as an impedance transformer is needed. 2) At the receiving contour, it is necessary to be enclosed by large port size in order to reduce the spillover loss, in other word, to increase the power efficiency.

The reflection coefficients that affect the coupling factors are functions of the impedance model at the radiating/receiving elements, which are in turn functions of the physical taper of the elements. Several types of impedance models can be adopted in the Rotman lens design, such as linear, triangular, exponential, Klopfenstein, Chebyshev and other types of tapers. Different models have different reflection patterns versus frequency. Existing approaches of analyzing the microstrip tapers are: small reflection theory [67], contour integral method [68], and general non-uniform line theory [69]. We use the small reflection theory as our basis to form a binomial tapered model for the current microwave lens design.

A triangular physical geometry taper is adopted in Figure 4- 20. Because of its ease of fabrication, it is commonly seen in the microwave lens models. It is worthwhile pointing

out that the geometrical triangular shape does not necessarily represent a triangular impedance tapering. We shall build a model suitable to simulate different type of tapers, hence in Figure 4- 21 a random geometry taper trace is assumed, denoted by $f(x)$, where the x axis is the taper length and y represents its y coordinate. The taper is symmetry with respect to x axis. W means the width of the taper cross-section here, and L is the total length.

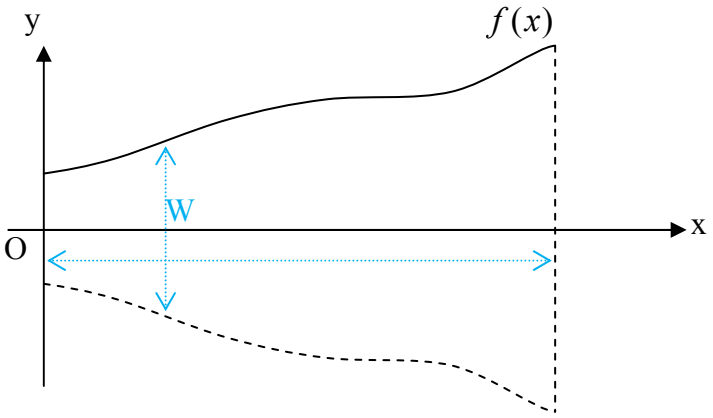

Figure 4- 21. Tapered Line Geometry Model

Given the microstrip material's permittivity ε_r, substrate height d, the effective permittivity single cross-section can be approximated by equation (4-1). The impedance model of the taper can be calculated by equation (4-3) [70].

$$\in_e = \frac{\in_r +1}{2} + \frac{\in_r -1}{2} \frac{1}{\sqrt{1+12d/W}} \tag{4-1}$$

where

$$W = 2f(x) \tag{4-2}$$

$$Z(x) = \begin{cases} \dfrac{60}{\sqrt{\in_e}} \ln\left(\dfrac{8d}{W} + \dfrac{W}{4d}\right) & for\ W/d \le 1 \\ \dfrac{120\pi}{\sqrt{\in_e}[W/d + 1.393 + 0.667\ln(W/d + 1.444)]} & for\ W/d \ge 1 \end{cases} \tag{4-3}$$

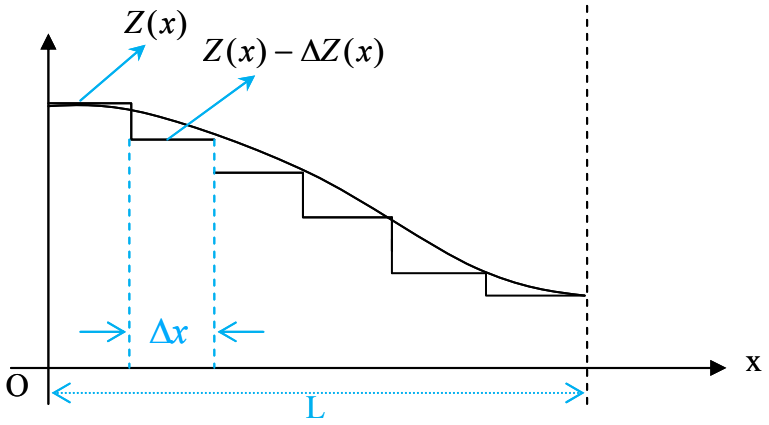

Figure 4- 22. Tapered Lines Impedance Model

Suppose the taper in Figure 4- 21 has an impedance model shown in Figure 4- 22, where Z_0 and Z_L stands for the input and output impedances. Assume the continuous impedance line is made up of a number of constant impedance segmentations with length of Δx . The incremental reflection coefficient due to the impedance deduction can be calculated by (4-4).

$$\Delta\Gamma(x) = \frac{[Z(x)-\Delta Z(x)]-Z(x)}{[Z(x)-\Delta Z(x)]+Z(x)} \simeq -\frac{\Delta Z(x)}{2Z(x)} \tag{4-4}$$

As Δx approaches to zero, equation (4-4) gives an exact differential form (4-5).

$$d\Gamma = -\frac{dZ(x)}{2Z(x)} = -\frac{d\ln[Z(x)]}{2dx}dx \tag{4-5}$$

By summing all the little reflections with proper phase shift yields the total reflection coefficient at x=0:

$$\Gamma = \int_0^L -e^{-j2kx}\frac{d\ln[Z(x)]}{dx}dx \tag{4-6}$$

where k is the wave number $\omega\sqrt{\epsilon_r\ \mu}$.

The aforementioned linear, triangular, exponential, Klopfenstein and Chebyshev tapers are named after their specific impedance curves. They are not suitable for simulating an

arbitrary taper geometry. For an arbitrary taper geometry given in Figure 4- 21, the reflection coefficient can be solved by the procedures described below.

For a given geometry model $f(x)$, use equation (4-3) to calculate its impedance curve $Z(x)$, to facilitate the integration of (4-6), we assume the impedance curve follows an expression of binomial expansions (4-7). It is found that 3 orders are sufficient for most smooth taper models for the microwave lens design.

$$Z(x) = \frac{Z_L}{Z_0} \sum_{i=0}^{N=3} a_i x^i \tag{4-7}$$

Use equation (4-7) to curve fit $Z(x)$ and the coefficients can be determined. Substitute equation (4-7) in (4-6). The return loss at the input is found as (4-8).

$$\Gamma_{pol} = \frac{1}{2}\int_0^L -e^{-2jkx} \frac{d \ln Z(x)}{dx} dz = \int_0^L -\frac{1}{2} e^{-2jkz} \frac{3a_3x^2 + 2a_2x + a_1}{a_3x^3 + a_2x^2 + a_1x + a_0} dz \tag{4-8}$$

It is also possible to design tapered line from a given frequency response. In this case, the coefficient parameters have to be firstly solved from equation (4-8). Then use a determined impedance model of (4-7) to solve the taper geometry function $W(x)$ or $f(x)$. Given the microstrip material property, the relation between the impedance model and the geometry parameters are solved in (4-9)-(4-11) [70].

$$\frac{W}{d} = \begin{cases} \dfrac{8e^A}{e^{2A} - 2} & \text{for } W/d < 2 \\ \dfrac{2}{\pi}\left\{ B - 1 - \ln(2B-1) + \dfrac{\varepsilon_r - 1}{2\varepsilon_r}\left[\ln(B-1) + 0.39 - \dfrac{0.61}{\varepsilon_r}\right]\right\} & \text{for } W/d \geq 2 \end{cases} \tag{4-9}$$

where

$$\text{A} = \frac{Z(x)}{60}\sqrt{\frac{\varepsilon_r + 1}{2}} + \frac{\varepsilon_r - 1}{\varepsilon_r + 1}\left(0.23 + \frac{0.11}{\varepsilon_r}\right) \tag{4-10}$$

$$\text{B} = \frac{377\pi}{2Z(x)\sqrt{\varepsilon_r}} \tag{4-11}$$

We now apply the theory described above to simulate two tapering port models (Figure 4- 23-Figure 4- 24). Figure 4- 23 is a triangular shape tapered line that was implemented

on the lens described in Section 4.1.1. Appling equations (4-1)-(4-3), the impedance model is solved as shown in Figure 4- 25. The taper line shown in Figure 4- 24 is achieved by optimizing the coefficients a_0, a_1, a_2, a_3 in equation (4-8). Its impedance model is determined by the optimized coefficients, whose result is shown in Figure 4- 25 as well. The geometry of the optimized binomial taper can be further calculated using (4-9)-(4-11), as shown in Figure 4- 24. The frequency response of both tapers across 2-6 GHz is given in Figure 4- 26. The results demonstrate that the optimized binomial taper has yielded a nonlinear locus in the geometry; however, it has much lower return loss than the geometrical triangular taper.

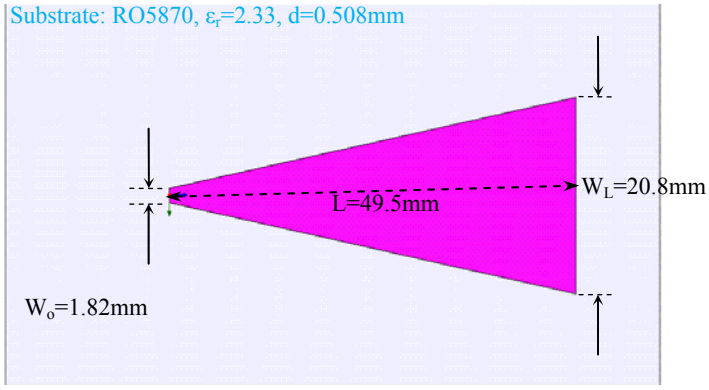

Figure 4- 23. Triangular Shape Tapered Line Impedance Model

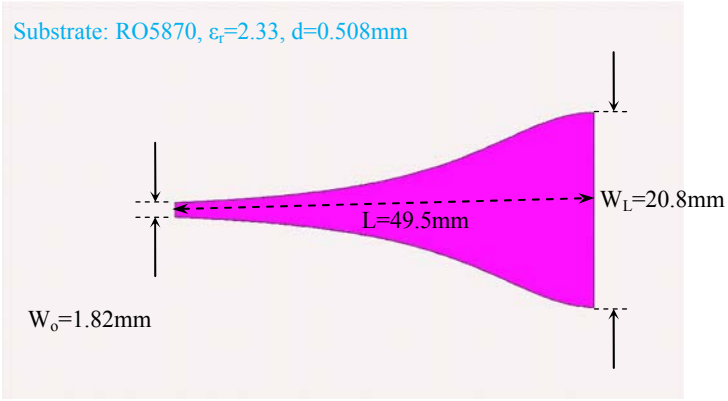

Figure 4- 24. Optimized Binomial Tapered Line Impedance Model

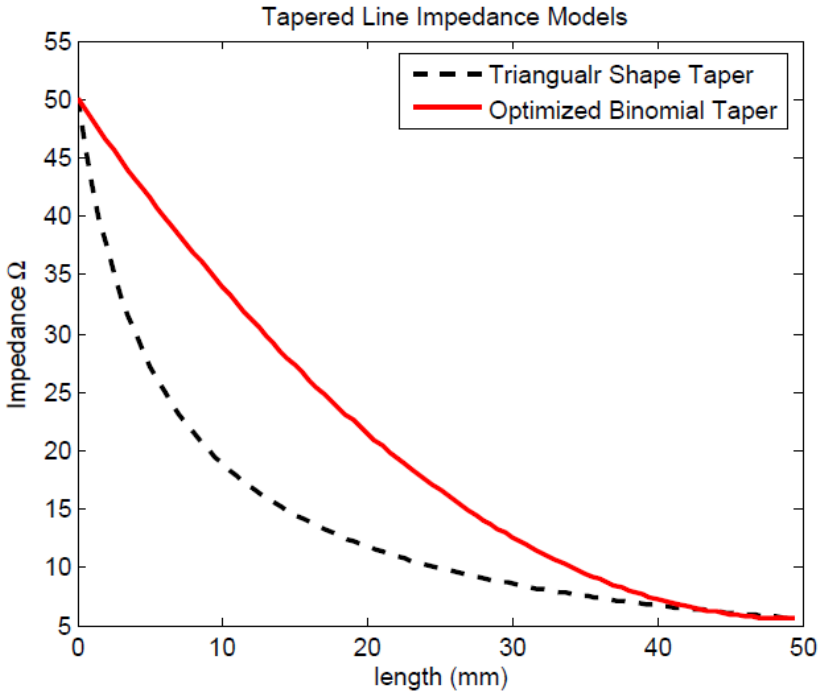

Figure 4- 25. Impedance Curves for Tapers in Figure 4- 23-Figure 4- 24

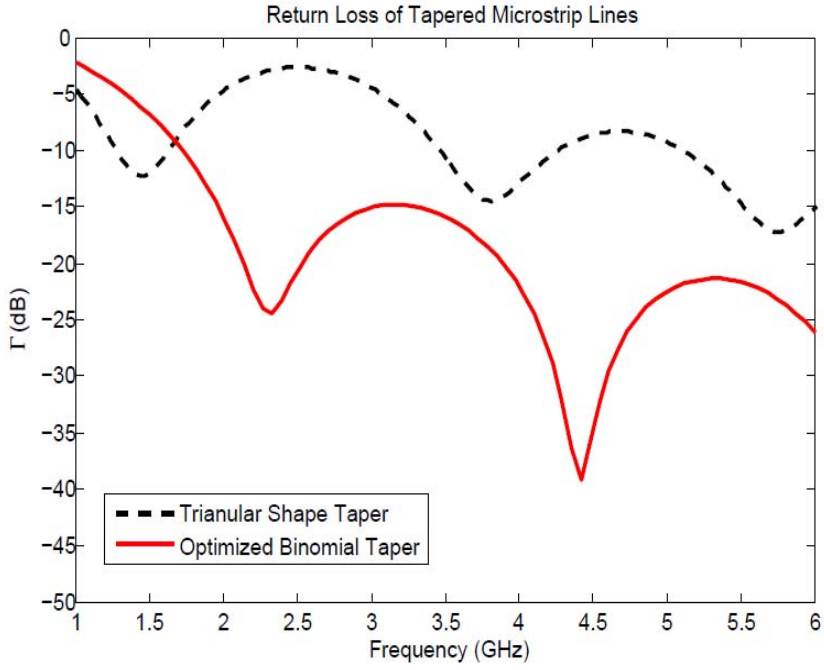

Figure 4- 26. Return Loss of the Tapers in Figure 4- 23-Figure 4- 24

3. Aperture to Aperture Coupling Models

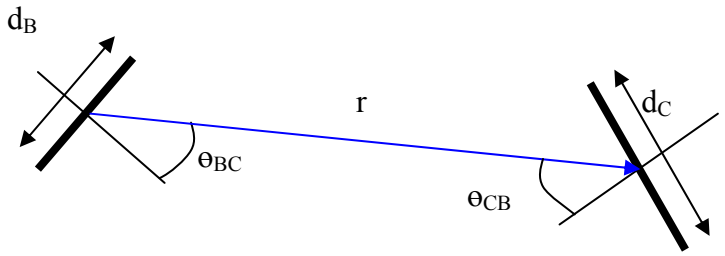

Figure 4- 27. Aperture to Aperture Coupling

The port-to-port coupling mentioned before determines how much energy is coupled from beam port to receiving port, which is a function of the port size, port pointing direction and port-to-port distance, as shown in Figure 4- 27. This model has been studied by using the two dimension aperture theory [71], the mode matching method [72], and the simplified ray equation model [42]. The results of these three models are shown in equations (4-12)-(4-14) respectively. Each of the three models may be used as the port-to-port coupling model in the ray tracing process. Initial ray tracing investigation in this paper adopt the first model given in [71], and represented by equation (4-12).

$$E_C = E_B * \sqrt{\frac{1}{\lambda r}} d_B \sin c(\frac{d_B \sin\theta_{BC}}{\lambda})\cos(\theta_{BC})\sin c(\frac{kd_C}{2}\sin\theta_{CB})\cos(\theta_{CB})e^{-j(kr-\pi/4)} \quad (4\text{-}12)$$

$$E_C = E_B * e^{-j(kr-\pi/4)}\sqrt{\frac{2}{\pi kr}}[\frac{\phi_{eff}(f)}{2\pi H_0^{(2)}(kr_0)} + \frac{2}{\pi}\sum_{n=1}^{\infty}\frac{1}{n}\sin(n\frac{\theta_{eff}(f)}{2})\cos(n\theta_{BC})\frac{\exp(jn\pi/2)}{H_n^{(2)}(kr_0)}] \quad (4\text{-}13)$$

$$E_C = E_B * \sqrt{\frac{d_B d_C}{\lambda r}}\sin c(\frac{kd_B}{2}\sin\theta_{BC})\sin c(\frac{kd_C}{2}\sin\theta_{CB})e^{-j(kr+\pi/4)} \quad (4\text{-}14)$$

4. Combination Process

The complete port-to-port coupling involves direct coupling and secondary couplings, as illustrated by Figure 4- 20. Take the coupling between port AB and CD in Figure 4- 20 for example; the final coupling coefficient is expressed in equation (4-15). The direct

coupling shall combine the taper coefficient and the port to port aperture coupling as well, and it is expressed in equation (4-16), where $E_{CB}(\theta_{BC},\theta_{CB},d_A,d_D)$ is a function of port size and pointing direction and stands for the aperture to aperture (B-to-C) model described previously. The secondary coupling shall combine all reflections from all other ports, which is expressed in equation (4-17), where port QZ of Figure 4- 20 has been considered as any arbitrary port beside of the transmitting and receiving ports. In equation (4-17), it assumes the total port number in the microwave lens is P.

$$E_{DA} = E_{DA(direct)} + E_{DA(indirect)} \tag{4-15}$$

$$E_{DA(direct)} = E_A * \sqrt{1-|\Gamma_{AB}|^2}\, e^{-jkL_{AB}} * E_{CB}(\theta_{BC},\theta_{CB},d_B,d_C)\sqrt{1-|\Gamma_{DC}|^2}\, e^{-jkL_{DC}} \tag{4-16}$$

$$\begin{aligned} E_{DA(indirect)} = & \sum_{n=1}^{N=P-1} E_A \sqrt{1-|\Gamma_{AB}|^2}\, e^{-jkL_{AB}} E_{QB}(\theta_{BQ},\theta_{QB},d_B,d_Q) \\ & * \Gamma_{QZ} E_{CQ}(\theta_{QC},\theta_{CQ},d_Q,d_C)\sqrt{1-|\Gamma_{DC}|^2}\, e^{-jkL_{DC}} \end{aligned} \tag{4-17}$$

In equations (4-16)-(4-17), k is the wave number in dielectric medium, given loss tangent of $\tan\delta$, the wave number is calculated in (4-18).

$$k = k' - jk'' = \omega\sqrt{\mu \in_r}\,(1 - j\frac{\tan\delta}{2}) \tag{4-18}$$

It is noted that the transmission lines in the microwave lens have not been taken into account during the ray trace formulation. Given transmission line length of T at either the transmitting port or receiving port, it can be readily involved by multiplying equation (4-15) with a phase term of e^{-jk_eT}, where $k_e = \omega\sqrt{\in_e \mu}$ and the effective permittivity $\in_e$ can be solved from equation (4-1).

4.2.2 Validation of Microwave Lens #1

Two lenses have been constructed, full-wave simulated and measured. The initial CST Microwave Studio simulation result of the first type of lenses (made in IAI Elta

Electronics Industries) was investigated in [54]. In this report, measurement results are used to validate the proposed ray tracing algorithms. The second lens was built and tested in the US Army Research Lab and extensive FEKO simulation and measurement results are used to perform the validation in Section 4.2.3.

The lens under test shown in Figure 4- 28 is designed at C-band and has 16 beam ports and 32 receiving ports, with dimension of 37cm X 44cm. The beam port is denoted as 1, receiving port is denoted as 2, and all dummy ports have signs of 0, marked at the narrow ends of the ports.

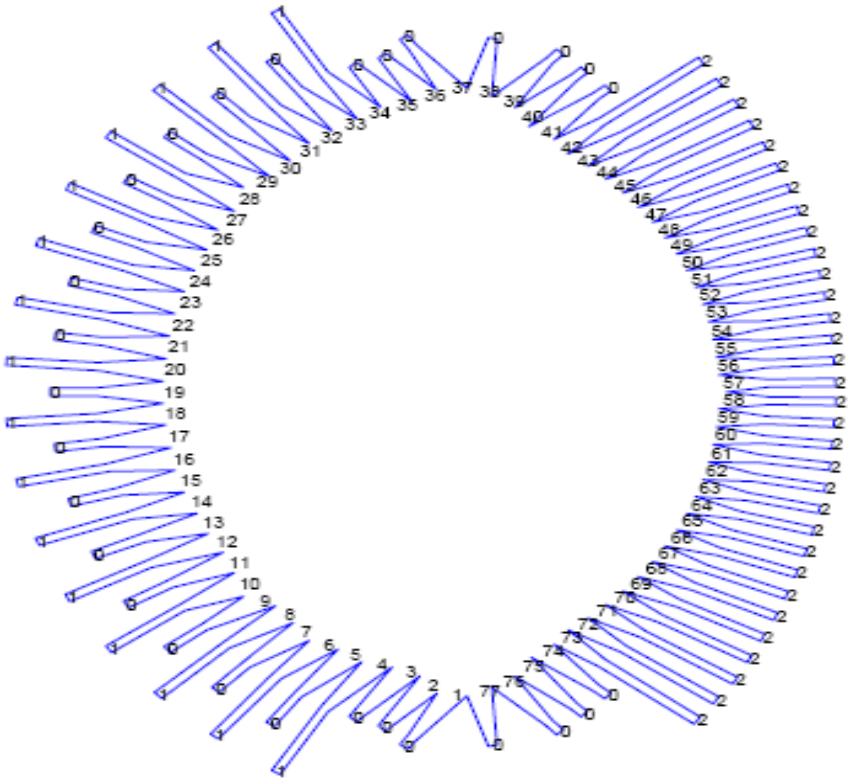

Figure 4- 28. Rotman Lens #1 under Test, 1 Stands for Beam port, 0 Dummy port, and 2 is the Receiving Port.

The measurement was conducted by two port network analyzer on the condition that all other ports are terminated by 50 Ohm loads. Because the performance of the microwave lens relies on the phase shift and amplitude couplings across the aperture, the measured data is usually post processed into two formats: the phase shift and amplitude couplings across the aperture (port 5-87 output) at single frequency, and the amplitude and phase

couplings between two ports across the band. The array factors can be further studied by using the simulated phase and amplitude information, based on equation (1-69). Since the amplitude is based on the S parameter between beam and receiving ports, it actually contains the loss in the lens, in the rest of the dissertion, the array factor can be also regarded as the gain for the isotropic-element array. In this section, the phase, amplitude and array factor performance for single port excitation are presented. Performance across frequency band is further studied in the second lens validation in next section.

At single frequencies of 8 and 10 GHz, the amplitude distributions and phase shifts across the aperture due to the center beam port #20 and edge beam port #4 illuminations are demonstrated in Figure 4- 29~Figure 4- 36. Two examples of the array factors due to the ray tracing simulation and measurement results are compared in Figure 4- 37~Figure 4- 38. More comparison results between the measurement and ray tracing program have been organized in Appendix E.

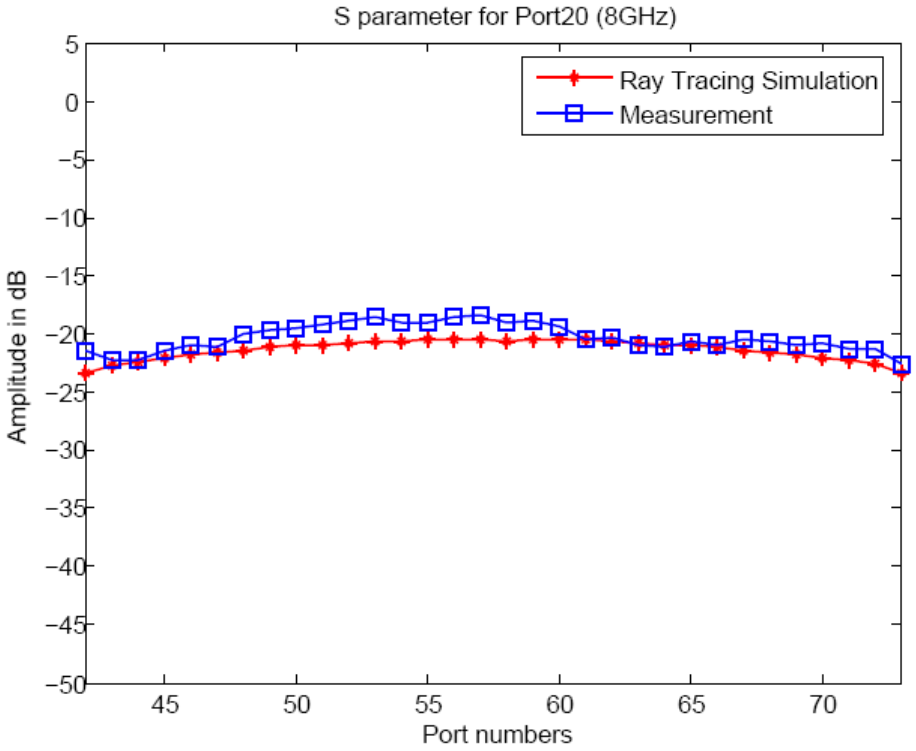

Figure 4- 29. Amplitude across Aperture for Port 20 Excitation at 8GHz

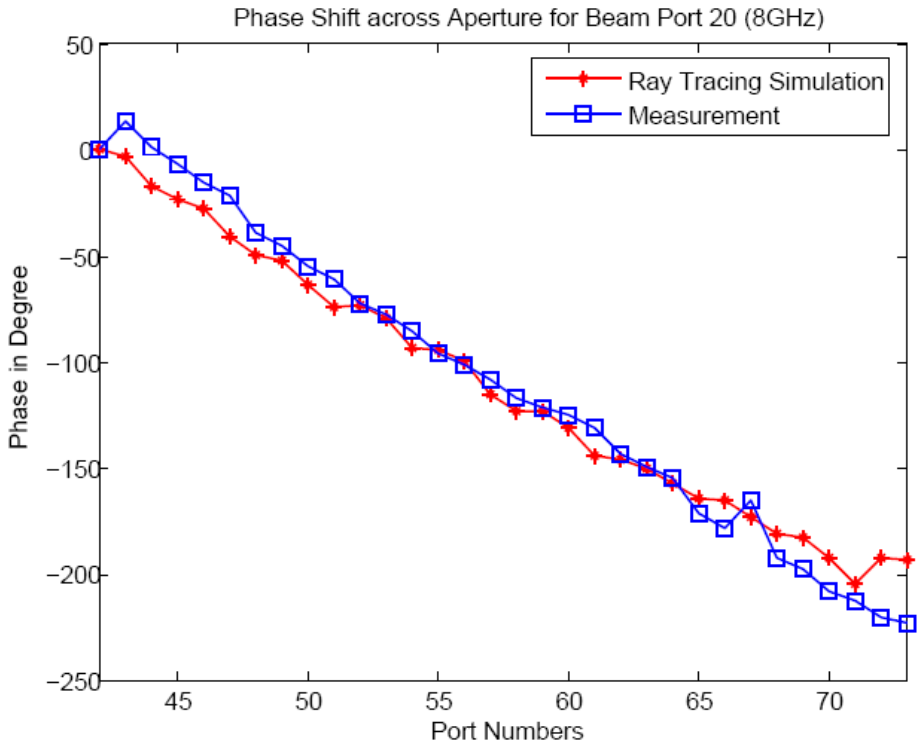

Figure 4- 30. Phase Shift across Aperture for Port 20 Excitation at 8GHz

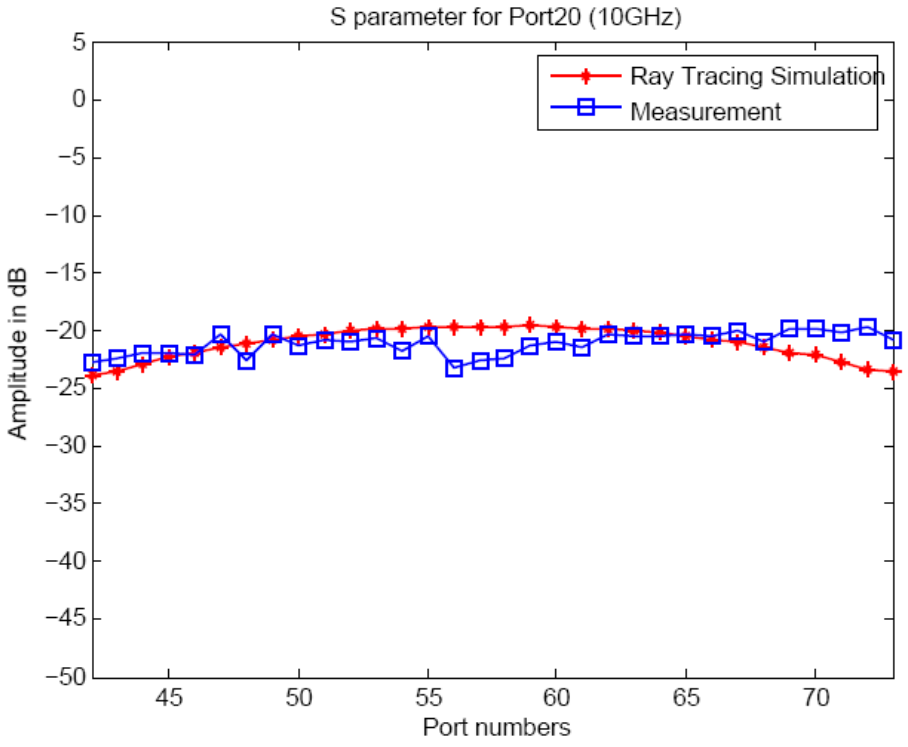

Figure 4- 31. Amplitude across Aperture for Port 20 Excitation at 10GHz

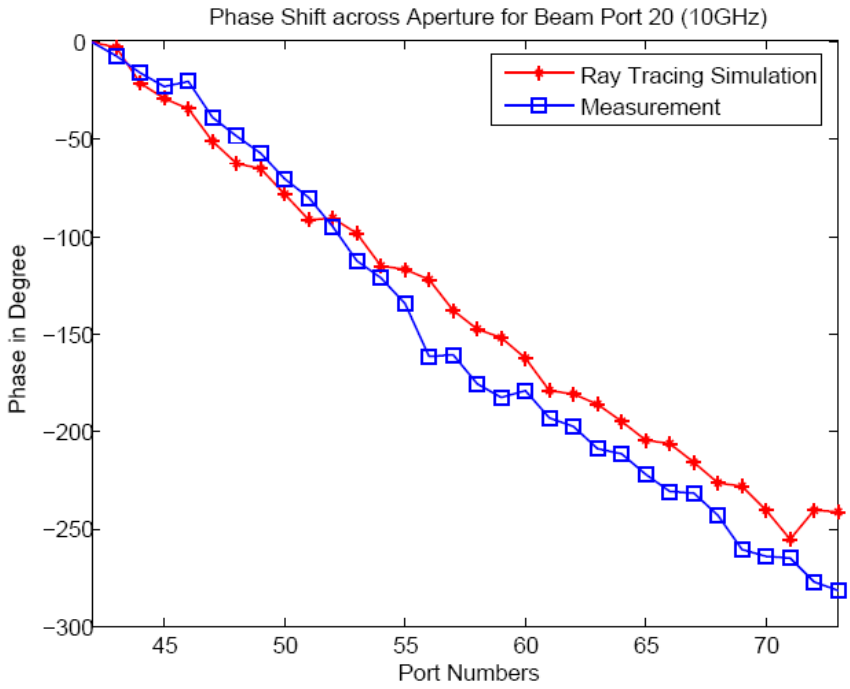

Figure 4- 32. Phase Shift across Aperture for Port 20 Excitation at 10GHz

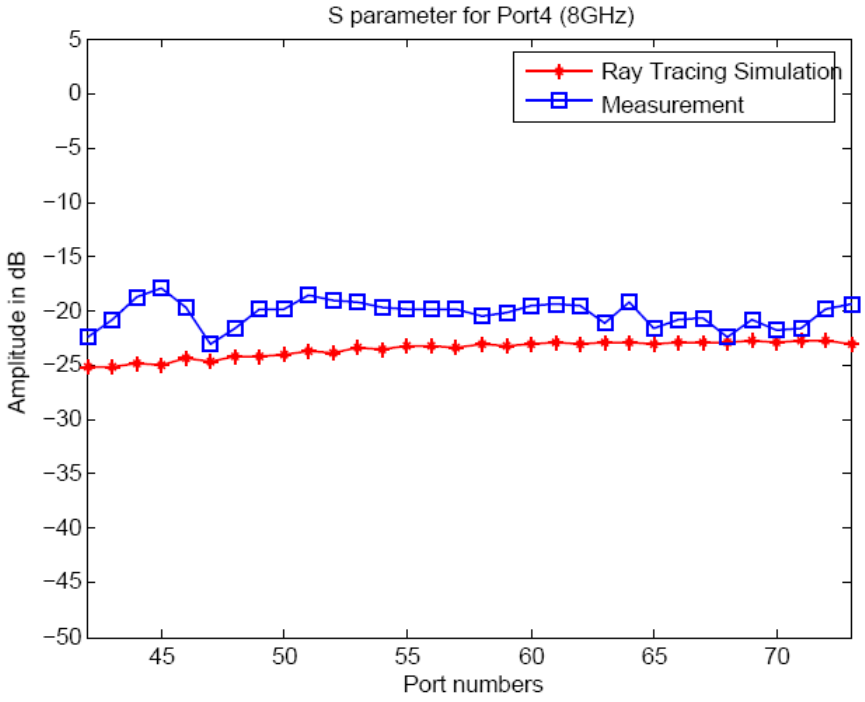

Figure 4- 33. Amplitude across Aperture for Port 4 Excitation at 8GHz

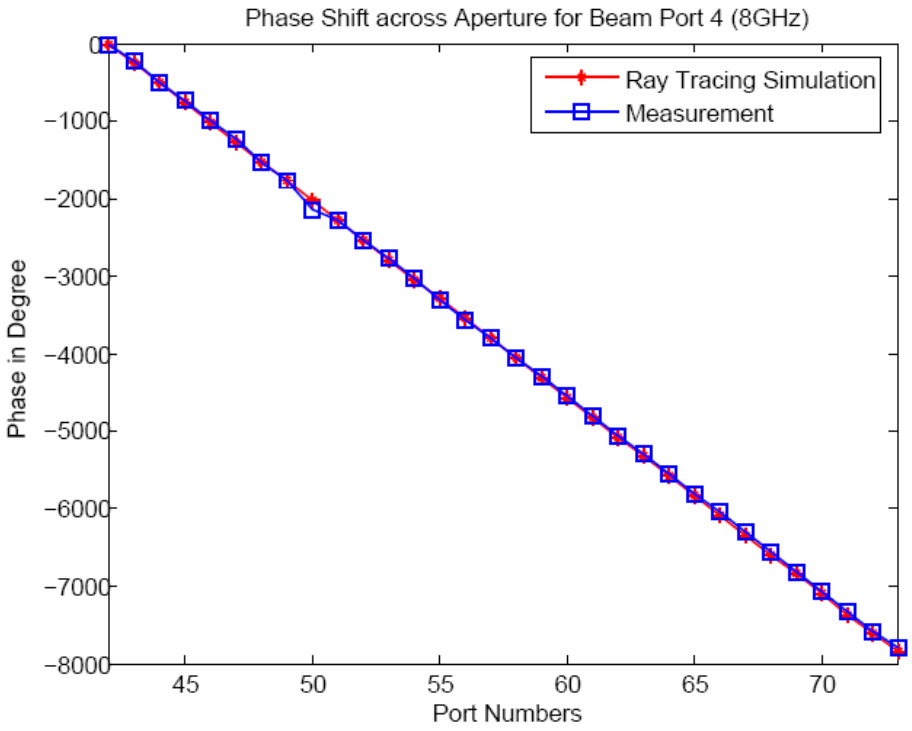

Figure 4- 34. Phase Shift across Aperture for Port 4 Excitation at 8GHz

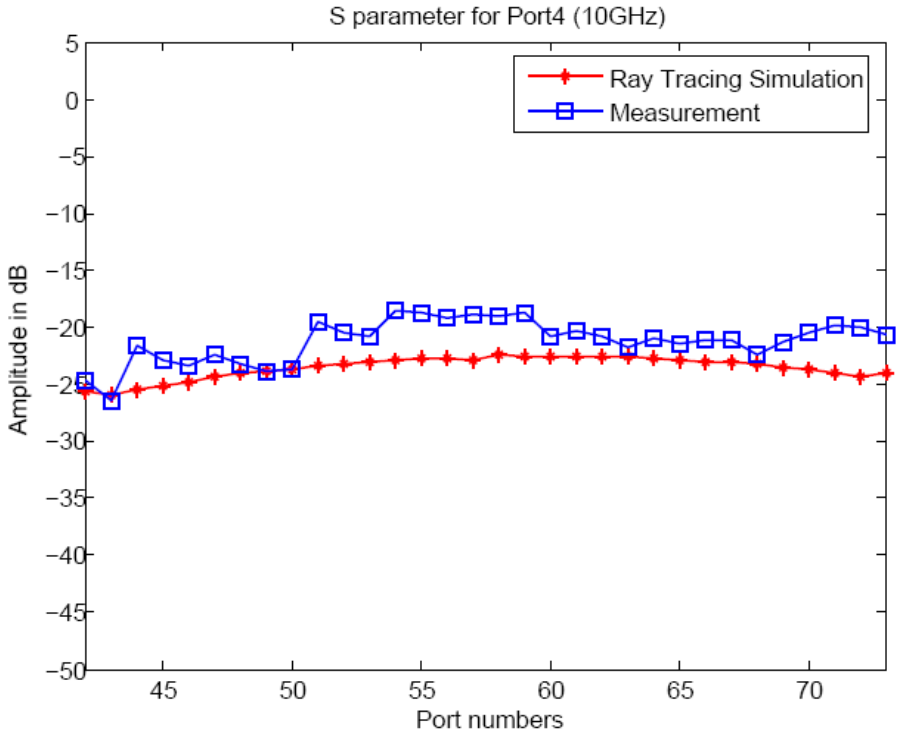

Figure 4- 35. Amplitude across Aperture for Port 4 Excitation at 10GHz

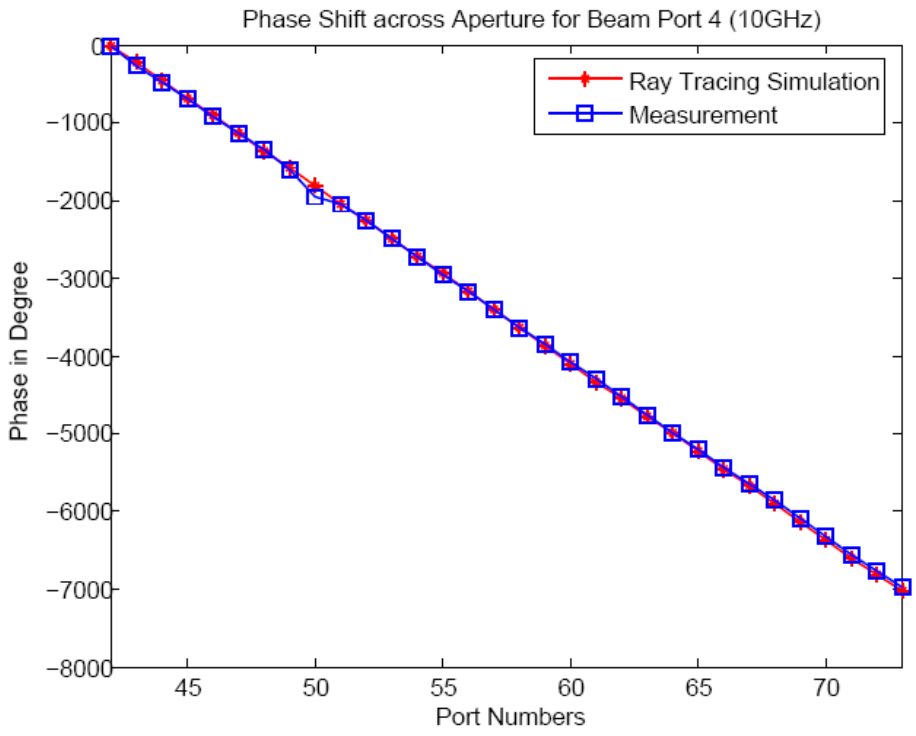

Figure 4- 36. Phase Shift across Aperture for Port 4 Excitation at 10GHz

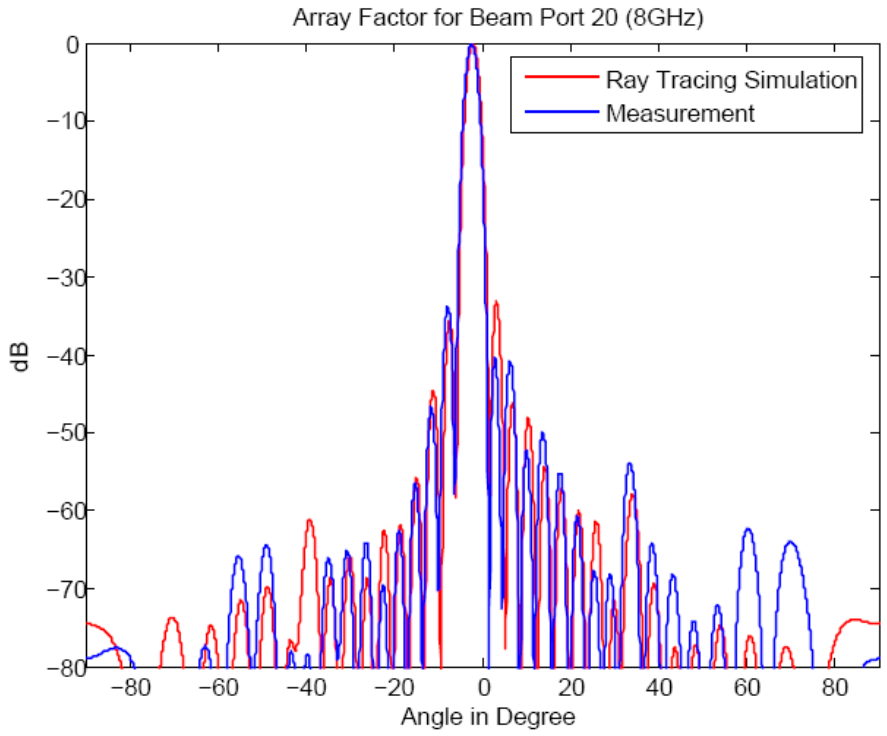

Figure 4- 37. Array Factor for Port 20 Excitation at 8GHz

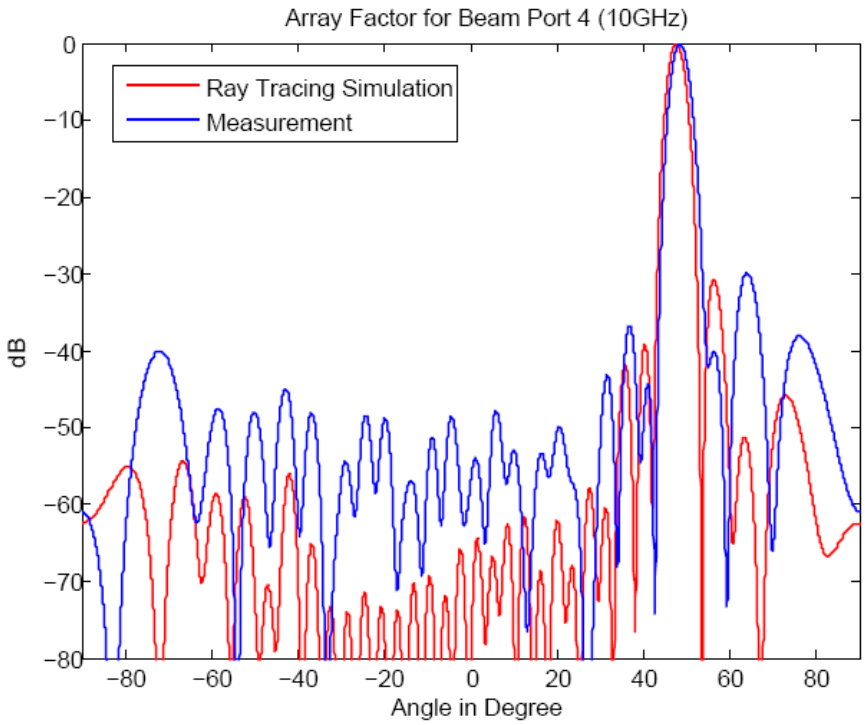

Figure 4- 38. Array Factor for Port 4 Excitation at 10GHz

The comparisons show that the amplitude coupling for the center beam exhibits strong agreement; however, the amplitude at the edge port has relatively higher error. This is probably due to two reasons, 1) current ray tracing model assume the port has symmetric structure, which does not hold true for the edge ports in Figure 4- 20 due to its bending geometry. 2) the aperture to aperture coupling model relies on the correct port pointing direction and radiation pattern, for the edge port, the phase center as well as the aperture pattern may encounter higher errors than the center port.

The phase shift comparisons show strong agreement between the simulation and measurement for both ports' excitations. The center beam indicated higher phase variations in degree, which is due to the fact that the aperture illuminated by the center beam possesses much slower phase progressions. In general, the phase variation error is acceptable. For example, given the material permittivity of 2.5, 10-degree variation shown in Figure 4- 30 actually implies the predicted physical distance error of about 0.65mm. For large angle scanning beams, this error is hardly seen due to the large phase shifts, as such agreed results demonstrated for port 4 excitations in Figure 4- 34 and Figure 4- 36. Besides, the array factor of the ray tracing model agrees with the

measurement. The higher side lobe predicted at the edge port is due to the high amplitude errors indicated in Figure 4- 38. To sum up, the ray tracing simulation has demonstrate ability of simulating both amplitude and phase couplings. The lens #1 measurement comparison shows that the current model is accurate in terms of phase shift, amplitude coupling for center ports, beam scanning angles, etc. To accurately predict the side lobe level (SLL), more accurate aperture coupling model may be required.

To further verify the preliminary results described above as well as to create comparison with diversities, we conduct another case study using an individual lens that has been simulated using commercial software FEKO and measured in Chapter 4.1. In the next section, the true-time delay (TTD) and phase, amplitude performance across the frequency are emphasized.

4.2.3 Validation of Microwave Lens #2

The microwave lens discussed in this section was designed at 4-5GHz, and it has 8 beam ports to feed 8 linear spacing arrays, as shown in Figure 4- 1. Technical data of the lens is shown in Table 4- 1, and the fabricated lens is demonstrated in Figure 4- 2. Similar to the one presented in Figure 4- 28, this lens has dummy port in between the beam ports and at sides (notation of '0'). The dummy ports between the beam ports are primarily used to increase the isolation between the adjacent beam ports and create similar environment for multiple beam operations at a time. Dummy ports at the side wall function as absorbers that minimize the energy reflected back into the cavity. The dummy ports sometimes are necessary to be incorporated because of the following reasons: 1) the reflection from the side wall may affect the amplitudes and phases at the receiving ports, hence degrading the lens performance; 2) the reflected wave and the forward wave may create standing waves that become a source of heating up the lens system. Different from the model in Figure 4- 28, the transmission lines in Figure 4- 1 are clearly recognized. Each transmission line was bent to certain extent so that proper line length can be yielded, which is an essential design factor in the microwave lens formulation.

Two port network measurement was done between every beam port and receiving port. Similar to the previous lens, 50-ohm loads have to be connected to all other ports while the two ports are being tested. The scatter matrix was further post processed into amplitude and phase information across the aperture and frequencies. The full-wave simulation was carried out by the planer Green's function MoM solver in FEKO. Beam ports 1-8 were separately excited across frequency 4-5 GHz. Eleven discrete frequency steps were requested for each beam port. The entire simulation took 8.965 hours on a 64bit workstation, using 4 core Intel(R) Xeon(R) 3.0GHz CPUs. The peak memory consumption of all processes was 2.136 GByte. The ray tracing simulation was executed in an personal computer with Intel(R) Celeron(R) 1.6GHz CPU (512M RAM). The same scatter matrix across the frequency was requested. The entire simulation took 11 seconds. The ray tracing simulation has achieved thousands of times accelerations versus the full-wave simulation. This is mainly because it was formulated using hybrid models that asymptotically approach the field behaviors. Whereas, the full-wave simulation achieves more accurate result as it is able to approach the exact solutions of the Maxwell equations.

For a single beam produced by the microwave lens, the amplitude distribution and phase shift across the aperture are of our interests. We emphasized this point in the first lens validation process. In this section, the simulated and measured results are presented from the frequency sweep perspective (Figure 4- 39~Figure 4- 42). Firstly, the amplitude coupling between two ports across the frequency implies how much gain variations occur when wide band signal is being sent through the channel. In general, constant amplitude coupling is expected. However, due to the facts that 1) the tapered port has a varied frequency response as indicated in Figure 4- 26, 2) different frequency has different path-length loss, 3) the multiple reflections within the lens cavity, the amplitude couplings across the frequency always have certain level of deviations. As examples, we compare the ray tracing results for port 2-port 15 and port 4- port 10 amplitude couplings with the FEKO and measurement in Figure 4- 39 and Figure 4- 41. Secondly, the phase couplings across the frequency, as indicated in Figure 4- 40 and Figure 4- 42 described the effective path length between the beam port and the receiving port. Basically, the higher offset it

shows between the simulation and measurement, the higher path-length errors are. Thirdly, the array factor performance across the frequency reflect the true-time delay properties of the microwave lenses, as the true-time delay device states that the far field scanning beams' pointing directions do not varies with frequency. Consequently, we have plotted the array factors of one edge beam (port #1) and one central beam (port #3) using the simulated and measured amplitude and phase information at the lowest (4GHz) and highest (5GHz) frequencies, in Figure 4- 43~ Figure 4- 46.

Both amplitude and phase couplings demonstrate agreeable results. The full-wave simulation has confirmed the accuracy of the measurement. The ray tracing simulation has accurately captured the phase variations in Figure 4- 40 and Figure 4- 42. Although its amplitude prediction has higher errors than the full-wave simulation, acceptable trend and variations have been achieved. Both simulations and measurement have yielded good true-time delay properties for the port #1 and port #3 excitations in Figure 4- 43 ~Figure 4- 46. It is observable that the ray tracing has predicted lower array factor gain at 5GHz, which is probably due to the higher amplitude variations across the aperture. This recalls the previous lens simulation results: the edge port generally has higher error due to the uneven port geometry and pointing directions.

Limited number of comparisons has been demonstrated below, considering the multiple port profile of the microwave lens, comprehensive ray tracing performance for all beam and receiving ports have been studied. Detailed comparison results are attached in Appendix F. The accuracy of the proposed algorithm is quantified in Table 4- 3. In Table 4-3, the gain, |SLL|, side-lobe amplitude, side-lobe position, main beam scanning angle and beam width have been compared respectively from Port 1 to Port 4 excitations at 4GHz and 5GHz. Take the measurement as reference, the results show that the accuracy of ray tracing of average error for each parameter: gain 0.77 dB, |SLL| 1.45 dB, side-lobe amplitude 1.48 dB, side-lobe position 0.44 degree, scanning angle 0.39 degree, and beam width 0.39 degree. Comparably, the full wave simualtion average errors are: gain 0.24 dB, |SLL| 0.35 dB, side-lobe amplitude 0.43 dB, side-lobe position 0.15 degree, scanning angle 0.14 degree, and beam width 0.09 degree.

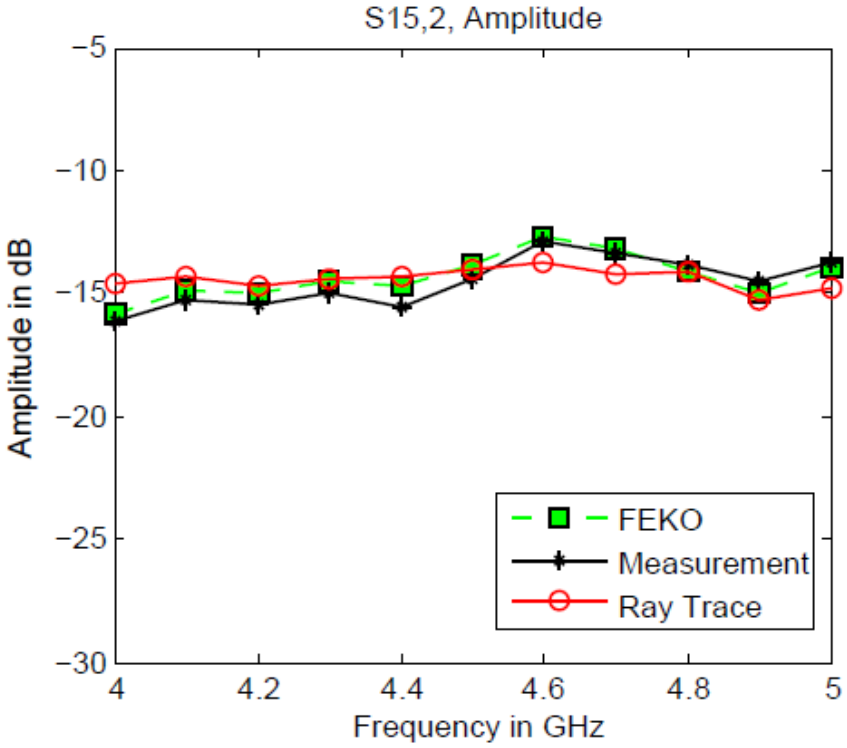

Figure 4- 39. Port 2-Port 15 Amplitude Couplings across Band

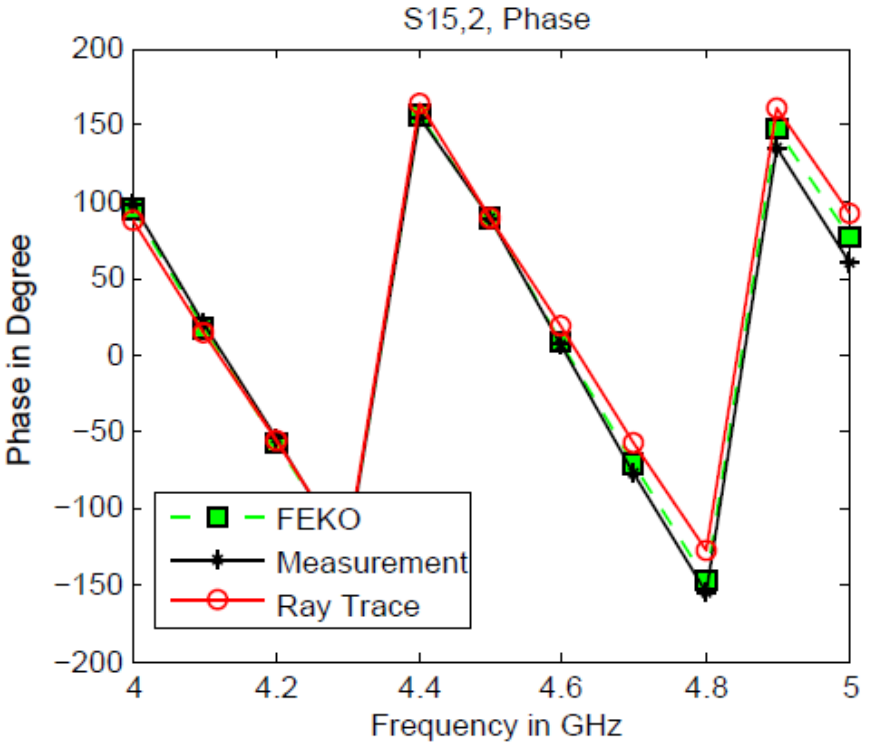

Figure 4- 40. Port 2-Port 15 Phase Couplings across Band

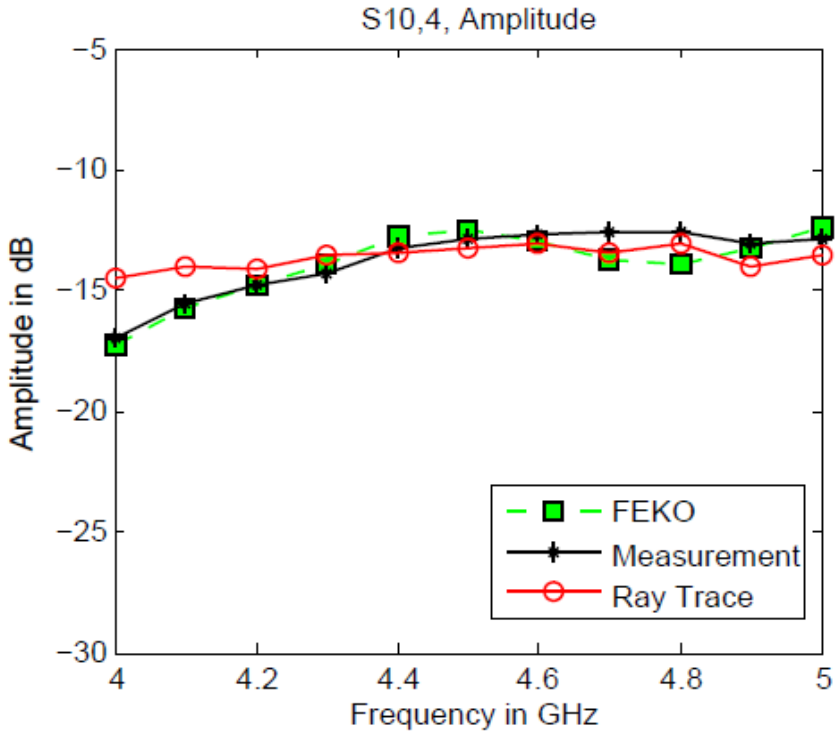

Figure 4- 41. Port 4-Port 10 Amplitude Couplings across Band

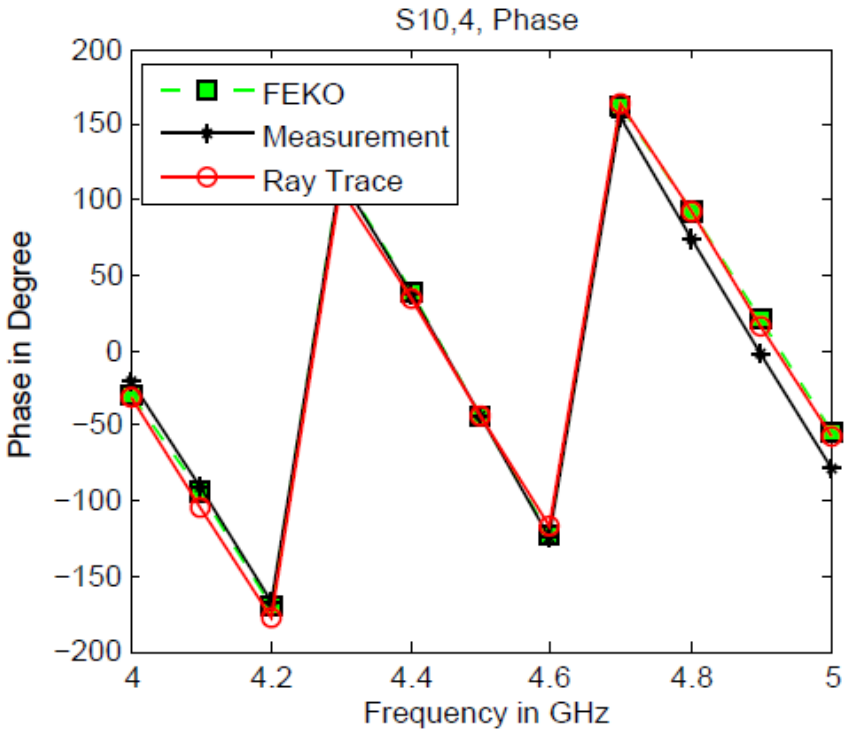

Figure 4- 42. Port 4-Port 10 Phase Couplings across Band

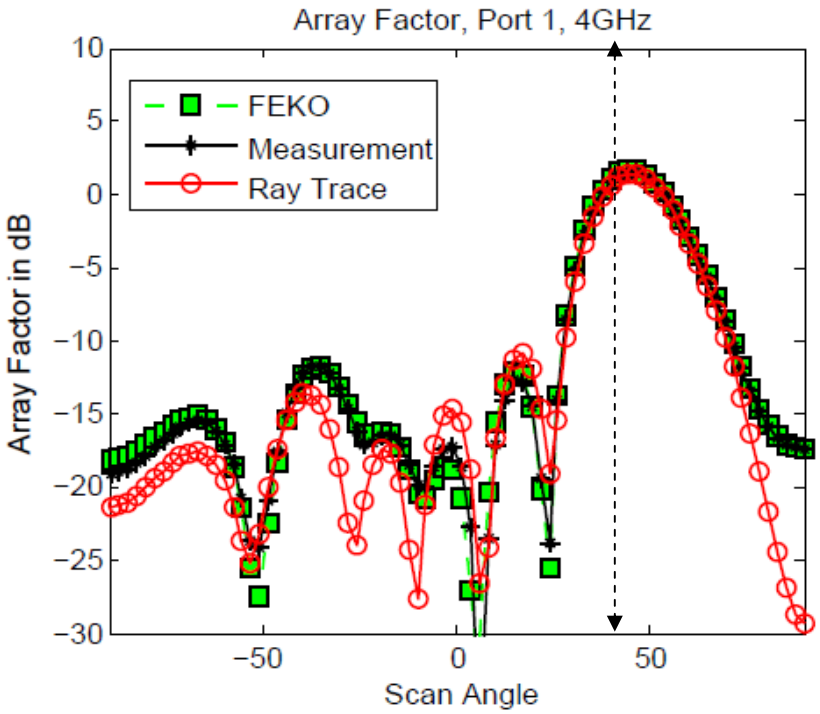

Figure 4- 43. Array Factor for Port 1 Excitation at 4GHz

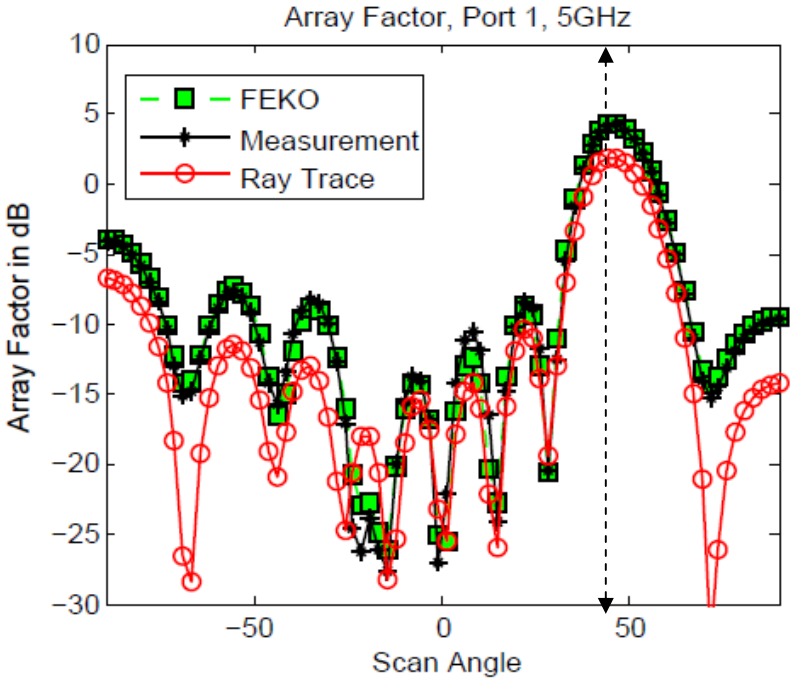

Figure 4- 44. Array Factor for Port 1 Excitation at 5GHz

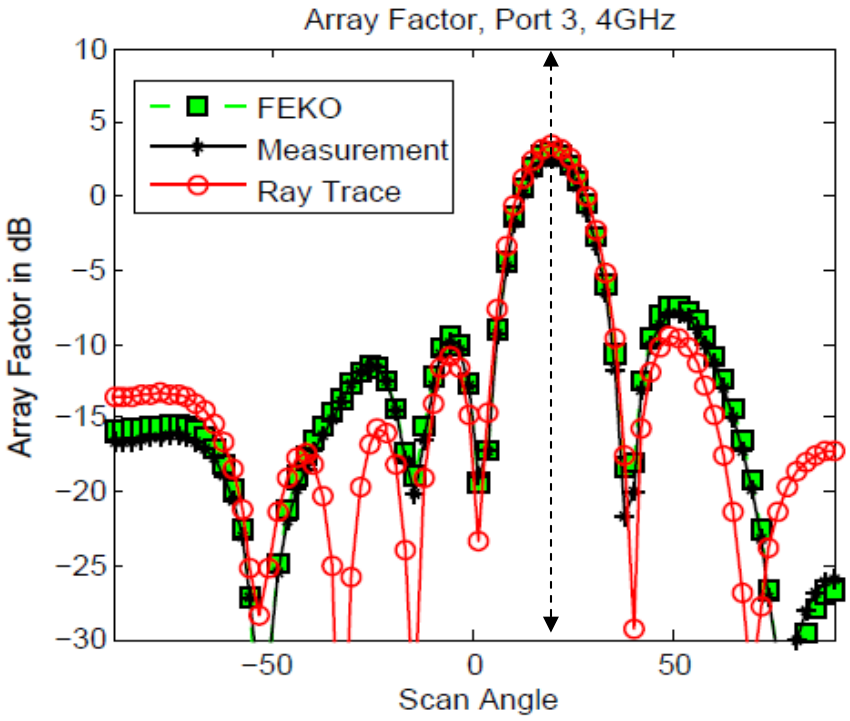

Figure 4- 45. Array Factor for Port 3 Excitation at 4GHz

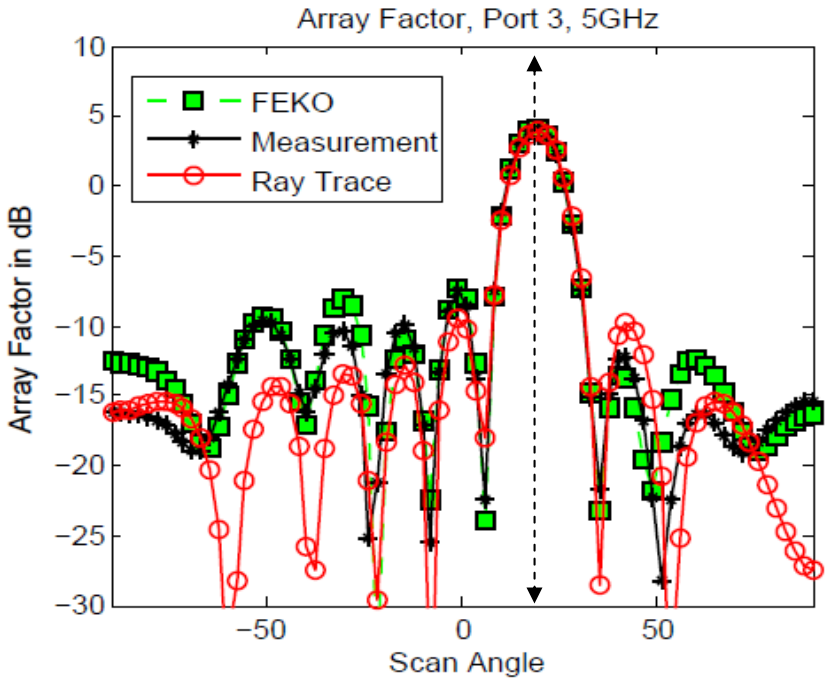

Figure 4- 46. Array Factor for Port 3 Excitation at 5GHz

Table 4- 3. Ray Tracing Simulation Accuracy Quantification for Lens #2 (v.s. FEKO and Measurement)

			Gain (AF for Isotropic Elements)	Side Lobes			Scanning Angle	Azimuth HPBW
				|SLL|	1st Side lobe	1st Side lobe Position		
			dBi	dB	dB	degree	degree	degree
4 GHz	Port #1	FEKO	1.6966	13.6786	-11.982	15.48	44.64	22.44
		Ray	1.3719	12.2419	-10.87	16.68	45	21.84
		Meas	1.6036	14.1266	-12.523	15.84	44.88	22.32
	Port #2	FEKO	1.924	12.681	-10.757	5.16	32.76	19.32
		Ray	2.4523	13.2813	-10.829	5.76	31.92	18.24
		Meas	1.4324	12.9594	-11.527	5.16	32.76	19.2
	Port #3	FEKO	2.9888	10.3908	-7.402	50.52	19.56	16.08
		Ray	3.4499	12.921	-9.4711	49.92	19.44	16.32
		Meas	2.5261	10.4268	-7.9007	50.52	19.56	15.96
	Port #4	FEKO	3.3479	11.5428	-8.1949	32.28	6.84	14.88
		Ray	3.9836	13.4748	-9.4912	32.52	6.48	15.24
		Meas	3.0007	11.3658	-8.3651	32.16	6.6	14.88
5 GHz	Port #1	FEKO	4.3093	12.9528	-8.6435	22.08	45.72	17.52
		Ray	1.9353	12.3163	-10.381	22.2	45.6	17.4
		Meas	4.23	12.5666	-8.3366	22.44	45.84	17.4
	Port #2	FEKO	3.1549	11.4687	-8.3138	10.68	31.32	13.8
		Ray	2.8972	13.3872	-10.49	11.16	32.4	14.52
		Meas	3.2075	12.005	-8.7975	10.68	31.56	14.04
	Port #3	FEKO	4.2235	11.4746	-7.2511	-0.72	18.72	12.72
		Ray	4.0214	13.3725	-9.3511	-0.72	19.2	12.96
		Meas	4.1688	11.714	-7.5452	-0.96	18.72	12.72
	Port #4	FEKO	4.0078	11.5304	-7.5226	-13.68	6.24	12.12
		Ray	4.5682	13.712	-9.1438	-13.44	6.36	12.36
		Meas	4.3067	12.1936	-7.8869	-13.56	6	12.12

4.2.4 Summary and Future Perspectives of the Ray Tracing Algorithms

A fast ray tracing algorithm is proposed for the microwave lens design. The proposed method treats the tapered ports, port to port couplings, and transmission lines individually and adopts a ray tracing process to combine different models. Two Rotman lenses simulated and measured have been used to validate the design concept. The results were investigated from the aspects of 1) the amplitude distribution and phase shift across the aperture couplings for single port excitation at single frequency; 2) the amplitude and phase couplings between the transmitting and receiving ports across the frequency band; 3) array factors for different beam ports excitations at different frequencies. Comparison results demonstrate that the ray tracing program is accurate to predict both phase variations and scanning beam properties (within 1 degree). The amplitude for the edge ports indicates relatively higher errors (up to 2dB) than the full-wave simulation and measurement, which is primarily due to the uneven edge port structure and pointing direction. The latter is expected to be improved by further edge ports' geometry and pattern investigation. In general, as a simulation tool that is thousands of times faster than the full-wave simulation, very prominent results have been achieved. This also offers possibility of incorporating the proposed method into the current microwave lens optimization process.

There are a few future perspectives that are subject to improve the current microwave lens simulation methodology. The true phase centers of the beam ports can be estimated by the phase frequency response between the beam port and receiving ports. Both measurement and full-wave simulation have indicated possibility of the phase center variation versus port profile, pointing direction and frequency. To accurately trace the phase center location helps build more accurate phase prediction models, besides, it also feed valuable information back to the original geometry optical formulation. Further improvement can be achieved by take advantage of the full-wave simulation as a toolkit to build more accurate sub-models of the ray tracing process. For instance, the aperture to aperture coupling can be accurately modeled by the full-wave simulation. The asymptotic models can be built to approach the exact results by incorporating extra design freedoms

such as verified field distributions across the aperture. This will probably lead to more accurate amplitude couplings in the ray tracing simulation.

4.3 Summary and Examples of Microwave Lens Synthesized by Computer Aided Design (CAD)

For decades, the Computer Aided Design (CAD) software has been indispensible toolkit for the microwave engineers. Sufficient CAD software allows components being constructed and accurately simulated in the computer, which not only maximizes the performance but also reduces the development cycle. For the microwave lens, due to its complicated geometry and various implementation approaches, commercial software that performs geometry formulation and performance optimization is hardly seen. In this Chapter, efforts have been put to explore the accurate and efficient simulation methods, with focus on facilitating the future CAD development for the microwave lenses.

The preliminary results achieved so far have led us to developing some of the state-of-the-art microwave lens components. This section serves to report some of the recent microwave lenses synthesized using the methods proposed in Chapter 3 and validated by software explored in Chapter 4. Two lenses will be discussed. The first one was presented in [53], designed at 8-24GHz, orientated for the UWB applications. The second one is optimized design at 2-8GHz under development in the Microwave Engineering Corporation (MEC). Note the works in current chapter also serve as tool of validating the new proposed 360-degree scanning microwave lenses, which is the primary topic in the next Chapter.

1. Quadruple Bandwidth Lens Operating at 6-25 GHz

Great interests have been drawn in the ultra wideband phased array development in recent years. The discoveries of some of the wideband antennas such as Vivaldi antenna, as well as the printed circuit fabrication technologies have accelerated such designs. These also bring engineers envision of low cost communications systems with fully integrations of navigation, detection, environment recognition, remote sensing, imaging, secure point-to-point communications and other functionalities, which may be possibly deployed on future spacecraft, transportation vehicles and robots. Potential candidate

considered is a phased array system operating in wide band, producing true-time delay (TTD) electrical steerable beams with large scanning angles. It consists of two challenges for the antenna engineers, design of wide band TTD beam-forming network and design of wide band phased array element. In this section, we only address the means of designing the beam-forming network and report the results of preliminary computer aided investigations. The beam-forming network is realized by printed microwave lens. Good performance based on full-wave simulation Method of Moment (MoM) is demonstrated across band 6GHz – 25 GHz.

The lens (Figure 4- 47) does not require dummy port(s) between the adjacent beam ports. However, the side walls are realized by dummy ports with length slightly shorter than the beam/receiving ports, which follows similar concept to the ones in previous works [51]. It is designed to scan azimuth ± 40^0 with initial design bandwidth of 6 GHz - 20 GHz. In order to yield electrically small array element spacing across the entire band, the adjacent output transmission lines' spacing is a fixed 8 mm. The entire lens is designed on low loss material, Rogers 5880 (ε_r=2.2, tanδ=0.0009), with overall dimensions of 20 cm X 15 cm. Because the transmission lines usually have very constrained length requirements, as described in [58], in order to receive smooth transmission behavior, each transmission line is performed based on Gaussian function curve. It is noted that all ports are designed to have coaxial connectors so that when one beam port gets excited, all other ports except the receiving ports are terminated with 50 Ohms. This also brings convenience that allows array elements being designed separately so that power amplifier and low noise amplifier can be independently integrated into the corresponding transmitting and receiving arrays.

Full scattering matrix for all beam port excitations across band 5 GHz – 25 GHz have been investigated numerically. Figure 4- 48 is the S11 for three typical inputs, port 1, port 3 and port 5. It is observed that the edge port 1 receives relatively higher return loss, which maybe mainly due to the higher mismatch that occurs at the off center beam port taper and its pointing direction. As it shows, acceptable return loss less than -10 dB were

achieved across band 6 GHz – 25 GHz, which gives such lens good performance over quadruple bandwidth.

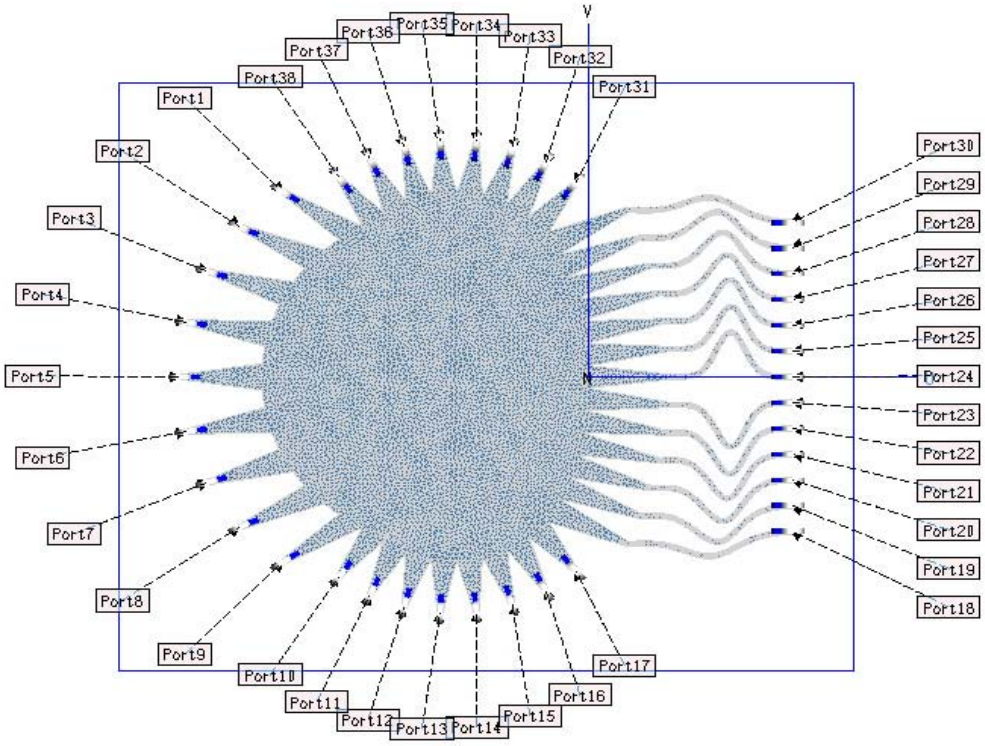

Figure 4- 47. The 9x13 Microstrip Microwave Lens Layout

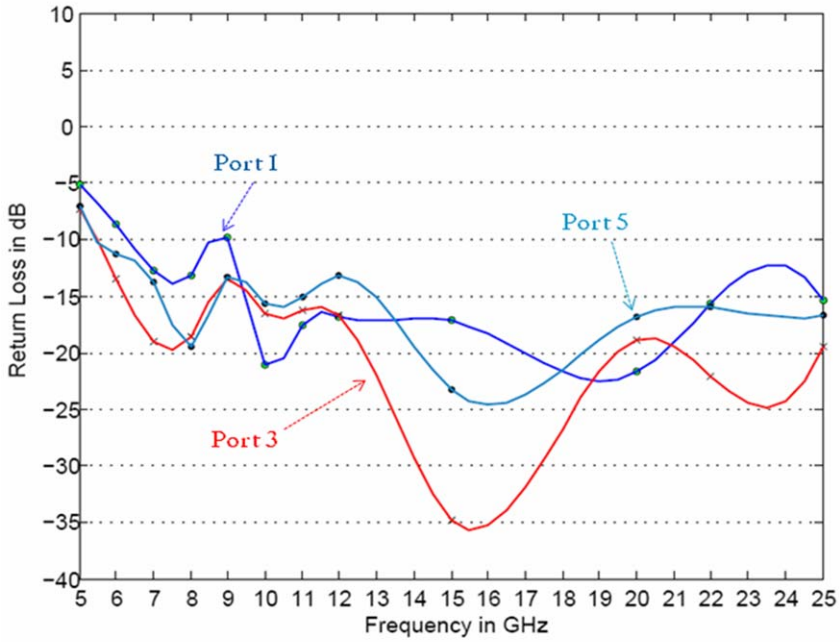

Figure 4- 48. Return Loss for Beam Ports 1, 3, and 5

The surface currents for port 3 excitations at frequencies 6 GHz, 12 GHz and 20 GHz are shown in Figure 4- 49 a-c. As frequency increases, the lens itself becomes electrically larger. At each frequency, given simulated transmission lines outputs of amplitude A_m and phase α_m, which in other words are the inputs for the phased array elements, the array factor pattern can be predicted by using equation (1-69). Plots a-c in Fig. 4 is the array factor at these three frequencies. As it shows, the pointing directions of all beams remains unchanged even the frequency changes from 6 GHz to 20 GHz. This clearly demonstrates the true-time delay behavior of the proposed microwave lens. Furthermore, it is noticed that as the frequency increases, the gain for specific beam is expected to vary within small range, the beam width decreases too, and beams at large angle degrade faster than the center beams.

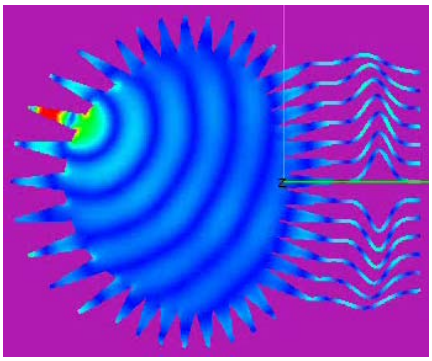

(a)

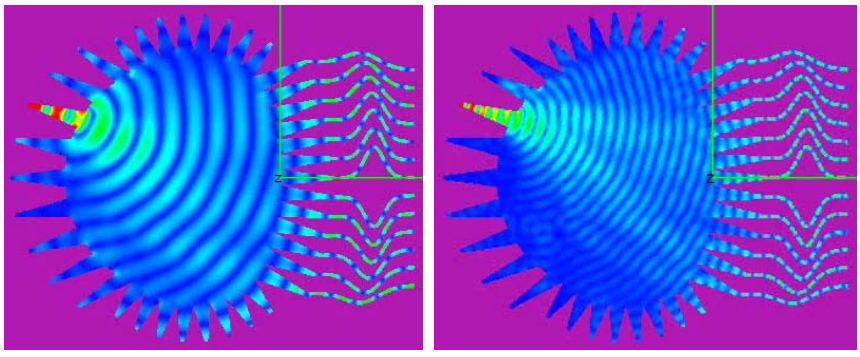

(b) (c)

Figure 4- 49. Surface Currents, (a) 6 GHz, (b) 12 GHz, (c) 20 GHz

(a)

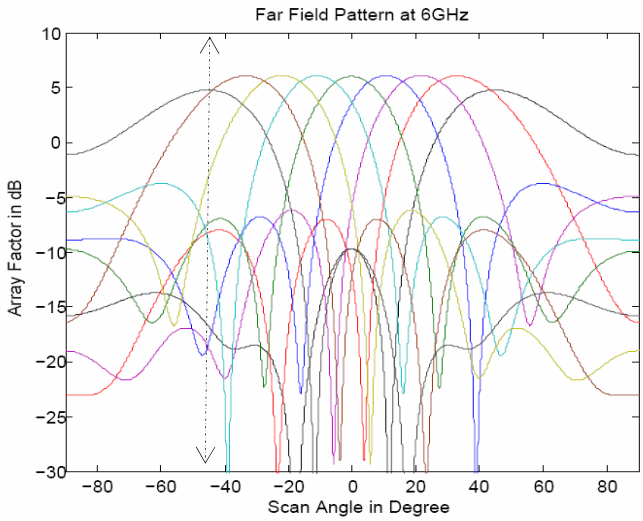

(b)

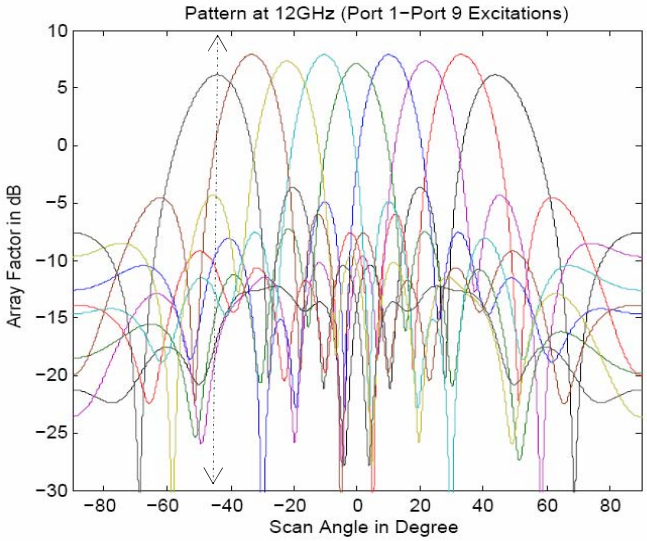

(c)

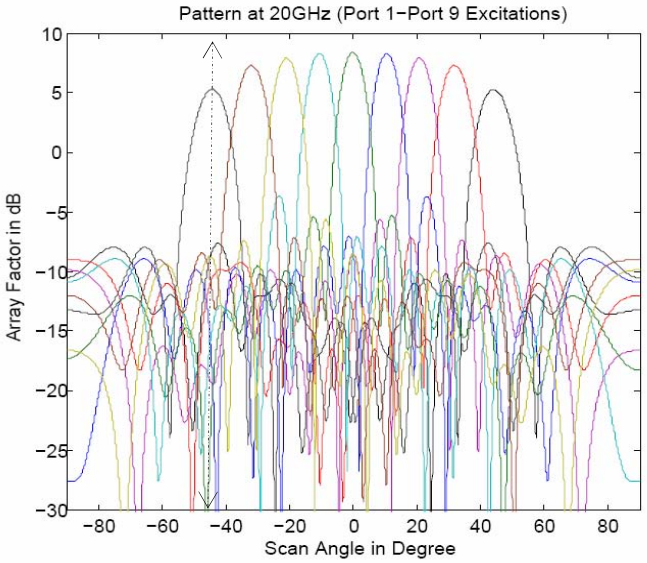

Figure 4- 50. Gain for Beam Ports 1, 3, and 5 Excitations

2. Improved Wideband Microwave Lens Design at 2-8 GHz

The microwave lens recently constructed at the Microwave Engineering Corporation has greatly improved the bandwidth, phase and amplitude performance. The layout of the lens is shown in Figure 4- 51. It was designed for feeding an 8-element uniform spacing linear array, as demonstrated in Figure 4- 52. The operation bandwidth of the lens is 2-8GHz with respect of return loss -13dB. The horn array operates at 2-6GHz. Due to the narrow beam width of the single array element, the lens was designed for maximum scanning angle of $\pm 26^{o}$ with beam separation of 6.5^{o}. The gain pattern of the horn array fed by the microwave lens at 4GHz is demonstrated in Figure 4- 53. The result is achieved using the FEKO full-wave simulation. It is observable that relatively slow tapering at the gain has been achieved for Port 2~Port 8 excitations, which is due to the approximate uniform amplitude illuminations across the aperture. From lens geometry point of view, it is noticed that the ports have been tapered differently. This is because for different given port dimensions, there are different port profiles that yield the minimum return loss. The overall size of the lens is 12"x18", which is the same as the lens presented in Chapter 4.1. However, current design has extended the bandwidth from 4-5GHz to 2-8GHz. Significant improvement has been accomplished.

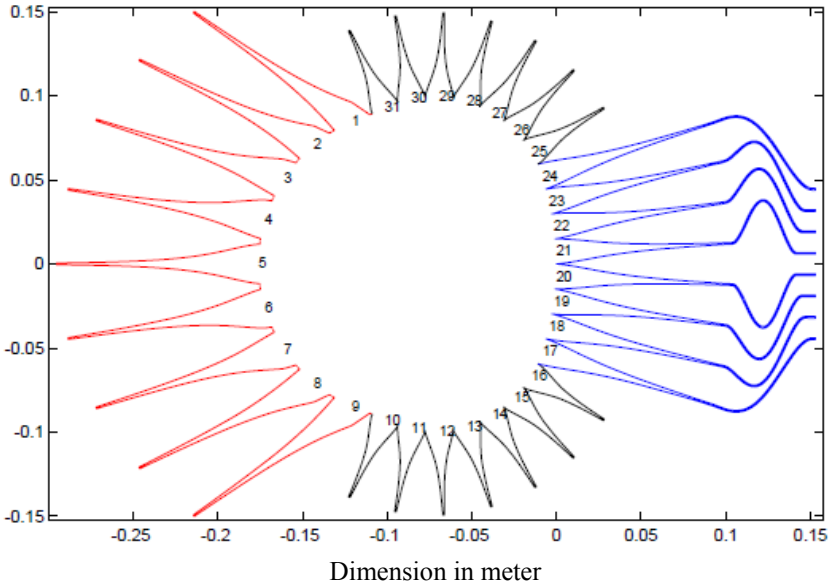

Figure 4- 51. Layout of the MEC Microwave Lens

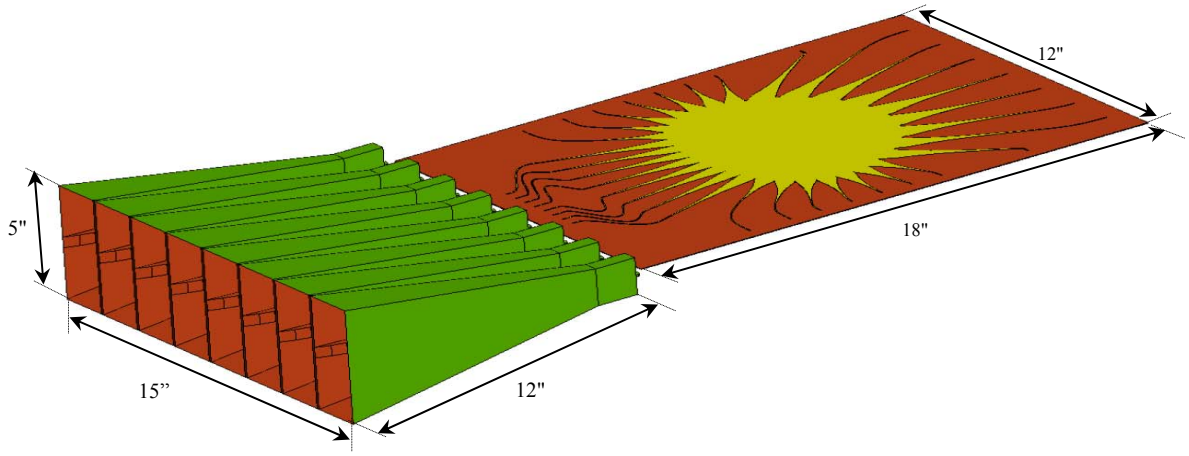

Figure 4- 52. Microwave Lens Fed Horn Array

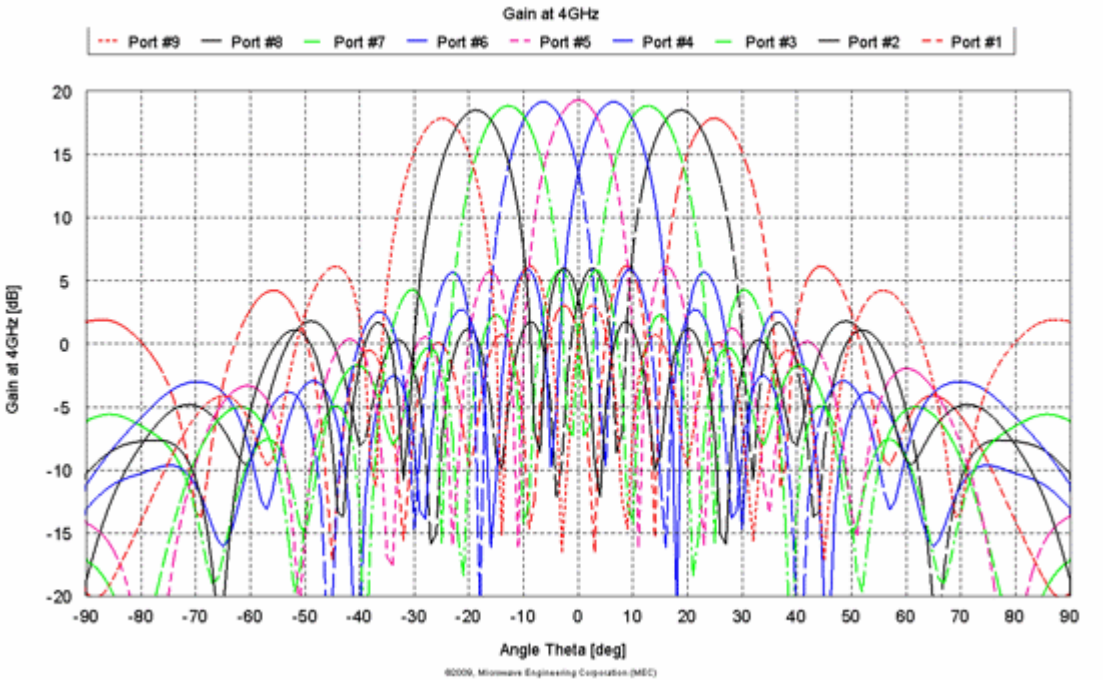

Figure 4- 53. Gain Pattern of Horn Array Fed by Microwave Lens at 4GHz

CHAPTER 5. 360-Degree Scanning Microwave Lens

Electronically scanning antenna system has proved one of the significant inventions in the array design realm since 1950. After many years of practice, wide band wide-angle multi-beam antenna such as the bootlace lens has been implemented on the satellite, radar and many other platforms. The scanning capability of these lenses reaches up to +/- 90 degrees; however, for applications such as remotely piloted vehicle radar and advanced robot sensing system which desire circular/spherical scanning operations with size, weight and cost limitations, should such lens is applied, it will require either lapping over more than one lens, or having mechanical scan involved, which consequently reduces the system compatibility and flexibility. Thus, it is our purpose to seek an improved design scheme that offers competitive performance but uses allowable resources.

This chapter starts with reviewing several 360-degree scanning antennas based on existing technologies. After understanding the fundamental limits of various designs, we propose a microwave lens design concept for 360-degree scanning. The formulation method, optimization algorithms, design examples will be given. The theoretical phase error performance is demonstrated by optimizing two even-facet shape lenses. Other aspects such as amplitude, array factor, efficiency and bandwidth are studied using the full-wave method validated in the previous Chapter. One particular square shape lens has been constructed, fabricated and tested. Both simulation and measurement have shown good agreement.

5.1 Brief Review of Existing 360-Degree Scanning Techniques

In many applications such as radar targeting, direction finding, imaging, and point-to-point communications, the antenna system is desired to produce single or multiple steerable narrow beams. The narrow beam can be realized by using antennas with larger aperture as discussed in Chapter 2, and the steerable capability can be established by either mechanical rotating or electrical scanning devices. Probably the simplest solution of achieving 360-degree scanning is to mechanically rotate the entire antenna such as the Air Route Surveillance Radar (ARSR) [73], or rotate the feed such as the released patent of

[74]. Due to the low cost and simplicity, most existing 360-degree scanning radars were implemented by mechanical rotation. However, there are three major disadvantages for such systems. Firstly, most radar only supports single beam and single mode of operation at a time. Second, considering the number of hits per second on the target affects the signal to noise ratio (SNR) and resolution of detection, the limited speed of rotation has become another major issue. Thirdly, because the rotation is usually achievable in 2 dimensions, it degrades the performance at applications desirable to have 3 dimensional scanning pencil beams.

One way of achieving the electrical scanning 360-degree beams is to use more than one classical BFN. This would be the typical case for Butler matrix and Bootlace lens. Because each component supports limited angle of coverage, as discussed in Chapter 3, more than one BFN have to be adopted. Figure 5- 1 indicates the strategy of using classical Rotman lens to perform circular scanning. Given a moderately achievable maximum scanning range of $\pm 60^0$, three lenses have to be used to cover the circular domain. Another example can be found in [75] that two overlapped R-2R lenses were adopted to achieve the 360-degree scanning. The disadvantage of such designs is mainly the requirement of more than one BFN unit, which leads to higher expense and system complexity.

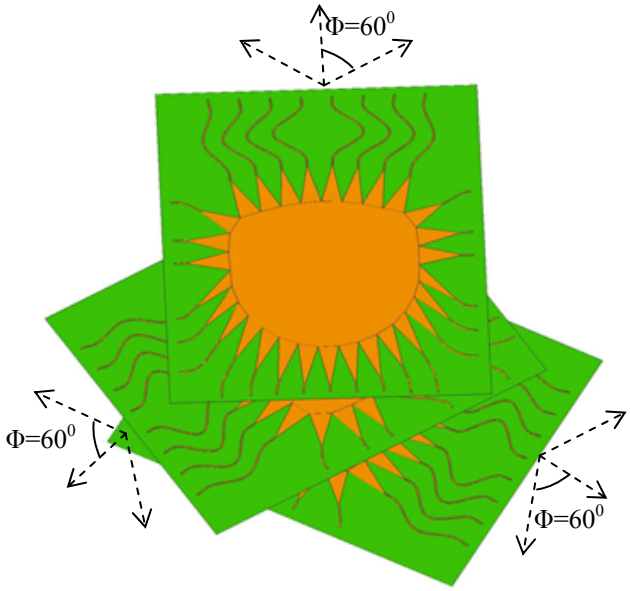

Figure 5- 1. 360-degree Scanning Achieved by Lapping over Lenses

Luneberg lens is capable of providing 360-degree scanning using single structure [76]. It is based on a multilayer spherical structure that uses concentric spheres with layers of different dielectric constants. The multiple refractions through the different layers produce the magnification of the feed aperture to a planar aperture on the other side of the sphere. The 360-degree scanning is achieved by rotating the feed around the spherical surface. The refraction index calculations require considerable numerical simulation, and the discontinuity within the structure may not be easy to implement in reality. According to [77], the effective feeding aperture by Luneberg lens is always less than the diameter of the lens. Besides, the refraction index realized using artificial dielectric may be frequency dependent, resulting non true-time delay or limited bandwidth of operation.

In this chapter, a new design concept of 360-degree scanning bootlace lens is proposed. It is capable to achieve the circular scanning coverage by using single lens configuration. The lens can be implemented using homogenous materials such as waveguide, stripline or microstrip. The true-time delay property is still achievable. Because the beam direction does not alter with frequency, the proposed microwave lenses can be deployed in the ultra-wideband communications systems, which presumably in favor of transmitting/receiving high speed data along a constant spatial direction.

5.2 360-Degree Scanning Microwave Lens Formulation

5.2.1 Basic Idea

As detailed analysis shows in Chapter 3, typical models of bootlace lens are the Rotman/Turner lens [17] and several modified lenses such as [26, 28, 30, 58]. These models allocate beam ports along one specific curve and use phase error conditions to determine the inner receiving port phase centers and the transmission line lengths. The transmission lines further direct the energy from the receiving ports to the radiation elements, as indicated in Figure 5- 2a. Figure 5- 2b is an example of the printed circuit implementation of the model described in Figure 5-2a. The resulted lens inner receiving contour is always different from the beam contour; hence the whole lens is in lack of left-right symmetry, as shown in Figure 5- 2. The scanning range of the conventional microwave lenses are consequently limited by the beam contour, as such less than $\pm 90^{o}$.

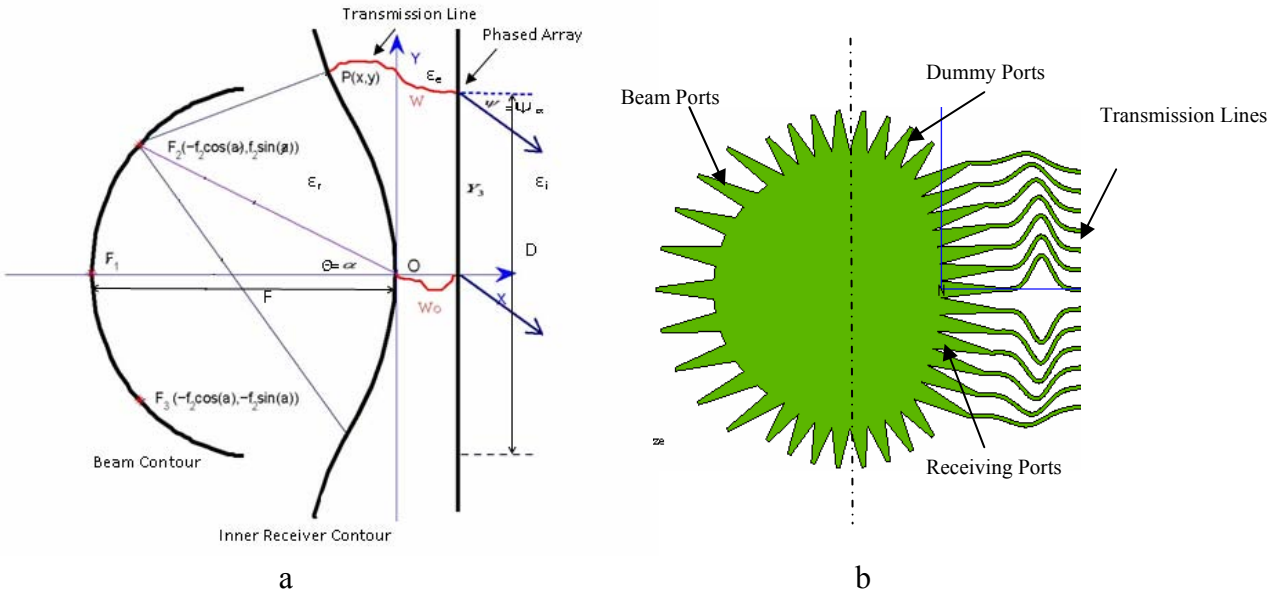

Figure 5- 2. a) The Beam Contour and Inner Receiving Contour are Asymmetric in the Rotman lens, b) Example of Conventional Printed Microstrip Lens

The current design objective is to use single lens cavity, forming several input controlled scanning beams along the azimuth of 360 degrees. In Figure 5- 3, basic idea is illustrated by showing a circular inner port contour followed by linear arrays of four facets. Each of the arrays indicates scanning capability of ± 45 degrees. Along the circular contour, the input ports (notation of o) are interleaved with the receiving ports (notation of *) that are connected to the radiating array elements through transmission lines. Each beam port excites a separate far field beam in the free space.

Similar to any established microwave lens, acceptable phase and amplitude errors across the aperture of each side of the lens have to be guaranteed in order to degrade the side lobe level (SLL) and maintain good scanning performance. The remaining geometrical parameters, transmission lines and material properties also affect the phase and amplitude distributions. The following sections will devise a method to achieve the objective function, optimize the phase errors and determine the unknown factors.

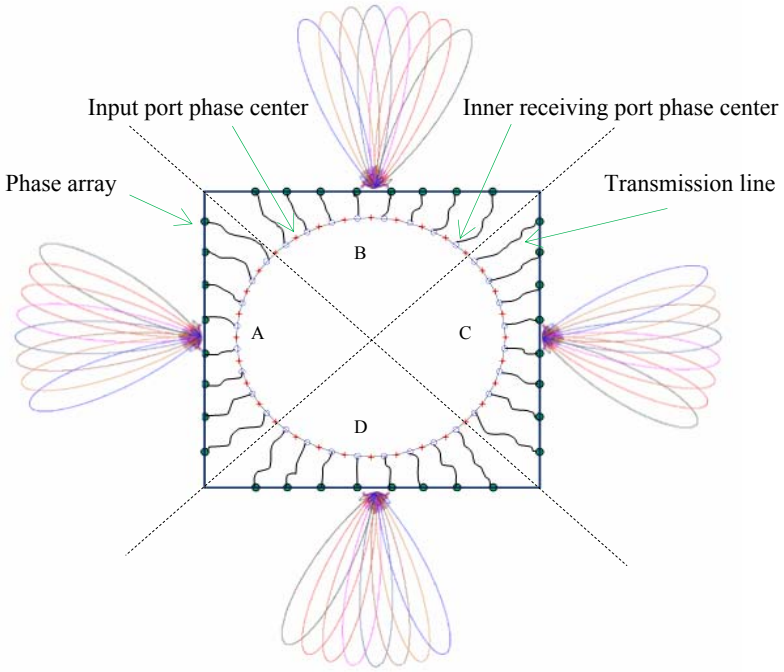

Figure 5- 3. The Basic Idea of Conducting Circular Scanning Lens

5.2.2 360-degree Lens and Parameters

Due to the symmetry condition, one sector of Figure 5- 3 is chosen as the basic model of formulation. Plot indicating design parameters is shown in the x-y plane of Figure 5- 4. N number of beam ports with locations (x_i,y_i) and M number of inner receivers with locations (x_j,y_j) are assumed. These two types of ports are interleaved, confined by their subtended angles denoted as θ_i and ϕ_j. As long as the symmetry conditions between the beam contour and inner receiving contour are satisfied, the determined transmission line lengths can apply to the rest of the sectors correspondently. So we shall stay with the sector figure to build the fundamental model here. Several parameters recognized from Figure 5- 4 are:

F: lens diameter, the distance between the center of the beam contour and the inner receiving contour;
D: Aperture size, for uniformly spaced linear array, D=Md, where d is the array element spacing;

T_j: Transmission length for the j^{th} array element, note the center transmission line T_0 does not exist, which is marked for explanation purpose. It is the transmission line difference $Td_j = T_j - T_0$ that is the real design parameter. This is similar to one of the conventional Rotman Lens design parameters.

φ_i: Scan angle, the beam angle referred to the phased array normal direction;

θ_i: Beam subtended angle, each θ_i corresponds to one specific beam port that generates one scan beam φ_i.

Θ: Maximum subtended beam angle, the angle refers to the beam port that generates maximum scan angle Ψ;

ε_r: the effective permittivity of the lens cavity;

ε_e: the effective permittivity of the transmission line;

D_j: the y coordinate of the j^{th} array element.

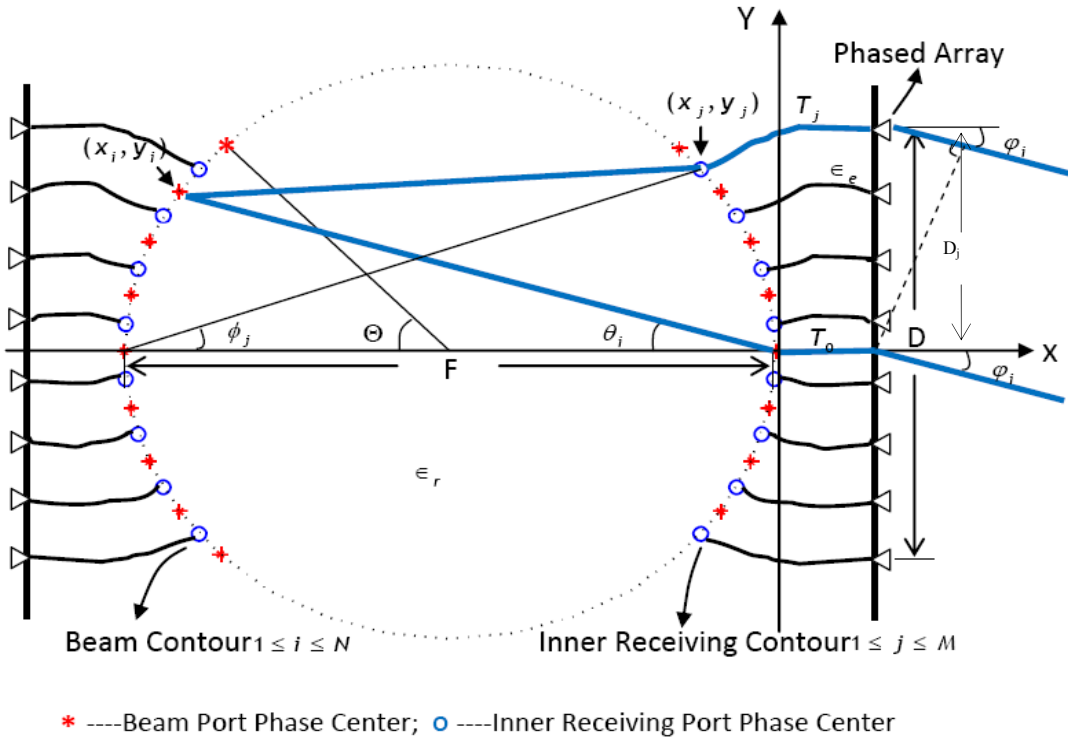

Figure 5- 4. Parameters in One Sector of the Microwave Lens

In Figure 5- 4, given maximum scan angle Ψ, the maximum subtended angle producing the beam is Θ. Note these two angles are always equal to each other in original Rotman lens model [17], however current model does not require such constraint. Without losing generality, we can solve the following parameters:

subtended angle increment:

$$|\theta_{i+1}-\theta_i|=\frac{2\Theta}{N} \qquad (1\le i\le N) \tag{5-1}$$

scan angle increment:

$$|\varphi_{i+1}-\varphi_i|=\frac{2\Psi}{N} \qquad (1\le i\le N) \tag{5-2}$$

array element spacing:

$$|D_{j+1}-D_j|=\frac{D}{M} \qquad (1\le j\le M) \tag{5-3}$$

Other predetermined parameters suggested include y_j: y coordinate of j^{th} receiving port, and y_i: y coordinate of i^{th} beam port. They can be solved by simultaneous functions given in (5-4) and (5-5), which are composed of one circle and one line functions.

$$\begin{cases}(x_i+\frac{F}{2})^2+y_i^{\,2}=\frac{F^2}{4}\\ y_i=x_i\tan\theta_i\end{cases} \tag{5-4}$$

$$\begin{cases}(x_j+\frac{F}{2})^2+y_j^{\,2}=\frac{F^2}{4}\\ y_i=(x_i+F)\tan\theta_j\end{cases} \tag{5-5}$$

The electrical path length of the i^{th} beam port to the middle array element phase front is:

$$L_1=\sqrt{\in_r}\sqrt{x_i^{\,2}+y_i^{\,2}}+\sqrt{\in_e}T_0 \tag{5-6}$$

As shown in Figure 5- 4, the i^{th} beam port phase center to the j^{th} array element phase front electrical length is:

$$L_2=\sqrt{\in_r}\sqrt{(x_i-x_j)^2+(y_i-y_j)^2}+\sqrt{\in_e}T_j+D_j\sin\varphi_i \tag{5-7}$$

The difference between (5-6) and (5-7) gives the theoretical phase error for the i^{th} beam port excitation at the j^{th} array element. The phased array would have zero phase errors if and only if the following electrical path-length equality is satisfied:

$$L_1 = L_2 \tag{5-8}$$

An optimal lens is desire to have such zero phase error for all of the excited beam ports, however, limited design freedoms only allow the beam contour forming very limited focal points, e.g. the classical Rotman lens [17] has 3 ideal focal points, and the quadrufocal lens [30] has four perfect focal points. Note the inner contours in these lenses are not left-right symmetric, thus when the symmetry constraint is incorporated, fewer focal points or non focal points lens would be expected. To seek systematic way of calculating the transmission lines and minimizing the phase error has become a need. A similar non-focal lens optimization method proposed in [31] is adopted in the current design. The average phase error function in degree is expressed in (5-9), where the dimensions are normalized to wavelength and the deviation of each beam off the zero line is addressed in taking the absolute value of the phase error for each beam. It is noticed that the number of ideal focal points is not stressed in current model, since it is more reasonable to achieve appropriate low-phase errors for all beams rather than to get perfect matches for only a few beam ports. Numerical techniques such as Genetic [59] and DSZ algorithms [60] are suitable to optimize function (5-9). The flow chart of such algorithms is shown in Figure 5-5. Section 5.2.3 will explain the DSZ algorithms in greater details.

$$Err = \frac{360}{NM}\sum_{i=1}^{N}\sum_{j=1}^{M}\left|\sqrt{\in_r}\left[\sqrt{x_i^2 + y_i^2} - \sqrt{(x_i - x_j)^2 + (y_i - y_j)^2}\right] - \sqrt{\in_e} T_j - D_j \sin\varphi_i\right| \tag{5-9}$$

In Figure 5- 4, the beam and receiving phase centers are along a circle, thus for any given θ_i, φ_i, the coordinate variables in (5-9) can be determined. However, these values are only real by given the parameters of F, D dimensions and Θ, Ψ, as shown in (5-1)-(5-5). Besides, the N, M and material properties are usually determined prior to the design. Hence, the error function is generally considered as function of variables shown in (5-10).

$$Err \propto \{T_1, \ldots T_j, \ldots T_M, F, D, \Theta, \Psi\} \tag{5-10}$$

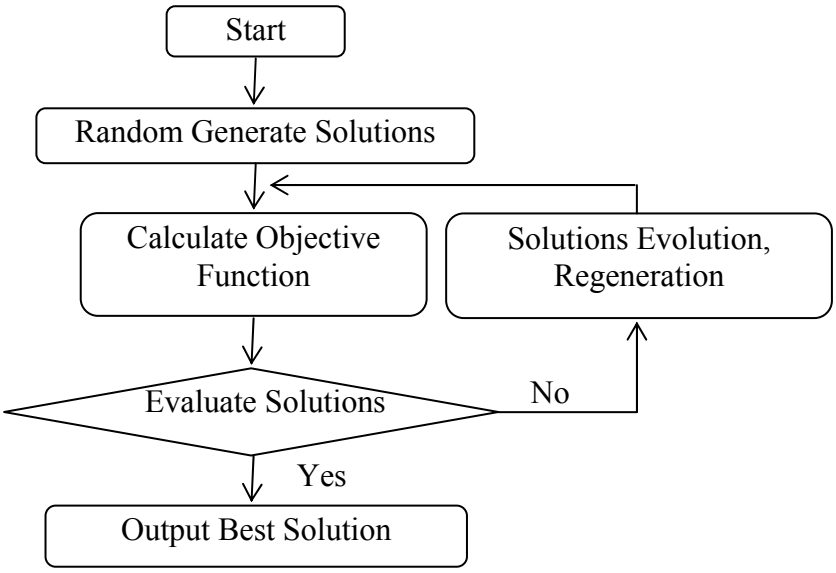

Figure 5- 5. Function Optimization Algorithms Flow Chart

The general procedure of designing circular scanning lens consists of the following steps:

1. Choose design frequency and array element spacing;
2. Select materials' ε_r and ε_e;
3. Determine number of elements M, N, hence D is determined;
4. Define Θ and Ψ, then θ_i and ϕ_j are calculated;
5. Choose r=F/D, after knowing the radius of beam contour and inner receiver contour, x_i, y_i, x_j, y_j are determined;
6. Use numerical optimization tools, whose whole process solves a M-dimensional global optimization problem, e.g. Genetic algorithm [59] and DSZ algorithms [60] to determine the transmission line lengths which yield considerably low-phase errors;
7. Use symmetry conditions to conduct spherical lens;
8. Further performance analysis.

5.2.3 Global Optimization Algorithms - DSZ Algorithms

Similar to Genetic Algorithms described in Section 3.3.2, the DSZ algorithms [60] is an alternative global optimization method. This algorithm was originally designed to eliminate the unpredictable behaviors of the selection, crossover, and mutation steps of the GA process. After some modification and through investigation, improved design has been proposed in [60]. Numerical results demonstrated its ability of handling both unconstraint and constraint optimization problems. Experiments using the standard testing functions have shown better performance than GA in terms of accuracy and efficiency. This section will briefly review the basic optimization principle of DSZ algorithms and present some simulation results compared to GA.

1. DSZ Algorithms Optimization Principle

The considered objective function is denoted as $f(x)$, $x:[x_1,\cdots,x_i,\cdots,x_n]$ where $x_i(1\le i\le n)$ is real number. D is the region of the independent variables, where D: $l\le x\le u$, $(l_i\le x_i\le u_i,1\le i\le n)$. Without losing generality, the optimization task is assumed to look for the minimum value of $f(x)$. The corresponding solution for the global minimum is $p:[p_1,\cdots,p_{i,}\cdots,p_n],(1\le i\le n)$.

$o=\dfrac{l+u}{2}$ denotes the center of D;

$D_k^x=(k(D-o)+x)\cap D,(x\in D,0<k\le 2)$, whose central point is x and ratio of similitude between D_k^x and D is k .

$$r_k^x=\max\left(\frac{2|x_i-p_i|}{k(u_i-l_i)},1\le i\le n\right),\ (x\in D,0<k\le 2) \tag{5-11}$$

The optimization problems considered in this section shall meet the following three conditions:

(1) Continuity:

Given that ε is a positive number however small $x1$ and $x2$ are any two points in D, and $0 < \|x1 - x2\| < \delta$, when δ is sufficiently small, the $f(x)$ always satisfies $|f(x1) - f(x2)| < \varepsilon$.

(2) Convergence Conditions I

Note $\theta(k)$ as a stochastic value correlated to k ($k \in (0,2]$), is defined as $\theta(k) = \dfrac{\|p - x'\|}{\|p - x\|}$

where $p \in D_k^x$, and x' subject to $f(x') < f(x)$ as a random point in D_k^x, then for any positive integer N_0, which is large enough,and $N > N_0$, we have:

$\prod_{i=1}^{N} \theta(k_i) < \varepsilon'$, where ε' is a positive number however small, and k_i $(1 \le i \le N)$ be any number in interval $(0,2]$.

(3) Convergence Conditions II

Assume $\lambda_0 \in (0, 1)$ and $P_0 \in (0,1)$ are fixed constants and x' is a point randomly selected in D_k^x . If $p \in D_k^x$ and $r_k^x \ge \lambda_0$, then $prob[f(x') < f(x)] \ge P_0$, where $prob[*]$ denotes the probability of event *.

Theorem:

According to the theoretical model, if max_iter is sufficiently large, then $|f(p) - f(x_{\max\_iter})| < \varepsilon$ *, where* ε *is a positive number however small,* $x_{\max\_iter}$ *is the optimum solution.*

Proof:

Let $[x_{\tau(1)}, \cdots, x_{\tau(i)}, \cdots, x_{\tau(M)}]$ be the maximum subset of $[x_1, \cdots, x_i, \cdots, x_{\max\_iter}]$ which holds:

(i) $\tau(i) \in [1, \max\_iter]$ is a positive integer and $\tau(i+1) > \tau(i)$, $(1 \le i \le M-1)$;

(ii) $f(x_{\tau(i+1)}) < f(x_{\tau(i)})$.

Because $p \in D_{k_j}^{x_j}, r_{k_j}^{x_j} \geq \lambda_0 (1 \leq j \leq \max\_iter)$, When max_iter is sufficient large, according to Convergence Conditions II , we have：

$$M \geq P_0 \times \max\_iter > N_0 + 1. \tag{5-12}$$

From the definition of $\theta(k)$ in Convergence Conditions I , we have :

$$\theta(k_{\tau(i)}) = \frac{\left\| p - x_{\tau(i+1)} \right\|}{\left\| p - x_{\tau(i)} \right\|}, (1 \leq i \leq M-1). \tag{5-13}$$

Thus, $\left\| x_{\max\_iter} - p \right\| \leq d_{\max}^{D} \prod_{i=1}^{M-1} \theta(k_{\tau(i)})$, where $d_{\max}^{D}$ is the maximum distance between p and other point in region D.

Because $M-1 > N_0$, according to Convergence Conditions I , Suppose $\varepsilon' < \frac{\delta}{d_{\max}^{D}}$, then we have:

$$\left\| x_{\max\_iter} - p \right\| < \varepsilon' d_{\max}^{D} < \delta \tag{5-14}$$

and due to Continuity condition , it can be found:

$$| f(p) - f(x_{\max\_iter}) | < \varepsilon, \tag{5-15}$$

where ε is a positive however small number, which means $x_{\max\_iter}$ is actually the optimum solution.

2. The Practical Model of DSZ Algorithm

Because of the uncertainty of point p before optimization, we cannot determine the values of k_1 and $c_j (1 \leq j \leq \max\_iter - 1)$ so as to satisfy the conditions illustrated in previous section. To avoid this difficulty, the practical procedure of DSZ algorithm is described in detail as following:

First, initialize $k_1 = 2$ and so that $\forall \mathbf{x}_1 \in D$, $p \in D_{k_1}^{x_1}$; set $c_j = c, (1 \leq j \leq \max\_iter)$ in our research, here c (0<c<1) is a parameter given in the initialization step of the algorithm, which is related to the specific optimization objective function. Unfortunately,

$p \in D_{k_j}^{x_j}, (1 \le j \le \max\_iter)$ will be no longer guaranteed by doing so. In order to enclose p in each search scope as much as possible, DSZ algorithm has been extended and modified as below:

(1) Let j=1 and randomly generate m points in D to form the initial set $S_1: [s_1^1, \cdots, s_i^1, \cdots, s_m^1]$; Initialize k_1 =2, the shrinking coefficient c (0<c<1) and the maximum iteration max_iter;

(2) For each point $s_i^j (1 \le i \le m)$ in S_j , a corresponding random point $s_i^j{}'$ is generated from $D_{k_j}^{s_i^j}$, thus new set is formed as $S_j{}': [s_1^j{}', \cdots, s_i^j{}', \cdots s_m^j{}']$;

(3) From set $S_j \cup S_j{}'$, choose m points according to their objective function values as the new set S_{j+1} .The maximal value of these chosen m points' function values should be smaller than the minimal value of the rest points' function values;

(4) Let $k_{j+1} = c \times k_j$ (0<c<1);

(5) Let j=j+1, return to step 2) until j=max_iter;

(6) Choose the solution $x0$ from $S_{\max\_iter}$ which makes f(x) minimum as the output;

Let $d_{\min}^j$ denote the minimum distance between the elements of S_j and p, also let $\alpha_j = \frac{d_{\min}^{j+1}}{d_{\min}^j}, (1 \le j \le \max - 1)$, then we have $d_{\min}^{\max\_iter} \le d_{\max}^D \prod_{j=1}^{\max\_iter-1} \alpha_j$. If we carefully choose values of c , m and max_iter to hold

$$\prod_{j=1}^{\max\_iter-1} \alpha_j \le c^{\max\_iter-1} \tag{5-16}$$

Then we would have $d_{\min}^{\max\_iter} \le 2c^{\max\_iter-1} d_{\max}^D$. Thus, $d_{\min}^{\max\_iter}$ could be controlled by varying $c^{\max\_iter-1}$, in other words, this meets a need to control the optimization precision.

3. Test Examples

In this section, DSZ algorithm is applied to 11 test cases from reference [78], as shown in Table 5-1. For each test case we list number of variables n, type of the function f , the relative size of the feasible region in the search space given by ρ , the number of

constraints of each categories such as LI (linear inequalities), NE (nonlinear equations) and NI (nonlinear inequalities). The feasibility ρ is determined experimentally in reference [79] by calculating the percentage of feasible solutions among the 1,000,000 randomly generated individuals.

Based on these test cases, Table 5-3 and Table 5-4 are the comparisons between DSZ algorithm and genetic algorithm in references [80], respectively. The independent variables of function G2 and G3 are 20 dimensions and 10 dimensions, respectively. The parameters of DSZ algorithm are shown in Table 5-2.

The test results clearly indicate that by using less than 1/5 of the iterations of genetic algorithm, the DSZ algorithm is capable of achieving better results than GA. It should be pointed out that DSZ algorithm has found a new solution x= [1.22780107298315, 3.74488659676571] for G8, which gives G8（x）=0.105460>0.095828. Besides, when the constraints contain equalities, DSZ algorithm handles them by transforming them into a format of inequalities or bound constrained problems. Take G3 as an example:

G3: Maximize $G3(x) = (\sqrt{n})^n \times \prod_{i=1}^{n} x_i$, where $\sum_{i=1}^{n} x_i^2 = 1, 0 \le x_i \le 1, for(1 \le i \le n)$.

G3 could be transformed into an equivalent form as following:

Maximize $G3(x) = (\sqrt{n})^n \times \prod_{i=1}^{n-1} x_i \times \sqrt{1 - \sum_{i=1}^{n-1} x_i^2}$, where $\sum_{i=1}^{n-1} x_i^2 \le 1, 0 \le x_i \le 1, \ for(1 \le i \le n-1)$.

In this way, the n-dimensional constrained optimization problem with equalities is transformed into the (n-1)-dimensional constrained optimization problem with only inequalities.

Take G11 as another example.

G11: Maximize $G11(x) = x_1^2 + (x_2 - 1)^2$, where $x_2 - x_1^2 = 0, -1 \le x_i \le 1, (i = 1, 2)$. G11 is equivalent to the problem below:

Maximize $G11(x) = x^2 + (x^2 - 1)^2$, where $-1 \le x \le 1$.

The above example shows that the two-dimensional problem constrained by equalities can be transformed into the one-dimensional unconstrained problem. If constraints contain multiple nonlinear equalities e.g. G5, the nonlinear equation toolkit shall be added to our current version of x algorithm so as to transform equality constraints into either inequality constraints or unconstrained conditions before DSZ algorithm is applied to problems like G5.

Table 5- 1. Summary of Test Case

Function	N	Type of f	ρ	LI	NE	NI	A
Min G1	13	Quadratic	0.0111%	9	0	0	6
Max G2	K	Nonlinear	99.8474%	0	0	2	1
Max G3	K	Polynomial	0.0000%	0	1	0	1
Min G4	5	Quadratic	52.1230%	0	0	6	2
Min G5	4	Cubic	0.0000%	2	3	0	3
Min G6	2	Cubic	0.0066%	0	0	2	2
Min G7	10	Quadratic	0.0003%	3	0	5	6
Max G8	2	Nonlinear	0.8560%	0	0	2	0
Min G9	7	Polynomial	0.5152%	0	0	4	2
Min	8	Linear	0.0010%	3	0	3	6
Min	2	Quadratic	0.0000%	0	1	0	1

Note: LI-linear inequalities, NE-nonlinear Equalities, NI-Nonlinear inequalities, A-active constraints and ρ - feasibility; for both G2 and G3, k=50.

Table 5- 2. Parameters of DSZ Algorithm

Function	n	m	Max_iter	$c^{\max\_iter}$
G1	13	30	1000	10^{-5}
G2	20	100	1000	10^{-3}
G3	10	20	100	10^{-3}
G4	5	20	1000	10^{-3}
G5	4			
G6	2	15	500	10^{-3}
G7	10	20	1000	10^{-3}
G8	2	10	500	10^{-3}
G9	7	20	1000	10^{-3}
G10	8	50	1000	10^{-3}
G11	2	5	20	10^{-5}

Note: n - dimensions of function's independent variables; m- number of elements in S; max_iter- the maximum iterations; c- the shrinking coefficient.

Table 5- 3. Test Results (1)

Function	Optimum value	GA in[80] （Experiment #3）			DSZ algorithm		
		Worst	Best	Average	Worst	Best	Average
G1	-15	-14.5732	-14.7184	-14.6478	-14.9606	-14.9999	-14.9609
G2	0.803553	0.78279	0.79486	0.78722	0.75686	0.80339	0.78671
G3	1.0	0.9960	0.9978	0.9970	1.0000	1.0000	1.0000
G4	-30665.5	-30645.6	-30661.5	-30653.1	-30664.7	-30665.1	-30665.0
G5	5126.4981						

G6	-6961.8	-6390.6	-6944.4	-6720.4	-6961.4	-6961.7	-6961.6
G7	24.306	26.182	25.090	25.545	24.702	24.401	24.493
G8	0.095828	0.095824	0.095825	0.095824	0.10545	0.10546	0.10545
G9	680.63	683.58	681.72	682.56	680.99	680.79	680.85
G10	7049.33	7685.8	7321.2	7498.6	7297.5	7053.4	7106.3
G11	0.75	0.75	0.75	0.75	0.75	0.75	0.75

Note: Independently run the genetic algorithm in [80] and DSZ algorithm 10 times, respectively; for the genetic algorithm, the maximum number of generations is 5,000, the population size is 70; for G3, k=10 and for G2, k=20. Parameters of DSZ algorithm are shown in Table 5-2.

Table 5- 4. Test results (2)

Function	Optimum value	GA in [6]			DSZ algorithm		
		Worst	Best	Median	Worst	Best	Median
G1	-15	-11.9999	-14.9999	-14.9997	-	-	-
G2	0.803553	0.672169	0.803190	0.755332	0.72074	0.80347	0.7851
G3	1.0	0.785582	1.00009	0.94899	1.0000	1.0000	1.0000
G4	-30665.5	-30652.0	-30665.5	-30663.4	-	-	-
G5	5126.498	6112.22	5126.51	5172.53			
G6	-6961.8	-6954.32	-6961.78	-6959.57	-6961.4	-6961.8	-6961.7
G7	24.306	35.8820	24.4110	26.7357	24.914	24.340	24.448
G8	0.095828	0.095824	0.095825	0.095824	0.10545	0.10546	0.10546
G9	680.63	684.131	680.762	681.706	681.15	680.79	680.83
G10	7049.33	12097.4	7060.55	7723.17	7297.5	7053.4	7070.4
G11	0.75	0.8094	0.7490	0.7493	0.75	0.75	0.75

Note: Run the genetic algorithm in [6] and DSZ algorithm 50 times independently; for the genetic algorithm, the maximum number of generations is 5,000, the population size is 10; for G3, k=10 and for G2, k=20. Parameters of DSZ algorithm are shown in Table 5-2.

5.2.4 Square and Hexagon Shape Lenses Geometrical Optics Investigation

In this section, two even polygon lenses mounted by linear arrays have been simulated. The purpose of this study is to see if the aforementioned approach can achieve acceptable phase errors. We assume the beam ports and receiving ports are realized by point sources and the amplitude variation across the aperture is ignored for the time being. Ideal cylindrical wave front is produced by the transmitting ports, and the receiving port is assumed locating at its far field. Theoretical phase errors have been estimated and the array factor is calculated. Both designs, one square, one hexagon, assume the array element spacing is half wavelength. Each side of the polygon has 8 array elements, hence M=8, D=3.5 in wavelength, and each sector's beam curve contains N=9 beam ports. For the square shape lens, the maximum subtended angle $\Theta=22.5^0$, at which the beam port aught to produce the scan beam of $\Psi=45^0$ since 360^0 space is required to be uniformly divided by the four side arrays, as indicated in Figure 5- 3. Respectively, $\Theta=15^0$ and $\Psi=30^0$ are satisfied for the hexagon lens. The subtended angles θ_i and ϕ_j are uniformly allocated between $-\Theta$ and Θ; the scan angle φ_i is uniformly divided from $-\Psi$ to Ψ. For specific given r=F/D, the diameter of the lens is solved, and port phase centers can are determined by (5-4) and (5-5).

Now, for given ε_r and ε_e, there is only T_j undetermined, the DSZ algorithms [60] indicated in Figure 5- 5 is adopted to minimize the phase error function of (5-9). Based on the design parameters shown in Table 5-5, we optimized T_j for both lenses. Results are shown in Table 5-6. The theoretical phase error for the square lens reaches average value of 3.3^0, and the hexagon lens obtains average value of 0.997^0.

Table 5- 5. Even Polygon Lens Design Parameters

Symbol	SQUARE LENS	Hexagon Lens
N	9	9
M	8	8
D	3.5λ	3.5λ
r	1.263	1.927
Θ	22.5^0	15^0
Ψ	45^0	30^0
ε_r	5	3
ε_e	5	3

Table 5- 6. Transmission Line Lengths for Square and Hexagon Lens

T_j-T_0	SQUARE LENS/ Λ	Hexagon Lens/ λ
1	0.3266	0.2258
2	0.1690	0.1160
3	0.0618	0.0419
4	0.0071	0.0047
5	0.0064	0.0045
6	0.0604	0.0418
7	0.1654	0.1146
8	0.3231	0.2243

The estimated phase errors across the linear aperture for each beam in the square and hexagon lenses are shown in Figure 5- 6 and Figure 5- 7. It is noticed that the maximum phase error takes place at the edge beam; as the beam port gets closer to the center, relatively lower phase errors are exhibited. Besides, the standard deviations for each beams' phase errors in both lenses are shown in Figure 5- 8. The hexagon lens demonstrates comparatively lower phase errors, which actually compensates the smaller receiving contour that probably reduces the power efficiency in real lens system. The power issue of the microstrip lens will be discussed in next section by full-wave investigation.

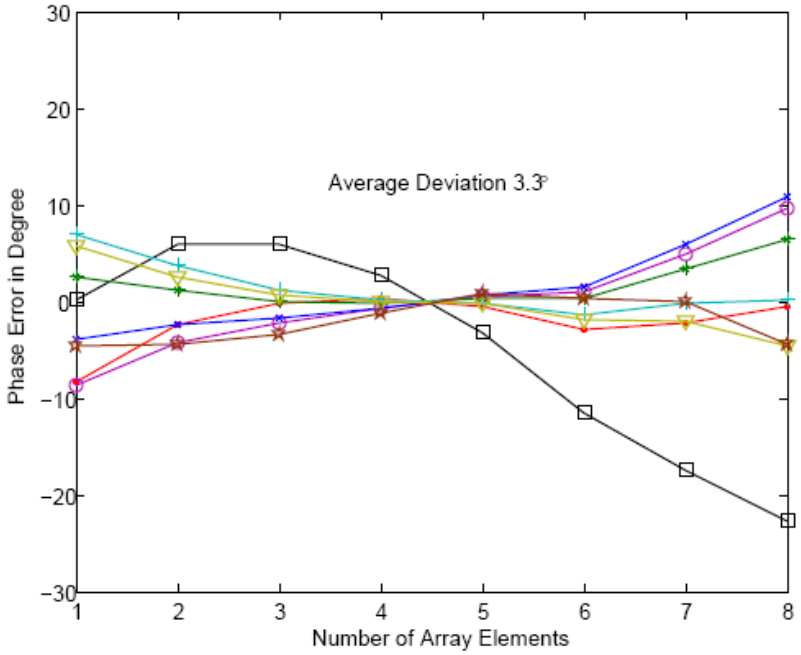

Figure 5- 6. Phase Errors across the Aperture for the Square Shaped Lens

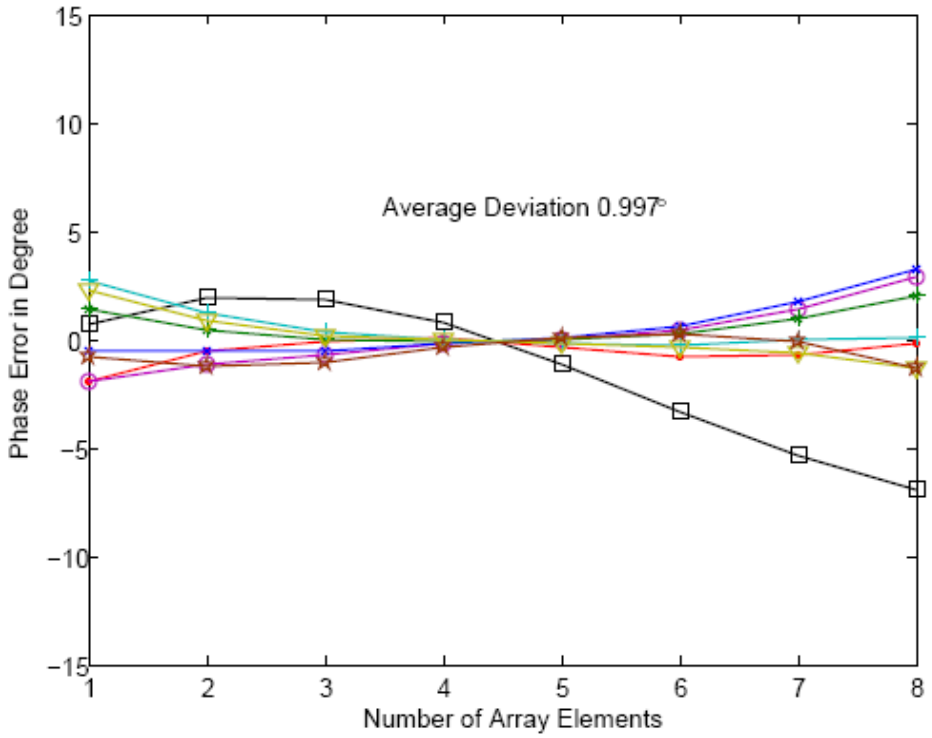

Figure 5- 7. Phase Errors across the Aperture for the Hexagon Shaped Lens

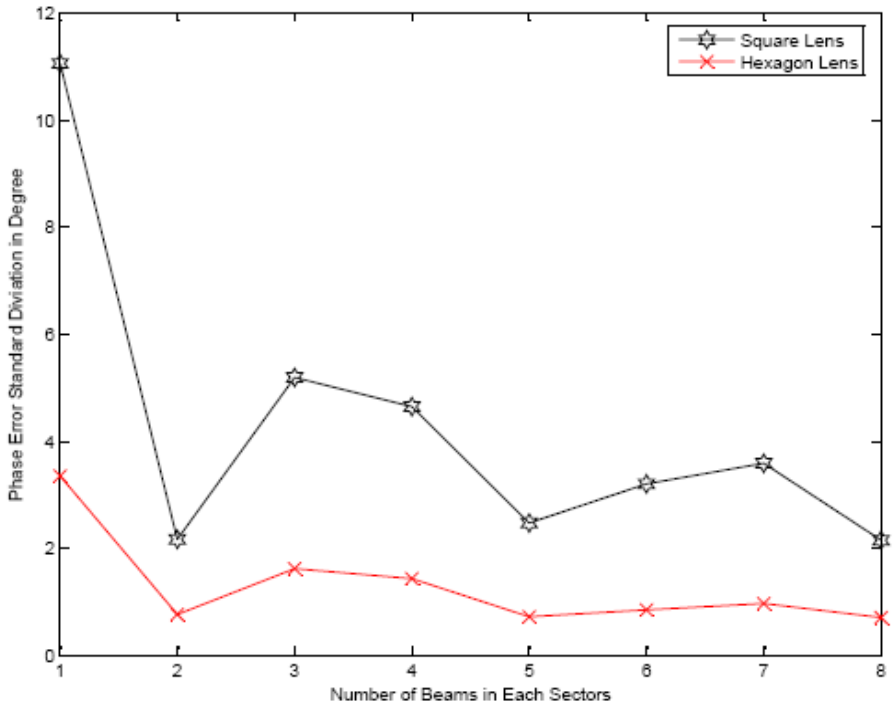

Figure 5- 8. Phase Error Standard Deviation for Each Beams of the Square and Hexagon Lens, Beam Number Notation is as shown in Figure 5- 11.

To view how these phase errors affect the pattern, the array factors for both lenses have been plotted in Figure 5- 9 and Figure 5- 10. The calculation is based on the equation (13) [81], where A_n is the amplitude feeding the i^{th} beam element, α_m is the feeding phase, k is the free space wave number, and d is the array element spacing. Note that the cosine amplitude distribution across the aperture is a reasonable assumption based on the investigations done in [34, 54]. For simplicity, the array factors in Figure 5- 9 and Figure 5- 10 assume cosine amplitude distributions. This study shows that phase errors achieved in the square and hexagon lens models yield good beam separations and scanning capabilities across the 360^0 azimuth angles. In the next section, specific port's profiles will be considered; the accurate amplitude and mutual couplings will be taken into account in the full-wave analysis.

$$f(\varphi) = \frac{\sum_{m=0}^{M-1} A_m e^{j(\alpha_m + mkd\cos\varphi)}}{\sum_{m=0}^{M-1} A_m} \tag{5-17}$$

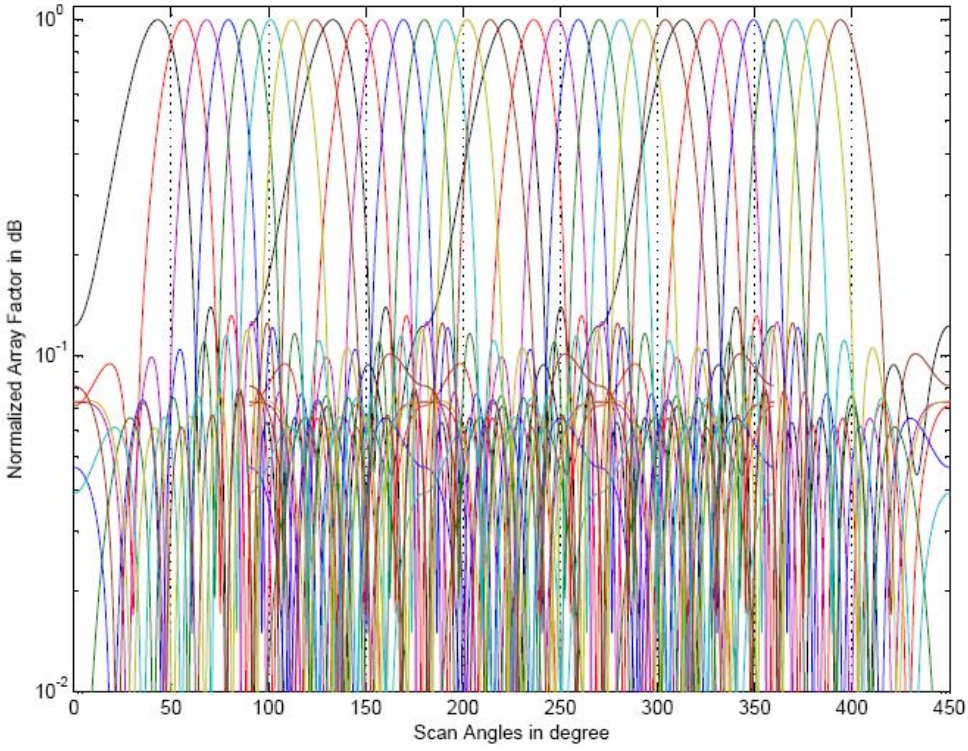

Figure 5- 9. Phase Array Factor of the Square Shaped Lens

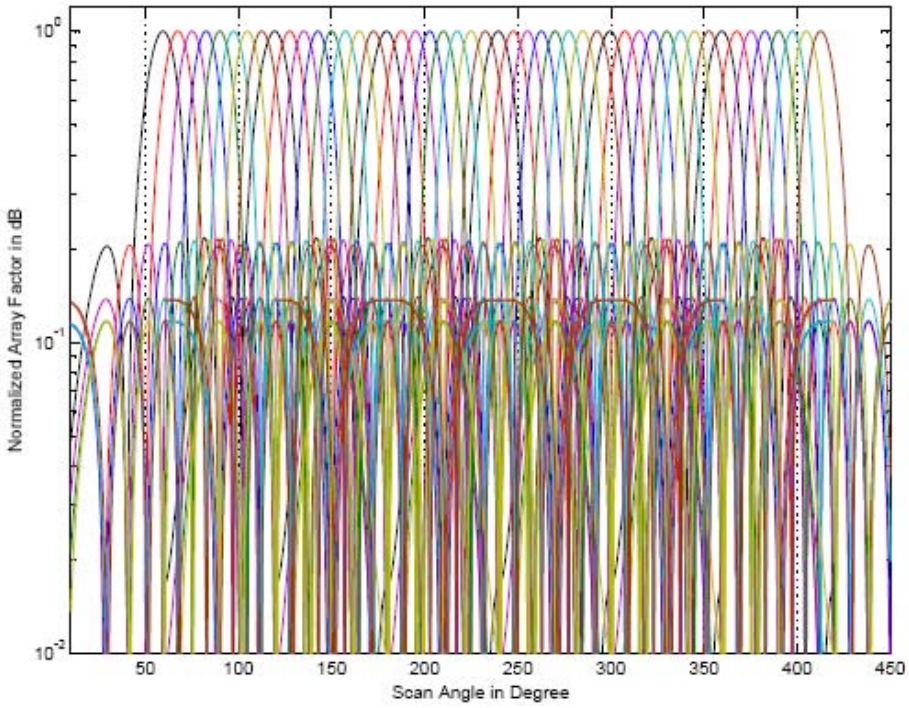

Figure 5- 10. Phase Array Factor of the Hexagon Shaped Lens

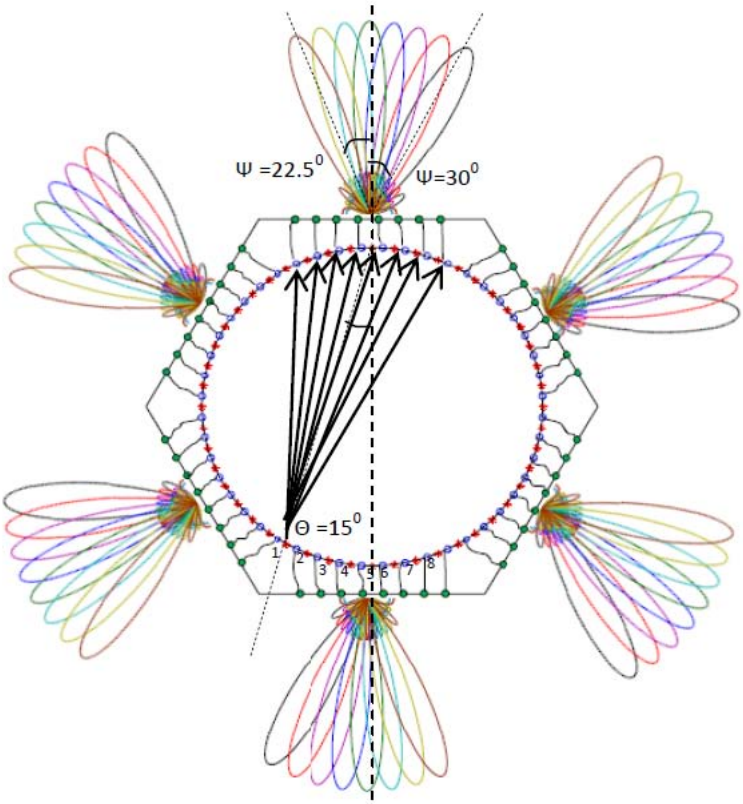

Figure 5- 11. The Multi Beams Generated by the Hexagon Lens

The diagram of the hexagon shape lens is shown in Figure 5- 11. It is worth mentioning that although 9 beams are allocated along the beam sides as shown in Figure 5-4, there are only 8 beams are actually involved in the optimization process, because one of the edge beam ports along the beam contour is not necessary to be covered again by the adjacent sector. As shown in Figure 5-11, the linear phased array along each facet has an efficient coverage angle of -22.50^0~30.00^0. This also explains the reason why the optimized transmission line lengths shown in Table 5-6, the phase errors in Figure 5- 6 and Figure 5- 7 are not exactly symmetric across the aperture output ports.

5.3 Printed 360-degree Microstrip Lens Construction and Full-wave Simulation

After applying the microwave lens design method described in previous section, the phase centers and transmission line lengths are solved. The microstrip lens implements transmitter and receiver's phase centers using tapered microstrip horns, while the constraint transmission lines are formulated via classical microstrip lines, as shown in Figure 5- 12. Due to the constraint length requirement, curved line has to be used. In current model, the transmission line curve is realized by curve fitting of a typical Gaussian function. The length of a Gaussian curve can be found from a line integral as shown in equation (5-18). Given a desired length L, the mean value μ and divergence σ, the unknown parameter A can be solved, thus the deterministic curve of (5-19) is solved too. In practical design, the transmission line usually has 50Ω characteristic impedance. Current design built for Rogers TMM6 has a transmission line width of approximate 1.1 mm.

$$L = \int_{x_1}^{x_2} x\sqrt{1+[df(x)/dx]^2}\,dx \tag{5-18}$$

where:

$$f(x) = \frac{A}{\sigma\sqrt{2\pi}}\exp[\frac{-(x-\mu)^2}{2\sigma^2}] \tag{5-19}$$

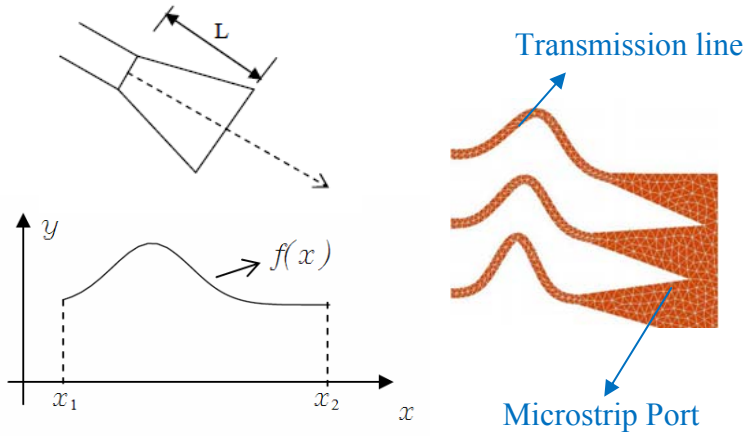

Figure 5- 12. Port and Transmission Line Implementation

The completed square shaped microstrip lens is shown in Figure 5- 13. Its design parameters are included in Table 5-7. Each side of the lens consists of 12 ports, among which ports 1-6 stand for the beam ports, and ports 7-12 indicate the ones of receiving functionality.

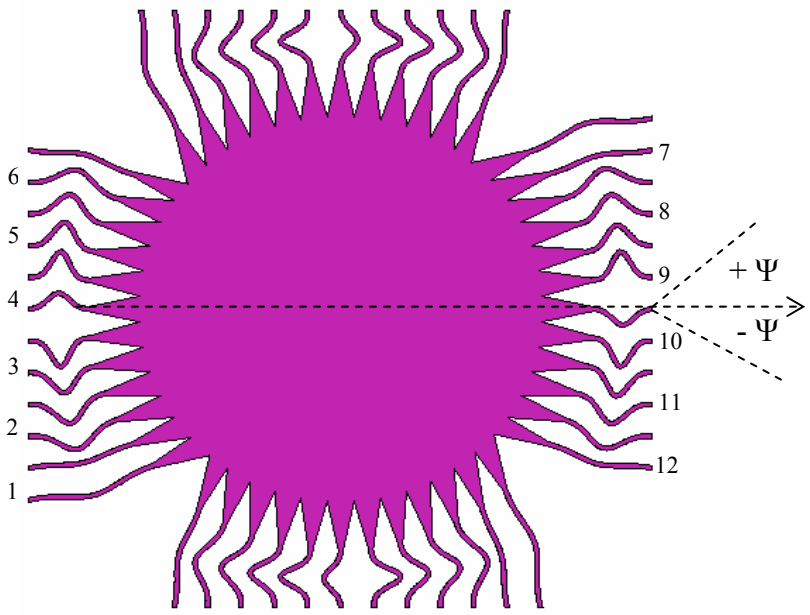

Figure 5- 13. Constructed Printed Microwave Lens

Table 5- 7. Square Shape Microwave Lens Parameters

SYMBOL	QUANTITY	VALUE
f_0	Center Frequency	10 GHz
N_b	Beam Port #	6x4
N_r	Receive Port #	6x4
ε_r	Relative ε	6.0 ± 0.08
tanδ	Loss tangent	0.0023
σ	Conductivity	5.7 e+7
d	Substrate Thickness	0.762 mm
t	Copper thickness	0.07 mm

*Terminal impedance is 50Ω, so the width of the transmission line is designed approximately 1.1449 mm.

The port to port scattering parameters are achieved using Method of Moment (MoM) full-wave simulation in FEKO [82]. Previous work in [55] has demonstrated that FEKO is very accurate tool to estimate the microwave lens performance. The phase, amplitude couplings as well as array factors are investigated by post processing. In Figure 5- 14 and Figure 5- 15, we demonstrate the array factors produced by single side beam port excitations at 6 GHz and 10 GHz. It is observed that the designed lens has obtained very good scanning pattern and the true-time delay property (as the beam pointing direction does not vary with frequencies). Besides, the described lens has 6 beam ports at each side, and the maximum subtended angle is $\Theta=22.5^0$, at which the beam port (# 1) is designed to produce the scan beam of $\Psi= -45^0$. Beam port # 6 is designed to generate scan beam of $\Psi=30^0$, as mentioned in previous section, the maximum scan angle for single sector is not necessary to be covered twice by its adjacency. This explains why the simulation results of port #1 excitation produces beam at $\Psi\sim -46^0$ and port #6 generates beam at $\Psi\sim 30^0$ in Figure 5- 14 and Figure 5- 15.

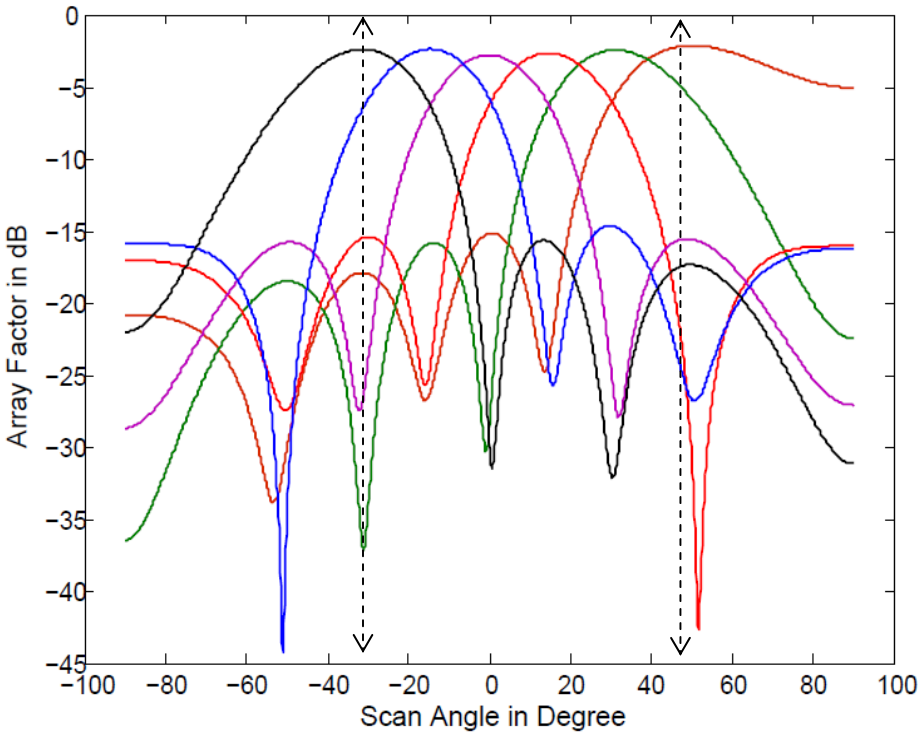

Figure 5- 14. Array Factor for Single Sector Excitation at 6GHz

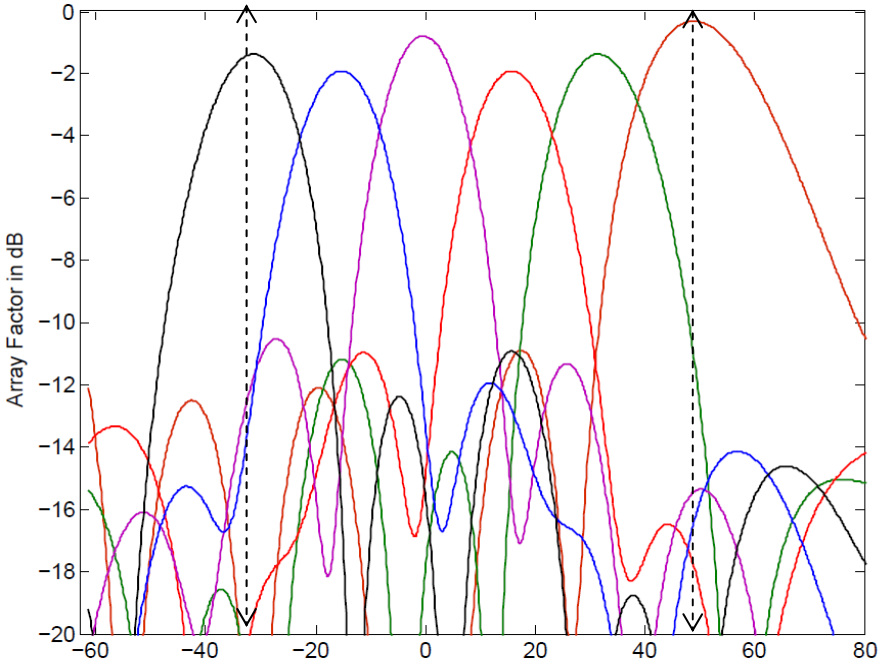

Figure 5- 15. Array Factor for Single Sector Excitation at 10GHz

It is also observed that the amplitudes of the array factor at 10GHz have higher variation than that of 6GHz. This is mostly due to the amplitude tapering variation across the aperture. At lower frequency, for a given beam port size, it produces more isotropic beams than that at higher frequency. Thus at 6GHz, the beams from different beam ports produce lower variation at amplitude distribution. Besides, at 10GHz, the aperture size in wavelength gets larger than that of 6GHz, as such narrower beams produced. As the amplitude errors increase, the side lobe also increases, as indicated in Figure 5- 15.

With the beam moving further away from the broadside, it gets wider and wider. This is because the aperture efficiency decreases as the scan angle increases. In both Figure 5- 14 and Figure 5- 15, the widest beam occurs at $\Psi=45^0$ only, because each sector is designed for scanning range of $-30^0 \sim 45^0$. It is worthwhile noting that the array factors are calculated based on the feeding phase and amplitude across single facet of the lens. In reality, should the array connect to the microwave lenses without circulators; the radiation due to the spillover energy may affect the large angle beams as well. Current design assumes that there is no spillover radiation from the adjacent facets.

The 360-degree multi-beams are achieved when multiple beam ports at each side are excited. Array factors produced at 6 GHz and 10 GHz in full azimuth angle scanning are plotted in polar coordinate in Figure 5- 16 and Figure 5- 17. Patterns in reoccurring color indicate far field beams produced by different sectors. In practical design, the proposed microwave lens can achieve 360-degree electrical scanning by electrically switching the beam ports at four sides. Should simultaneous beams are needed, two things should be aware of. First, it is suggested different beams operate at different frequencies so that the signals from different channels do not interfere with each other; second, because multiple ports are functioning in beam port mode (not load mode), the effect of their mutual couplings has to be incorporated. Note all simulation results shown in this section are based on single port excitation on the premise that all other ports are loaded.

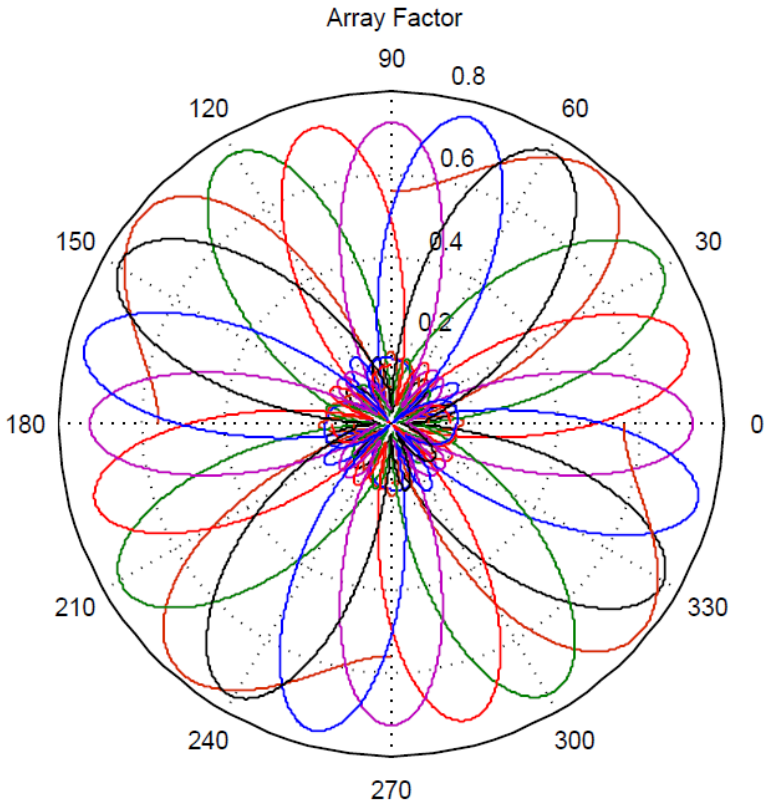

Figure 5- 16. Array Factor for all Beam Port Excitations at 6 GHz

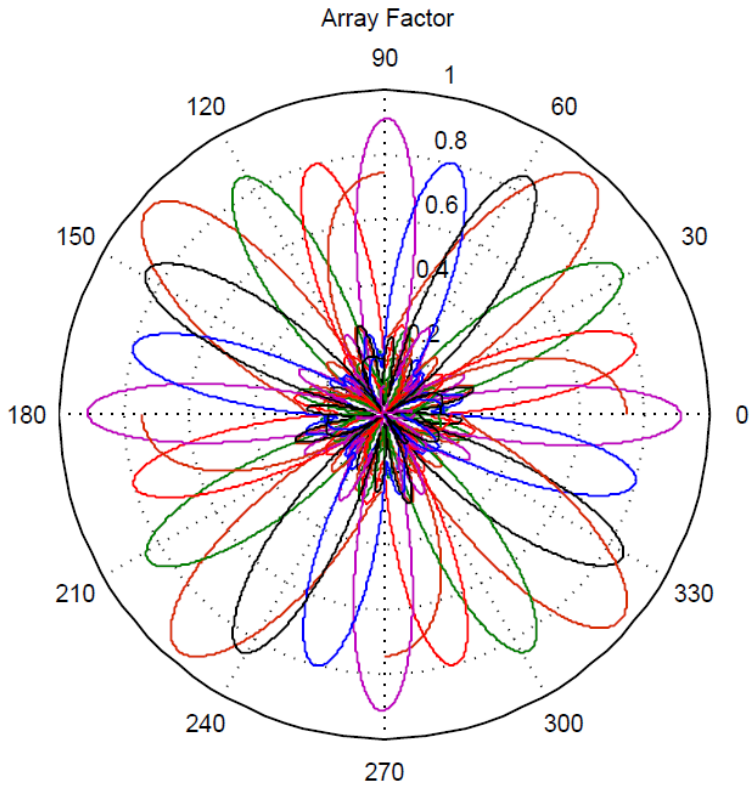

Figure 5- 17. Array Factor for all Beam Port Excitations at 10 GHz

5.4 360-Degree Lens Fabrication and Measurement

The microstrip lens in Section 5.3 was fabricated and measured. The fabrication process adopts the traditional tuner transfer method. It was etched in house using the mixture of hydrochloric (HCl) and hydrogen peroxide (H_2O_2). This helps control the etching process as such etchant is more transparent than the classical ferric chloride ($FeCl_3$) liquid, as shown in Figure 5- 18. Detailed fabrication process is described in Appendix G. The fabricated lens with coaxial-microstrip residuals is shown in Figure 5- 19. The beam ports are marked from #1-6, receiving ports from #7-12.

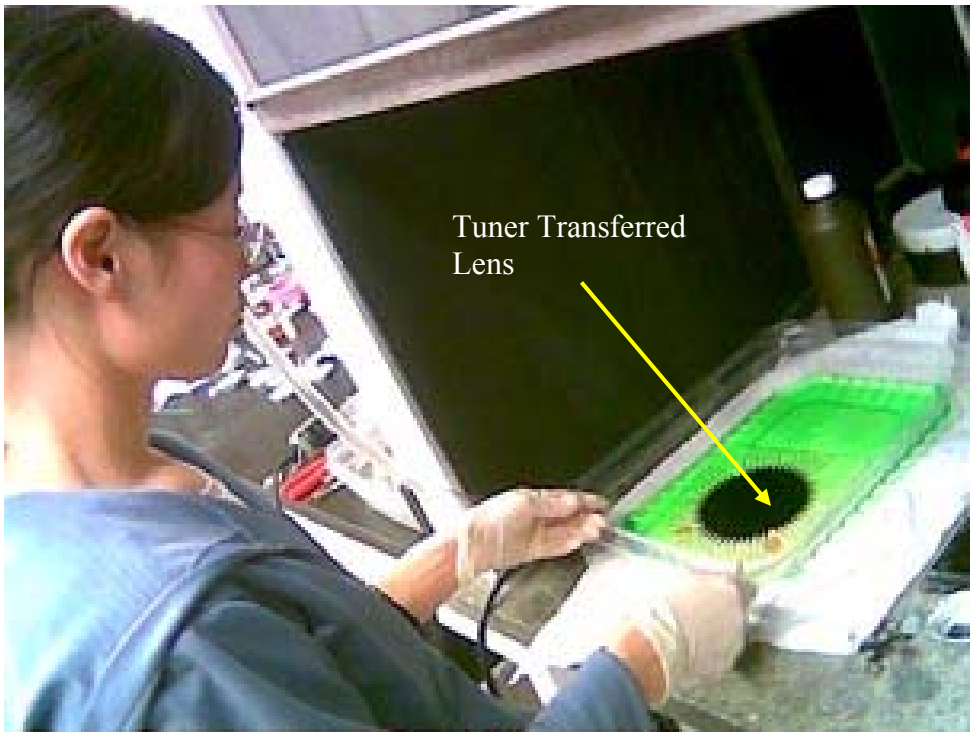

Figure 5- 18. Microstrip Lens Fabrication

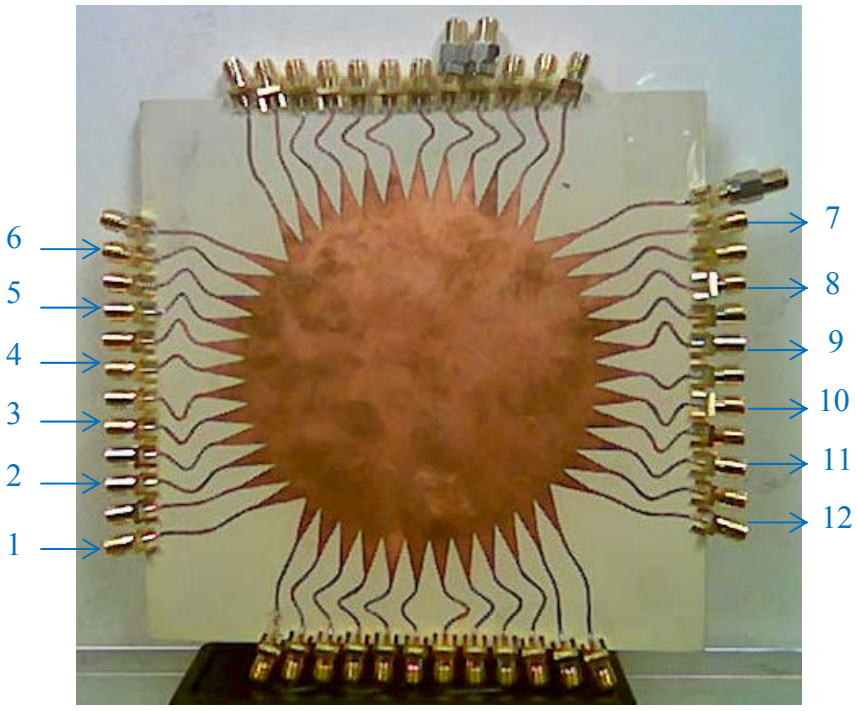

Figure 5- 19. Fabricated Microwave Lens

During the two-port network measurement, all ports except the present beam and receiving ports are terminated by 50-Ohm loads, as shown in Figure 5- 20. Perhaps the most important parameter for the lens performance in terms of electrical scanning is the phase shift across the aperture (from port #7- port #12) for single beam port excitation. We compared the measured phase shifts across aperture with the full-wave results for port 1 and 2 excitations at 10 GHz in Figure 5- 21 and Figure 5- 22. Clear linearity has been exhibited. Note that port 1 and port 2 provide different phase slope from one another, which guarantees their far field beams scan into different directions. By combining the measured feeding phase and amplitude information, the array factor has been estimated. Figure 5- 23 and Figure 5- 24 demonstrate the array factors for both measurement and full-wave analysis for port 1 and 2 excitations at 10GHz. It is noticed that the main beam scanning angles of measurement and simulation agree with each other, however, the amplitudes indicate clear shift. The amplitude errors probably due to the higher reflection occurred at the terminators. It is also found that the soldering has resulted in higher contacting resistants, which consequently leads to higher reflections in

the cavity as well. More accurate fabrication has to be done in future to improve the amplitude performance.

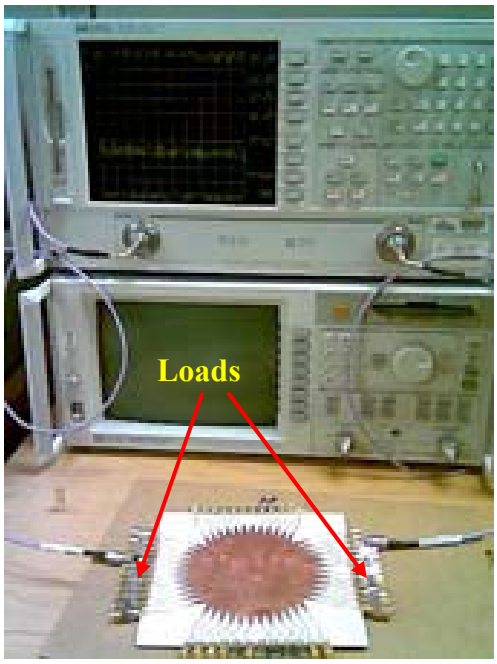

Figure 5- 20. Microwave Lens Measurement

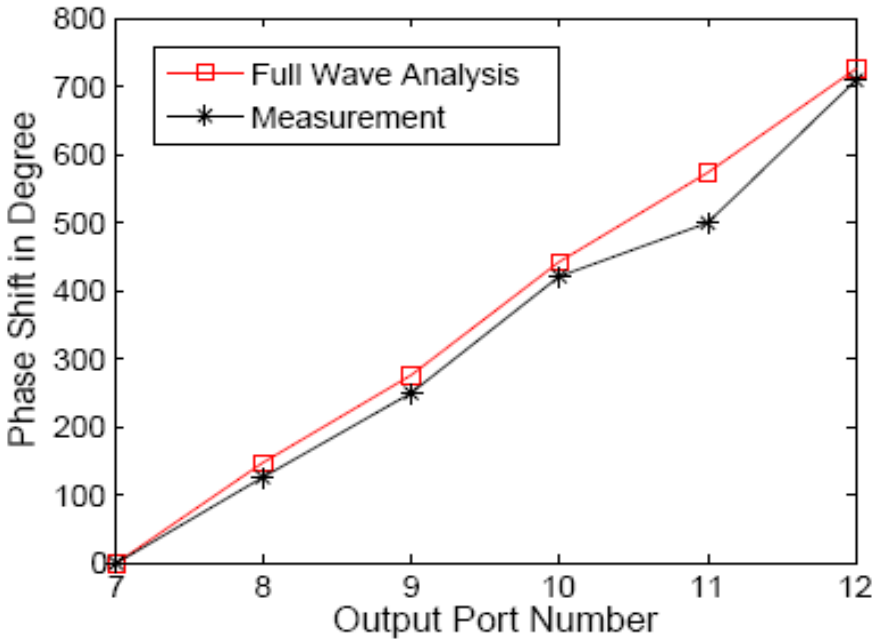

Figure 5- 21. Phase Shift across Outputs for Port 1 Excitation at 10 GHz

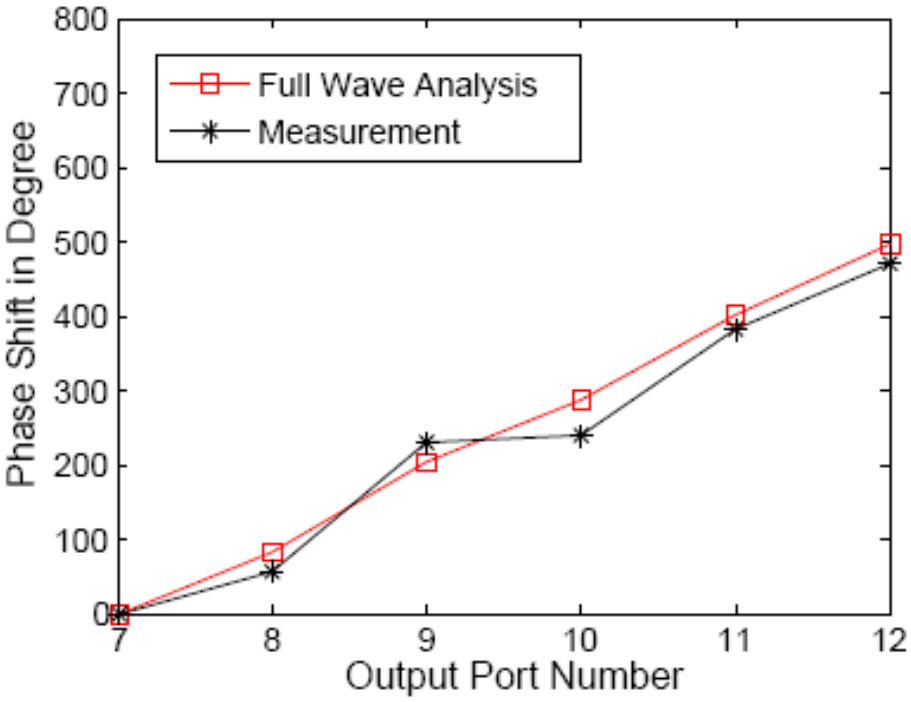

Figure 5- 22. Phase Shift across Outputs for Port 2 Excitation at 10 GHz

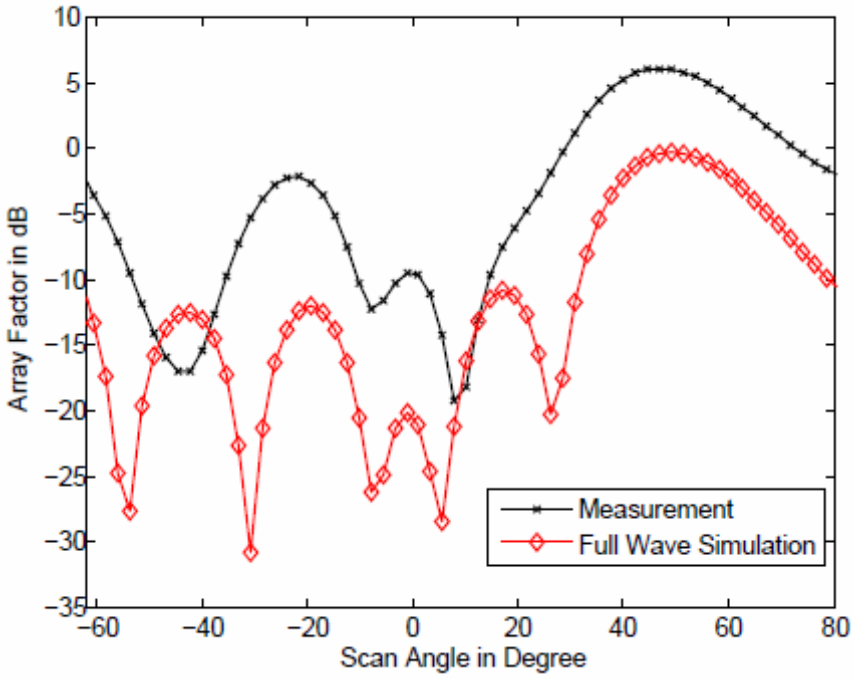

Figure 5- 23. Array Factor for Port 1 Excitation at 10 GHz

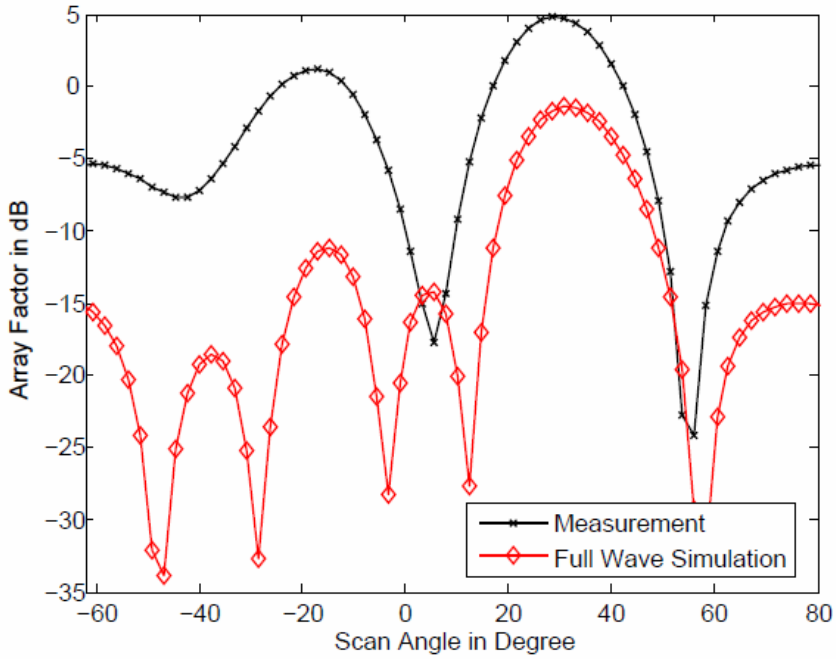

Figure 5- 24. Array Factor for Port 2 Excitation at 10 GHz

5.5 Notes on 360-Degree Lens's Feeding Arrangement, Efficiency and Bandwidth

The above description implies that beam and array ports alternate between transmit and receive functions. Scanning is achieved by switching the transmit port over the 360-degree range. Multiple beams can also be generated at the right frequency with an appropriate switch matrix. This can be represented by the port input and output arrows in Figure 5- 25. Alternatively, all ports can be used to transmit and receive in order to increase the scanning resolution as illustrated in Figure 5- 26. If a single beam is produced by switching the beam port, the ports will operate in either transmit or receive mode at a time. If multiple beams are required, some of the ports will operate in both transmit and receive modes simultaneously. This will be the case if the multiple beams are at opposite sides of the lens. This configuration increases the number of scanning steps, or increases the scanning resolution within certain scanning range. Again, a switch matrix may be needed in this mode.

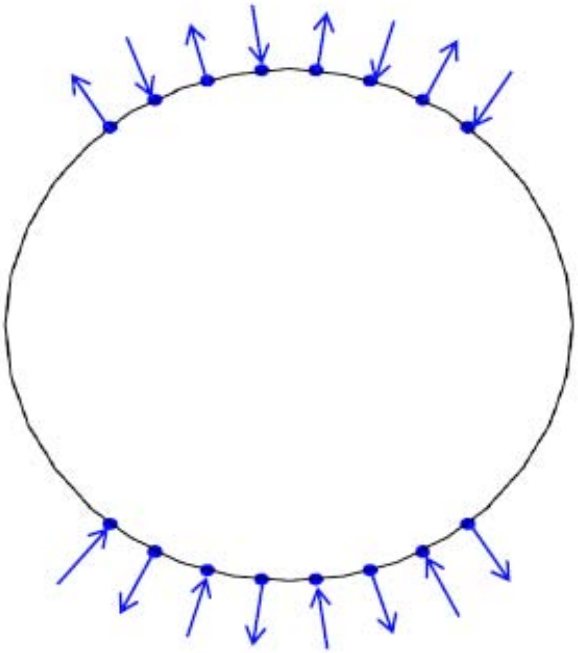

Figure 5- 25. Beam and Receiving Arrays with Separate Transmit and Receive

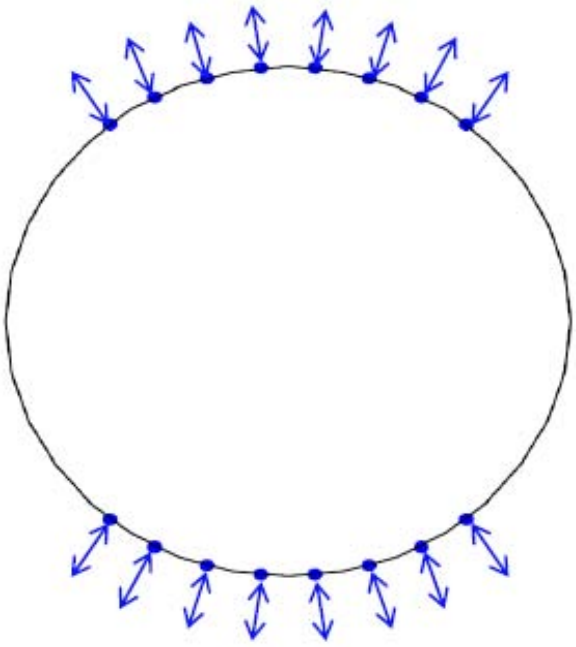

Figure 5- 26. Beam and Receiving Arrays with Simultaneous Transmit/Receive

To realize the transmit only/receive only modes at the beam and array ports and to ensure the direction of radiation flow from one side of the lens to the opposite side, a feeding arrangement is shown in Figure 5- 27 that contains circulators at the transmitting ports. Radiation received by these elements will be directed to matched loads and will not interfere with the transmitting function. The variation of this concept that allows for simultaneous transmit/receive operation of the ports can be realized by using the same circulators to discriminate between the transmitting and receiving functions of the ports as shown in Figure 5- 28. As pointed above, this has the effect of increasing the number of scanning directions.

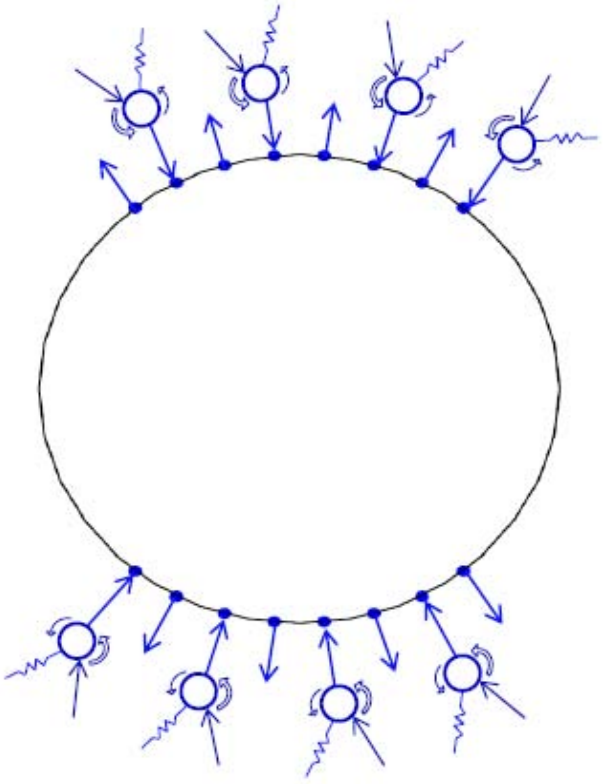

Figure 5- 27. Feeding Arrangements Using Circulators to Prevent Receiving in Transmitting Ports

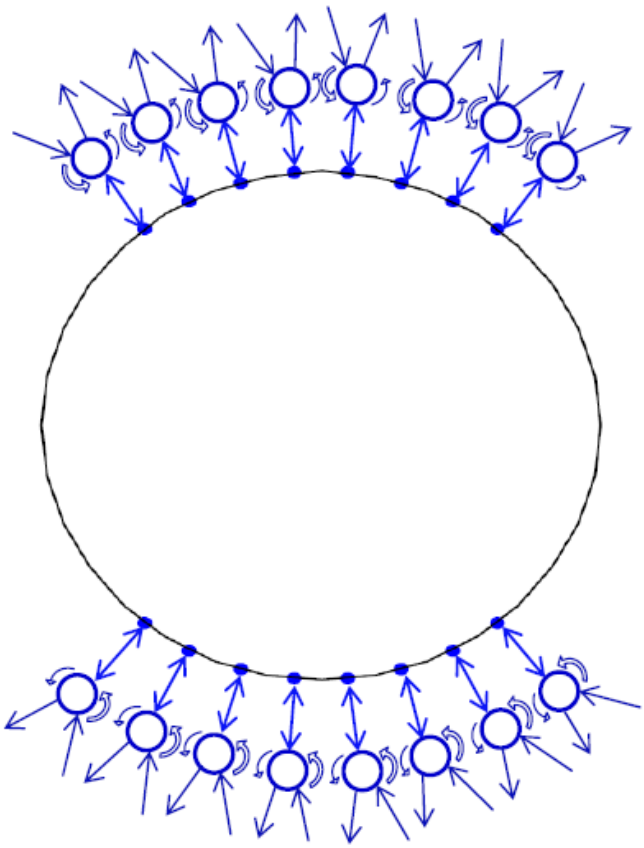

Figure 5- 28. Feeding Arrangements Using Circulators to Allow Simultaneous Receiving and Transmitting at the Same Port

For simplicity, the array factor (or gain for the isotropic elements) in the previous sections put no specific assumption on the spillover loss and the side panel radiation. In reality, depending on the antenna elements, array spacing, and spillover loss, the primary beam may be significantly affected. As an example, assume isotropic elements are directly deloyed at the receiving-port output of prototype lens. The solid line in Figure 5-29 indicates the array pattern due to the radiation of one primary and two adjacent panels, and the dashed line implies the previous result of a single aperture. All calculation is based on a full-wave simulation. Result shows that the average gain of the prototype lens has increased by 3dB, while its average side lobe gain has increased by 5dB. Note that real antenna elements may not produce such large fluctuation. Further improvement can be done by 1) increasing the dimension of the beam port so that energy can be confined

in the receiving-port region, 2) using larger array spacing so that no grating lobes appear in adjacent panel scanning region, 3) adding switch before the radiation antenna to assure that the spillover couplings are terminated by load.

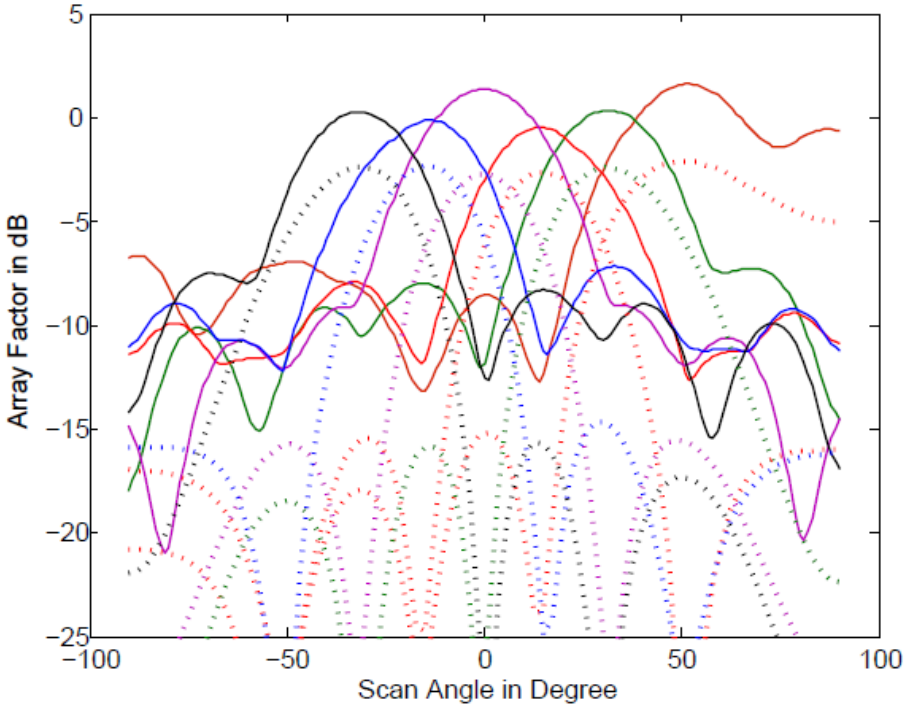

Figure 5- 29. Array Factor for Single Panel Excitation at 6GHz When Considering the Side-Panel Radiation

A limitation in this design is the restrictions on the contours of the beam array and the receiving array. These restrictions may result in increases in the phase errors on the radiating aperture of the phased array. Initial results as shown in the example of the square and hexagon lens in Section 5.2.4, the fabricated lens in Section 5.4, however, show that acceptable phase errors are still achievable with this arrangement.

Similar to any microwave component design, efficiency is an important factor. Because the beam ports function independently to each other and different port has different efficiency of coupling the power into the receiving aperture, it is easier to consider total insertion loss between single beam port and the receiving aperture as the efficiency of this single port. Figure 5- 30 plots the efficiency for beam ports 1-6 of the square lens at

6GHz and 10GHz. It is observed that as the frequency increases, the efficiency increases. As discussed above, as frequency increases, the beam port electrical size increases, resulting in narrower patterns, hence more energy is coupled to the receiving ports. Similarly, the higher spillover loss for 6GHz is due to the more isotropic pattern of the beam port.

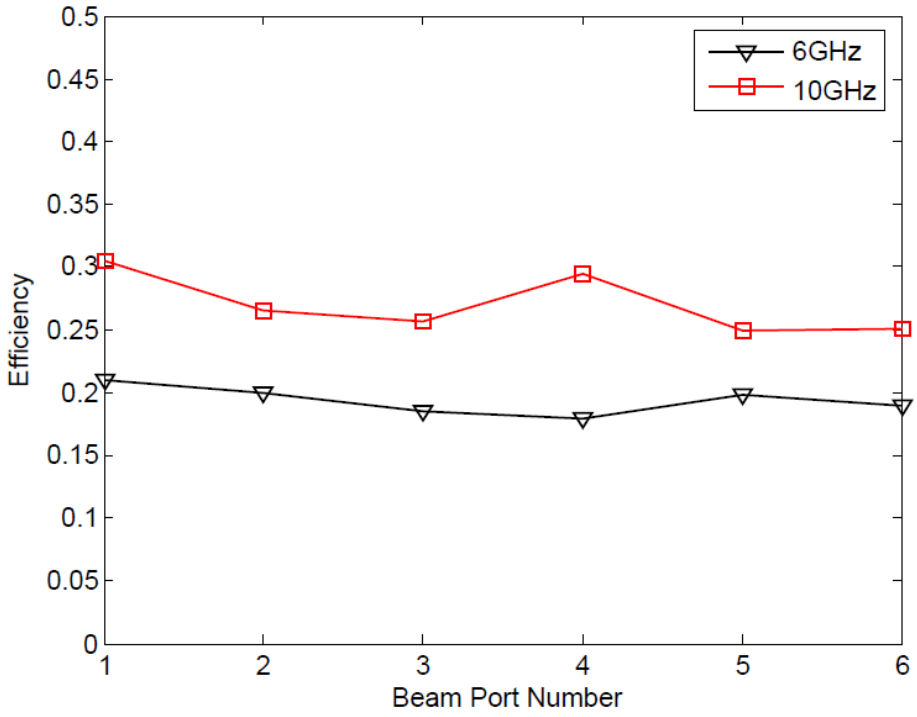

Figure 5- 30. Efficiency of Port 1-6 at 6GHz and 10GHz

The microwave lens constructed in this paper is not optimized in terms of efficiency. Similar to Rotman lens design, the efficiency can be increased by increasing the width of the beam port or tapering the port geometry. Given required number of scanning steps N, larger beam port width usually leads to larger F. Thus efficiency trade off to the size of the lens geometry, in some lens systems with hundred of scanning beams such as [50], very small beam ports have to be used given an limited dimension, as a result, the efficiency might be less emphasized. In reality, the spillover loss of the microwave lens is less critical than that of reflector design. Take the transmitting system for example, the power amplifier of the antenna is usually deployed before the reflector, however, for

microwave lens system, it is applied right after BFN, as indicated in Figure 5- 31. For this reason, although the microstrip lens described above is meant to handle low power, it is possible to be deployed in high power applications as well.

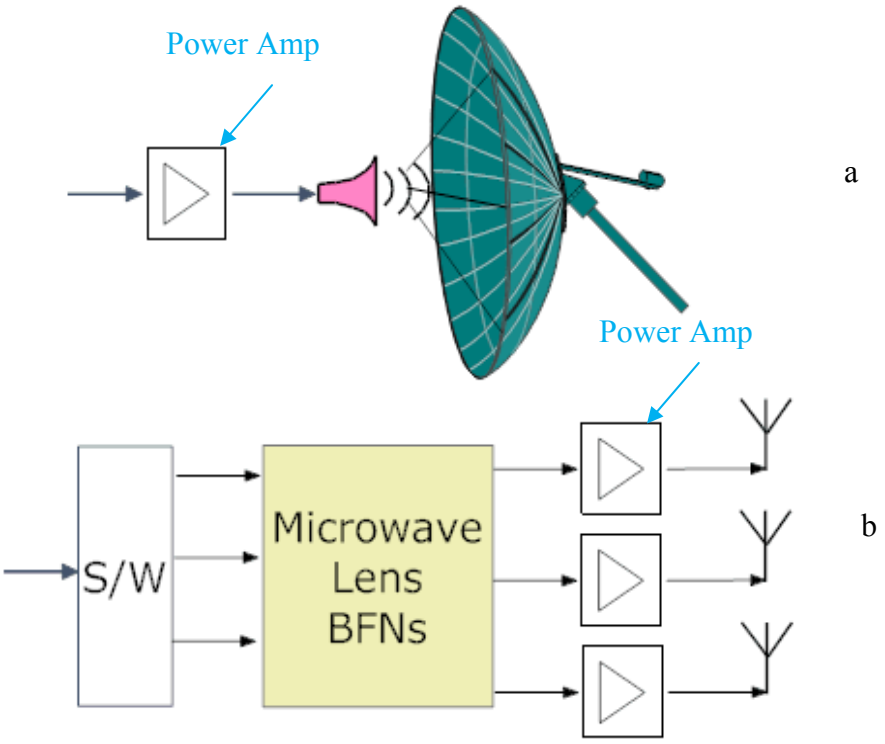

Figure 5- 31. Microwave Lens BFN vs. Reflector

Microwave lens is generally considered as wideband passive device. Its lower frequency bound is mainly determined by the beam port frequency response. We used triangular shape taper in the current design for simplicity, as shown in Figure 5- 32a. It can be further improved by adopting optimized taper lines, such as the one shown in Figure 5- 32b. The higher frequency bound is generally constraints by the array spacing. This is due to the fact that given any constant spacing array, as the frequency increases, the side lobes start to emerge in the far field. Method for extending the upper limit is to apply coaxial connectors at the lens output instead of feeding the antenna directly. In doing so, when the array spacing gets larger than e.g. half wavelength, one can adjust the array spacing to a smaller value. This will lead to new azimuth scanning range, however, for

constant array space, a reasonable wideband signal can still be sent into nearly constant direction due to the intrinsic true-time delay (TTD) property of the proposed lens.

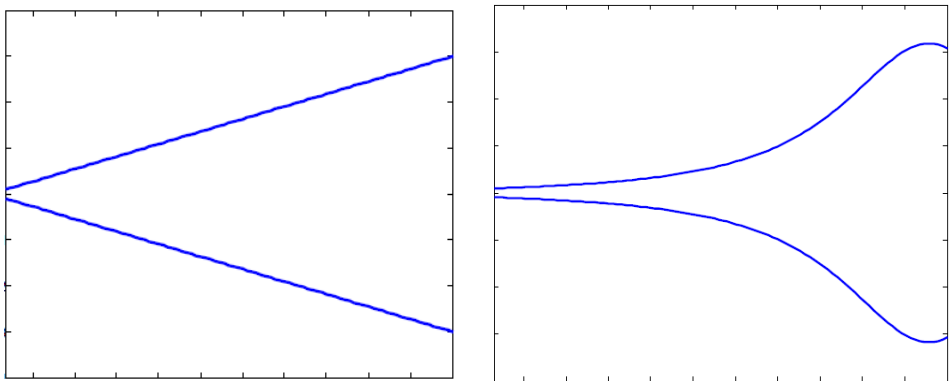

Figure 5- 32. Examples of Tapered Line Models a) Triangular Shape, b) Curved Shape

5.6 Summary and Future Perspectives of 360-Degree Scanning Microwave Lens

Microwave lens that produces scanned beams over the full azimuth angular domain of 360 degrees is presented. The proposed design method adopts geometry symmetry to achieve the lens contour reusing. Beam ports and receiving ports can be interleaved to each other or totally reoccupied. Low-phase errors can be achieved by global optimization algorithms.

Two even-facet polygon lenses (square and hexagon) were investigated by geometry optical calculations. The square lens uses maximum subtended angle of 22.5^0 to achieve 45^0 scanning beam, while the hexagon lens applies maximum subtended angle of 15^0 to achieve 30^0 scanning beam. Average phase errors of 3.3^0 and 0.994^0 were achieved for the square and hexagon lenses respectively. Array factors calculated by assuming cosine amplitude distributions demonstrate good results.

A square shape lens was further constructed, full-wave simulated, fabricated and measured. Detail description of each procedure has been explained in this Chapter. The true-time delay (TTD), efficiency, and bandwidth were investigated by the full-wave simulation. Both measurement and simulation results demonstrate linearity in the phase shift. Measurement results show higher amplitude errors due to the coarse fabrication. In general, the scanning angle has agreed well with the simulation results.

The concept presented in this paper can be further improved and extended. Beside of the efficiency and bandwidth improvement strategies discussed before, there are some other future aspects for the microwave lens of 360-degree scanning.

1. None-even-facet array fed by circular shape lens

In this paper we only discussed even-facet array fed by a circular shape lens. The formulation method described in Section 5.2 can be adopted to feed other types of lenses. Figure 5- 33 indicates an example of a circular shape array fed by circular lens.

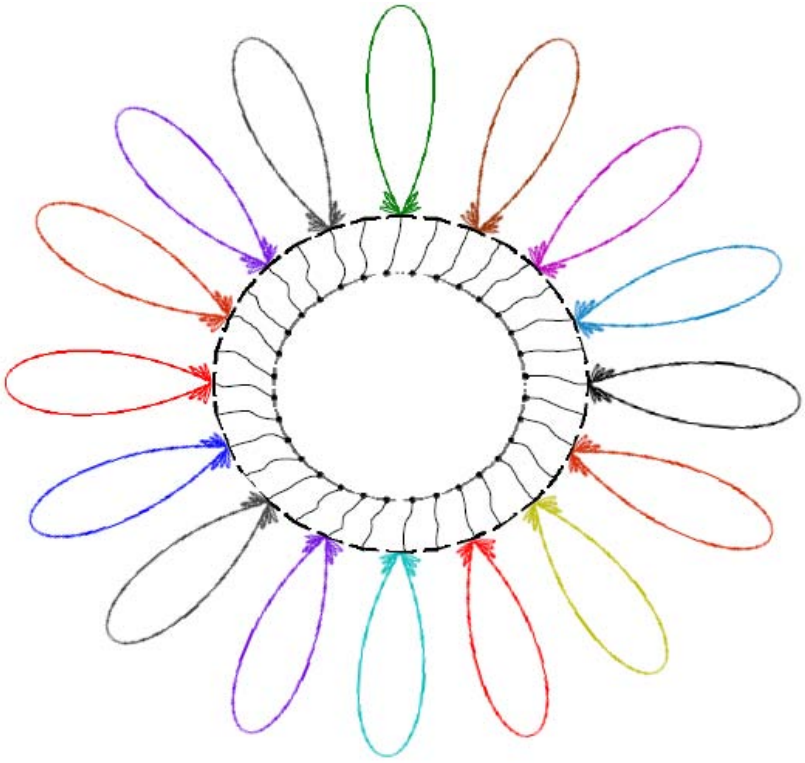

Figure 5- 33. Circular Array Fed by Circular Lens Configuration

2. None-circular microwave lens for 360-degree scanning

It is probably necessary to maintain the symmetric contours during the 360-degree scanning lens formulation. However, the contour is not necessary to be always circular. It is suggested that by introducing design freedoms to the shapes of the beam and receiving contours, the phase errors can be further reduced. Figure 5- 34 demonstrates the idea of using non-circular but symmetric lens contours.

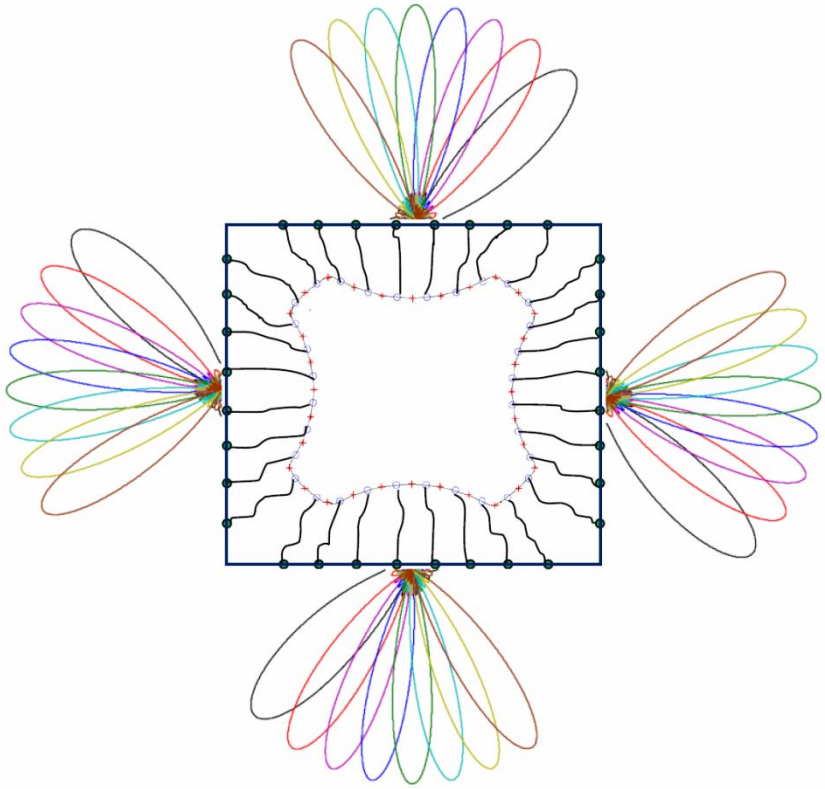

Figure 5- 34. None-circular Lens Contour Configuration

3. Spherical Scanning Pencil Beam Former

The two dimensional microwave lens can be extended to feed planar array so as to produce pencil beams. Figure 5- 35 shows the basic principle of operation. Take the broadside beam for example, the center port of lens A is first excited to produce nearly uniform amplitude and zero phase shift output signals across its linear aperture. These signals are further guided to feed the stacked lenses' center beam ports, resulting nearly uniform amplitude and zero-phase-shift illumination across the entire planar aperture, as

such pencil beam at broadside produced. As the beam port of lens A switches, the pencil beam scans in the vertical plane correspondingly.

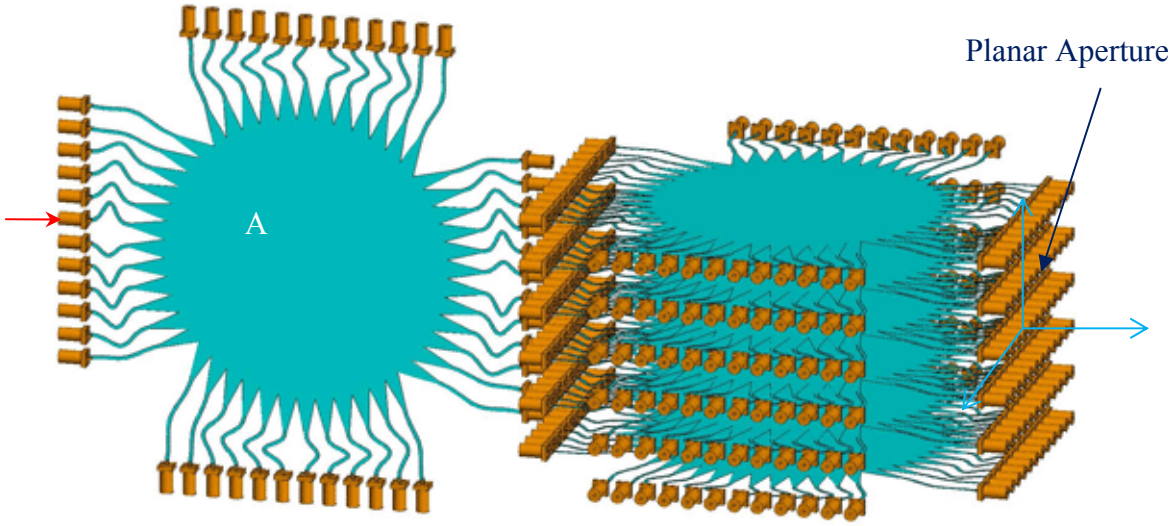

Figure 5- 35. Example of Pencil Beam Former

It is possible to design lens system that produce pencil beams capable of scanning the whole globular space. Because the 360-degree lens proposed in this paper allow fully reusing the facets. Four blocks of stacked square shape lenses organized in the sequence shown in Figure 5- 36 can produce the 3D coverage. Note the 4 blocks of stacked lenses are not necessarily attached to each other as shown in the figure. In practical design, they can be connected using transmission lines so that each of the unit can be deployed at different locations of the electronic systems.

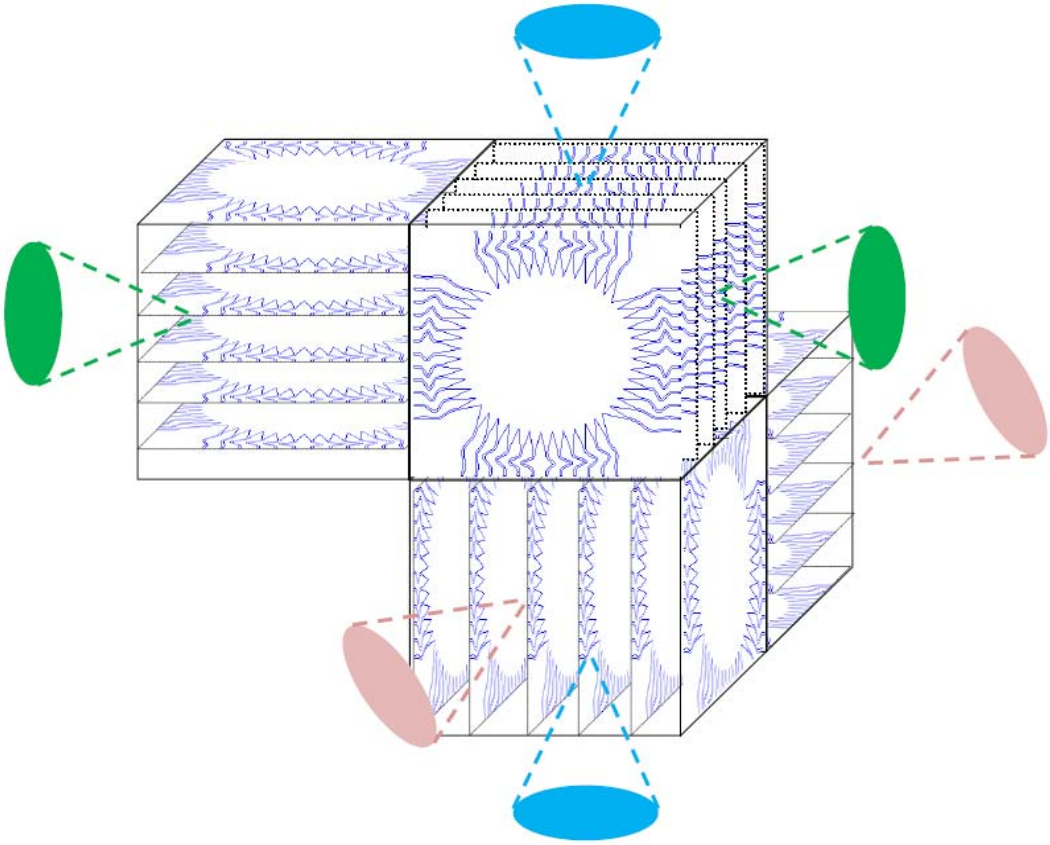

Figure 5- 36. Microwave Lens BFN for 3D Pencil Beam Scanning

CHAPTER 6. Conclusion and Future Works

6.1 Conclusions

Novel methods of optimizing the microwave lenses have been developed in this dissertation. The boundary of conventional design approaches have been modified from three aspects. Firstly, the conventional microwave lens design theories are limited by the path-length equations due to limited number of foci, the non-focal lens design concept proposed in this dissertation does not rely on such constraint. It has demonstrated that the minimum theoretical phase errors are still achievable by numerical optimizations even though the lens structure has zero theoretical focal point. Secondly, the classical bootlace lenses used to solely depend on the geometry optical theories that predict only the phase information, in this dissertation, to treat both phase and amplitude, a simulation algorithm based on ray tracing concept has been developed. Comparison with the commercial software and measurement show that this proposed method has computation speed of thousands of times faster than the full wave simulation, and it is capable of predicting far field beam patterns with amplitude error around 1 dB and beam angle error within 1 degree. Thirdly, the maximum scanning capability of the microwave lens has been greatly improved from the conventional 90 degrees to 360 degrees.

The concept of non-focal design is validated by comparing with the published results of the tri-focal and quadru-focal lenses in the literature. Because the existing models are based on geometry optical concepts with assumptions that physical lenses do not necessarily obey, different methods are conventionally compared in the theoretical domain. Thus, in Chapter 3, rigorous comparison procedures have been followed. The results of existing lenses are reproduced first, and then compared to the theoretical phase error of the proposed method. Comparison demonstrated that the non-focal lens has achieved the minimum phase errors for all beam ports, and the improvement can significantly reduce the side lobe level of a large aperture array. Besides, considering our primarily focus is to design printed microwave lenses that are light-weighted, low cost

and ease of fabrication, several extended design freedoms have been incorporated during the reformulation.

Two simulation models that are sufficient to predicting both phase and amplitude couplings have been investigated in this dissertation. The planer Green's function simulation was implemented by the commercial full-wave simulation software FEKO. Comparison with the measurement has graphically demonstrated its high accuracy in section 4.2.2. Another approach is developed based on the ray tracing concept. This method can model the tapering port, port to port couplings and transmission lines separately and have them integrated in a full ray tracing process. Both full-wave simulation and measurement data have been used to validate the design. Comparison result shows that the ray tracing method is relatively inferior to the full-wave simulation in terms of amplitude performance; however, it is thousands of times faster in terms of computation speed. In general, with the assamption of the isotropic array element, it is capable of predicting the far field pattern with average gain error about 1 dB, and scanning angle error less than 1 degree. The ray tracing algorithm is potentially suitable for large lens structure and iterative lens optimization.

The concepts of 360-degree microwave lens applies interleaved beam and receiving port to co-occupy the lens contour, and it relies on a non-focal microwave lens strategy to enforcing symmetry condition during the geometry formulation. In doing so, reasonable phase performance can still be achieved. The proposed concepts allow design multiple even-facet polygon lenses and circular shape lenses. Preliminary results of several lenses by geometry optical method have demonstrated good performance. A four-facet printed microwave lens for 360-degree scanning has been constructed, full-wave simulated, fabricated and tested. Both simulation and measurement have established validity of high level confidence.

6.2 Future Perspectives

Due to resource and time constraints, only limited topics have been covered in this dissertation. The ever evolving development of the microwave lens technology, together

with some of the discoveries in current study have resulted a few perspectives as future research topics.

6.2.1 Microwave Lens Optimizations Using Efficient Simulation Method

A few aspects of using full-wave simulation to optimize the microwave lens have been discussed in Section 4.1.3. Note the efficient simulation method such as the proposed ray tracing approach can be applied to the study as well. Because these algorithms can accurately predict the phase and amplitude information, the efficiency and array pattern can be estimated as well. As far as efficiency concerns, the simulation method can be adopted to design microwave lens functioning as power divider with maximum power efficiency. As far as array pattern concerns, it can be used to simulate the microwave lens that produces given amplitude tapering yielding desirable patterns such as zero side lobe.

Besides, due to the high computation speed of the fast ray tracing method, it can be adopted to simulate and optimize the extremely large size microwave lenses. For example, for the imaging system beam former, the beam port numbers might easily go hundreds. In a high resolution imaging microwave lens system, the reflection and mutual couplings within the cavity may exhibit more traceable patterns.

6.2.1 Microwave Lens Feeding Broadband Array Element

The microwave lenses are generally regarded as wideband devices. Preliminary investigation on the vehicular sensor using microwave lenses has adopted a patch antenna as the radiation elements in [51]. This is not the ideal choice. There are a few types of radiation elements are ideally suitable for microwave lenses, such as Vivaldi antenna, and spiral antennas. These two candidates can be chosen based on their polarization diversities and methods of implementation. Basically, the Vivaldi antenna can be implemented directly on the same material as the lens, which produces the end fire beams. The spiral antenna maximizes the bandwidth in the real communications systems, as the information can be transmitted and received in the two linearly polarized modes, orthogonal by 90-degree phase shift.

6.2.1 Three-Dimensional Microwave Lens Design

The 3-dimensional microwave lens is primarily used to produce pencil beams. In the literature, it is hardly seen that the performance of pencil beam formers is estimated by accurate simulation software. The methods described in this dissertation are possible to handle such large structure. It may be worthwhile investigating the three-dimensional beam-forming method using the ray tracing algorithms hybrid by the planar array theory.

The idea of using numerical methods to formulate lens structure has been seen in Chapter 1 and Chapter 5. The primary focus of this dissertation is the 2-dimentional lenses. There is possibility of extending it to 3 dimensions. In this case, each beam port is used to feed an undetermined planar receiving area. The optimization scheme might be established by correctly trading the geometry and the phase errors representations.

6.2.1 Microwave Lens Reformulation using Complex Medium

This dissertation only focuses on microwave lens designs for homogeneous medium. Several concepts such as the non-focal lens optimizations, ray tracing algorithms and the 360-degree scanning lenses are possibly migrated in the domain of complex medium based lenses. Especially, the advancement of complex medium such as the uniaxial medium, electrical band gap (EBG) material, artificial magnetic material, and ‘metamaterials’ have offered great space of exploration for the microwave lenses applications. The size, geometry, and performance might be greatly improved using hybrid medium concepts. Future works along this line seem quite fascinating.

APPENDICES

APPENDIX A: Basic EM and Antenna Equation Derivation

The purpose of this appendix is to serve the Chapter 1 of this dissertation that described some of the basic concepts in Electromagnetic field and waves. The EM theories govern the behavior of the antenna and array that intimately relates to the microwave lens design. Theories are reviewed in a way of answering questions relating to the dipole. In doing so, several fundamental terminologies such as Maxwell equations, time domain, frequency domain, wave equations, gauge and potentials, field from antenna, field and current, near field, far field, Fourier transform and far field approximation etc can be reasonably linked together via specific examples.

The first question is to derive field solutions for fundamental dipole from the time-domain Maxwell equations. The basic relation between field and current are studied first, and then specific example of elemental dipole is illustrated.

1. Field and Current Relation

Time-domain Maxwell equations:

$$\nabla \times \mathscr{E} = -\frac{\partial \mathscr{B}}{\partial t} \tag{A-1}$$

$$\nabla \times \mathscr{H} = \frac{\partial \mathscr{D}}{\partial t} + \mathscr{J} \tag{A-2}$$

Consecutive Relations:

$$\begin{aligned} \mathscr{D} &= \varepsilon \mathscr{E} \\ \mathscr{B} &= \mu \mathscr{H} \\ \mathscr{J} &= \sigma \mathscr{E} \end{aligned} \tag{A-3}$$

Time Domain & Frequency domain:

$$\begin{aligned} \mathscr{E} &= E\cos(\omega t + \phi_e) = E\,\mathrm{Re}[e^{j(\omega t+\phi_e)}] \\ \mathscr{B} &= B\cos(\omega t + \phi_h) = B\,\mathrm{Re}[e^{j(\omega t+\phi_h)}] \end{aligned} \tag{A-4}$$

$$\begin{aligned} \therefore \nabla \times \{E\,\mathrm{Re}[e^{j(\omega t+\phi_e)}]\} &= -\frac{\partial}{\partial t}\{B\,\mathrm{Re}[e^{j(\omega t+\phi_h)}]\} \\ \mathrm{Re}\{\nabla \times [Ee^{j(\omega t+\phi_e)}]\} &= -\mathrm{Re}\{\frac{\partial}{\partial t}[Be^{j(\omega t+\phi_h)}]\} \end{aligned} \tag{A-5}$$

$$\nabla \times [Ee^{j(\omega t+\phi_e)}] = -\frac{\partial}{\partial t}[Be^{j(\omega t+\phi_h)}]$$
$$\nabla \times [Ee^{j\phi_e}]e^{j(\omega t)} = -Bj\omega e^{j(\omega t)}e^{j\phi_h} \quad \text{(A-6)}$$
$$\nabla \times [Ee^{j\phi_e}] = -j\omega[Be^{j\phi_h}]$$

Suppose $Ee^{j\phi_e} \longleftrightarrow \overline{E} \qquad Be^{j\phi_h} \longleftrightarrow \overline{B}$

$$\nabla \times \overline{E} = -j\omega\overline{B} \quad \text{(A-7)}$$

Similarly, (A-4)~(A-6) applied to (A-2), it yields

$$\nabla \times \overline{H} = j\omega\overline{D} + \overline{J} \quad \text{(A-8)}$$

$$\overline{D} = \varepsilon\overline{E}$$
$$\overline{B} = \mu\overline{H} \quad \text{(A-9)}$$
$$\overline{J} = \sigma\overline{E}$$

Let us try to solve fields using:

$$\nabla \times \overline{E} = -j\omega\mu\overline{H} \quad \text{(A-10)}$$

$$\nabla \times \overline{H} = j\omega\varepsilon\overline{E} + \overline{J}_c + \overline{J}_i \quad \text{(A-11)}$$

Substitute $\overline{H} = \frac{1}{-j\omega\mu}\nabla \times \overline{E}$ into (A-11),

$$\frac{1}{-j\omega\mu}\nabla \times \nabla \times \overline{E} = j\omega\varepsilon\overline{E} + \overline{J}_c + \overline{J}_i \quad \text{(A-12)}$$

$$\because \nabla \times \nabla \times \overline{E} = \nabla(\nabla \cdot \overline{E}) - \nabla^2\overline{E}$$

$$\therefore \frac{1}{-j\omega\mu}[\nabla(\nabla \cdot \overline{E}) - \nabla^2\overline{E}] = j\omega\varepsilon\overline{E} + \overline{J}_c + \overline{J}_i \quad \text{(A-13)}$$

$$\nabla \cdot \overline{E} = \frac{1}{\varepsilon}(\nabla \cdot \overline{D}) = \frac{\rho_v}{\varepsilon} \quad \text{(A-14)}$$

Assume the field region of interest has no source, then

$$\nabla \cdot \overline{E} = 0 \quad \text{(A-15)}$$

(A-13) now becomes (A-16),

$$\frac{1}{j\omega\mu}\nabla^2\overline{E} = j\omega\varepsilon\overline{E} + \sigma\overline{E} + \overline{J}_i \quad \text{(A-16)}$$

$$\frac{1}{j\omega\mu}\nabla^2\overline{E} - (j\omega\varepsilon + \sigma)\overline{E} = \overline{J}_i \quad \text{(A-17)}$$

$$\nabla^2 \overline{E} + (\omega^2 \varepsilon\mu + j\omega\mu\sigma)\overline{E} = \overline{J}_i \tag{A-18}$$

Wave number is defined as:

$$\omega^2 \varepsilon\mu + j\omega\mu\sigma \Leftrightarrow k^2 \tag{A-19}$$

(A-13) and (A-19) applied to H field, similar result can be achieved:

$$\nabla \times \nabla \times \overline{H} = \nabla(\nabla \cdot \overline{H}) - \nabla^2 \overline{H}$$
$$\nabla \cdot \overline{H} = 0$$
$$\overline{E} = (\nabla \times \overline{H} - \overline{J}_i) / (j\omega\varepsilon + \sigma)$$
$$\nabla \times \nabla \times \overline{H} - \nabla \times \overline{J}_i = (\omega^2 \varepsilon\mu - j\omega\mu\sigma)\overline{H}$$
$$-\nabla^2 \overline{H} + (j\omega\mu\sigma - \omega^2 \varepsilon\mu)\overline{H} = \nabla \times \overline{J}_i$$
$$\nabla^2 \overline{H} + (\omega^2 \varepsilon\mu - j\omega\mu\sigma)\overline{H} = -\nabla \times \overline{J}_i$$

Hence, Maxwell reduced to the following wave functions for <u>*source-free condition*</u>:

$$\begin{aligned} &\nabla^2 \overline{E} + k^2 \overline{E} = 0 \\ &\nabla^2 \overline{H} + k^2 \overline{H} = 0 \end{aligned} \tag{A-20}$$

The solution for these equations is plane waves. Now we shall consider the case with source(s) in the domain of interest. This problem will be solved using the potential method. The problem equations are:

$$\nabla \times \overline{E} = -j\omega\mu\overline{H} \tag{A-21}$$

$$\nabla \times \overline{H} = j\omega\varepsilon\overline{E} + \overline{J} \tag{A-22}$$

Because $\nabla \cdot \overline{H} = 0$, we express H field in terms of magnetic potential $\overline{A}$:

$$\overline{H} = \nabla \times \overline{A} \tag{A-23}$$

$$\begin{aligned} &\therefore \nabla \times \overline{E} = -j\omega\mu\nabla \times \overline{A} \\ &\quad \nabla \times (\overline{E} + j\omega\mu\overline{A}) = 0 \end{aligned} \tag{A-24}$$

Assume $\overline{E} + j\omega\mu\overline{A} = \nabla\Phi$, Φ is a scale potential. Substitute $\overline{E} = \nabla\Phi - j\omega\mu\overline{A}$ into (A-22), we have

$$\nabla \times \nabla \times \overline{A} = j\omega\varepsilon(\nabla\Phi - j\omega\mu\overline{A}) + \overline{J} \tag{A-25}$$

Use vector identity of $\nabla \times \nabla \times \overline{A} = \nabla(\nabla \cdot \overline{A}) - \nabla^2 \overline{A}$,

$$\nabla(\nabla \cdot \overline{A}) - \nabla^2 \overline{A} = j\omega\varepsilon\nabla\Phi + \omega^2 \varepsilon\mu\overline{A} + \overline{J} \tag{A-26}$$

Lorentz gauge assumes

$$\nabla(\nabla\cdot\overline{A}) = j\omega\varepsilon\nabla\Phi \tag{A-27}$$

$$\therefore \nabla^2\overline{A} + k^2\overline{A} = -\overline{J} \tag{A-28}$$

Without proof, we give the solution of the potential with respect to current as

$$\overline{A} = \frac{1}{4\pi}\iiint_v \frac{\overline{J}(\overline{r}_0)e^{-jk|\overline{r}-\overline{r}_0|}}{|\overline{r}-\overline{r}_0|}dv_0 \tag{A-29}$$

From equation (A-27), we know

$$\nabla\Phi = \frac{\nabla(\nabla\cdot\overline{A})}{j\omega\varepsilon} \tag{A-29}$$

$$\therefore \overline{E} = -j\omega\mu\overline{A} + \frac{1}{j\omega\varepsilon}\nabla(\nabla\cdot\overline{A}) \tag{A-30}$$

To sum up, we have found the solution of the fields as:

$$\begin{cases} \overline{H} = \nabla\times\overline{A} \\ \overline{E} = -j\omega\mu\overline{A} + \dfrac{1}{j\omega\varepsilon}\nabla(\nabla\cdot\overline{A}) \end{cases} \tag{A-31}$$

2. The Elemental Dipole Solution

Now we setup an elemental dipole problem and apply the theory described above to solve its fields. The dipole is assumed to be along z axis and have a current in the form of (A-32).

$$\overline{J} = \hat{z}J_0\delta(x_0)\delta(y_0)\delta(z_0) \tag{A-32}$$

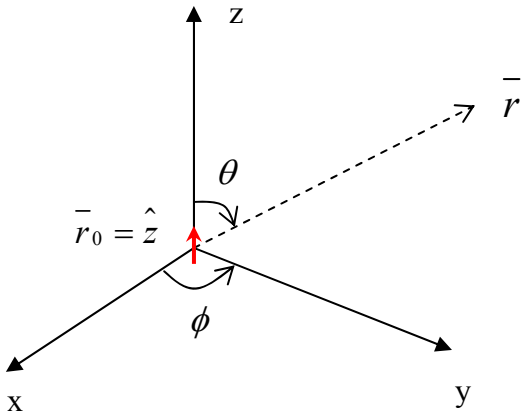

Figure A- 1. Elemental Dipole along z Axis

Use equation (A-29) to solve the potential

$$\begin{aligned}\overline{A}(\bar{r}) &= \frac{1}{4\pi}\iiint_v \frac{\overline{J}(\bar{r}_0)e^{-jk|\bar{r}-\bar{r}_0|}}{|\bar{r}-\bar{r}_0|}dv_0 \\ &= \frac{1}{4\pi}\iiint_v \frac{\hat{z}J_0\delta(x_0)\delta(y_0)\delta(z_0)e^{-jk|\bar{r}-\bar{r}_0|}}{|\bar{r}-\bar{r}_0|}dx_0dy_0dz_0 \\ &= \hat{z}\frac{J_0}{4\pi r}e^{-jkr}\end{aligned} \tag{A-33}$$

Since the field results are generally viewed in spherical coordinates, the $(\hat{x},\hat{y},\hat{z})$ is converted into $(\hat{r},\hat{\theta},\hat{\phi})$.

$$\begin{aligned}\hat{z} &= (\hat{z}\bullet\hat{r})\hat{r}+(\hat{z}\bullet\hat{\theta})\hat{\theta}+(\hat{z}\bullet\hat{\varphi})\hat{\varphi} \\ &= \cos\theta\hat{r}+\cos(\theta+90^\circ)\hat{\theta}+0 \\ &= \cos\theta\hat{r}-\sin\theta\hat{\theta}\end{aligned} \tag{A-34}$$

$$\begin{aligned}\overline{A}(\overline{r}) &= \overline{J_0}(\cos\theta\hat{r}-\sin\theta\hat{\theta})\frac{e^{-jkr}}{4\pi r} \\ &= \hat{r}J_0\cos\theta\frac{e^{-jkr}}{4\pi r}-\hat{\theta}J_0\sin\theta\frac{e^{-jkr}}{4\pi r}\end{aligned} \tag{A-35}$$

Thus,

$$\begin{aligned}H &= \nabla\times\overline{A}(\hat{\theta},\hat{r}) \\ &= \hat{\phi}\frac{1}{r}[\frac{\partial}{\partial r}(rA_\theta)-\frac{\partial A_r}{\partial\theta}] \\ &= \hat{\phi}\frac{1}{r}[\frac{\partial}{\partial r}(-J_0\sin\theta\frac{e^{-jkr}}{4\pi r})]+J_0\sin\theta\frac{e^{-jkr}}{4\pi r} \\ &= \hat{\phi}J_0\frac{e^{-jkr}}{4\pi r}(+jk+\frac{1}{r})\sin\theta\end{aligned} \tag{A-36}$$

According to (A-31), we need $\nabla(\nabla\cdot\overline{A})$ to accurately calculate the E field. Hence

$$\begin{aligned}\nabla\bullet\overline{A} &= \frac{1}{r^2}\frac{\partial}{\partial r}(r^2A_r)+\frac{1}{r\sin\theta}\frac{\partial}{\partial\theta}(A_\theta\sin\theta)+\frac{1}{r\sin\theta}\frac{\partial A_\phi}{\partial\phi} \\ &= \frac{1}{r^2}\frac{\partial}{\partial r}[J_0r\cos\theta\frac{e^{-jkr}}{4\pi}]+\frac{1}{r\sin\theta}\frac{\partial}{\partial\theta}[-J_0\sin^2\theta\frac{e^{-jkr}}{4\pi r}] \\ &= \frac{1}{r^2}\frac{J_0\cos\theta}{4\pi}[e^{-jkr}+r(-jk)e^{-jkr}]-\frac{1}{r\sin\theta}J_0\frac{e^{-jkr}}{4\pi r}2\sin\theta\cos\theta\end{aligned}$$

$$= J_0 \cos\theta \frac{e^{-jkr}}{4\pi r}[\frac{1}{r} - jk - \frac{2}{r}]$$
$$= J_0 \cos\theta \frac{e^{-jkr}}{4\pi r}[-jk - \frac{1}{r}] \quad \text{(A-37)}$$

$$\nabla(\nabla\bullet\overline{A}) = \hat{r}\frac{\partial(\nabla\bullet\overline{A})}{\partial r} + \hat{\theta}\frac{1}{r}\frac{\partial(\nabla\bullet\overline{A})}{\partial\theta} + \hat{\varphi}\frac{1}{r\sin\theta}\frac{\partial(\nabla\bullet\overline{A})}{\partial\varphi}$$
$$= \hat{r}J_0\cos\theta\frac{1}{4\pi}\frac{\partial}{\partial r}[-\frac{e^{-jkr}}{r^2} - \frac{jke^{-jkr}}{r}] - \hat{\theta}\frac{1}{r}J_0\sin\theta\frac{e^{-jkr}}{4\pi r}[-jk - \frac{1}{r}]$$
$$= \hat{r}J_0\cos\theta\frac{1}{4\pi}[\frac{2re^{-jkr} + jkr^2e^{-jkr}}{r^4} + \frac{jke^{-jkr} - rk^2e^{-jkr}}{r^2}] - \hat{\theta}\frac{1}{r}J_0\sin\theta\frac{e^{-jkr}}{4\pi r}[-jk - \frac{1}{r}]$$
$$= \hat{r}J_0\cos\theta\frac{1}{4\pi}[\frac{2e^{-jkr}}{r^3} + \frac{2jke^{-jkr}}{r^2} - \frac{k^2e^{-jkr}}{r}] - \hat{\theta}J_0\sin\theta\frac{e^{-jkr}}{4\pi r}[-\frac{jk}{r} - \frac{1}{r^2}]$$
$$= \hat{r}J_0\cos\theta\frac{e^{-jkr}}{4\pi r}(-k^2 + \frac{2jk}{r} + \frac{2}{r^2}) + \hat{\theta}J_0\sin\theta\frac{e^{-jkr}}{4\pi r}[\frac{jk}{r} + \frac{1}{r^2}] \quad \text{(A-38)}$$

Thus,

$$\overline{E} = -j\omega\mu\overline{A} + \frac{1}{j\omega\in}\nabla(\nabla\bullet\overline{A})$$
$$= -j\omega\mu\hat{r}J_0\cos\theta\frac{e^{-jkr}}{4\pi r} + \hat{\theta}j\omega\mu J_0\sin\theta\frac{e^{-jkr}}{4\pi r} + \hat{r}\frac{1}{j\omega\in}J_0\cos\theta\frac{e^{-jkr}}{4\pi r}(-k^2 + \frac{2jk}{r} + \frac{2}{r^2}) + \hat{\theta}\frac{1}{j\omega\in}J_0\sin\theta\frac{e^{-jkr}}{4\pi r}(\frac{jk}{r} + \frac{1}{r^2})$$
$$= \hat{r}J_0\cos\theta\frac{e^{-jkr}}{4\pi r}[-j\omega\mu - \frac{k^2}{j\omega\in} + \frac{2jk}{j\omega\in r} + \frac{2}{j\omega\in r^2}] + \hat{\theta}J_0\sin\theta\frac{e^{-jkr}}{4\pi r}[j\omega\mu + \frac{1}{j\omega\in}\frac{jk}{r} + \frac{1}{j\omega\in r^2}]$$
$$\downarrow \quad (Note: \sqrt{\frac{\mu}{\in}} = \eta, \quad -j\frac{k^2}{\omega\in} = -j\omega\mu, \quad \frac{\eta}{k} = \frac{1}{\omega\in})$$
$$= \hat{r}J_0\cos\theta\frac{e^{-jkr}}{4\pi r}[0 + \frac{2\eta}{r} + \frac{2}{j\omega\in r^2}\frac{1}{r^2}] + \hat{\theta}J_0\sin\theta\frac{e^{-jkr}}{4\pi r}[j\omega\mu + \frac{\eta}{r} + \frac{1}{j\omega\in r^2}\frac{1}{r^2}]$$
$$= \hat{r}\frac{2\eta J_0}{k}\cos\theta\frac{e^{-jkr}}{4\pi r}[\frac{k}{r} - \frac{j}{r^2}] + \hat{\theta}\frac{z}{k}J_0\sin\theta\frac{e^{-jkr}}{4\pi r}[jk^2 + \frac{k}{r} - \frac{j}{r^2}]$$
$$= \hat{r}j\frac{2\eta}{k}J_0\cos\theta\frac{e^{-jkr}}{4\pi r}(-\frac{jk}{r} - \frac{1}{r^2}) + \hat{\theta}j\frac{\eta}{k}J_0\sin\theta\frac{e^{-jkr}}{4\pi r}(k^2 - j\frac{k}{r} - \frac{1}{r^2})$$
$$= \hat{r}(-j)\frac{2\eta}{k}J_0\cos\theta\frac{e^{-jkr}}{4\pi r}(\frac{jk}{r} + \frac{1}{r^2}) + \hat{\theta}(-j)\frac{\eta}{k}J_0\sin\theta\frac{e^{-jkr}}{4\pi r}(-k^2 + j\frac{k}{r} + \frac{1}{r^2}) \quad \text{(A-39)}$$

It is found that both magnetic and electrical fields have high order fields respect to radial direction. This indicates that the high order terms dies down much faster than the lower ones. These field components are generally regarded as near fields. At the far fields of $r \gg r_0$, the fields become into

$$\overline{H}_{farfield} = \hat{\phi} jkJ_0 \frac{e^{-jkr}}{4\pi r} \sin\theta \tag{A-40}$$

$$\overline{E}_{farfield} = \hat{\phi} j\eta kJ_0 \frac{e^{-jkr}}{4\pi r} \sin\theta \tag{A-41}$$

We happen to find that the far fields of the E and H satisfy the right hand rule, and they are different from a factor of wave impedance.

We have seen that solving the divergence and gradient of the potential is not easy. In reality, when the problem domain has complex structures, it becomes nearly impossible to find the exact solution. Previous scholars have found a way to approach only the far field of the radiation element. This method is very valuable for antenna designs. Here we will review the basis of far field approximation and setup a question for regular dipole antenna.

1. Far Field Approximation

We start with substituting the assumption of $r \gg r_0$ into equation (A-29) and see if an approximate expression can be found. The first term we shall work on is

$$\begin{aligned} \left|\bar{r} - \bar{r_0}\right| &= \sqrt{(x-x_0)^2 + (y-y_0)^2 + (z-z_0)^2} \\ &= \sqrt{x^2 + y^2 + z^2 - 2xx_0 - 2yy_0 - 2zz_0 + {x_0}^2 + {y_0}^2 + {z_0}^2} \\ &= \sqrt{r^2 - 2(xx_0 + yy_0 + zz_0) + {r_0}^2} \\ &= r\sqrt{1 - \frac{2(xx_0 + yy_0 + zz_0)}{r^2} + (\frac{r_0}{r})^2} \end{aligned} \tag{A-42}$$

Express this result in spherical coordinate using (A-43) to get (A-44).

$$\begin{aligned} x &= r\sin\theta\cos\varphi \\ y &= r\sin\theta\sin\varphi \\ z &= r\cos\theta \end{aligned} \tag{A-43}$$

$$\left|\bar{r} - \bar{r_0}\right| = r\sqrt{1 - \frac{2}{r}(x_0\sin\theta\cos\varphi + y_0\sin\theta\sin\varphi + z_0\cos\theta) + (\frac{r_0}{r})^2} \tag{A-44}$$

Note:
$$\bar{r_0} = x_0\hat{x} + y_0\hat{y} + z_0\hat{z}$$
$$\hat{r} = \hat{r}\sin\theta\sin\varphi + \hat{\theta}\sin\theta\sin\varphi + \hat{\varphi}\cos\theta$$

$$\therefore x_0 \sin\theta\sin\varphi + y_0 \sin\theta\sin\varphi + z_0\cos\theta = \bar{r_0}\cdot\hat{r}$$

(A-44) is written as

$$\begin{aligned}\left|\bar{r}-\bar{r_0}\right| &= r\sqrt{1-\frac{2}{r}(\vec{r_0}\bullet\hat{r})+(\frac{r_0}{r})^2} \\ &= r\sqrt{1-2(\frac{r_0}{r})(\hat{r_0}\bullet\hat{r})+(\frac{r_0}{r})^2}\end{aligned} \tag{A-45}$$

Use binomial expansion

$$\begin{aligned}(1-\alpha)^{\frac{1}{2}} &= 1-\binom{\frac{1}{2}}{1}\alpha+\binom{\frac{1}{2}}{2}\alpha^2-... \\ &= 1-\frac{1}{2}\alpha+\frac{1}{2}(-\frac{1}{2})(\frac{1}{2})\alpha^2-... \\ &= 1-\frac{1}{2}\alpha-\frac{1}{8}\alpha^2-...\end{aligned} \tag{4-46}$$

Consider $\alpha = 2(\frac{r_0}{r})(\hat{r_0}\bullet\hat{r})-(\frac{r_0}{r})^2$, then

$$\begin{aligned}\left|\bar{r}-\bar{r_0}\right| &= r\{1-\frac{1}{2}[2(\frac{r_0}{r})(\hat{r_0}\bullet\hat{r})-(\frac{r_0}{r})^2]-\frac{1}{8}[2(\frac{r_0}{r})(\hat{r_0}\bullet\hat{r})-(\frac{r_0}{r})^2]^2\} \\ &= r\{1-(\frac{r_0}{r})(\hat{r_0}\bullet\hat{r})+\frac{1}{2}(\frac{r_0}{r})^2-\frac{1}{8}[4(\frac{r_0}{r})^2(\hat{r_0}\bullet\hat{r})^2-4(\frac{r_0}{r})^3(\hat{r_0}\bullet\hat{r})+(\frac{r_0}{r})^4]\} \\ &= r\{1-(\frac{r_0}{r})(\hat{r_0}\bullet\hat{r})+\frac{1}{2}(\frac{r_0}{r})^2[1-(\hat{r_0}\bullet\hat{r})^2]+o(\frac{r_0}{r})^3\}\end{aligned} \tag{4-47}$$

Assume $|\theta-\theta_0|=\psi_0$, then $\hat{r_0}\cdot\hat{r}=\cos\psi_0$. When $\frac{r_0}{r}\ll 1$,

$$\left|\bar{r}-\bar{r_0}\right| = r\{1-\frac{r_0}{r}\cos\varphi_0+\frac{1}{2}(\frac{r_0}{r})^2\sin^2\varphi_0+o(\frac{r_0}{r})^3\} \tag{4-48}$$

Hence,

$$\frac{e^{-jk\left|\bar{r}-\bar{r_0}\right|}}{\left|\bar{r}-\bar{r_0}\right|} = \frac{e^{-jk[r-r_0\cos\varphi_0+\frac{r_0^2}{2r}\sin^2\psi_0+o(\frac{r_0^3}{r^2})}}{r-r_0\cos\varphi_0+\frac{r_0^2}{2r}\sin^2\varphi_0+o(\frac{r_0^3}{r^2})} \tag{4-49}$$

At the far field, we can ignore the $o(\frac{1}{r^2})$ term, thus

$$\frac{e^{-jk\left|\bar{r}-\bar{r_0}\right|}}{4\pi\left|\bar{r}-\bar{r_0}\right|}\approx\frac{e^{-jkr}}{4\pi r}e^{jkr_0\cos\varphi_0-jkr_0^2\sin^2\varphi_0/2r} \tag{4-50}$$

Experimental results show that when the observation distance satisfies $r > D_{\max}{}^2/\lambda$, then the phase term of $(\frac{r_0^2}{r})$ can be ignored. Hence the typical far field approximation is written as

$$\frac{e^{-jk\left|\bar{r}-\bar{r_0}\right|}}{4\pi\left|\bar{r}-\bar{r_0}\right|}\approx\frac{e^{-jkr}}{4\pi r}e^{jkr_0\cos\varphi_0} \tag{4-51}$$

Now use (4-51) to solve the potential and fields

$$\begin{aligned}\bar{A}&=\int_s\bar{J}(\bar{r_0})\frac{e^{-jk\left|\bar{r}-\bar{r_0}\right|}}{4\pi\left|\bar{r}-\bar{r_0}\right|}dv_0\\&=\int_s\bar{J}(\bar{r_0})\frac{e^{-jkr}}{4\pi r}e^{j\bar{k}\bullet\bar{r_0}}dv_0\\&=\frac{e^{-jkr}}{4\pi r}\int_s\bar{J}(\bar{r_0})e^{j\bar{k}\bullet\bar{r_0}}dv_0\end{aligned} \tag{4-52}$$

$$\begin{aligned}\overline{H_F}&=\nabla\times\bar{A}\\&=\hat{k}\times\bar{A}\\&=\hat{r}\times\bar{A}\\&=\hat{\theta}[\frac{1}{r\sin\theta}\frac{\partial A_r}{\partial\varphi}-\frac{\partial A_\varphi}{\partial r}-\frac{A_\varphi}{r}]+\hat{\varphi}[\frac{\partial A_\theta}{\partial r}-\frac{1}{r}\frac{\partial A_r}{\partial\theta}+\frac{A_\theta}{r}]\end{aligned} \tag{4-53}$$

Note (4-52) shows A has the same direction as current and is only function of r, which make the operation on A much easier to solve.

$$\begin{aligned}\overline{H_F}&=\hat{\theta}[-\frac{\partial A_\varphi}{\partial r}-\frac{A_\varphi}{r}]+\hat{\varphi}[\frac{\partial A_\theta}{\partial r}+\frac{A_\theta}{r}]\\&=\hat{\theta}[-\frac{-jke^{-jkr}\bullet r-e^{-jkr}}{4\pi r^2}]\int_s\overline{J_\varphi}(\bar{r_0})e^{j\bar{k}\bullet\bar{r_0}}dv_0-\frac{e^{-jkr}}{4\pi r^2}\int\overline{J_\varphi}(\bar{r_0})e^{j\bar{k}\bullet\bar{r_0}}dv_0\\&\quad+\hat{\varphi}[\frac{-jke^{-jkr}\bullet r-e^{-jkr}}{4\pi r^2}\int\overline{J_\theta}(\bar{r_0})e^{j\bar{k}\bullet\bar{r_0}}dv_0+\frac{e^{-jkr}}{4\pi r^2}\int\overline{J_\theta}(\bar{r_0})e^{j\bar{k}\bullet\bar{r_0}}dv_0\\&=\hat{\theta}[\frac{jkre^{-jkr}}{4\pi r^2}\int_s\overline{J_\varphi}(\bar{r_0})e^{j\bar{k}\bullet\bar{r_0}}dv_0]+\hat{\varphi}[\frac{-jkre^{-jkr}}{4\pi r^2}\int\overline{J_\theta}(\bar{r_0})e^{j\bar{k}\bullet\bar{r_0}}dv_0]\\&=\frac{jke^{-jkr}}{4\pi r}\int_s(\overline{J_\theta}-\overline{J_\varphi})e^{j\bar{k}\bullet\bar{r_0}}dv_0\end{aligned}$$

$$
\begin{aligned}
&= \frac{jke^{-jkr}}{4\pi r}\int_s \overline{J}_{\perp(r)}(\overline{r_0})e^{j\overline{k}\cdot\overline{r_0}}dv_0 \\
&= -\frac{jke^{-jkr}}{4\pi r}\int_s \hat{r}\times\overline{J}(\overline{r_0})e^{j\overline{k}\cdot\overline{r_0}}dv_0
\end{aligned}
\tag{4-54}
$$

Note:
$$\hat{r}\times[\widehat{J_r}+\widehat{J_\theta}+\widehat{J_\varphi}] = 0+\widehat{J_\varphi}-\widehat{J_\theta}$$
$$\hat{r}\times\hat{r}\times\overline{J} = \hat{r}\times[\widehat{J_\varphi}-\widehat{J_\theta}] = -\widehat{J_\theta}-\widehat{J_\varphi} = \widehat{J_r}-\widehat{J}$$

$$
\begin{aligned}
\overline{E_F} &= (-\hat{k})\times\overline{H_F}\cdot\eta \\
&= -\eta\frac{e^{-jkr}}{4\pi r}\int_s \hat{k}\times\hat{k}\times\overline{J}(\overline{r_0})e^{j\overline{k}\cdot\overline{r_0}}dv_0 \\
&= jk\eta\frac{e^{-jkr}}{4\pi r}\int[(\overline{J}\cdot\hat{k})\hat{k}-\overline{J}]e^{j\overline{k}\cdot\overline{r_0}}dv_0
\end{aligned}
\tag{4-55}
$$

The relationship between the far field and current (in the normal direction) is very similar to the Fourier Transform, but in k-r domain, as shown in (4-56).

$$\widetilde{\overline{J_\perp}}(\overline{k}) = \iiint \overline{J_\perp}(r_0)e^{j\overline{k}\cdot\overline{r_0}}dx_0dy_0dz_0 \tag{4-56}$$

To sum up, it is found that the far field of the real radiation element can be solved by

$$\overline{H}_f = -jk\frac{e^{-jkr}}{4\pi r}\iiint_{r_0}[\hat{k}\times\overline{J}(\overline{r}_0)]e^{j\overline{k}\cdot\overline{r}_0}dv_0 \tag{4-57}$$

$$\overline{E}_f = -jk\eta\frac{e^{-jkr}}{4\pi r}\iiint_{r_0}[(\hat{k}\cdot\overline{J}_0)\hat{k}-\overline{J}(\overline{r}_0)]e^{j\overline{k}\cdot\overline{r}_0}dv_0 \tag{4-58}$$

2. Far Fields of Dipole

Suppose a dipole of length L is along z axis (Figure A- 2), and it has a uniform current distribution of (4-59). The following is to solve the far fields by relationship given in (4-57)~(4-58).

$$\overline{J}(\overline{r_0}) = \begin{cases}\hat{z}J_0\delta(x_0)\delta(y_0) & |z|\le L/2 \\ 0 & |z|> L/2\end{cases} \tag{4-59}$$

$$\hat{k} = \hat{x}\sin\theta\cos\varphi+\hat{y}\sin\theta\sin\varphi+\hat{z}\cos\theta$$
$$\overline{r_0} = x_0\hat{x}+y_0\hat{y}+z_0\hat{z}$$
$$\therefore \overline{k}\cdot\overline{r_0} = k\cos\theta z_0 \tag{4-60}$$

In the spherical coordinate, solving the $\hat{k}\times\overline{J}(\overline{r_0})$ seems a little more complex than $\hat{k}\cdot\overline{J}(\overline{r_0})$. Probably that is why people tend to solve the E field first and use the right hand rule to solve the H field.

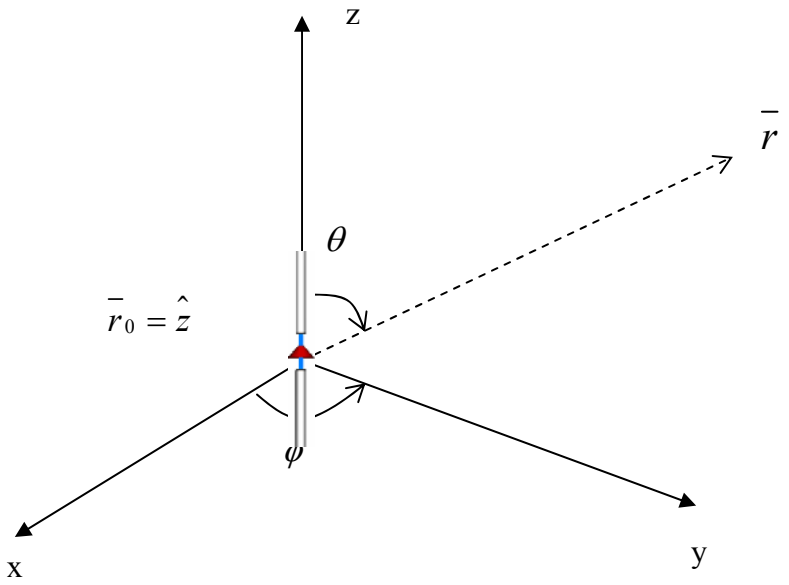

Figure A- 2. Regular Dipole along z Axis

$$\hat{k}\cdot\overline{J}_0 = \cos\theta J_0\delta(x_0)\delta(y_0) \tag{4-61}$$

$$\begin{aligned}(\hat{k}\cdot\overline{J}_0)\hat{k}-\overline{J}_0 &= \hat{k}\cos\theta J_0\delta(x_0)\delta(y_0)-\hat{z}J_0\delta(x_0)\delta(y_0)\\ &= J_0\delta(x_0)\delta(y_0)(\hat{k}\cos\theta-\hat{z})\end{aligned} \tag{4-62}$$

$$\begin{aligned}\overline{E_F} &= jk\eta\frac{e^{-jkr}}{4\pi r}\int[(\overline{J}\cdot\hat{k})\hat{k}-\overline{J}]e^{j\overline{k}\cdot\overline{r_0}}dv_0\\ &= jk\eta\frac{e^{-jkr}}{4\pi r}\iiint_{x_0y_0z_0} J_0\delta(x_0)\delta(y_0)(\hat{k}\cos\theta-\hat{z})e^{jk\cos\theta z_0}dx_0dy_0dz_0\\ &= jk\eta\frac{e^{-jkr}}{4\pi r}\int_{z_0} J_0(\hat{k}\cos\theta-\hat{z})e^{jk\cos\theta z_0}dz_0\\ &= jk\eta\frac{e^{-jkr}}{4\pi r}J_0(\hat{k}\cos\theta-\hat{z})\int_{z_0} e^{jk\cos\theta z_0}dz_0\\ &= jk\eta\frac{e^{-jkr}}{4\pi r}J_0(\hat{k}\cos\theta-\hat{z})\frac{1}{jk\cos\theta}e^{jk\cos\theta z_0}\Big|_{-L/2}^{L/2}\end{aligned} \tag{4-63}$$

Convert coordinate from $(\hat{x},\hat{y},\hat{z})$ to $(\hat{r},\hat{\theta},\hat{\phi})$, using

$$\begin{aligned}\hat{z} &= (\hat{z}\cdot\hat{r})\hat{r}+(\hat{z}\cdot\hat{\theta})\hat{\theta}+(\hat{z}\cdot\hat{\varphi})\hat{\varphi} \\ &= \hat{r}\cos\theta-\hat{\theta}\sin\theta\end{aligned} \tag{4-64}$$

$$\begin{aligned}\overline{E_f} &= jk\eta\frac{e^{-jkr}}{4\pi r}J_0(\cos\theta\hat{r}-\cos\theta\hat{r}+\sin\theta\hat{\theta})\frac{1}{jk\cos\theta}(e^{jk\cos\theta\frac{L}{2}}-e^{-jk\cos\theta\frac{L}{2}}) \\ &= jk\eta J_0\frac{e^{-jkr}}{4\pi r}\sin\theta\hat{\theta}\frac{1}{jk\cos\theta}[\cos(k\cos\theta\frac{L}{2})-j\sin((k\cos\theta\frac{L}{2})-\cos(k\cos\theta\frac{L}{2})-j\sin(k\cos\theta\frac{L}{2}) \\ &= \hat{\theta}jk\eta J_0\frac{e^{-jkr}}{4\pi r}\sin\theta\frac{2\sin(k\cos\theta\frac{L}{2})}{k\cos\theta} \\ &= \hat{\theta}jk\eta J_0L\frac{e^{-jkr}}{4\pi r}\frac{\sin(k\cos\theta\frac{L}{2})}{k\cos\theta L/2}\sin\theta\end{aligned} \tag{4-65}$$

$$\overline{H_f} = \frac{\hat{r}\times\overline{E_f}}{\eta} = -\hat{\varphi}jkJ_0L\frac{e^{-jkr}}{4\pi r}\frac{\sin(k\cos\theta L/2)}{k\cos\theta L/2}\sin\theta$$

APPENDIX B: Program Codes for Phase Error GA Optimization

This appendix lists some of the source codes on phase error reduction using the Genetic Algorithms. The example demonstrated below is to use GA to minimum the average total phase errors for all beam port excitations. The functions are described in Table A- 1.

Table A- 1. Program Source Codes for Microwave Lens GA Optimization

Function Name	Description
GAquadru.m	Main function that performs Microwave Lens GA optimization. The maximum number of iteration, mutation rate, crossover, and selection parameters are all configurations in this function.
Focdim.m	Lens contour initialization. Using basic lens design parameter to create the initial beam and receiving contours. This function can be related by other types of Rotman Lens design equations.
fitness.m	This is fitness function for the Genetic Algorithms. In this example, the average absolute phase errors for all beam ports excitations are considered as the objective function.
CRTRP.m	Create real-valued initial population. Refer to Genetic Algorithms Toolbox for Matlab User Guide by University Sheffield.
RANKING.m	Generalized rank-based fitness assignment. Refer to Genetic Algorithms Toolbox for Matlab User Guide by University Sheffield.
SELECT.m	High-level selection routine. Refer to Genetic Algorithms Toolbox for Matlab User Guide by University Sheffield.
RECOMBIN.m	High-level recombination operator. Refer to Genetic Algorithms Toolbox for Matlab User Guide by University Sheffield.
MUTBGA,m	Real-value mutation. Refer to Genetic Algorithms Toolbox for Matlab User Guide by University Sheffield.
REINS.m	Uniform random and fitness-based reinsertion. Refer to Genetic Algorithms Toolbox for Matlab User Guide by University Sheffield.

1.
```
function GAquadru(r,n,d,alpha,beta,phim,Num,CtrN)

tic;
NIND=200;
MAXGEN=200;
MAXCYC=1;
GGAP=0.6;
trace=ones(MAXCYC,MAXGEN);
[Ze,Zr,Xr,L,Ne,Theta0,F,U]=focdim(r,n,d,alpha,beta,phim,Num);
p=0.25/100;
for counter=1:MAXCYC,
    Zerfield=[[Ze,Zr]*(1+p);[Ze,Zr]*(1-p)];
    e=1;
    chrom=CRTRP(NIND,Zerfield);
ObjV=fitness(chrom,Xr,L,F,Theta0,U,1);
```

```
    for gen=1:MAXGEN,
        FitnV=RANKING(ObjV);
SelCh=SELECT('sus',chrom,FitnV,GGAP);
SelCh=RECOMBIN('recdis',SelCh,0.5);
Selch=MUTBGA(SelCh,Zerfield,[0.50 1
[ObjVsel]=fitness(Selch,Xr,L,F,Theta0,U,1);
[chrom ObjV]=REINS(chrom,Selch,1,1,ObjV,ObjVsel);
[e,v]=min(ObjV);
        trace(counter,gen)=e;
        if e<0.1*10^-4;
            break;
        end
    end
    Ze=chrom(v,1:Ne);
    Zr=chrom(v,Ne+1:end);
    store(counter,:)=(chrom(v,:));
    end

[v1,v2]=min(min(trace,[],2));
Ze=store(v2,1:Ne);
Zr=store(v2,Ne+1:end);

if CtrN==1,
    fitness(store(v2,:),Xr,L,F,Theta0,U,2);
else if CtrN==2,
        Theta=Theta0*pi/180;
        Xe=-Ze.*tan(Theta);
        plot([fliplr(Ze(2:end)),Ze],[-fliplr(Xe(2:end)),Xe]);
        hold on; plot([0,fliplr(Zr(2:end)),Zr,0],[-n*d,-
n*d:d:n*d,n*d],'lineWidth',1.5);
        axis([-2*n*d-2*d,0,-n*d*4/3,n*d*4/3]);
        figure; fitness(store(v2,:),Xr,L,F,Theta0,U,2);
    end
toc
end
```

2.
```
function [Ze,Zr,Xr,L,Ne,Theta0,F,U]=focdim(r,n,d,alpha,beta,phim,Num)
alpha=alpha*pi/180;beta=beta*pi/180;
phimax=phim*pi/180;
Ne=phim+1;
D=2*d*n; F=r*D;
Theta0=linspace(0,phim,Ne);
Theta=linspace(0,phimax,Ne);
U=(0:n)*d;
V=0;
Zr0=-U.^2*(cos(alpha)+cos(beta))/(2*F);
T=(1+1./(F^2-U.^2).*(V^2-
(U.^2)*cos(alpha)*cos(beta)+(U.^4)*((cos(alpha)+cos(beta))/2/F)^2)).^.5;
Xr=U.*T;
L=F*(1-T);
Zr=Zr0;
Yr=V;
Ze=-F*cos(Theta);
end
```

3.
```
function ObjV=fitness(chrom,Xr,L,F,Theta0,U,CtrN)

Theta=Theta0*pi/180;
pop=size(chrom);
Ne=length(Theta0);
n=length(Xr)-1;
ObjV=zeros(pop(1),1);
Ye=0*Theta;
Yr=0;
  for t=1:pop(1),
      Ze=chrom(t,1:Ne);
      Zr=chrom(t,Ne+1:end);
      Xe=-Ze.*tan(Theta);
      F0=(Xe.^2+Ze.^2).^.5;
      for i=1:Ne,
        Fi=((Xr-Xe(i)).^2+(Yr-Ye(i)).^2+(Zr-Ze(i)).^2).^.5;
        Fi2=((Xr+Xe(i)).^2+(Yr+Ye(i)).^2+(Zr-Ze(i)).^2).^.5;
        Phase=U*sin(Theta(i));
        Erri(1:n+1)=fliplr(Fi2+L-Phase-F0(i))/F;
        Erri(n+1:2*n+1)=(Fi+L+Phase-F0(i))/F;
        Errmax0(i)=max(abs(Erri));
      end
      if CtrN==2,
          plot(Theta0,Errmax0);
      end
      ObjV(t)=sum(Errmax0(1:25))/Ne;
  end
```

APPENDIX C: Program Codes for Producing Microwave Lens Geometry

Table A- 2. Program Codes for Producing Microwave Lens Geometry

Function Name	Description
`MainLens.m`	Main function that produce the GUI above in Matlab. Basic Rotman lens geometry with triangular shape tapers can be automatically generated. Dimension of the transmission lines will be given as well. Basic array factor analysis is included as well.
`strucLens.m`	By using the initial design parameters to produce the lens geometry as well as the port profile matrix.
`RotmBRW.m`	Produce lens contour info and transmission line lengths for given design parameters.

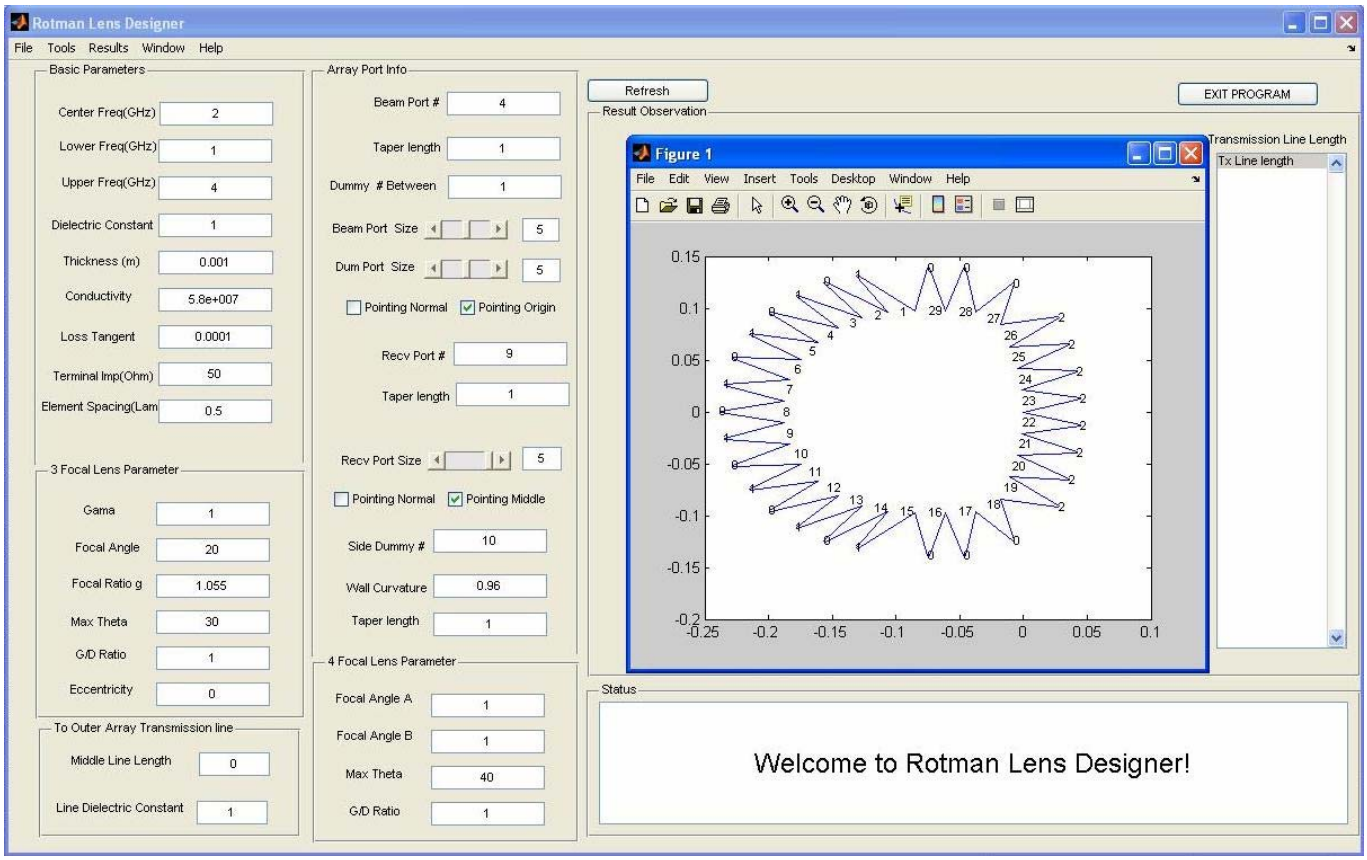

Figure A- 3. Rotman Lens Designer Graphical User Interface

```
1. function varargout = MainLens(varargin)
gui_Singleton = 1;
gui_State = struct('gui_Name',       mfilename, ...
                   'gui_Singleton',  gui_Singleton, ...
                   'gui_OpeningFcn', @MainLens_OpeningFcn, ...
                   'gui_OutputFcn',  @MainLens_OutputFcn, ...
                   'gui_LayoutFcn',  [] , ...
                   'gui_Callback',   []);
if nargin && ischar(varargin{1})
    gui_State.gui_Callback = str2func(varargin{1});
end

if nargout
    [varargout{1:nargout}] = gui_mainfcn(gui_State, varargin{:});
else
    gui_mainfcn(gui_State, varargin{:});
end
function MainLens_OpeningFcn(hObject, eventdata, handles, varargin)
handles.output  = hObject;
handles.CenterF = 2;
set(handles.Center_Freq,'String',handles.CenterF);
handles.LoF     = 1;     set(handles.Lower_Freq,'String',handles.LoF);
handles.UpF     = 4;     set(handles.Upper_Freq,'String',handles.UpF);
handles.Eps     = 1;     set(handles.Epso,'String',handles.Eps);
handles.thick   = 0.001; set(handles.Dthick,'String',handles.thick);
handles.Condu   = 5.8e7; set(handles.Conduc,'String',handles.Condu);
handles.Lstang  = 0.0001;set(handles.Lstan,'String',handles.Lstang);
handles.TrmImp  = 50;    set(handles.TermImp,'String',handles.TrmImp);
handles.Dspace  = .5;    set(handles.Dspacing,'String',handles.Dspace);
handles.LenGama  = 1;     set(handles.LensGama,'String',handles.LenGama);
handles.FocalAlph= 20;
set(handles.FocalAlpha,'String',handles.FocalAlph);
handles.g3foc    = 1.055;set(handles.g3focal,'String',handles.g3foc);
handles.MaxThet   = 30;    set(handles.MaxTheta,'String',handles.MaxThet);
handles.r3Len    = 1;    set(handles.r3Lens,'String',handles.r3Len);
handles.eCentr   = 0;    set(handles.eCentri,'String',handles.eCentr);
handles.MidLineLengt=0;
set(handles.MidLineLength,'String',handles.MidLineLengt);
handles.TxEpss      =1;  set(handles.TxEps,'String',handles.TxEpss);
handles.Nbeams   = 4;    set(handles.Nbeam,'String',handles.Nbeams);
handles.LBtapers = 1;     set(handles.LBtaper,'String',handles.LBtapers);
handles.Ndums    = 1;    set(handles.Ndum,'String',handles.Ndums);
handles.BeamSiz  = 5;
set(handles.BeamSize,'String',handles.BeamSiz);set(handles.BeamSizeSlid
er,'Value',handles.BeamSiz);
handles.DumSiz   = 5;
set(handles.DumSize,'String',handles.DumSiz);set(handles.DumSizeSlider,
'Value',handles.DumSiz);
handles.BeamNormals = 0;
set(handles.BeamNormal,'Value',0);set(handles.BeamOrigin,'Value',1);
handles.RcvNormals  = 0;
set(handles.RcvNormal,'Value',0);set(handles.RcvMid,'Value',1);
handles.Nrcvs    = 9;    set(handles.Nrcv,'String',handles.Nrcvs);
handles.LRtapers = 1;     set(handles.LRtaper,'String',handles.LRtapers);
```

```
handles.RrcvSiz  = 5;
set(handles.RrcvSize,'String',handles.RrcvSiz);set(handles.RrcvSizeSlid
er,'Value',handles.RrcvSiz);
handles.Nsides   = 10;   set(handles.Nside,'String',handles.Nsides);
handles.tCurvatur= 0.96;
set(handles.tCurvature,'String',handles.tCurvatur);
handles.LDtapers = 1;     set(handles.LDtaper,'String',handles.LDtapers);
handles.Focal4Alph= 1;
set(handles.Focal4Alpha,'String',handles.Focal4Alph);
handles.Focal4Bet = 1;
set(handles.Focal4Beta,'String',handles.Focal4Bet);
handles.Max4Thet  = 40;
set(handles.Max4Theta,'String',handles.Max4Thet);
handles.r4Len     = 1;   set(handles.r4Lens,'String',handles.r4Len);
handles.TransmDif='Tx Line length';
set(handles.TransmDiff,'String',handles.TransmDif);
handles.Lamda=0.3/handles.CenterF;handles.WidthTrans=micstripW(handles.
Eps,handles.thick,handles.TrmImp);
handles.Pinfo=0;
handles.Xite=0;
handles.Wtrans=0;
setappdata(0,'hMainLens',gcf);
hMainLens=getappdata(0,'hMainLens');
setappdata(hMainLens,'Dspace',handles.Dspace);
setappdata(hMainLens,'CenterF',handles.CenterF);
setappdata(hMainLens,'Wtrans',handles.Wtrans);
setappdata(hMainLens,'WidthTrans',handles.WidthTrans);
setappdata(hMainLens,'tCurvatur',handles.tCurvatur);
setappdata(hMainLens,'LBtapers',handles.LBtapers);
setappdata(hMainLens,'LDtapers',handles.LDtapers);
setappdata(hMainLens,'LRtapers',handles.LRtapers);
setappdata(hMainLens,'BeamSiz',handles.BeamSiz);
setappdata(hMainLens,'DumSiz',handles.DumSiz);
setappdata(hMainLens,'RrcvSiz',handles.RrcvSiz);
setappdata(hMainLens,'eCentr',handles.eCentr);
setappdata(hMainLens,'LenGama',handles.LenGama);
setappdata(hMainLens,'FocalAlph',handles.FocalAlph);
setappdata(hMainLens,'g3foc',handles.g3foc);
setappdata(hMainLens,'MaxThet',handles.MaxThet);
setappdata(hMainLens,'r3Len',handles.r3Len);
setappdata(hMainLens,'Nbeams',handles.Nbeams);
setappdata(hMainLens,'Ndums',handles.Ndums);
setappdata(hMainLens,'Nsides',handles.Nsides);
setappdata(hMainLens,'Nrcvs',handles.Nrcvs);
setappdata(hMainLens,'BeamNormals',handles.BeamNormals);
setappdata(hMainLens,'RcvNormals',handles.RcvNormals);

setappdata(hMainLens,'Status','Welcome to Rotman Lens Designer!');
set(handles.Status,'String',getappdata(hMainLens,'Status'),'FontSize',1
8.0);

[handles.Pinfo,handles.Xite,handles.Wtrans]=strucLens0(handles.Dspace,h
andles.CenterF,handles.WidthTrans,handles.tCurvatur,handles.LBtapers,ha
ndles.LDtapers,handles.LRtapers,handles.BeamSiz,handles.DumSiz,handles.
RrcvSiz,handles.eCentr,handles.LenGama,handles.FocalAlph,handles.g3foc,
```

```
handles.MaxThet,handles.r3Len,handles.Nbeams,handles.Ndums,handles.Nsid
es,handles.Nrcvs,handles.BeamNormals,handles.RcvNormals);

setappdata(hMainLens,'WidthTrans',handles.WidthTrans);
setappdata(hMainLens,'Lamda',handles.Lamda);
setappdata(hMainLens,'Pinfo',handles.Pinfo);
setappdata(hMainLens,'Xite',handles.Xite);
setappdata(hMainLens,'Wtrans',handles.Wtrans);
setappdata(hMainLens,'NN',1);
setappdata(hMainLens,'SCcontrl',1);
setappdata(hMainLens,'TrmImp',handles.TrmImp);
setappdata(hMainLens,'Eps',handles.Eps);
setappdata(hMainLens,'thick',handles.thick);
setappdata(hMainLens,'Lstang',handles.Lstang);
setappdata(hMainLens,'SCFreq',handles.CenterF);
setappdata(hMainLens,'fhSCoupling',@SCoupling);
setappdata(hMainLens,'fhS2Coupling',@S2Coupling);
setappdata(hMainLens,'NN2',1);
setappdata(hMainLens,'MM2',1);
setappdata(hMainLens,'LowFreq2',handles.LoF);
setappdata(hMainLens,'HighFreq2',handles.UpF);
setappdata(hMainLens,'Nfre2',100);
setappdata(hMainLens,'CtrlRefe',1);
setappdata(hMainLens,'CtrlRefe2',1);
guidata(hObject, handles);

function varargout = MainLens_OutputFcn(hObject, eventdata, handles)
varargout{1} = handles.output;

function r4Lens_Callback(hObject, eventdata, handles)
handles.r4Len=str2double(get(handles.r4Lens,'String'));
set(handles.r4Lens,'String',handles.r4Len);
hMainLens=getappdata(0,'hMainLens');
setappdata(hMainLens,'r4len',handles.r4Len);
guidata(hObject, handles);

function r4Lens_CreateFcn(hObject, eventdata, handles)
if ispc && isequal(get(hObject,'BackgroundColor'),
get(0,'defaultUicontrolBackgroundColor'))
    set(hObject,'BackgroundColor','white');
end

function Upper_Freq_Callback(hObject, eventdata, handles)
handles.UpF=str2double(get(handles.Upper_Freq,'String'));
set(handles.Upper_Freq,'String',handles.UpF);
hMainLens=getappdata(0,'hMainLens');
setappdata(hMainLens,'UpF',handles.UpF);
guidata(hObject, handles);

function Upper_Freq_CreateFcn(hObject, eventdata, handles)
if ispc && isequal(get(hObject,'BackgroundColor'),
get(0,'defaultUicontrolBackgroundColor'))
    set(hObject,'BackgroundColor','white');
end
```

```
function Nbeam_Callback(hObject, eventdata, handles)
handles.Nbeams=str2double(get(handles.Nbeam,'String'));
set(handles.Nbeam,'String',handles.Nbeams);
hMainLens=getappdata(0,'hMainLens');
setappdata(hMainLens,'Nbeams',handles.Nbeams);
guidata(hObject, handles);

function Nbeam_CreateFcn(hObject, eventdata, handles)
if ispc && isequal(get(hObject,'BackgroundColor'),
get(0,'defaultUicontrolBackgroundColor'))
    set(hObject,'BackgroundColor','white');
end

function LensGama_Callback(hObject, eventdata, handles)
handles.LenGama=str2double(get(handles.LensGama,'String'));
set(handles.LensGama,'String',handles.LenGama);
hMainLens=getappdata(0,'hMainLens');
setappdata(hMainLens,'LenGama',handles.LenGama);
guidata(hObject, handles);

function LensGama_CreateFcn(hObject, eventdata, handles)

if ispc && isequal(get(hObject,'BackgroundColor'),
get(0,'defaultUicontrolBackgroundColor'))
    set(hObject,'BackgroundColor','white');
end

function g3focal_Callback(hObject, eventdata, handles)

handles.g3foc=str2double(get(handles.g3focal,'String'));
set(handles.g3focal,'String',handles.g3foc);
hMainLens=getappdata(0,'hMainLens');
setappdata(hMainLens,'g3foc',handles.g3foc);
guidata(hObject, handles);

function g3focal_CreateFcn(hObject, eventdata, handles)
if ispc && isequal(get(hObject,'BackgroundColor'),
get(0,'defaultUicontrolBackgroundColor'))
    set(hObject,'BackgroundColor','white');
end

function MaxTheta_Callback(hObject, eventdata, handles)
handles.MaxThet=str2double(get(handles.MaxTheta,'String'));
set(handles.MaxTheta,'String',handles.MaxThet);
hMainLens=getappdata(0,'hMainLens');
setappdata(hMainLens,'MaxThet',handles.MaxThet);
guidata(hObject, handles);

function MaxTheta_CreateFcn(hObject, eventdata, handles)
if ispc && isequal(get(hObject,'BackgroundColor'),
get(0,'defaultUicontrolBackgroundColor'))
    set(hObject,'BackgroundColor','white');
end

function Conduc_Callback(hObject, eventdata, handles)
```

```
handles.Condu = str2double(get(handles.Conduc,'String'));
set(handles.Conduc,'String',handles.Condu);
hMainLens=getappdata(0,'hMainLens');
setappdata(hMainLens,'Condu',handles.Condu);
guidata(hObject, handles);

function Conduc_CreateFcn(hObject, eventdata, handles)
if ispc && isequal(get(hObject,'BackgroundColor'),
get(0,'defaultUicontrolBackgroundColor'))
    set(hObject,'BackgroundColor','white');
end

function Epso_Callback(hObject, eventdata, handles)
handles.Eps = str2double(get(handles.Epso,'String'));
set(handles.Epso,'String',handles.Eps);
hMainLens=getappdata(0,'hMainLens');
setappdata(hMainLens,'Eps',handles.Eps);
guidata(hObject, handles);

function Epso_CreateFcn(hObject, eventdata, handles)
if ispc && isequal(get(hObject,'BackgroundColor'),
get(0,'defaultUicontrolBackgroundColor'))
    set(hObject,'BackgroundColor','white');
end

function Dthick_Callback(hObject, eventdata, handles)
handles.thick = str2double(get(handles.Dthick,'String'));
set(handles.Dthick,'String',handles.thick);
hMainLens=getappdata(0,'hMainLens');
setappdata(hMainLens,'thick',handles.thick);
guidata(hObject, handles);

function Dthick_CreateFcn(hObject, eventdata, handles)
if ispc && isequal(get(hObject,'BackgroundColor'),
get(0,'defaultUicontrolBackgroundColor'))
    set(hObject,'BackgroundColor','white');
end

function Nside_Callback(hObject, eventdata, handles)
handles.Nsides = str2double(get(handles.Nside,'String'));
set(handles.Nside,'String',handles.Nsides);
hMainLens=getappdata(0,'hMainLens');
setappdata(hMainLens,'Nsides',handles.Nsides);
guidata(hObject, handles);

function Nside_CreateFcn(hObject, eventdata, handles)
if ispc && isequal(get(hObject,'BackgroundColor'),
get(0,'defaultUicontrolBackgroundColor'))
    set(hObject,'BackgroundColor','white');
end

function tCurvature_Callback(hObject, eventdata, handles)
handles.tCurvatur = str2double(get(handles.tCurvature,'String'));
set(handles.tCurvature,'String',handles.tCurvatur);
hMainLens=getappdata(0,'hMainLens');
```

```
setappdata(hMainLens,'tCurvatur',handles.tCurvatur);
guidata(hObject, handles);

function tCurvature_CreateFcn(hObject, eventdata, handles)

if ispc && isequal(get(hObject,'BackgroundColor'),
get(0,'defaultUicontrolBackgroundColor'))
    set(hObject,'BackgroundColor','white');
end

function r3Lens_Callback(hObject, eventdata, handles)
handles.r3Len = str2double(get(handles.r3Lens,'String'));
set(handles.r3Lens,'String',handles.r3Len);
hMainLens=getappdata(0,'hMainLens');
setappdata(hMainLens,'r3Len',handles.r3Len);
guidata(hObject, handles);

function r3Lens_CreateFcn(hObject, eventdata, handles)
if ispc && isequal(get(hObject,'BackgroundColor'),
get(0,'defaultUicontrolBackgroundColor'))
    set(hObject,'BackgroundColor','white');
end

function Nrcv_Callback(hObject, eventdata, handles)
handles.Nrcvs = str2double(get(handles.Nrcv,'String'));
set(handles.Nrcv,'String',handles.Nrcvs);
hMainLens=getappdata(0,'hMainLens');
setappdata(hMainLens,'Nrcvs',handles.Nrcvs);
guidata(hObject, handles);

function Nrcv_CreateFcn(hObject, eventdata, handles)
if ispc && isequal(get(hObject,'BackgroundColor'),
get(0,'defaultUicontrolBackgroundColor'))
    set(hObject,'BackgroundColor','white');
end

function Center_Freq_Callback(hObject, eventdata, handles)
handles.CenterF = str2double(get(handles.Center_Freq,'String'));
set(handles.Center_Freq,'String',handles.CenterF);

hMainLens=getappdata(0,'hMainLens');
setappdata(hMainLens,'CenterF',handles.CenterF);
handles.WidthTrans=micstripW(handles.Eps,handles.thick,handles.TrmImp);
hMainLens=getappdata(0,'hMainLens');
setappdata(hMainLens,'WidthTrans',handles.WidthTrans);
guidata(hObject, handles);

function Lower_Freq_Callback(hObject, eventdata, handles)
handles.LoF = str2double(get(handles.Lower_Freq,'String'));
set(handles.Lower_Freq,'String',handles.LoF);
hMainLens=getappdata(0,'hMainLens');
setappdata(hMainLens,'LoF',handles.LoF);
guidata(hObject, handles);

function FSave_Callback(hObject, eventdata, handles)
```

```
[filename, pathname]=uiputfile;
save(filename,'-struct','handles');
guidata(hObject, handles);

function ToolSpara_Callback(hObject, eventdata, handles)

MenuSpara

function [Snew]=SCoupling
hMainLens =getappdata(0,'hMainLens');
Wtrans    =getappdata(hMainLens,'Wtrans');
SCFreq    =getappdata(hMainLens,'SCFreq');
CtrlRefe  =getappdata(hMainLens,'CtrlRefe');

NN      = getappdata(hMainLens,'NN');
TrmImp  = getappdata(hMainLens,'TrmImp');
Eps     = getappdata(hMainLens,'Eps');
thick   = getappdata(hMainLens,'thick');
Lstang  = getappdata(hMainLens,'Lstang');
SCcontrl= getappdata(hMainLens,'SCcontrl');
Pinfo   = getappdata(hMainLens,'Pinfo');
Xite    = getappdata(hMainLens,'Xite');

[Snew]=Menu_Coupling(NN,Wtrans,TrmImp,Eps,thick,Lstang,SCFreq,Pinfo,Xit
e,SCcontrl,CtrlRefe);

function S2Coupling
hMainLens = getappdata(0,'hMainLens');
Wtrans    = getappdata(hMainLens,'Wtrans');
TrmImp   = getappdata(hMainLens,'TrmImp');
Eps      = getappdata(hMainLens,'Eps');
thick    = getappdata(hMainLens,'thick');
Lstang   = getappdata(hMainLens,'Lstang');
SCcontrl2= getappdata(hMainLens,'SCcontrl2');
Pinfo    = getappdata(hMainLens,'Pinfo');
Xite     = getappdata(hMainLens,'Xite');
NN2      = getappdata(hMainLens,'NN2');
MM2      = getappdata(hMainLens,'MM2');
LowFreq2 = getappdata(hMainLens,'LowFreq2');
HighFreq2= getappdata(hMainLens,'HighFreq2');
Nfre2    = getappdata(hMainLens,'Nfre2');
CtrlRefe2= getappdata(hMainLens,'CtrlRefe2');
Menu_Coupling2(NN2,MM2,Wtrans,LowFreq2,HighFreq2,Nfre2,TrmImp,Eps,thick
,Lstang,Pinfo,Xite,SCcontrl2,CtrlRefe2);

function FocalAlpha_Callback(hObject, eventdata, handles)
handles.FocalAlph = str2double(get(handles.FocalAlpha,'String'));
set(handles.FocalAlpha,'String',handles.FocalAlph);
hMainLens=getappdata(0,'hMainLens');
setappdata(hMainLens,'FocalAlph',handles.FocalAlph);
guidata(hObject, handles);

function FocalAlpha_CreateFcn(hObject, eventdata, handles)
```

```
if ispc && isequal(get(hObject,'BackgroundColor'),
get(0,'defaultUicontrolBackgroundColor'))
    set(hObject,'BackgroundColor','white');
end

function Focal4Beta_Callback(hObject, eventdata, handles)
handles.Focal4Bet = str2double(get(handles.Focal4Beta,'String'));
set(handles.Focal4Beta,'String',handles.Focal4Bet);
hMainLens=getappdata(0,'hMainLens');
setappdata(hMainLens,'Focal4Bet',handles.Focal4Bet);
guidata(hObject, handles);

function Focal4Beta_CreateFcn(hObject, eventdata, handles)
if ispc && isequal(get(hObject,'BackgroundColor'),
get(0,'defaultUicontrolBackgroundColor'))
    set(hObject,'BackgroundColor','white');
end

function Max4Theta_Callback(hObject, eventdata, handles)
handles.Max4Thet = str2double(get(handles.Max4Theta,'String'));
set(handles.Max4Theta,'String',handles.Max4Thet);
hMainLens=getappdata(0,'hMainLens');
setappdata(hMainLens,'Max4Thet',handles.Max4Thet);
guidata(hObject, handles);

function Max4Theta_CreateFcn(hObject, eventdata, handles)
if ispc && isequal(get(hObject,'BackgroundColor'),
get(0,'defaultUicontrolBackgroundColor'))
    set(hObject,'BackgroundColor','white');
end

function eCentri_Callback(hObject, eventdata, handles)
handles.eCentr = str2double(get(handles.eCentri,'String'));
set(handles.eCentri,'String',handles.eCentr);
hMainLens=getappdata(0,'hMainLens');
setappdata(hMainLens,'eCentr',handles.eCentr);
guidata(hObject, handles);

function eCentri_CreateFcn(hObject, eventdata, handles)
if ispc && isequal(get(hObject,'BackgroundColor'),
get(0,'defaultUicontrolBackgroundColor'))
    set(hObject,'BackgroundColor','white');
end

function BeamNormal_Callback(hObject, eventdata, handles)
if (get(handles.BeamNormal,'Value') == get(handles.BeamNormal,'Max')),
    set(handles.BeamOrigin,'Value',0);
    handles.BeamNormals=1;
else
    set(handles.BeamOrigin,'Value',1);
    handles.BeamNormals=0;
end
hMainLens=getappdata(0,'hMainLens');
setappdata(hMainLens,'BeamNormals',handles.BeamNormals);
guidata(hObject, handles);
```

```
function BeamOrigin_Callback(hObject, eventdata, handles)

if (get(handles.BeamOrigin,'Value') == get(handles.BeamOrigin,'Max')),
    set(handles.BeamNormal,'Value',0);
    handles.BeamNormals=0;
else
    set(handles.BeamNormal,'Value',1);
    handles.BeamNormals=1;
end
hMainLens=getappdata(0,'hMainLens');
setappdata(hMainLens,'BeamNormals',handles.BeamNormals);
guidata(hObject, handles);

function RcvNormal_Callback(hObject, eventdata, handles)
if (get(handles.RcvNormal,'Value') == get(handles.RcvNormal,'Max')),
    set(handles.RcvMid,'Value',0);
    handles.RcvNormals=0;
else
    set(handles.RcvMid,'Value',1);
    handles.RcvNormals=1;
end
hMainLens=getappdata(0,'hMainLens');
setappdata(hMainLens,'RcvNormals',handles.RcvNormals);
guidata(hObject, handles);

function RcvMid_Callback(hObject, eventdata, handles)
if (get(handles.RcvMid,'Value') == get(handles.RcvMid,'Max')),
    set(handles.RcvNormal,'Value',0);
    handles.RcvNormals=1;
else
    set(handles.RcvNormal,'Value',1);
    handles.RcvNormals=1;
end
hMainLens=getappdata(0,'hMainLens');
setappdata(hMainLens,'RcvNormals',handles.RcvNormals);
guidata(hObject, handles);

function LRtaper_Callback(hObject, eventdata, handles)
handles.LRtapers = str2double(get(handles.LRtaper,'String'));
set(handles.LRtaper,'String',handles.LRtapers);

hMainLens=getappdata(0,'hMainLens');
setappdata(hMainLens,'LRtapers',handles.LRtapers);
guidata(hObject, handles);

function LRtaper_CreateFcn(hObject, eventdata, handles)
if ispc && isequal(get(hObject,'BackgroundColor'),
get(0,'defaultUicontrolBackgroundColor'))
    set(hObject,'BackgroundColor','white');
end

function Ndum_Callback(hObject, eventdata, handles)
handles.Ndums = str2double(get(handles.Ndum,'String'));
set(handles.Ndum,'String',handles.Ndums);
hMainLens=getappdata(0,'hMainLens');
```

```
setappdata(hMainLens,'Ndums',handles.Ndums);
guidata(hObject, handles);

function Ndum_CreateFcn(hObject, eventdata, handles)
if ispc && isequal(get(hObject,'BackgroundColor'),
get(0,'defaultUicontrolBackgroundColor'))
    set(hObject,'BackgroundColor','white');
end

function BeamSize_Callback(hObject, eventdata, handles)
handles.BeamSiz = round(str2double(get(handles.BeamSize,'String')));
handles.DumSiz  = round(str2double(get(handles.DumSize,'String')));
set(handles.BeamSize,'String',handles.BeamSiz);
set(handles.BeamSizeSlider,'Value',handles.BeamSiz);
if handles.BeamSiz+handles.DumSiz>10,
    handles.DumSiz=10-handles.BeamSiz;
    set(handles.DumSize,'String',handles.DumSiz);
    set(handles.DumSizeSlider,'Value',handles.DumSiz);
end
hMainLens=getappdata(0,'hMainLens');
setappdata(hMainLens,'BeamSiz',handles.BeamSiz);
setappdata(hMainLens,'DumSiz',handles.DumSiz);
guidata(hObject, handles);

function BeamSize_CreateFcn(hObject, eventdata, handles)
if ispc && isequal(get(hObject,'BackgroundColor'),
get(0,'defaultUicontrolBackgroundColor'))
    set(hObject,'BackgroundColor','white');
end

function BeamSizeSlider_Callback(hObject, eventdata, handles)
handles.BeamSiz = round(get(handles.BeamSizeSlider,'Value'));
handles.DumSiz  = round(str2double(get(handles.DumSize,'String')));
set(handles.BeamSize,'String',handles.BeamSiz);
if handles.BeamSiz+handles.DumSiz>10,
    handles.DumSiz=10-handles.BeamSiz;
    set(handles.DumSize,'String',handles.DumSiz);
    set(handles.DumSizeSlider,'Value',handles.DumSiz);
end
hMainLens=getappdata(0,'hMainLens');
setappdata(hMainLens,'BeamSiz',handles.BeamSiz);
setappdata(hMainLens,'DumSiz',handles.DumSiz);

function BeamSizeSlider_CreateFcn(hObject, eventdata, handles)

if isequal(get(hObject,'BackgroundColor'),
get(0,'defaultUicontrolBackgroundColor'))
    set(hObject,'BackgroundColor',[.9 .9 .9]);
end

function RrcvSize_Callback(hObject, eventdata, handles)
handles.RrcvSiz = round(str2double(get(handles.RrcvSize,'String')));
set(handles.RrcvSize,'String',handles.RrcvSiz);
set(handles.RrcvSizeSlider,'Value',handles.RrcvSiz);
hMainLens=getappdata(0,'hMainLens');
setappdata(hMainLens,'RrcvSiz',handles.RrcvSiz);
```

```
guidata(hObject, handles);

function RrcvSizeSlider_Callback(hObject, eventdata, handles)
handles.RrcvSiz = round(get(handles.RrcvSizeSlider,'Value'));
set(handles.RrcvSize,'String',handles.RrcvSiz);
hMainLens=getappdata(0,'hMainLens');
setappdata(hMainLens,'RrcvSiz',handles.RrcvSiz);
guidata(hObject, handles);

function RrcvSize_CreateFcn(hObject, eventdata, handles)
if ispc && isequal(get(hObject,'BackgroundColor'),
get(0,'defaultUicontrolBackgroundColor'))
    set(hObject,'BackgroundColor','white');
end

function Lstan_Callback(hObject, eventdata, handles)
handles.Lstang = str2double(get(handles.Lstan,'String'));
set(handles.Lstan,'String',handles.Lstang);
hMainLens=getappdata(0,'hMainLens');
setappdata(hMainLens,'Lstang',handles.Lstang);
guidata(hObject, handles);

function Lstan_CreateFcn(hObject, eventdata, handles)
if ispc && isequal(get(hObject,'BackgroundColor'),
get(0,'defaultUicontrolBackgroundColor'))
    set(hObject,'BackgroundColor','white');
end

function TermImp_Callback(hObject, eventdata, handles)
handles.TrmImp = str2double(get(handles.TermImp,'String'));
set(handles.TermImp,'String',handles.TrmImp);
hMainLens=getappdata(0,'hMainLens');
setappdata(hMainLens,'TrmImp',handles.TrmImp);
guidata(hObject, handles);

function Dspacing_Callback(hObject, eventdata, handles)
handles.Dspace = str2double(get(handles.Dspacing,'String'));
set(handles.Dspacing,'String',handles.Dspace);
hMainLens=getappdata(0,'hMainLens');
setappdata(hMainLens,'Dspace',handles.Dspace);
guidata(hObject, handles);

function LBtaper_Callback(hObject, eventdata, handles)
handles.LBtapers = str2double(get(handles.LBtaper,'String'));
set(handles.LBtaper,'String',handles.LBtapers);
hMainLens=getappdata(0,'hMainLens');
setappdata(hMainLens,'LBtapers',handles.LBtapers);
guidata(hObject, handles);

function Focal4Alpha_Callback(hObject, eventdata, handles)
handles.Focal4Alph = str2double(get(handles.Focal4Alpha,'String'));
set(handles.Focal4Alpha,'String',handles.Focal4Alph);
hMainLens=getappdata(0,'hMainLens');
setappdata(hMainLens,'Focal4Alph',handles.Focal4Alph);
guidata(hObject, handles);
```

```
function DumSize_Callback(hObject, eventdata, handles)
handles.DumSiz = round(str2double(get(handles.DumSize,'String')));
handles.BeamSiz= round(str2double(get(handles.BeamSize,'String')));
set(handles.DumSize,'String',handles.DumSiz);
set(handles.DumSizeSlider,'Value',handles.DumSiz);
if handles.BeamSiz+handles.DumSiz>10,
    handles.BeamSiz=10-handles.DumSiz;
    set(handles.BeamSize,'String',handles.BeamSiz);
    set(handles.BeamSizeSlider,'Value',handles.BeamSiz);
end
hMainLens=getappdata(0,'hMainLens');
setappdata(hMainLens,'DumSiz',handles.DumSiz);
setappdata(hMainLens,'BeamSiz',handles.BeamSiz);
guidata(hObject, handles);

function DumSize_CreateFcn(hObject, eventdata, handles)
if ispc && isequal(get(hObject,'BackgroundColor'),
get(0,'defaultUicontrolBackgroundColor'))
    set(hObject,'BackgroundColor','white');
end

function DumSizeSlider_Callback(hObject, eventdata, handles)
handles.DumSiz = round(get(handles.DumSizeSlider,'Value'));
handles.BeamSiz= round(str2double(get(handles.BeamSize,'String')));
set(handles.DumSize,'String',handles.DumSiz);
if handles.DumSiz+handles.BeamSiz>10,
    handles.BeamSiz=10-handles.DumSiz;
    set(handles.BeamSize,'String',handles.BeamSiz);
    set(handles.BeamSizeSlider,'Value',handles.BeamSiz);
end
hMainLens=getappdata(0,'hMainLens');
setappdata(hMainLens,'DumSiz',handles.DumSiz);
setappdata(hMainLens,'BeamSiz',handles.BeamSiz);
guidata(hObject, handles);

function DumSizeSlider_CreateFcn(hObject, eventdata, handles)
if isequal(get(hObject,'BackgroundColor'),
get(0,'defaultUicontrolBackgroundColor'))
    set(hObject,'BackgroundColor',[.9 .9 .9]);
end

function RefreshButton_Callback(hObject, eventdata, handles)
handles.WidthTrans=micstripW(handles.Eps,handles.thick,handles.TrmImp);
hMainLens=getappdata(0,'hMainLens');
setappdata(hMainLens,'WidthTrans',handles.WidthTrans);
off;
hMainLens=getappdata(0,'hMainLens');
Dspace=getappdata(hMainLens,'Dspace');
CenterF=getappdata(hMainLens,'CenterF');
 WidthTrans=getappdata(hMainLens,'WidthTrans');
tCurvatur=getappdata(hMainLens,'tCurvatur');
LBtapers=getappdata(hMainLens,'LBtapers');
LDtapers=getappdata(hMainLens,'LDtapers');
LRtapers=getappdata(hMainLens,'LRtapers');
BeamSiz=getappdata(hMainLens,'BeamSiz');
```

```
DumSiz=getappdata(hMainLens,'DumSiz');
RrcvSiz=getappdata(hMainLens,'RrcvSiz');
eCentr=getappdata(hMainLens,'eCentr');
LenGama=getappdata(hMainLens,'LenGama');
FocalAlph=getappdata(hMainLens,'FocalAlph');
g3foc=getappdata(hMainLens,'g3foc');
MaxThet=getappdata(hMainLens,'MaxThet');
r3Len=getappdata(hMainLens,'r3Len');
Nbeams=getappdata(hMainLens,'Nbeams');
Ndums=getappdata(hMainLens,'Ndums');
Nsides=getappdata(hMainLens,'Nsides');
Nrcvs=getappdata(hMainLens,'Nrcvs');
BeamNormals=getappdata(hMainLens,'BeamNormals');
RcvNormals=getappdata(hMainLens,'RcvNormals');

[handles.Pinfo,handles.Xite,handles.Wtrans]=strucLens(Dspace,CenterF,Wi
dthTrans,tCurvatur,LBtapers,LDtapers,LRtapers,BeamSiz,DumSiz,RrcvSiz,eC
entr,LenGama,FocalAlph,g3foc,MaxThet,r3Len,Nbeams,Ndums,Nsides,Nrcvs,Be
amNormals,RcvNormals);
setappdata(hMainLens,'Pinfo',handles.Pinfo);
setappdata(hMainLens,'Xite',handles.Xite);

axis equal;
handles.TransmDif=handles.MidLineLengt+handles.Wtrans;
set(handles.TransmDiff,'String',handles.TransmDif);
setappdata(hMainLens,'Wtrans',handles.TransmDif);
setappdata(hMainLens,'Status','Please click Refresh button after you
update the lens parameters.');
set(handles.Status,'String',getappdata(hMainLens,'Status'),'FontSize',1
5.0);
guidata(hObject, handles);

function LDtaper_Callback(hObject, eventdata, handles)
handles.LDtapers = str2double(get(handles.LDtaper,'String'));
set(handles.LDtaper,'String',handles.LDtapers);

hMainLens=getappdata(0,'hMainLens');
setappdata(hMainLens,'LDtapers',handles.LDtapers);

guidata(hObject, handles);

function LDtaper_CreateFcn(hObject, eventdata, handles)
if ispc && isequal(get(hObject,'BackgroundColor'),
get(0,'defaultUicontrolBackgroundColor'))
    set(hObject,'BackgroundColor','white');
end

function TransmDiff_Callback(hObject, eventdata, handles)
hMainLens=getappdata(0,'hMainLens');
setappdata(hMainLens,'TransmDiffs',handles.TransmDiffs);

function TransmDiff_CreateFcn(hObject, eventdata, handles)
if ispc && isequal(get(hObject,'BackgroundColor'),
get(0,'defaultUicontrolBackgroundColor'))
    set(hObject,'BackgroundColor','white');
```

```
end

function MidLineLength_Callback(hObject, eventdata, handles)
handles.MidLineLengt = str2double(get(handles.MidLineLength,'String'));
set(handles.MidLineLength,'String',handles.MidLineLengt);

hMainLens=getappdata(0,'hMainLens');
setappdata(hMainLens,'MidLineLengt',handles.MidLineLengt);
guidata(hObject, handles);

function MidLineLength_CreateFcn(hObject, eventdata, handles)
if ispc && isequal(get(hObject,'BackgroundColor'),
get(0,'defaultUicontrolBackgroundColor'))
    set(hObject,'BackgroundColor','white');
end

function TxEps_Callback(hObject, eventdata, handles)
handles.TxEpss = str2double(get(handles.TxEps,'String'));
set(handles.TxEps,'String',handles.TxEpss);
hMainLens=getappdata(0,'hMainLens');
setappdata(hMainLens,'TxEpss',handles.TxEpss);
guidata(hObject, handles);

function TxEps_CreateFcn(hObject, eventdata, handles)
if ispc && isequal(get(hObject,'BackgroundColor'),
get(0,'defaultUicontrolBackgroundColor'))
    set(hObject,'BackgroundColor','white');
end
```

2. function

```
[Pinfo,Xite,Wtrans]=strucLens(Dspacing,CenterF,WidthTrans,SidCurvature,
LB,LD,LR,Nbh,Ndh,Nrh,e,gama,ap,g,phim,r,Nbeam,Ndum,Nside,Nrcv,CtrN1,Ctr
N2)
Lamda=0.3/CenterF;
Np=Nbeam*(Ndum+1);
Nr=10*Nrcv;
w=WidthTrans;
W=ones(1,Np)*w;
L=ones(1,Np)*LB*Lamda;
for i=1:Ndum+1:Np, L(i+1:i+Ndum)=LD*Lamda; end;
Ne=Nbeam*(Ndum+1)*10
[xb,yb,xr,yr,Wtran]=RotmBRW(eps,e,gama,r,Nr,ap,g,phim,Ne);
F1=(Nrcv-1)*0.6*r/CenterF*Dspacing;
xb=F1*xb;yb=F1*yb;xr=xr*F1;yr=yr*F1;Wtran=Wtran*F1;
index=(1:Nrcv)*10-9;
Wtrans=Wtran(index);
Wtrans=[fliplr(Wtrans),Wtrans(2:end)];
yb(1)=10e-10;yr(1)=10e-9;

K=zeros(1,Np);
for j=1:Np,
    if CtrN1==0,
        K(j)=yb(10*j-9)/xb(10*j-9);
    else if CtrN1==1,
            K(j)=-(xb(10*j-8)-xb(10*j-9))/(yb(10*j-8)-yb(10*j-9));
```

```
        end
    end
end
Edge=zeros(2,2*Np);
for j=1:Np,
    Pout=PCarmcal([xb(10*j-9),yb(10*j-9),K(j),L(j),W(j),0,xb(1)/2,0]);
    Edge(1,(2*j-1):(2*j))=Pout(1:2);
    Edge(2,(2*j-1):(2*j))=Pout(3:4);
end
T=[1];
for j=1:Nbeam,
    T=[T,zeros(1,Ndum),1];
end
trace_edge=zeros(2,2*Np-1);
for j=1:Np,
    if j==1,
        Joint(:,1)=Edge(:,j);
        Joint(:,2)=Edge(:,j+1);
        Joint(:,3)=[xb(Nbh+1);yb(Nbh+1)];
        Nr=Nbh+1;
        Nj=3;
        trace_edge(:,1)=[xb(Nbh+1);yb(Nbh+1)];
    else if T(j)==0,
            Nm=(j-1)*10-Nr-Ndh;
            Joint(:,Nj+1:Nj+Nm+1)=[xb(Nr+1:Nr+Nm+1);yb(Nr+1:Nr+Nm+1)];
            Nr=Nr+Nm;
            Nj=Nj+Nm+1;
            trace_edge(:,2*j-2)=[xb(Nr+1),yb(Nr+1)];
            Joint(:,Nj+1:Nj+2)=Edge(:,2*j-1:2*j);
            Joint(:,Nj+3)=[xb(Nr+2*Ndh+1),yb(Nr+2*Ndh+1)];
            Nr=Nr+2*Ndh+1;
            Nj=Nj+3;
            trace_edge(:,2*j-1)=[xb(Nr),yb(Nr)];
        else
            Nm=(j-1)*10-Nr-Nbh;
            Joint(:,Nj+1:Nj+Nm+1)=[xb(Nr+1:Nr+Nm+1);yb(Nr+1:Nr+Nm+1)];
            Nr=Nr+Nm;
            Nj=Nj+Nm+1;
            trace_edge(:,2*j-2)=[xb(Nr+1),yb(Nr+1)];
            Joint(:,Nj+1:Nj+2)=Edge(:,2*j-1:2*j);
            Joint(:,Nj+3)=[xb(Nr+2*Nbh+1),yb(Nr+2*Nbh+1)];
            Nr=Nr+2*Nbh+1;
            Nj=Nj+3;
            trace_edge(:,2*j-1)=[xb(Nr),yb(Nr)];
        end
    end
end

Nm2=9-2*Nrh;
Nm22=Nm2;
if Nrh==5,
    Nm22=0;
end
Kr=zeros(1,Nrcv);
for j=1:Nrcv,
    if CtrN2==0,
        Kr(j)=(yr(10*j-9)-yb(1))/(xr(10*j-9)-xb(1));
```

```
    else if CtrN2==1,
            Kr(j)=-(xr(10*j-8)-xr(10*j-9))/(yr(10*j-8)-yr(10*j-9));
        end
    end
end
wr=WidthTrans;
Wr=ones(1,Nrcv)*wr;
Lr=ones(1,Nrcv)*LR*Lamda;
Nr2=1; Nj2=1;
xr=[xr,xr(end)];yr=[yr,yr(end)];
for j=1:Nrcv,
    Pout_r=PCarmcal([xr(10*j-9),yr(10*j-
9),Kr(j),Lr(j),Wr(j),1,xb(1)/2,0]);
    Joint2(:,Nj2:Nj2+1)=[Pout_r(2),Pout_r(1);Pout_r(4),Pout_r(3)];
    if j==1,
        if Nm2==-1,

Joint2(:,Nj2+2:Nj2+3+Nm22)=[xr(Nr2+Nrh),xr(Nr2+1+Nrh+Nm2);yr(Nr2+Nrh),y
r(Nr2+1+Nrh+Nm2)];
        else
Joint2(:,Nj2+2:Nj2+3+Nm22)=[xr(Nr2+Nrh:Nr2+1+Nrh+Nm2);yr(Nr2+Nrh:Nr2+1+
Nrh+Nm2)];
        end
        trace_edge2(:,1)=[xr(Nr2+Nrh);yr(Nr2+Nrh)];
        Nr2=Nr2+Nrh+1;
    else
        if Nm2==-1,
Joint2(:,Nj2+2:Nj2+3+Nm22)=[xr(Nr2+2*Nrh+Nm2),xr(Nr2+2*Nrh+Nm2);yr(Nr2+
2*Nrh+Nm2),yr(Nr2+2*Nrh+Nm2)];
        else
Joint2(:,Nj2+2:Nj2+3+Nm22)=[xr(Nr2+2*Nrh+Nm2:Nr2+1+2*Nrh+2*Nm2);yr(Nr2+
2*Nrh+Nm2:Nr2+1+2*Nrh+2*Nm2)];
        end
        trace_edge2(:,2*(j-1))=[xr(Nr2+Nm2);yr(Nr2+Nm2)];
        trace_edge2(:,2*j-1)=[xr(Nr2+2*Nrh+Nm2);yr(Nr2+2*Nrh+Nm2)];
        Nr2=Nr2+2*Nrh+Nm2+1;
    end
    Nj2=Nj2+Nm22+4;
end

t=SidCurvature;
Ls=ones(1,Nside)*LD*Lamda;
ws=WidthTrans;
Ws=ones(1,Nside)*ws;

Joint2=fliplr(Joint2);
[X,Y,a,b]=PCsidewall(Joint(1,end),Joint(2,end),Joint2(1,1),Joint2(2,1),
t,Nside+1);
Xs=(X(2:end)+X(1:end-1))/2;
Ys=(Y(2:end)+Y(1:end-1))/2;
Ks=(Ys-b)./(Xs-a);
for j=1:Nside,
    Pout_s=PCarmcal([Xs(j),Ys(j),Ks(j),Ls(j),Ws(j),2,xb(1)/2,0]);
    Joint3(:,3*j-2)=[X(j);Y(j)];
    Joint3(:,3*j-1:3*j)=[Pout_s(1:2);Pout_s(3:4)];
end
```

```
Joint3(:,end+1)=Joint2(:,1);
figure;
XYpt(1,:) = [fliplr(Joint(1,2:end)),Joint(1,2:end),Joint3(1,2:end-
1),Joint2(1,1:end-1),fliplr(Joint2(1,2:end-1)),fliplr(Joint3(1,2:end))];
XYpt(2,:) = [fliplr(Joint(2,2:end)),-Joint(2,2:end),-Joint3(2,2:end-
1),-Joint2(2,1:end-1),fliplr(Joint2(2,2:end-
1)),fliplr(Joint3(2,2:end))];
plot(XYpt(1,:),XYpt(2,:));

Nport=2*(Nbeam*(Ndum+1)+Nrcv+Nside)-2;
Pinfo=zeros(10,Nport);
Pinfo(1,:)=1:Nport;
Pinfo(2,:)=zeros(1,Nport);Pinfo(2,(1:2*Nbeam-1)*(Ndum+1))=1;
Pinfo(2,(2*Nbeam-1)*(Ndum+1)+Ndum+Nside+1:(2*Nbeam-
1)*(Ndum+1)+Ndum+Nside+2*Nrcv-1)=2;
JJ=1:Np;
JR=1:Nrcv;
Pinfo(3,:)=[fliplr(xb(10*JJ-9)),xb(10*JJ(2:end)-9),Xs,fliplr(xr(10*JR-
9)),xr(10*JR(2:end)-9),fliplr(Xs
Pinfo(4,:)=[fliplr(yb(10*JJ-9)),-yb(10*JJ(2:end)-9),-Ys,-
fliplr(yr(10*JR-9)),yr(10*JR(2:end)-9),fliplr(Ys)];
Pinfo(5,:)=[fliplr(K),-K(2:end),-Ks,-fliplr(Kr),Kr(2:end),fliplr(Ks)];
Pinfo(6,:)=[fliplr(L),L(2:end),Ls,fliplr(Lr),Lr(2:end),fliplr(Ls)];
Pinfo(7,:)=[fliplr(trace_edge(1,2*JJ(1:Np-
1))),trace_edge(1,2*JJ(1:end)-
1),X(2:end),fliplr(trace_edge2(1,2*JR(1:Nrcv-1))),trace_edge2(1,2*JR-
1),fliplr(X(1:end-1))];
Pinfo(8,:)=[fliplr(trace_edge(2,2*JJ(1:Np-1))),-
trace_edge(2,2*JJ(1:end)-1),-Y(2:end),-
fliplr(trace_edge2(2,2*JR(1:Nrcv-1))),trace_edge2(2,2*JR-
1),fliplr(Y(1:end-1))];
Pinfo(9,:)=[fliplr(trace_edge(1,2*JJ-1)),trace_edge(1,2*JJ(1:end-
1)),X(1:end-1),fliplr(trace_edge2(1,2*JR-1)),trace_edge2(1,2*JR(1:Nrcv-
1)),fliplr(X(2:end))];
Pinfo(10,:)=[fliplr(trace_edge(2,2*JJ-1)),-trace_edge(2,2*JJ(1:end-
1)),-Y(1:end-1),-fliplr(trace_edge2(2,2*JR-
1)),trace_edge2(2,2*JR(1:Nrcv-1)),fliplr(Y(2:end))];
Xite=(1:2*Nbeam-1)*(Ndum+1);
for i=1:Nport,
    text(Pinfo(3,i),Pinfo(4,i),num2str(Pinfo(1,i)),'FontSize',8);
end
GeoData.XYpt  = XYpt;
GeoData.Pinfo = Pinfo;
GeoData.w     = Wtrans;
save('GeoData.mat','GeoData'); end
```

3. `function [xb,yb,xr,yr,w]=RotmBRW(eps,e,gama,r,n,ap,g,phim,Num)`

```
be=1/g;
phimax=phim*pi/180;
ap=ap*pi/180;
a=1/2*(-be^2*cos(ap)^2+2*be*cos(ap)+be^2*sin(ap)^2*e^2-1-
be^2*sin(ap)^2)/(1-e^2)^(1/2)/(be*cos(ap)-1);
b=(1-e^2)^0.5*a;
Theta0=linspace(0,phim,Num);
Theta=linspace(0,phimax,Num);
xb=(0.5)./(a^2+tan(Theta).^2*b^2).*(-2*a+2*a*b-
2*(b^2*a^2+2*tan(Theta).^2*b^3-tan(Theta).^2*b^2).^(1/2))*a;
```

```
yb=-xb.*tan(Theta);
D=1/r;
y3=linspace(0,D/2,n)/sqrt(eps);
ze=y3*gama;
C=cos(ap);S=sin(ap);
a2=1-((1-be)/(1-be*C))^2-(ze/be).^2;
b2=-2+2.*ze.^2/be+2*(1-be)/(1-be*C)-(1-be).*((S.*ze)./(1-be*C)).^2;
c2=-ze.^2+(S*ze).^2/(1-be*C)-((S*ze).^2./(1-be*C)/2).^2;
Bcd=b2.^2-4.*a2.*c2;
w=(-b2-(Bcd).^0.5)./a2/2;
xr=((ze.*sin(ap)).^2-2*be.*w+2*w)./(be.*cos(ap)-1)/2;
yr=ze.*(1-w./be);
end
```

APPENDIX D: Microwave Lens Simulation Using Planar Green's Function in FEKO

The new feature of FEKO 5.3 supports importing point series with various delimiters to create a polygon. The exterior shape of lens can be created as polygon if only their (x,y) coordinates get known. Using the program provided in Appendix C probably achieved the coordinate directly. However, in case of having .dxf file, extra works have to be done in order to import the correct data. This appendix starts with file conversion method, and then addresses the procedures of FEKO simulation using the planar Green's function solvers.

There are two ways of convert the .dxf files into FEKO recognizable format. The first is to use FEMAP to import the .dxf file and export the coordinate data, as shown in the procedure below.

1) Import .dxf into FEMAP, as shown in Figure A- 4, the geometry is recognized as non-meshed framed structure.

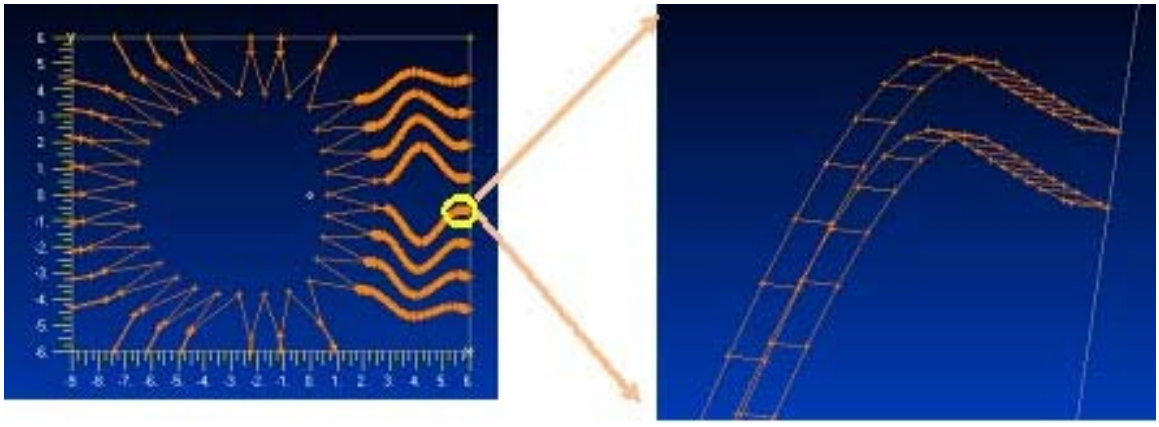

Figure A- 4. dxf File Imported into FEMAP

2) Operate Menu>List>Geometry>Point, list all the points as shown in Figure A- 5. Copy the all points into .txt file.

3) Use Matlab/Excel to view and process the data. The original sequence may look like what is shown in Figure A-6a, which can be reordered as Figure A- 6b.

4) Create lens polygon by importing points in FEKO, result should be similar to Figure A- 7.

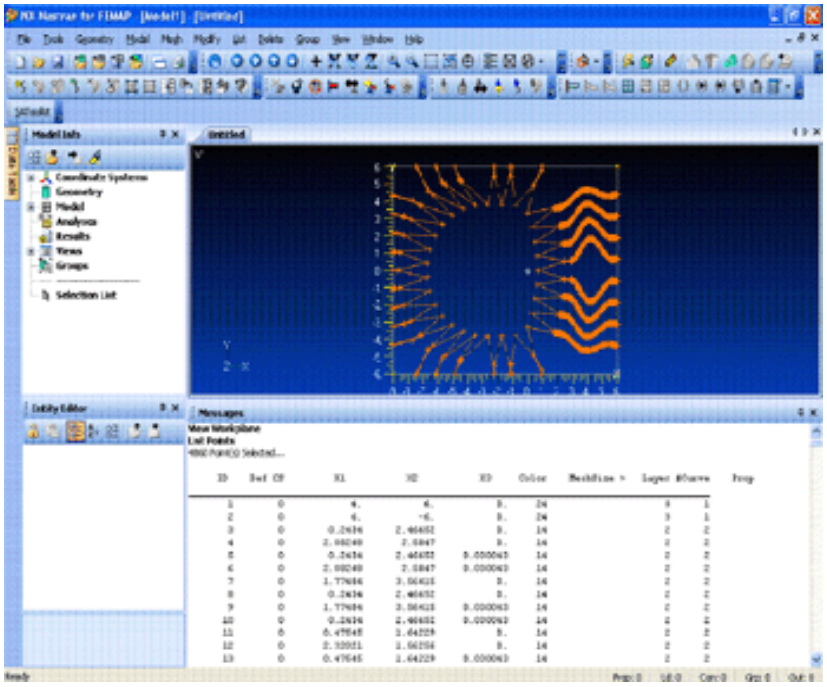

Figure A- 5. List All Coordinates in FEMAP

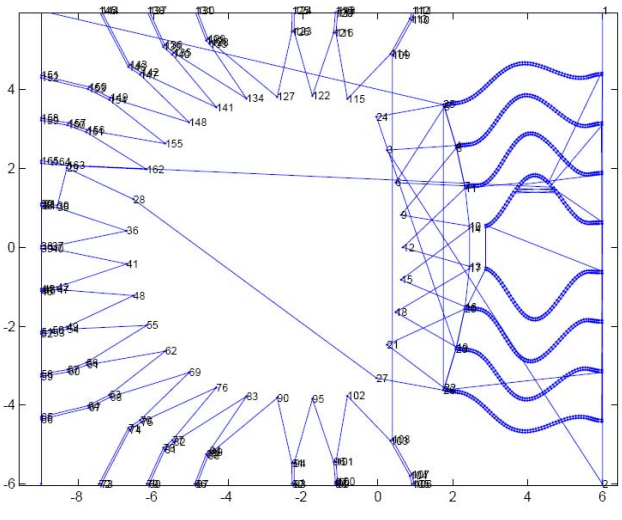

Figure A- 6.a. Data out of Order

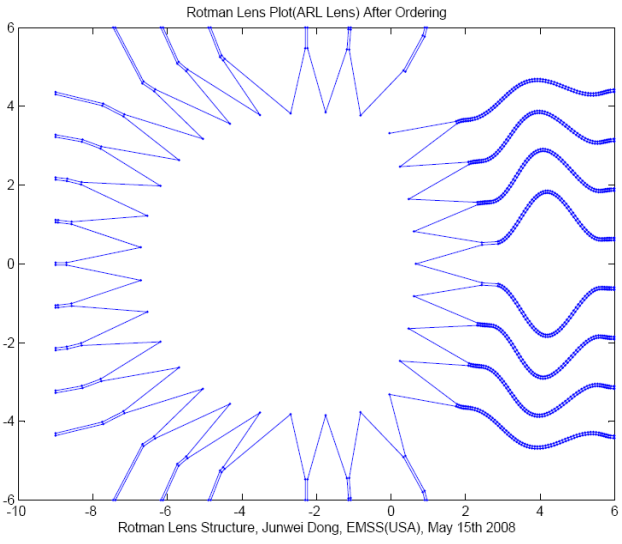

Figure A- 6b. Data in Order

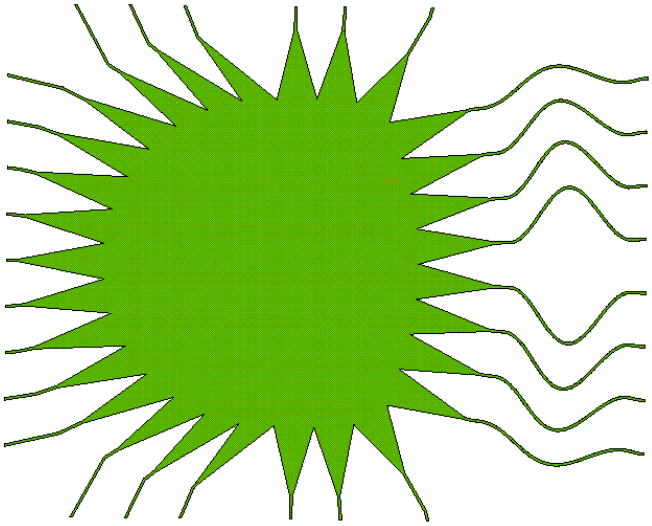

Figure A- 7. Rotman Lens Geometry Model in FEKO

Another way of handing the file is converting the .dxf file to .sat file by doing so:

1) Import .dxf into AutoCAD;

2) Explode any block reference to simple element by operating Modify>Explode;

3) Select lens region and operate Draw>Region;

4) Convert Region to surface by using 3D Operation>Convert to Surface.

5) Save file as .sat format and import file into FEKO.

The ACIS file import tool in FEKO supports unit conversion; however, it is always good to check the models unit after importation. In our case, model unit is set as millimeter in Figure A- 8 a-b. Make sure the structure extent is less than 500, the default extent in CADFEKO; if not, reset the model to proper extent by selecting Menu>Model>Set Extents. Define a polygon enclose the lens region and union it with original structure. Delete the lens exterior face from detail tree, left out complete lens geometry, as procedures shown in Figure A- 8 c-e.

After adding other design variables and medium properties, the 'infinite plane' has to be assigned. In the window of Figure A- 9, use the "planar multilayer substrate" option and create two planes correspondingly.

(a) Unit

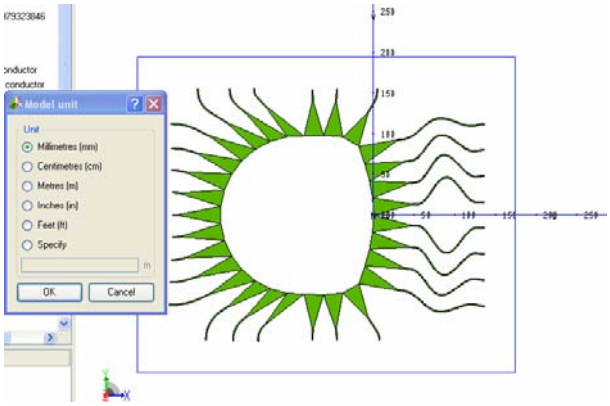

(b) Initial Import

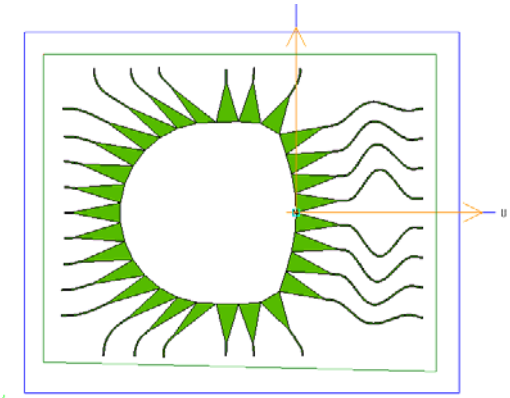

(c) Reset Extent

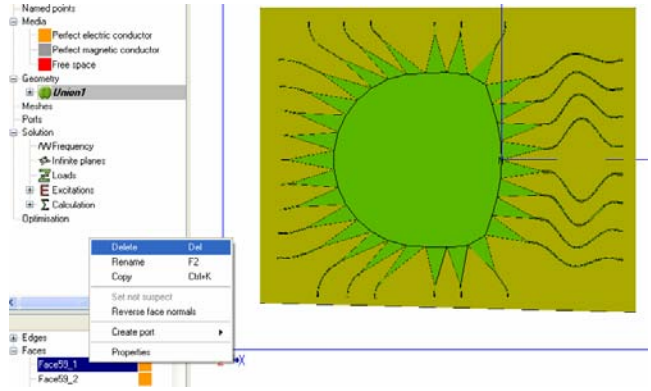

(d) Geometry Correction

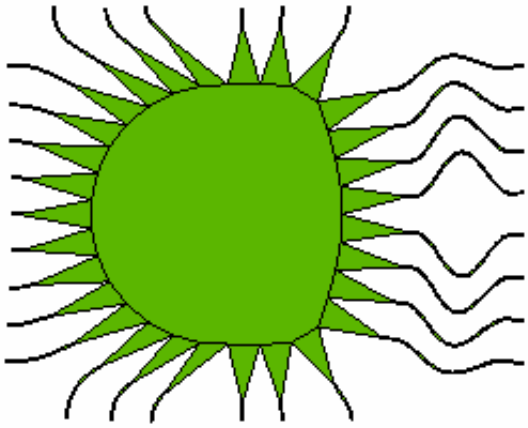

(e) Final Structure

Figure A- 8. Steps of Formulating Final Lens Geometry in FEKO

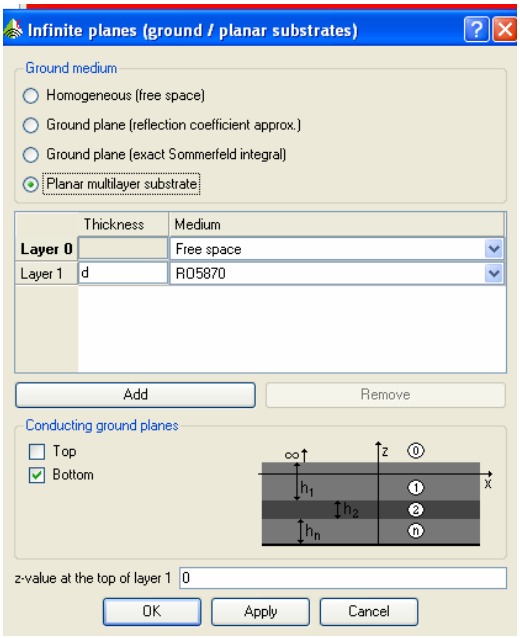

Figure A- 9. Create Infinite Ground Plane

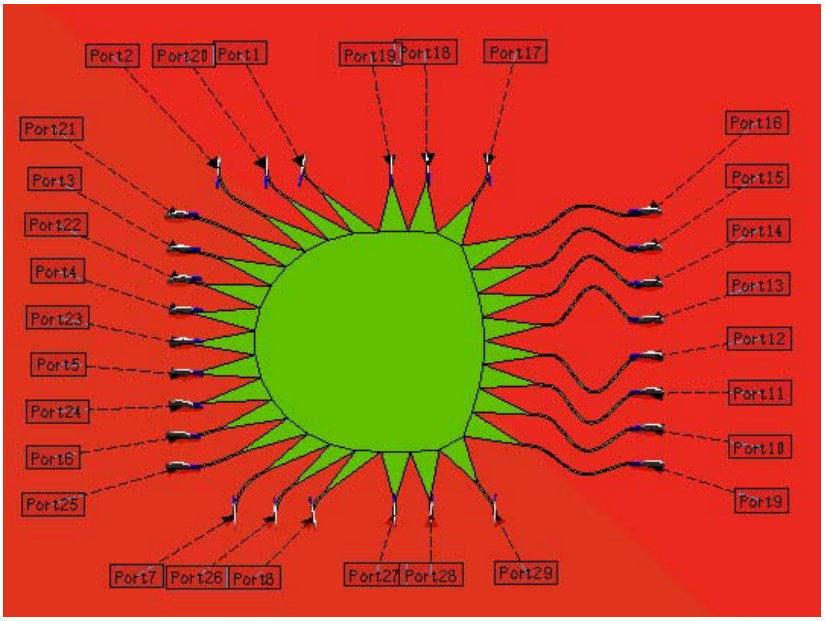

Figure A- 10. Create Microstrip Port

Highlight the edge of each port, and right click to create microstrip port. Port nominations are illustrated in Figure A- 10. Mesh parameters are usually chosen based on empirical results or typical rules of thumb. In the simulation in Chapter 4.1, the mesh edge length is

chosen $\lambda_e/12$, as shown in Figure A- 11. Note that $\lambda_e/8$ mesh edge length gives much lower accuracy.

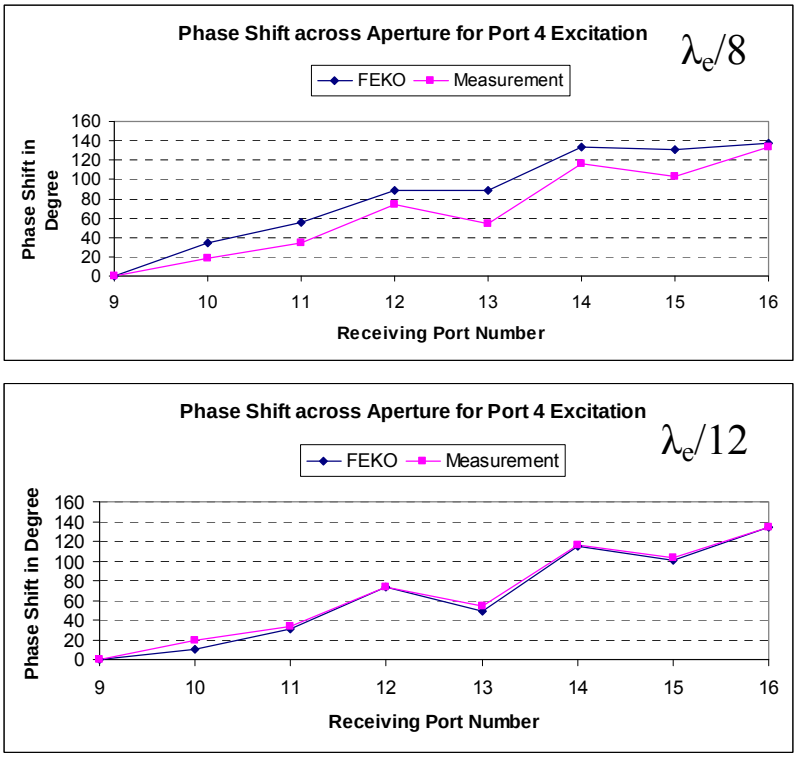

Figure A- 11. Mesh Edge Size of $\lambda_e/12$ Has Better Convergence than That of $\lambda_e/8$

In the microwave lens simulation, two important parameters requested are the surface currents and S-parameters, as shown in Figure A- 12. It is also suggested to activate the option "Export S-parameter to Touchstone file", in doing so, it helps process data directly from touchstone file from POSTFEKO.

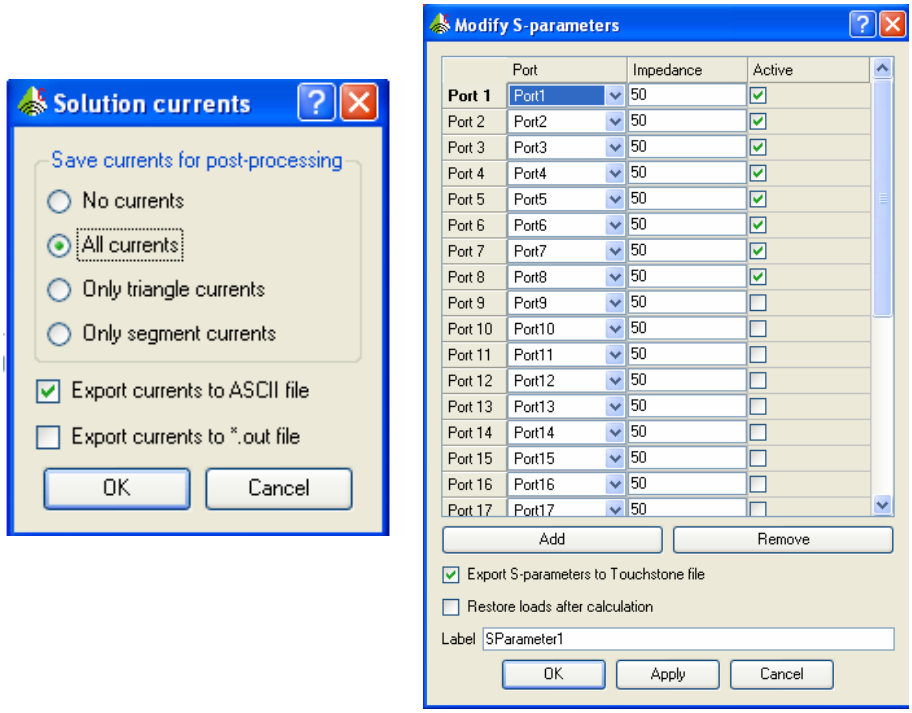

Figure A- 12. Windows for Requesting Currents and S-parameters

APPENDIX E: Program Codes for Microwave Lens Ray Tracing Method

Table A- 3. Program Codes for Ray Tracing Method in Microwave Lens

Function Name	Description
`Menu_Coupling2.m`	Main function produces amplitude and phase simulation for given beam ports using the ray tracing algorithms. Parameters in the example codes are for the microwave lens simulation in Chapter 4.2.2. Note the input parameters e.g. the port profiles are achieved during the geometry formulation.
`PRflct.m`	Calculate the reflection coefficient matrix for the given port profiles.
`micstripW .m`	Calculate the width of the microstrip line for given substrate materials and height.
`micoIMP.m`	Calculate the impedance of the microstrip line for given strip information.

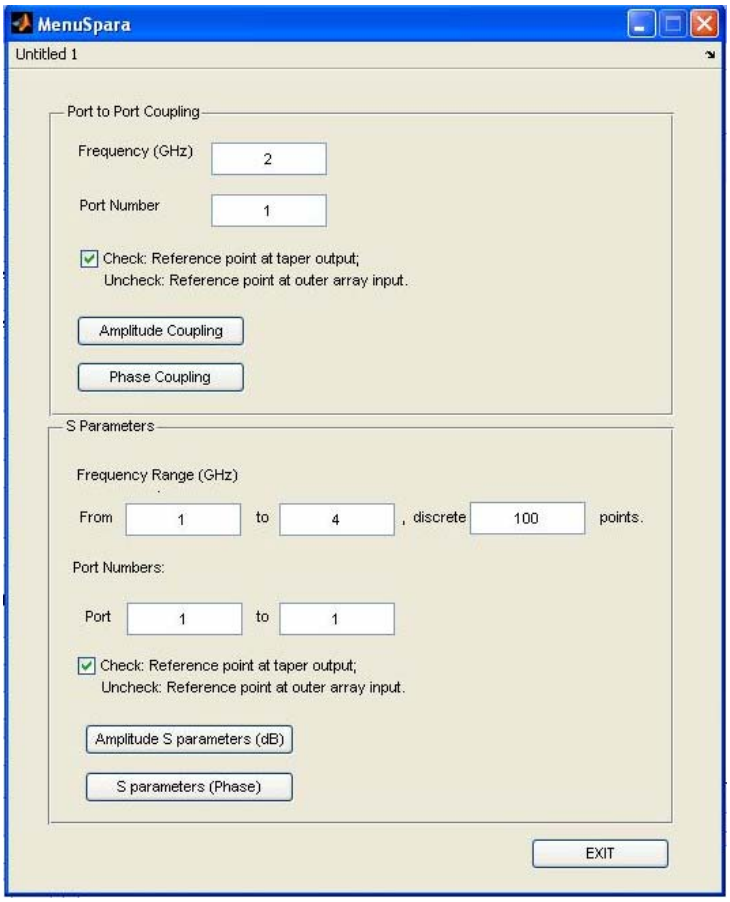

Figure A- 13. GUI Window Performing Ray Tracing Simulation

```
1. function
Menu_Coupling2(NN,MM,Wtrans,LowFreq,HighFreq,Nfre,Imp_terminal,eps,d,Ls
tan,Pinfo,Xite,Ctrl,CtrlRefe2)
[JJ,Nport]=size(Pinfo);
LowFreq=LowFreq*10^9; HighFreq=HighFreq*10^9;
FreqPnt=linspace(LowFreq,HighFreq,Nfre);Srecord=zeros(1,Nfre);
for FreqStep=1:Nfre,
    Freq=FreqPnt(FreqStep);
    lamda=3*10^8/(eps)^.5/Freq;
    k=2*pi*Freq/c*eps.^.5*(1-j*Lstan/2);
    M1=ones(Nport,Nport);
    M2=zeros(Nport,Nport);
    M0=zeros(Nport,Nport);
    M0(end,1:end-1)=((Pinfo(10,end)-Pinfo(8,end))^2+(Pinfo(9,end)-
Pinfo(7,end))^2)^.5;
    for i=1:Nport-1,
        M0(i,:)=((Pinfo(10,i)-Pinfo(8,i))^2+(Pinfo(9,i)-
Pinfo(7,i))^2)^.5;
        M0(i,i)=0;
        M1(i,i+1:Nport)=((Pinfo(4,i+1:end)-
Pinfo(4,i)).^2+(Pinfo(3,i+1:end)-Pinfo(3,i)).^2).^.5;
        K0=Pinfo(3,i)-Pinfo(3,i+1:end);
        K0(find(K0==0))=10^-10;
        K(1:Nport-i)=(Pinfo(4,i)-Pinfo(4,i+1:end))./K0;
        K=atan(K);
        M2(i,i+1:end)=abs(atan(Pinfo(5,i))-K);
        M2(i+1:end,i)=abs(atan(Pinfo(5,i+1:end))-K);
        K0=0;
        K=0;
    end
    M1=M1'.*M1;
    M3=zeros(Nport,Nport);
    M3=sinc(M0.*sin(M2)/lamda).*cos(M2);
    Thta=2*pi*Freq/c*eps.^.5.*Pinfo(6,:);
    Rflct=PRflct(k,Nport,eps,d,Imp_terminal,Pinfo,M0);
    Count_beam=1;
    S=zeros(Count_beam,Nport);
    S1=zeros(Nport,Nport);
    for i=1:Count_beam,
        eps1=(eps+1)/2+(eps-1)/2.*(1./(1+12*0.508./1.526).^0.5);
        k2=2*pi*Freq/c*((eps1+eps)/2).^.5*(1-j*Lstan/2);
        S(i,:)=exp(-j*k2*Pinfo(6,Xite(i))).*sqrt(1-
(Rflct(NN)).^2)*M3(NN,:).*exp(j*pi/4)./(lamda)^.5.*M0(NN,:).*exp(-
j*k*M1(NN,:))./(M1(NN,:)).^.5.*M3(:,NN)';
        S(i,NN)=+Rflct(NN);
        for t=1:Nport,
S1(t,:)=S(i,t).*(Rflct(t)).*M3(t,:).*exp(j*pi/4)./(lamda)^.5.*M0(t,1).*
exp(-j*k*M1(t,:))./(M1(t,:)).^.5.*M3(:,t)';
        end
        S(i,:)=(S(i,:)+sum(S1,1)).*sqrt(1-(Rflct(NN)).^2).*exp(-
j*k2*Pinfo(6,:));S(i,NN)=S(i,NN)+Rflct(NN)^2;
        S1=zeros(Nport,Nport);
    end

dBf=[28.4341;59.645;34.6632;12.5703;12.5703;34.6632;59.645;28.4341]*10^
-3;
```

```
eps1=(eps+1)/2+(eps-1)/2.*(1./(1+12*0.508./1.526).^0.5);
k1=2*pi*Freq/c*eps1.^.5*(1-j*Lstan/2);
S=S.*(exp(-j*k1*dBf(4))*ones(1,29));

if CtrlRefe2==0,
    [,RecvPsit]=find(Pinfo(2,:)==2);

    df=Wtrans';
    eps1=(eps+1)/2+(eps-1)/2.*(1./(1+12*0.508./1.526).^0.5);
    k1=2*pi*Freq/c*eps1.^.5*(1-j*Lstan/2);
    S=S(:,RecvPsit).*(ones(Count_beam,1)*exp(-j*k1*df));
    S=[ones(1,RecvPsit(1)-1),S,ones(1,Nport-RecvPsit(end))];
end
if CtrlRefe2==1,
    [,RecvPsit1]=find(Pinfo(2,:)==2);
    df1=Wtrans(RecvPsit1);
    [,RecvPsit2]=find(Pinfo(2,:)==1);
    df2=Wtrans(RecvPsit2)*1;
    eps1=(eps+1)/2+(eps-1)/2.*(1./(1+12*1.6./4.4).^0.5);
    k1=2*pi*Freq/c*eps1.^.5*(1-j*Lstan/2);
    S=S(:,RecvPsit1).*(ones(Count_beam,1)*exp(-j*k1*df1)).*(exp(-
j*k1*df2(1))*ones(1,32));
    S=[ones(1,RecvPsit1(1)-1),S,ones(1,Nport-RecvPsit1(end))];
end
SaveAmp(FreqStep,:)=20*log10(abs(S(1,19:26)));SavePha(FreqStep,:)=angle
(S(1,19:26))*180/pi;
Srec_Amp(FreqStep)=20*log10(abs(S(1,MM)));
Srec_Pha(FreqStep)=angle(S(1,MM))*180/pi;
end
if Ctrl==1,
    figure;plot(FreqPnt,Srec_Amp,'.-');
    axis([LowFreq,HighFreq,-50,5]);
    title(['S parameter for
Port',num2str(NN),',',num2str(MM),'(Amplitude)']);xlabel('Frequency
(Hz)');ylabel('Amplitude in dB');
else if Ctrl==0,
        figure;plot(FreqPnt,Srec_Pha,'.-');
        title(['S parameter for
Port',num2str(NN),',',num2str(MM),'(Phase)']);xlabel('Frequency
(Hz)');ylabel('Phase in Degree');
    end
end

end
```

2.
```
function [Rflct]=PRflct(k,Nport,eps,d,Imp_terminal,Pinfo,M0)
Npoint=100;
Mwidth=zeros(Nport,Npoint);
Mtermi=micstripW(eps,d,Imp_terminal);
Mwidth(1,:)=linspace(Mtermi,M0(1,2));
X=zeros(Nport,Npoint);
X(1,:)=linspace(0,Pinfo(6,1),Npoint);
for i=2:Nport,
Mwidth(i,:)=linspace(Mtermi,M0(i,1));
X(i,:)=linspace(0,Pinfo(6,i),Npoint);
```

```
end
Y=micoIMP(eps,Mwidth,d);
for i=1:Nport,
A123(i,:)=polyfit(X(i,:),Y(i,:),3)/Imp_terminal;
a3=A123(i,1);a2=A123(i,2);a1=A123(i,3);a0=A123(i,4);
F = @(z)0.5*exp(-
2*j*k*z).*(3*a3*z.^2+2*a2*z+a1)./(a3*z.^3+a2*z.^2+a1*z+a0);
Rflct(i)=quad(F,0,Pinfo(6,i));

end

end
```

3.
```
function [Width]=micstripW(eps,d,Imp)
A=Imp/60*((eps+1)/2)^.5+(eps-1)/(eps+1)*(0.23+0.11/eps);
B=377*pi./Imp/((eps)^.5)/2;
Wd=8*exp(A)./(exp(2*A)-2); %The value of W/d
if Wd>2|Wd<0;
    Wd=2/pi*(B-1-log(2*B-1)+(eps-1)/2/eps*(log(B-1)+0.39-0.61/eps));
end
Width=Wd*d;
end
```

4.
```
function [Imp]=micoIMP(eps,W,d)
eps=(eps+1)/2+(eps-1)/2.*(1./(1+12*d./W).^0.5);
Wd=W/d;
if Wd<1;
    Imp=60/(eps)^.5*log(8/Wd-Wd/4);
else
    Imp=120*pi./((eps).^.5.*(Wd+1.393+0.667*log(Wd+1.444)));
end

end
```

APPENDIX F: Detailed Ray Tracing Validation Comparison Results

1. Validation of Lens #1

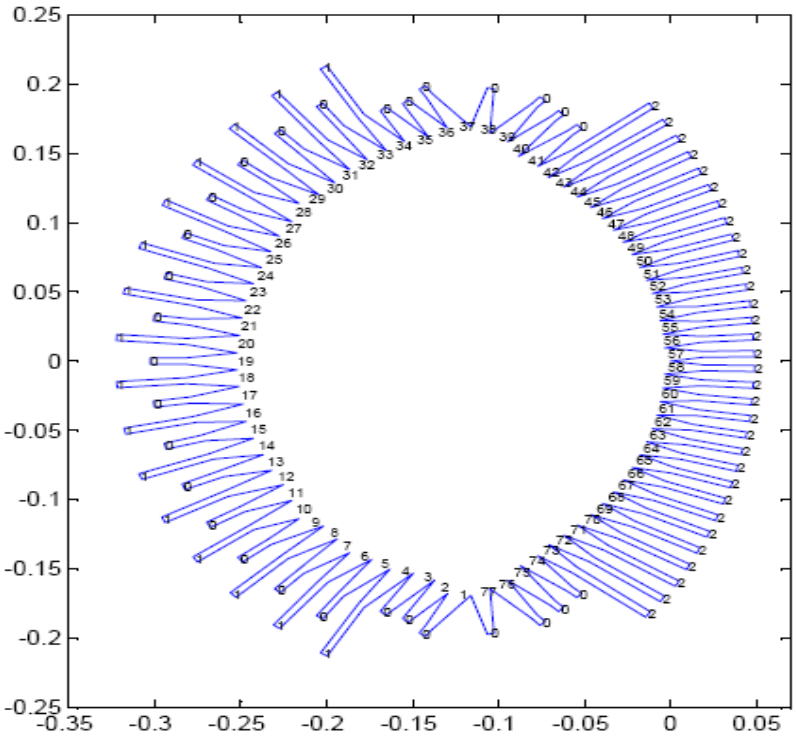

Figure A- 14. Microwave Lens #1 Port Number Nominations

Table A- 4. Microwave lens #1 Parameters and Comparison Organization

Parameters	Permittivity	Loss Tangent	Substrate Thickness	Port Termination
Values	2.5	0.0019	1.6mm	50 Ohm

Figure Numbers	Description
Figure A- 15 ~Figure A- 22	Compare S parameter (Amplitude and Phase) between beam port 20 and different single receiving ports across the given frequency band. Note the constant phase shift is due to the constant reference line difference between the simulation and measurement.
Figure A- 23 ~Figure A- 28	Compare S parameter (Amplitude and Phase) between beam port 4 and different single receiving ports across the given frequency band.
Figure A- 29 ~Figure A- 34	Compare the amplitude and phase shift from beam port 20 to all receiving ports at different frequencies.
Figure A- 35 ~Figure A- 40	Compare the amplitude and phase shift from beam port 4 to all receiving ports at different frequencies.
Figure A- 41 ~Figure A- 43	Compare the Array Factor when beam port 20 is excited at different frequencies.
Figure A- 44 ~Figure A- 46	Compare the Array Factor (pattern) when beam port 4 is excited at different frequencies

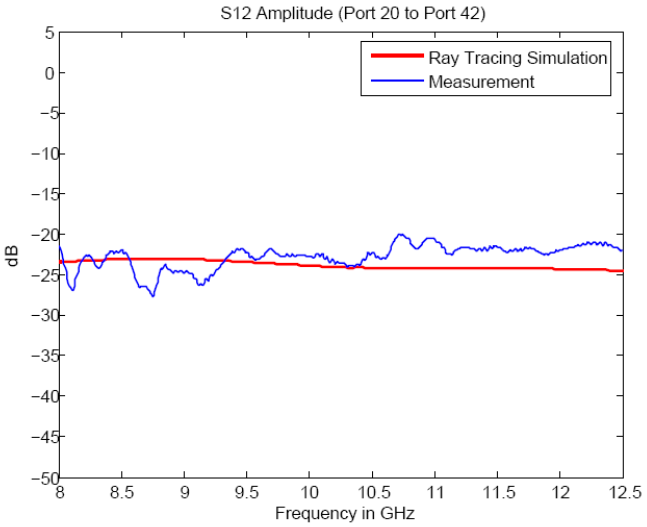

Figure A- 15. Amplitude Coupling between Port 20 and Port 42

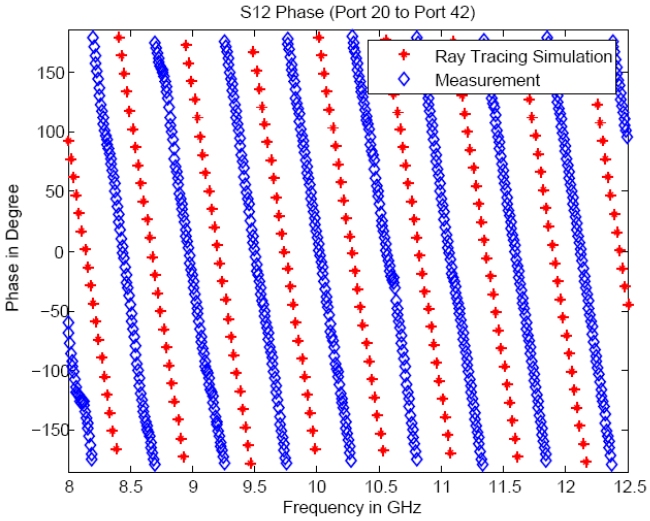

Figure A- 16. Phase Coupling between Port 20 and Port 42

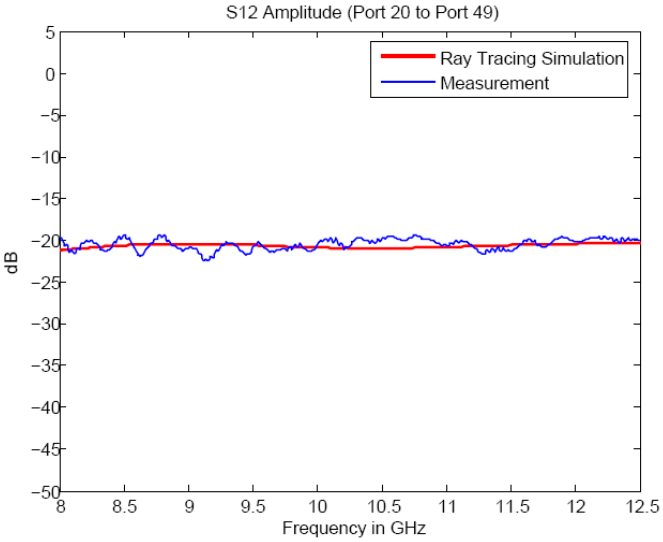

Figure A- 17. Amplitude Coupling between Port 20 and Port 49

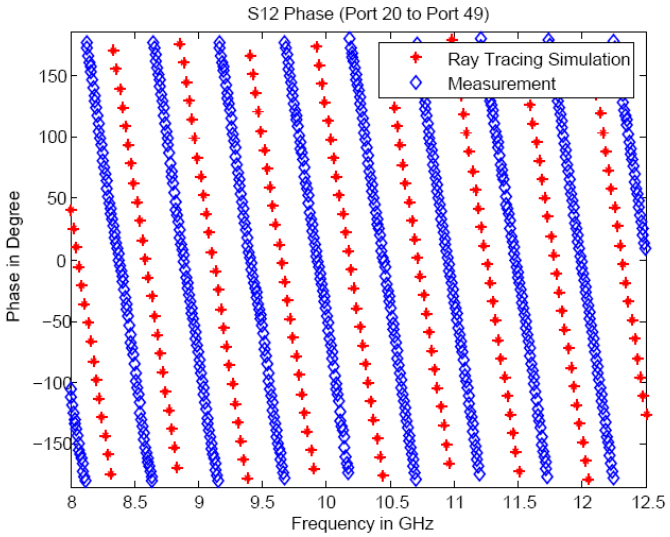

Figure A- 18. Phase Coupling between Port 20 and Port 49

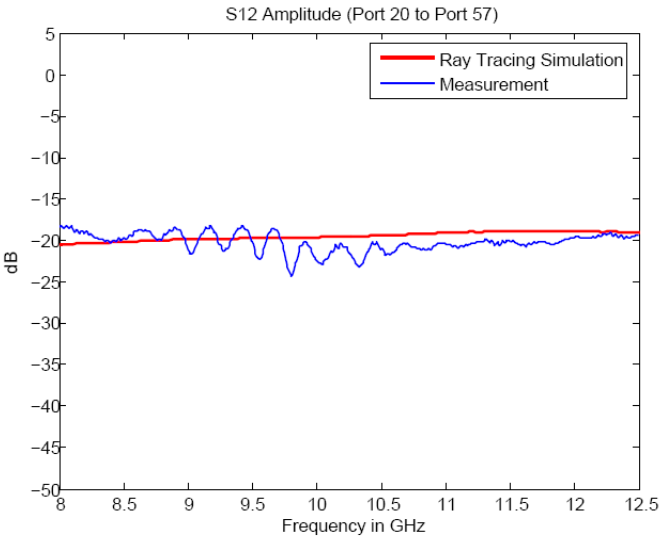

Figure A- 19. Amplitude Coupling Between Port 20 and Port 57

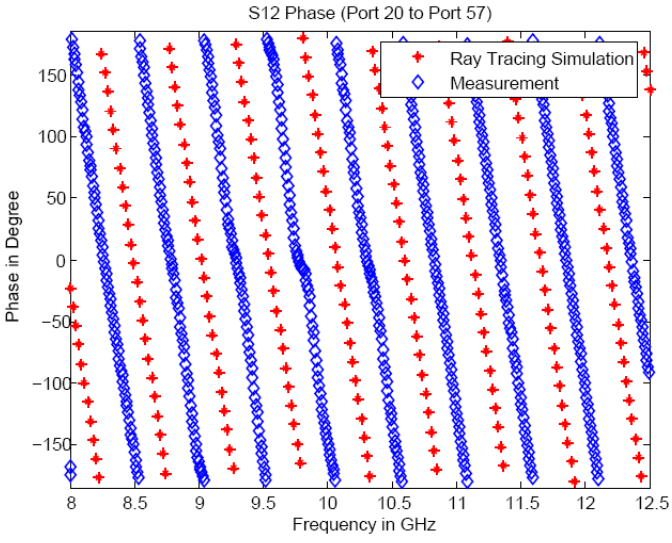

Figure A- 20. Phase Coupling Between Port 20 and Port 57

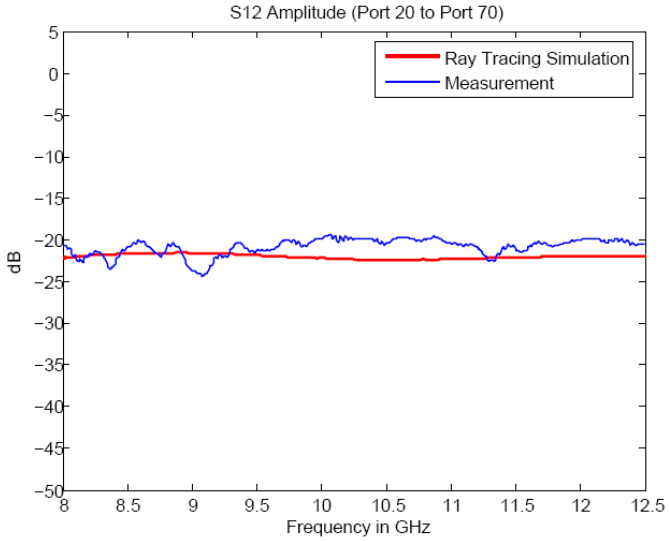

Figure A- 21. Amplitude Coupling Between Port 20 and Port 70

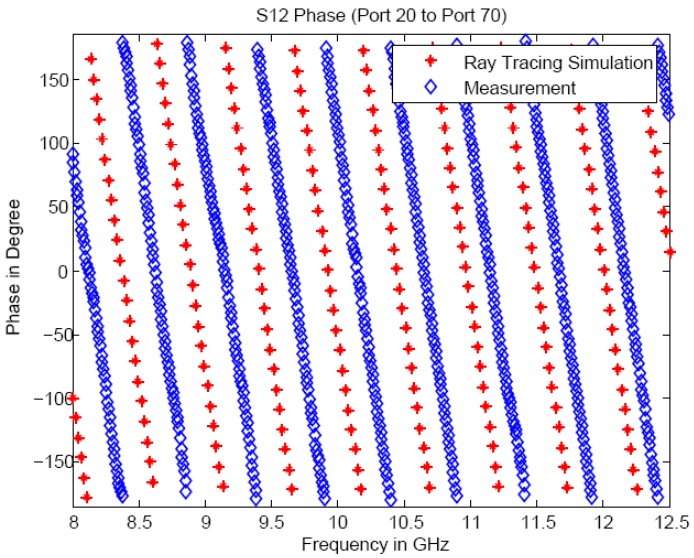

Figure A- 22. Phase Coupling Between Port 20 and Port 70

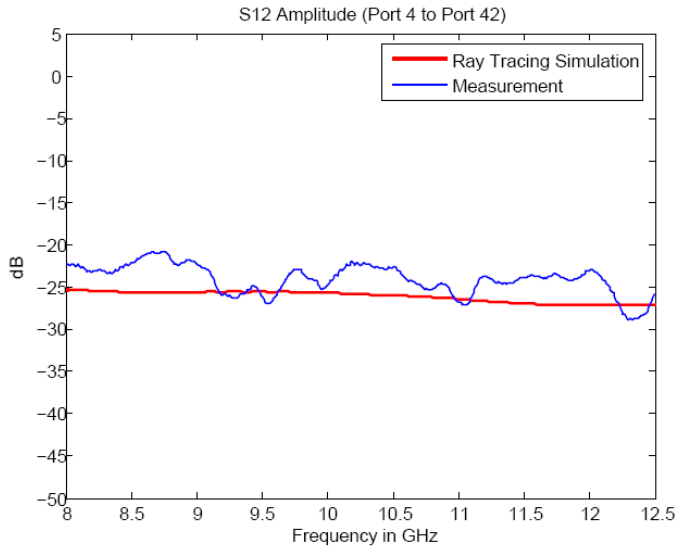

Figure A- 23. Amplitude Coupling Between Port 4 and Port 42

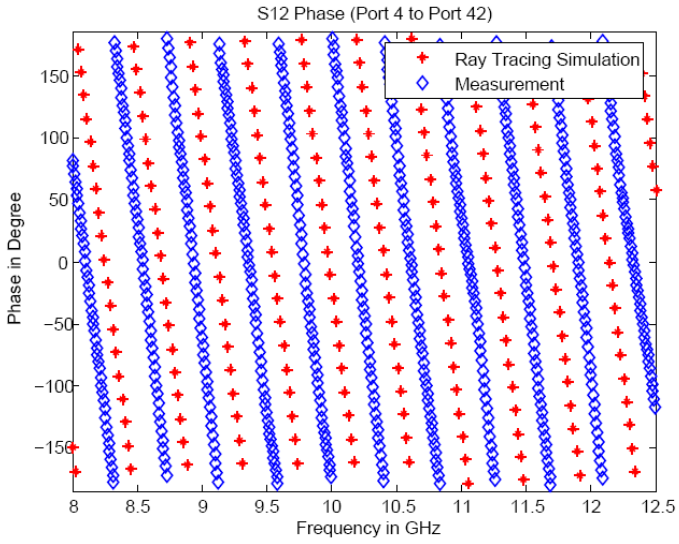

Figure A- 24. Phase Coupling Between Port 4 and Port 42

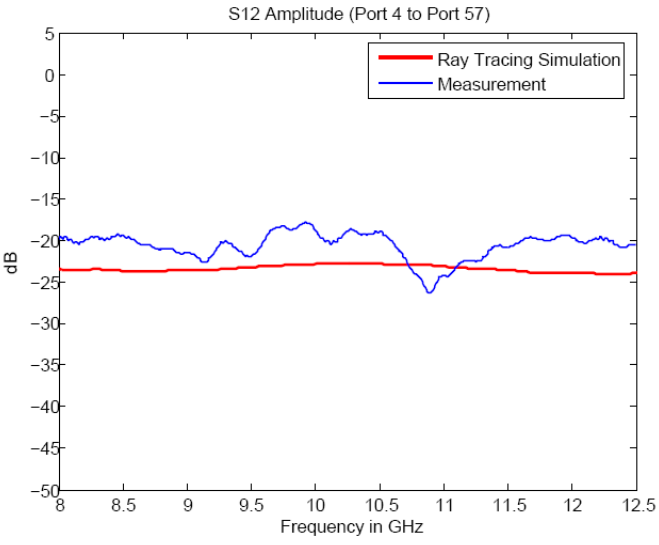

Figure A- 25. Amplitude Coupling Between Port 4 and Port 57

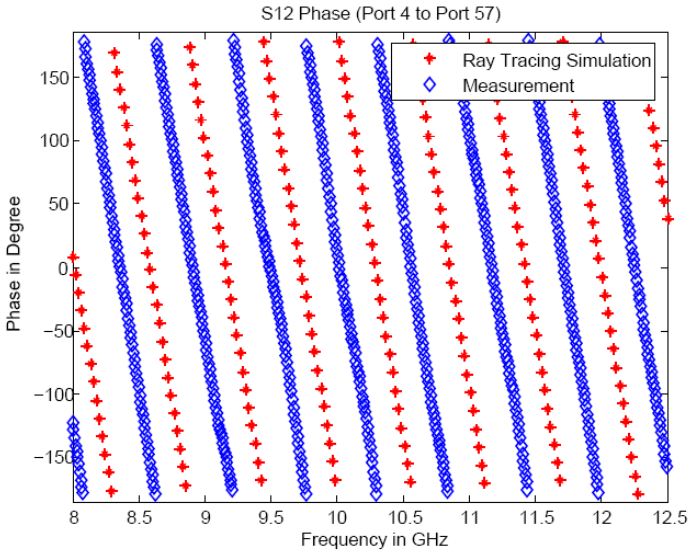

Figure A- 26. Phase Coupling Between Port 4 and Port 57

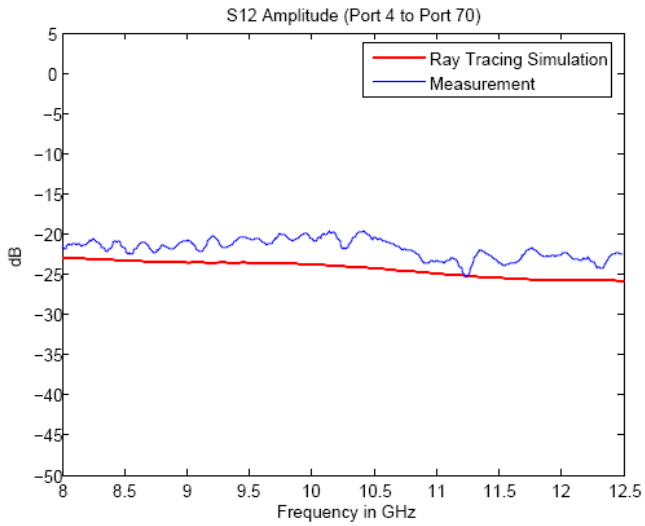

Figure A- 27. Amplitude Coupling Between Port 4 and Port 70

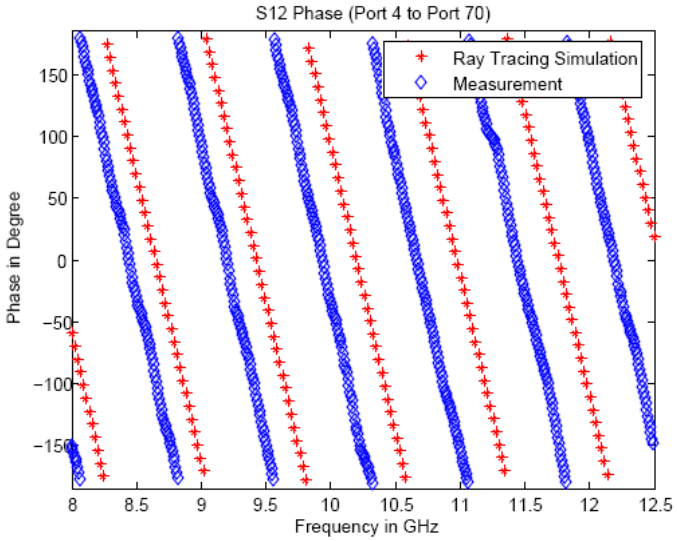

Figure A- 28. Phase Coupling Between Port 4 and Port 70

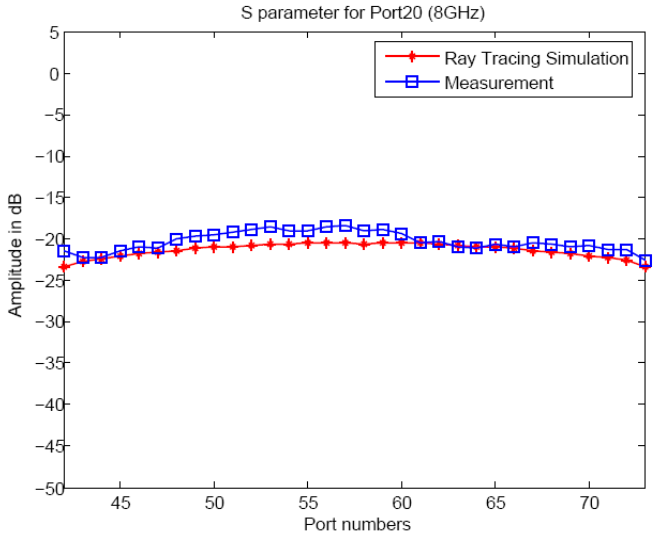

Figure A- 29. Amplitude across Aperture for Port 20

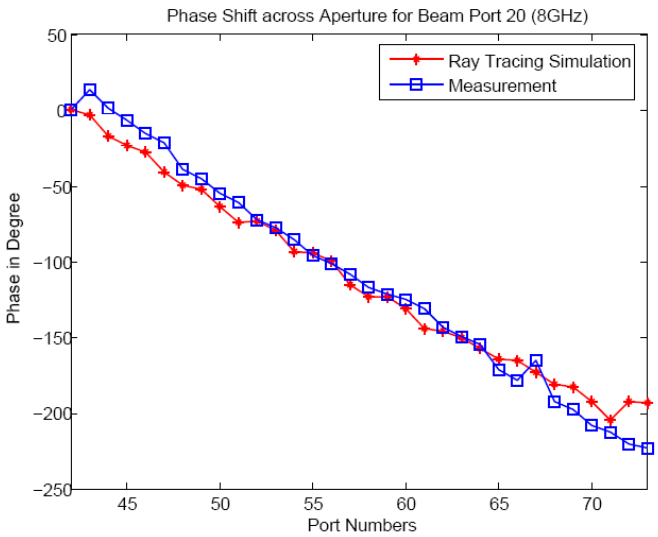

Figure A- 30. Phase Shift across Aperture for Port 20 (8GHz)

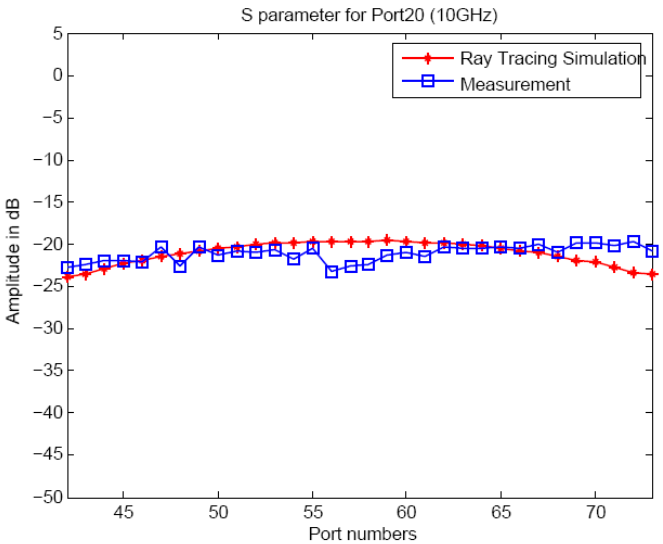

Figure A- 31. Amplitude across Aperture for Port 20 (10GHz)

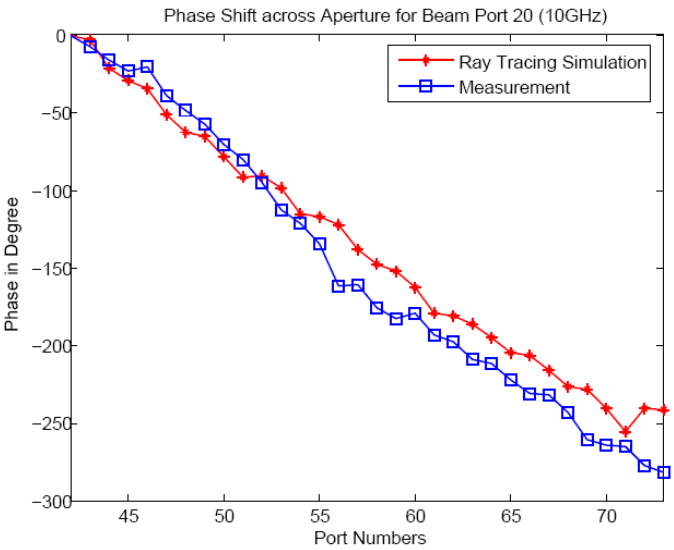

Figure A- 32. Phase Shift across Aperture for Port 20 (10GHz)

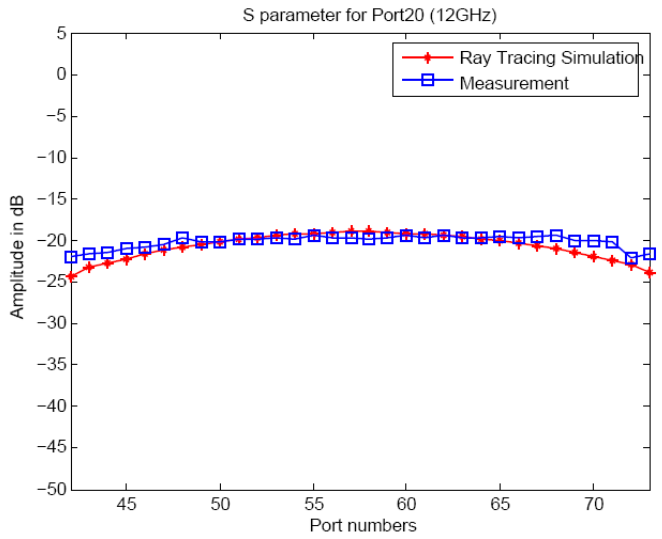

Figure A- 33. Amplitude across Aperture for Port 20 (12GHz)

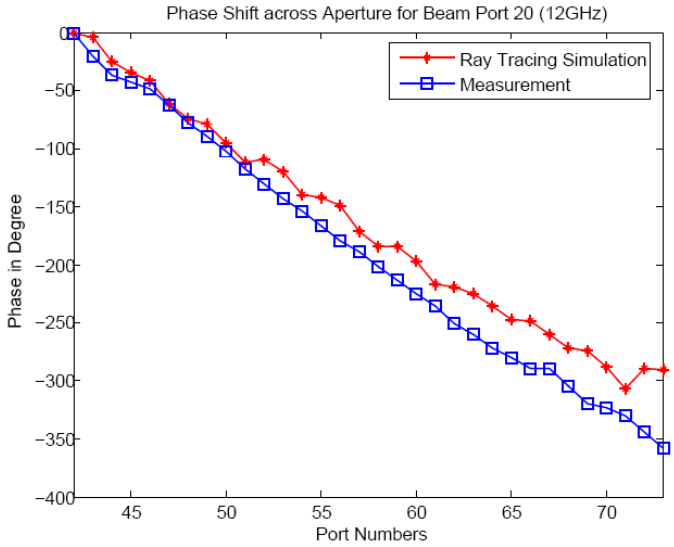

Figure A- 34. Phase Shift across Aperture for Port 20 (12GHz)

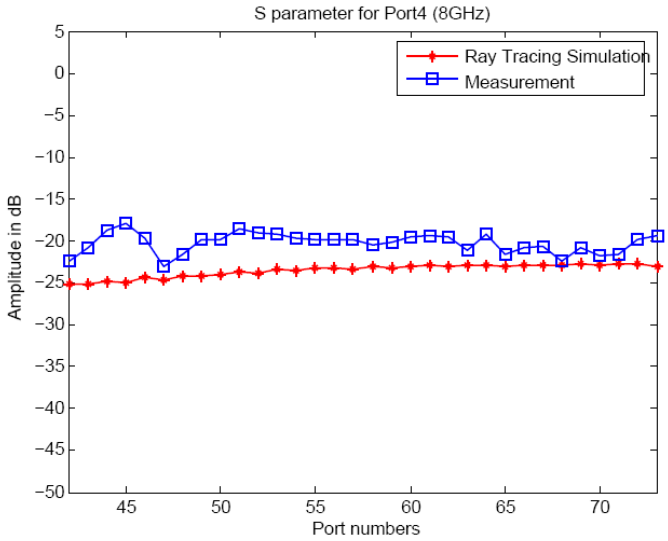

Figure A- 35. Amplitude across Aperture for Port 4 (8GHz)

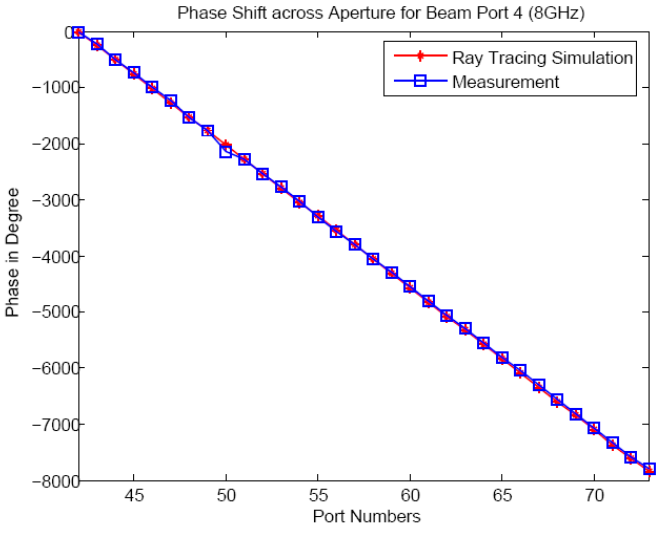

Figure A- 36. Phase Shift across Aperture for Port 4 (8GHz)

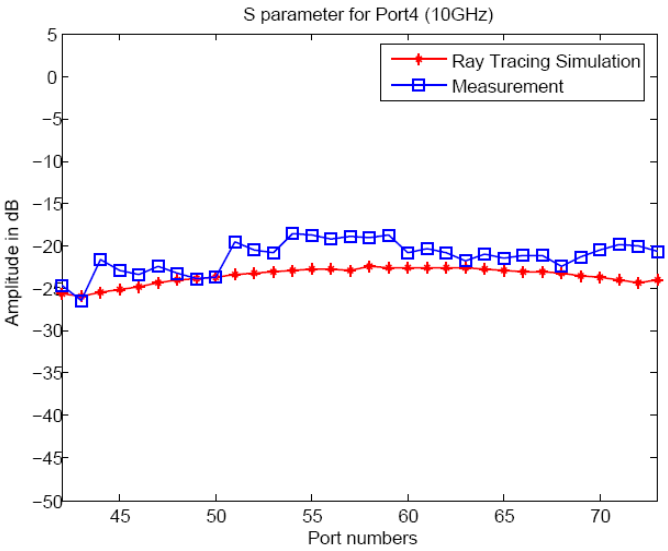

Figure A- 37. Amplitude across Aperture for Port 4 (10GHz)

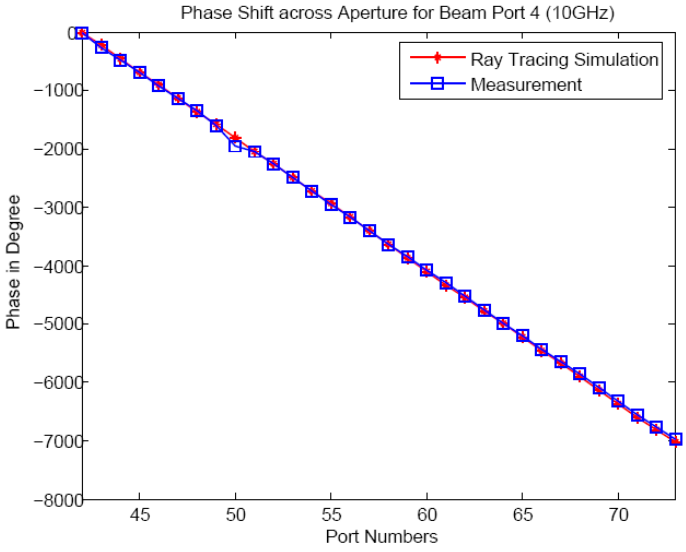

Figure A- 38. Phase Shift across Aperture for Port 4 (10GHz)

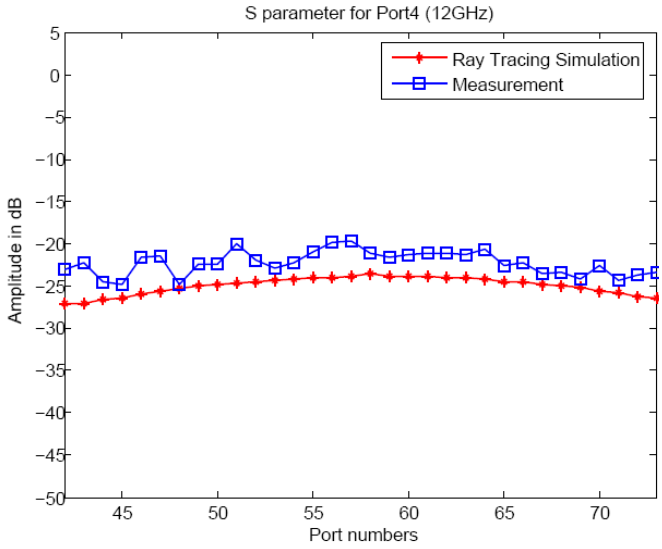

Figure A- 39. Amplitude across Aperture for Port 4 (12GHz)

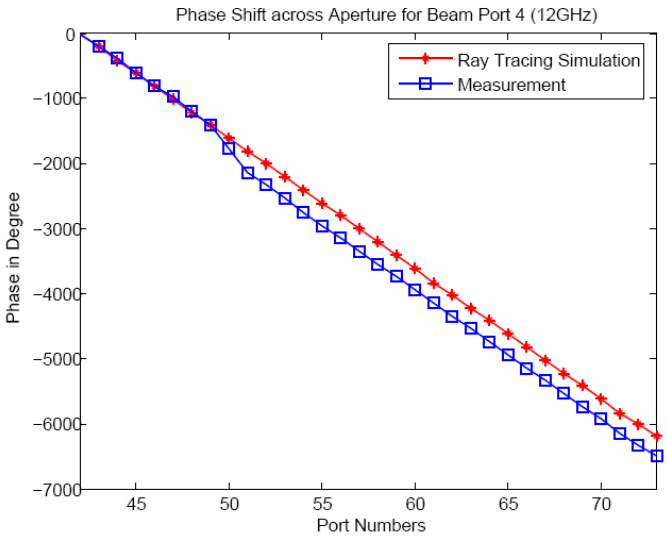

Figure A- 40. Phase Shift across Aperture for Port 4 (12GHz)

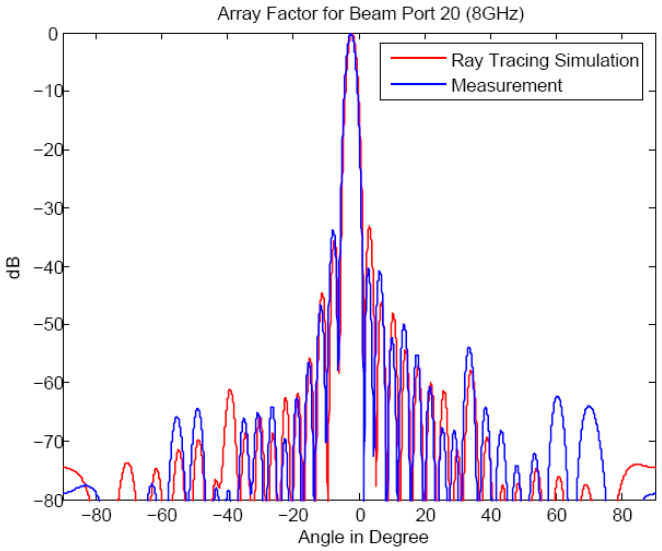

Figure A- 41. AF for Port 20 Excitation at 8GHz

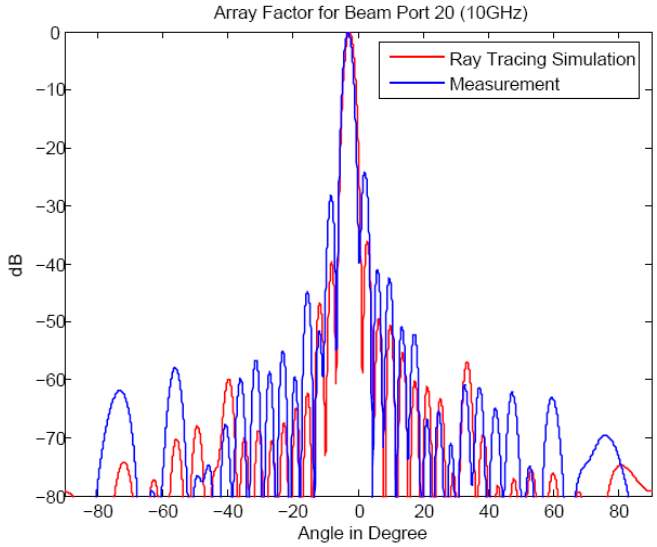

Figure A- 42. AF for Port 20 Excitation at 10GHz

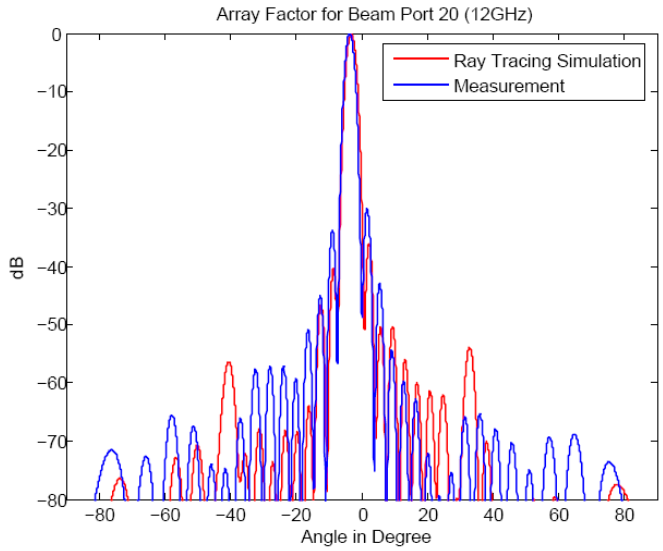

Figure A- 43. AF for Port 20 Excitation at 12GHz

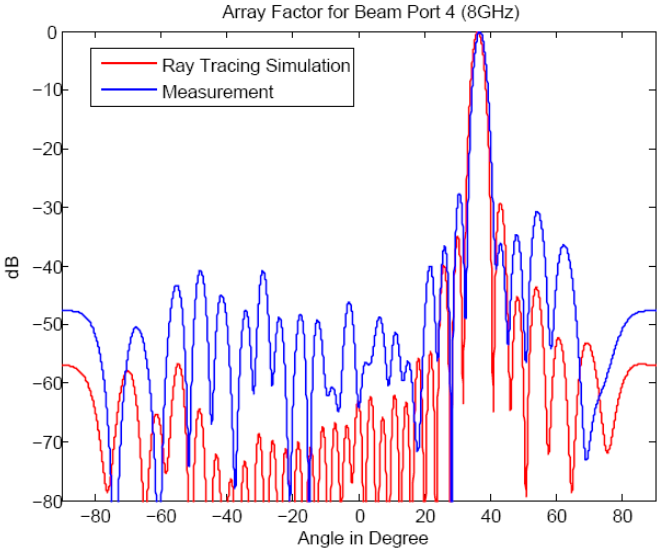

Figure A- 44. AF for Port 4 Excitation at 8GHz

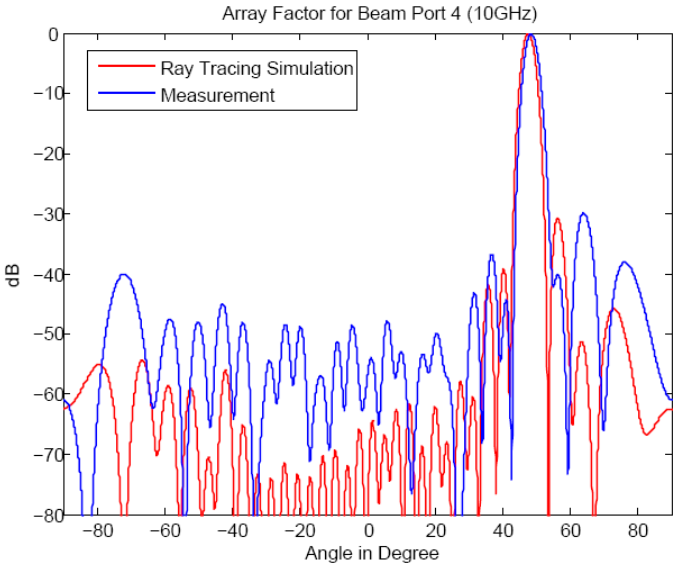

Figure A- 45. AF for Port 4 Excitation at 10GHz

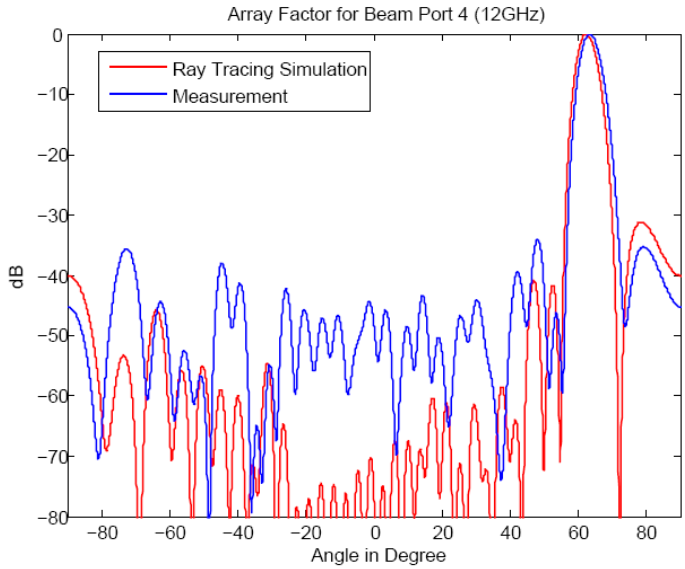

Figure A- 46. AF for Port 4 Excitation at 12GHz

2. Validation of Lens #2

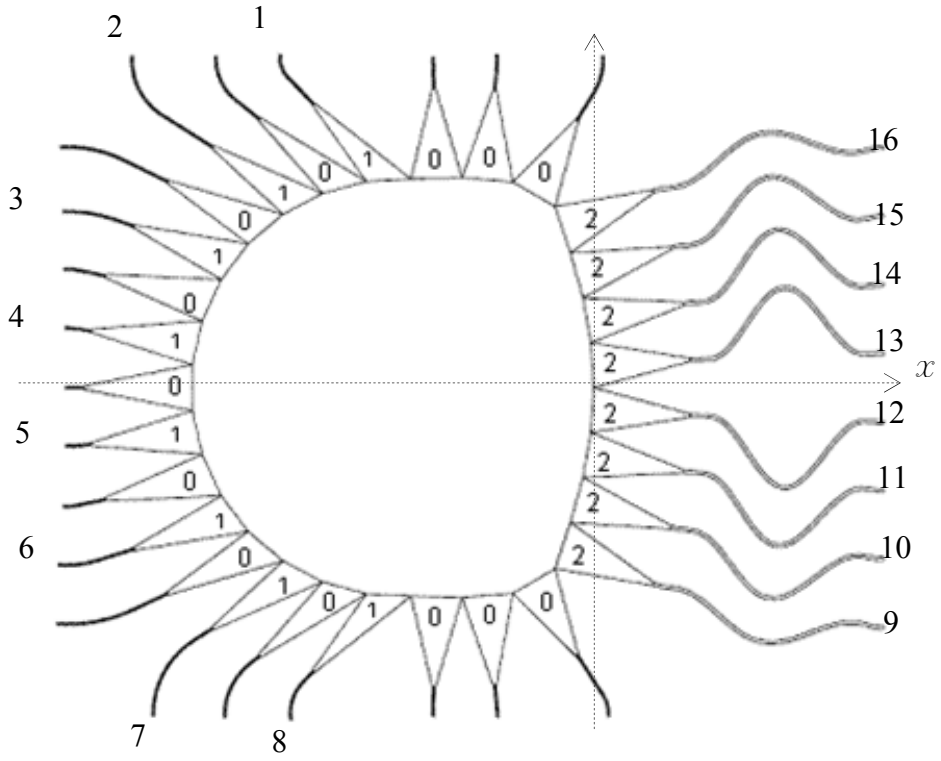

Figure A- 47. Microwave Lens #2 Port Number Nominations

Table A- 5. Ray Tracing Simulation Compared to FEKO and Measurement for Microwave Lens #2

Figure Numbers	Description
Figure A- 48 ~Figure A- 55	Compare S parameter (Amplitude and Phase) between each beam port (1~4) and receiving port 9 across the given frequency band. Note the constant phase shift due to the constant reference line difference in Lens #1 has been eliminated because the exact transmission lines have been used in both measurement and simulation.
Figure A- 56 ~Figure A- 63	Compare S parameter (Amplitude and Phase) between each beam port (1~4) and receiving port 10 across the given frequency band.
Figure A- 64 ~Figure A- 71	Compare S parameter (Amplitude and Phase) between each beam port (1~4) and receiving port 11 across the given frequency band.
Figure A- 72 ~Figure A- 79	Compare S parameter (Amplitude and Phase) between each beam port (1~4) and receiving port 12 across the given frequency band.
Figure A- 80 ~Figure A- 87	Compare S parameter (Amplitude and Phase) between each beam port (1~4) and receiving port 13 across the given frequency band.
Figure A- 88 ~Figure A- 95	Compare S parameter (Amplitude and Phase) between each beam port (1~4) and receiving port 14 across the given frequency band.
Figure A- 96 ~Figure A- 103	Compare S parameter (Amplitude and Phase) between each beam port (1~4) and receiving port 15 across the given frequency band.
Figure A- 104 ~Figure A- 111	Compare S parameter (Amplitude and Phase) between each beam port (1~4) and receiving port 16 across the given frequency band.
Figure A- 112 ~Figure A- 115	Amplitude Distribution across the aperture for Ports 1-4 excitations at 4GHz.
Figure A- 116 ~Figure A- 119	Phase Shift across the aperture for Ports 1-4 excitations at 4GHz.
Figure A- 120 ~Figure A- 123	Array Factor for Ports 1-4 excitations at 4GHz.
Figure A- 124 ~Figure A- 127	Amplitude Distribution across the aperture for Ports 1-4 excitations at 4.6GHz.
Figure A- 128 ~Figure A- 131	Phase Shift across the aperture for Ports 1-4 excitations at 4.6GHz.
Figure A- 132 ~Figure A- 135	Array Factor for Ports 1-4 excitations at 4.6GHz.
Figure A- 136 ~Figure A- 139	Amplitude Distribution across the aperture for Ports 1-4 excitations at 5GHz.
Figure A- 140 ~Figure A- 143	Phase Shift across the aperture for Ports 1-4 excitations at 5GHz.
Figure A- 144 ~Figure A- 147	Array Factor for Ports 1-4 excitations at 5GHz.

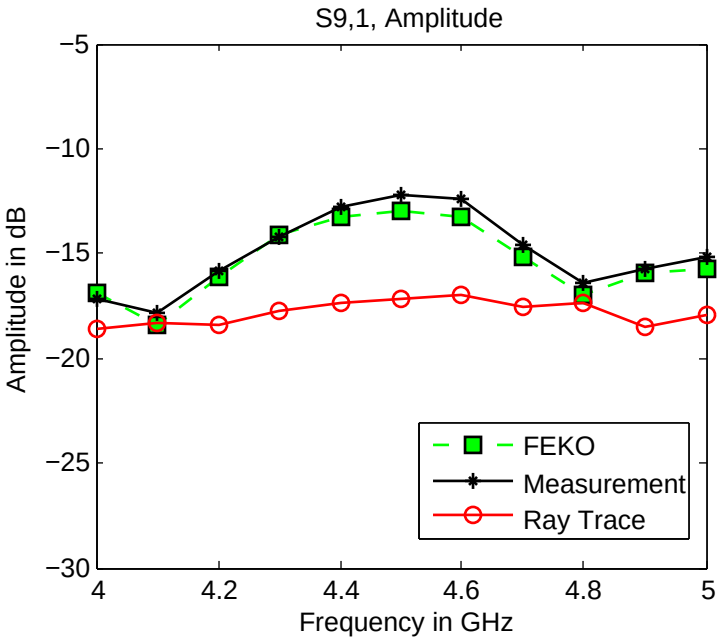

Figure A- 48. Phase Coupling between Port 1 and Port 9

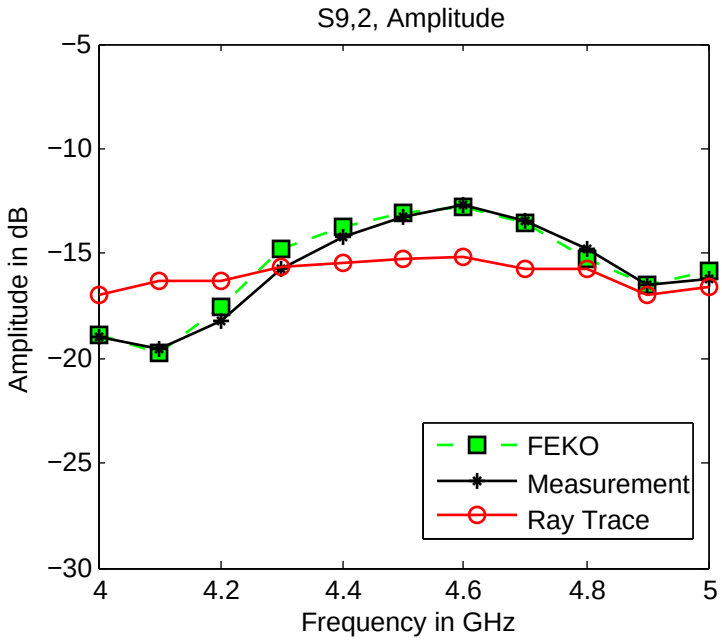

Figure A- 49. Amplitude Coupling between Port 2 and Port 9

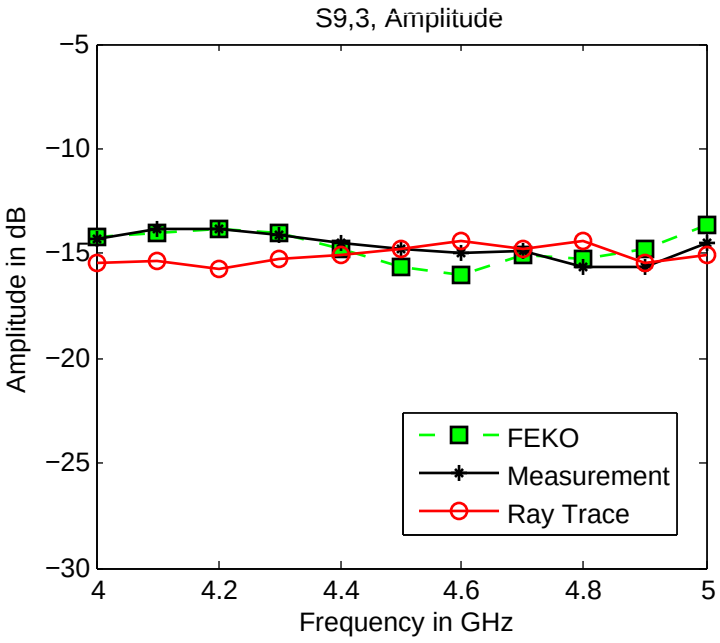

Figure A- 50. Amplitude Coupling between Port 3 and Port 9

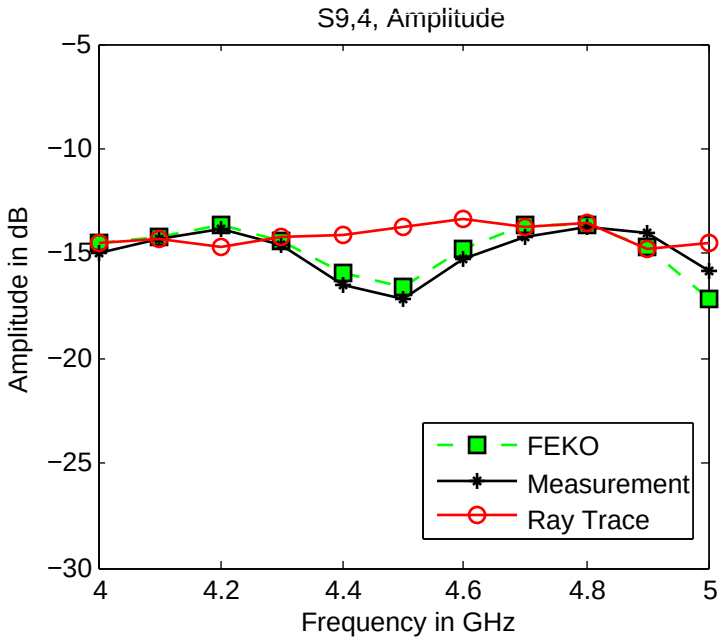

Figure A- 51. Amplitude Coupling between Port 4 and Port 9

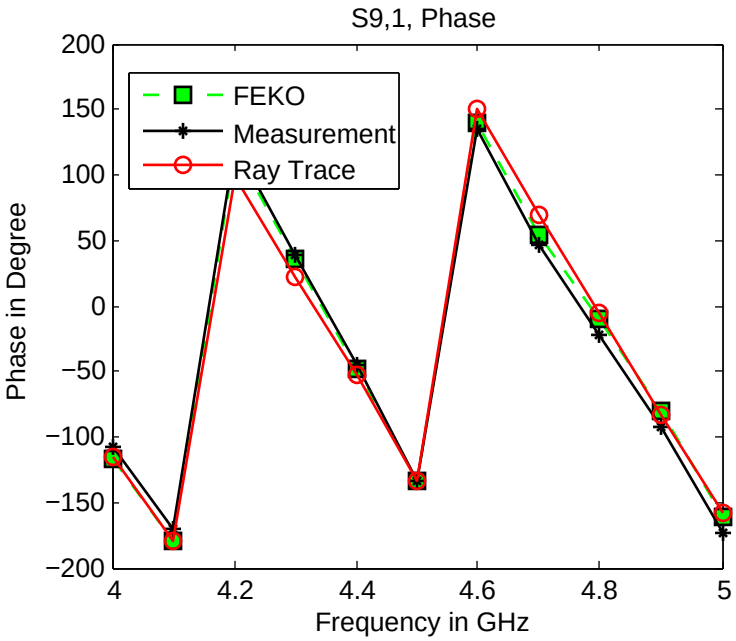

Figure A- 52. Phase Coupling between Port 1 and Port 9

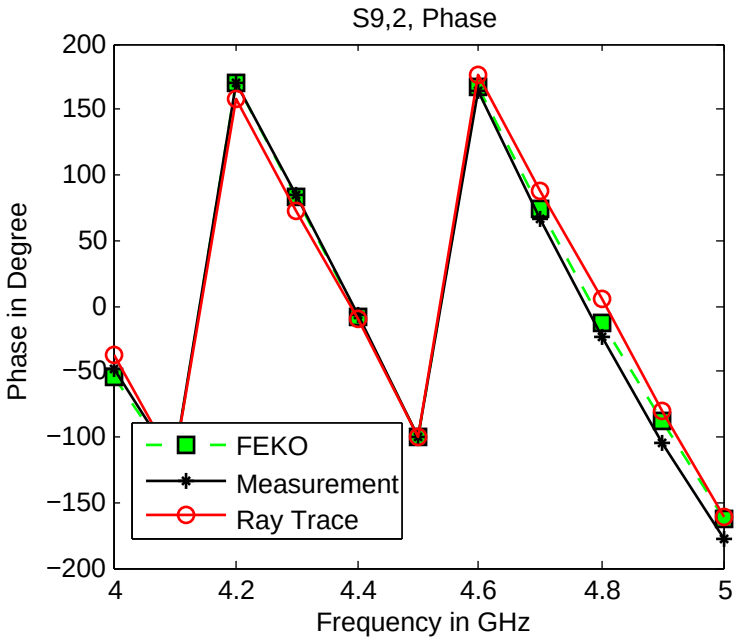

Figure A- 53. Phase Coupling between Port 2 and Port 9

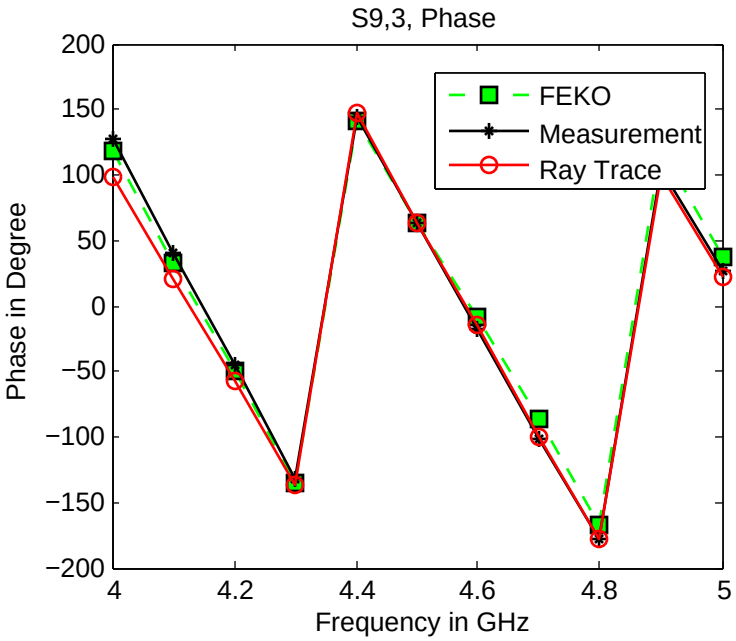

Figure A- 54. Phase Coupling between Port 3 and Port 9

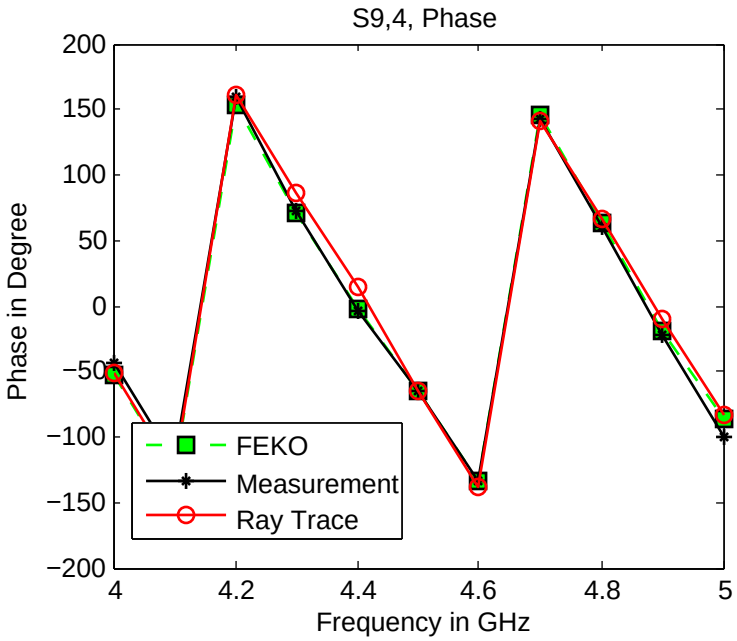

Figure A- 55. Phase Coupling between Port 4 and Port 9

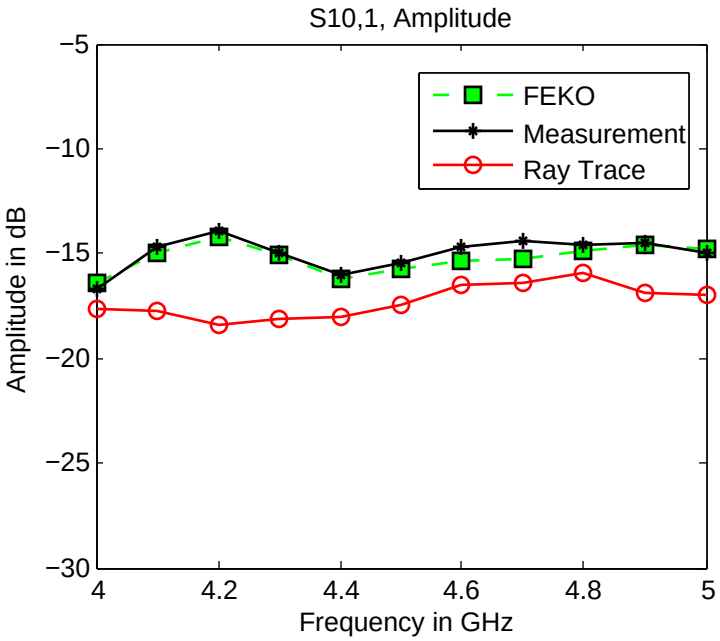

Figure A- 56. Amplitude Coupling between Port 1 and Port 10

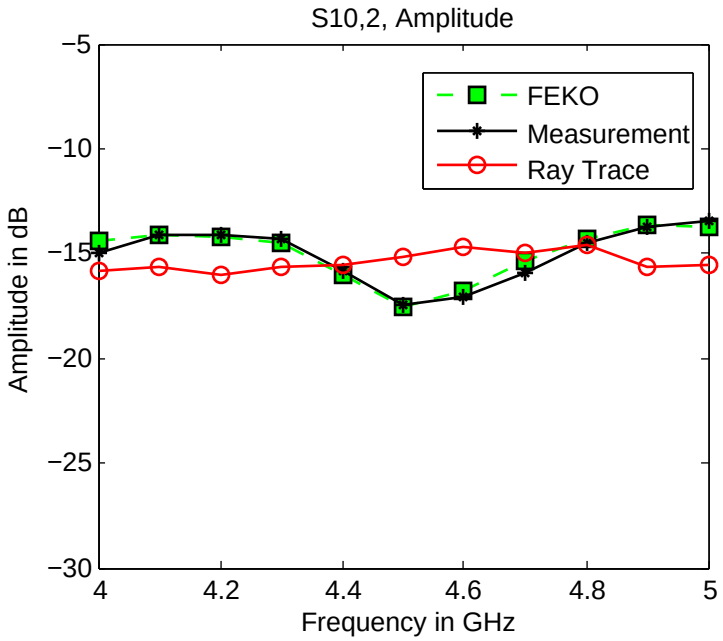

Figure A- 57. Amplitude Coupling between Port 2 and Port 10

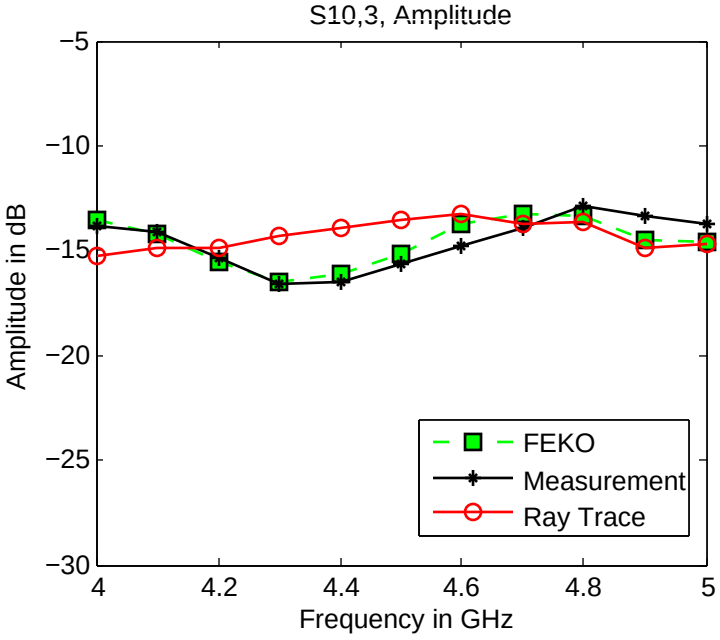

Figure A- 58. Amplitude Coupling between Port 3 and Port 10

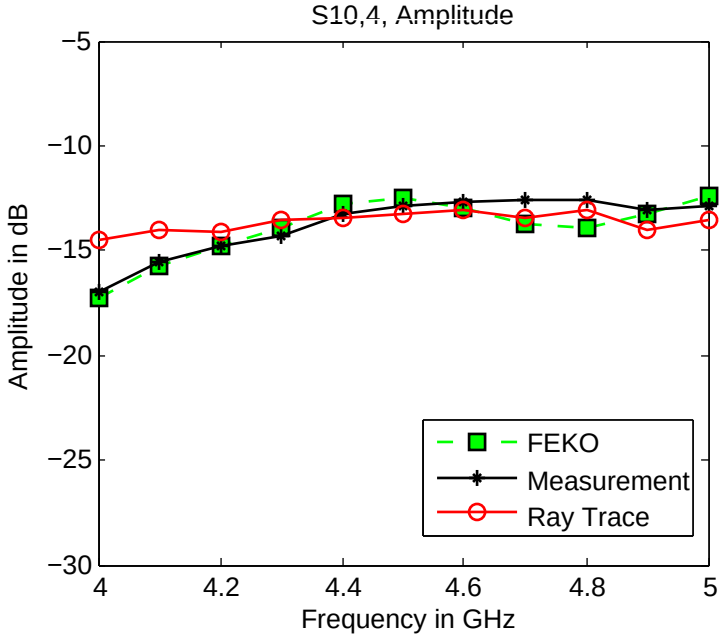

Figure A- 59. Amplitude Coupling between Port 4 and Port 10

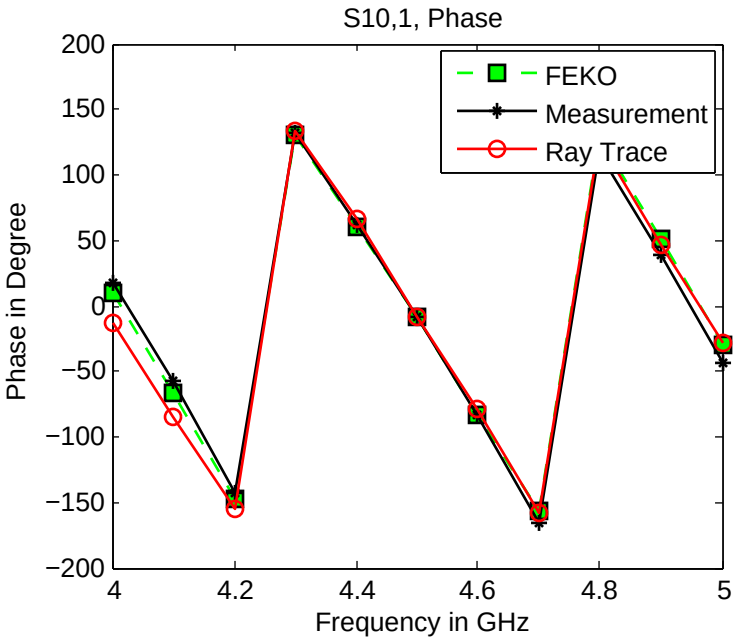

Figure A- 60. Phase Coupling between Port 1 and Port 10

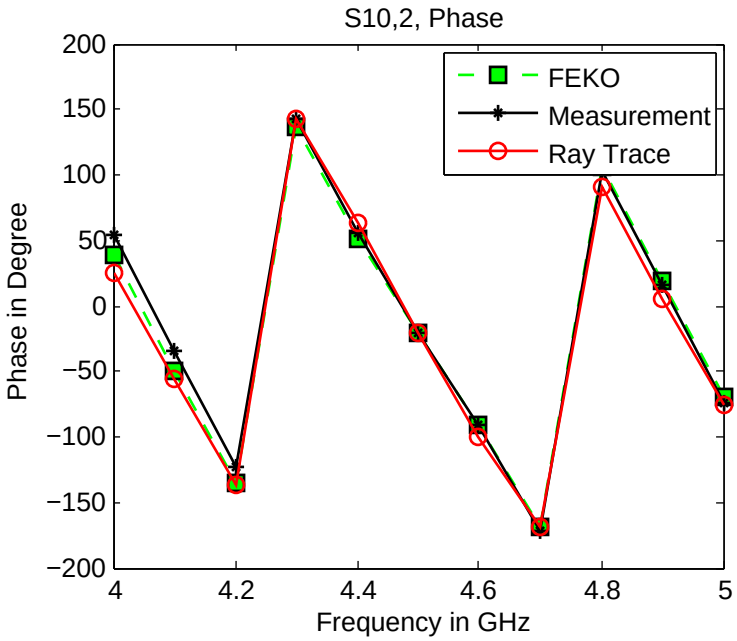

Figure A- 61. Phase Coupling between Port 2 and Port 10

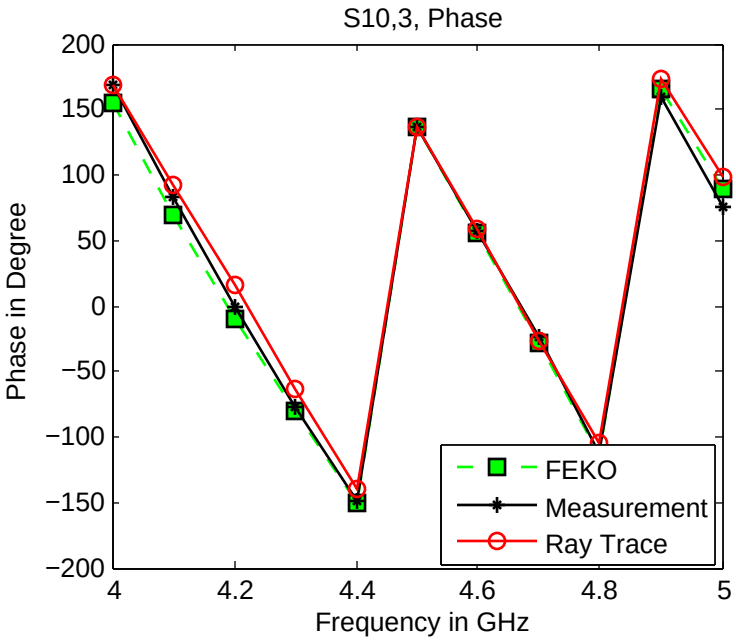

Figure A- 62. Phase Coupling between Port 3 and Port 10

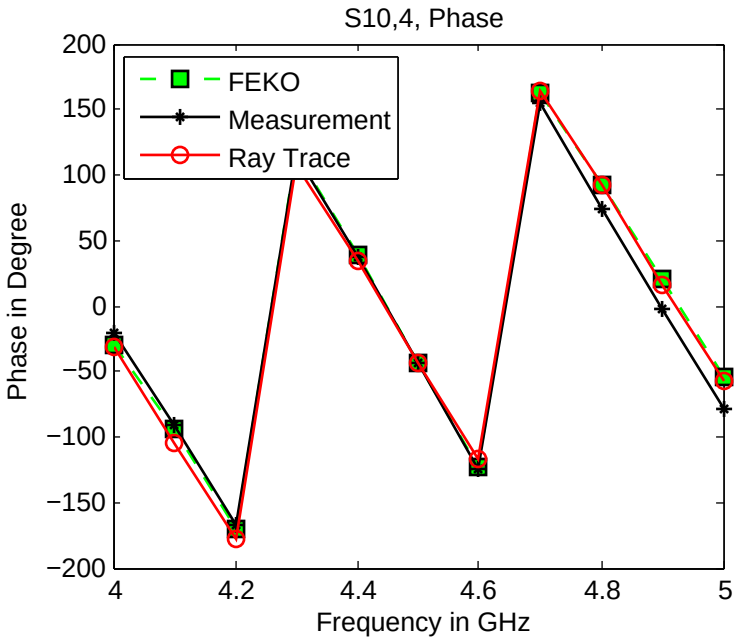

Figure A- 63. Phase Coupling between Port 4 and Port 10

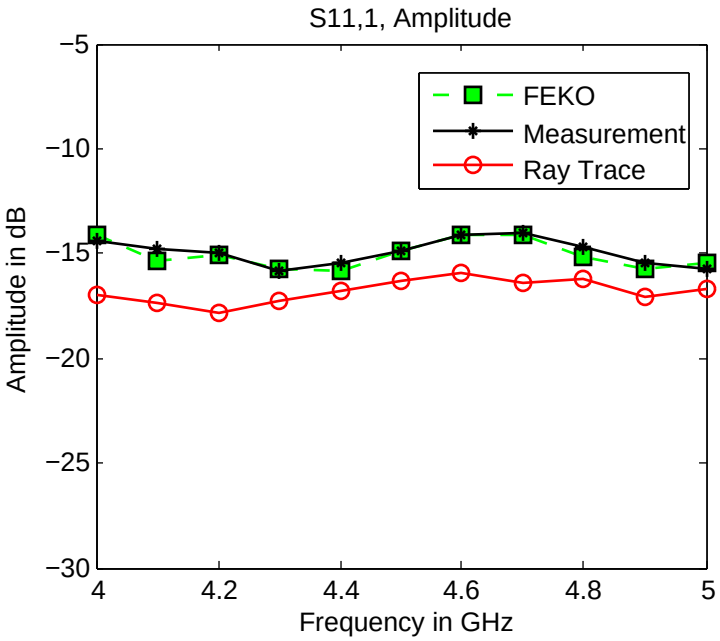

Figure A- 64. Amplitude Coupling between Port 1 and Port 11

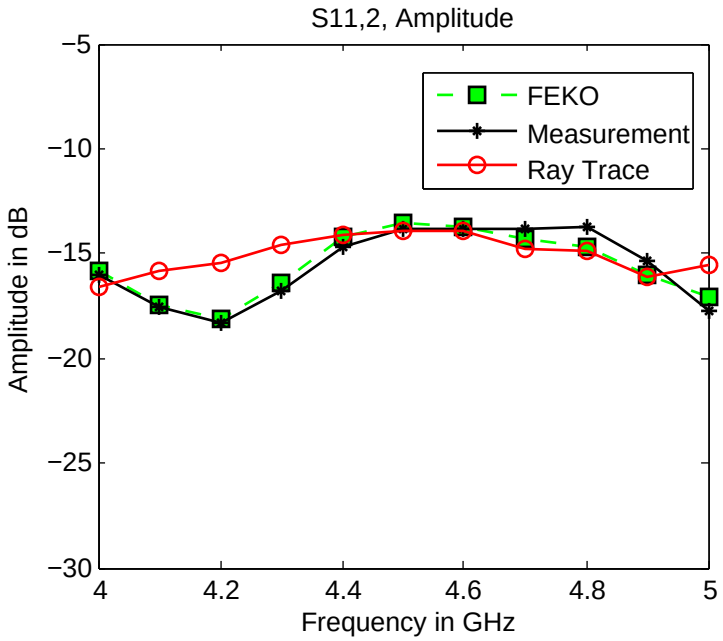

Figure A- 65. Amplitude Coupling between Port 2 and Port 11

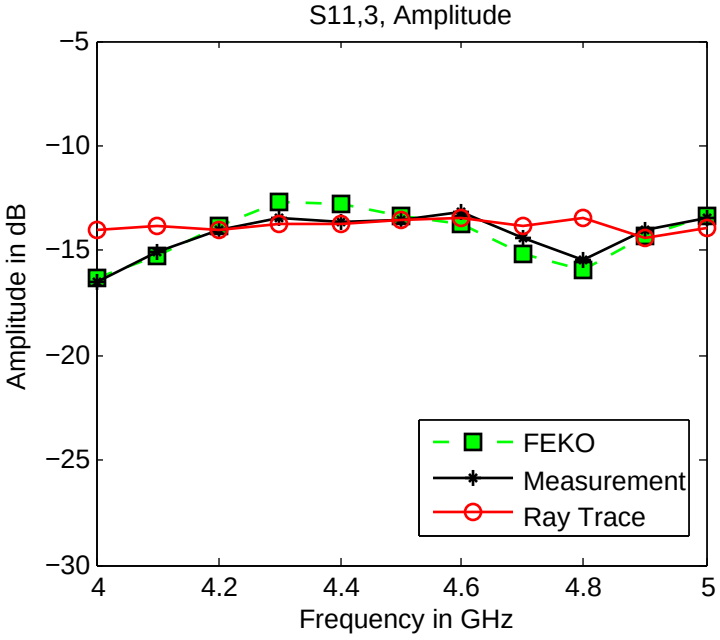

Figure A- 66. Amplitude Coupling between Port 3 and Port 11

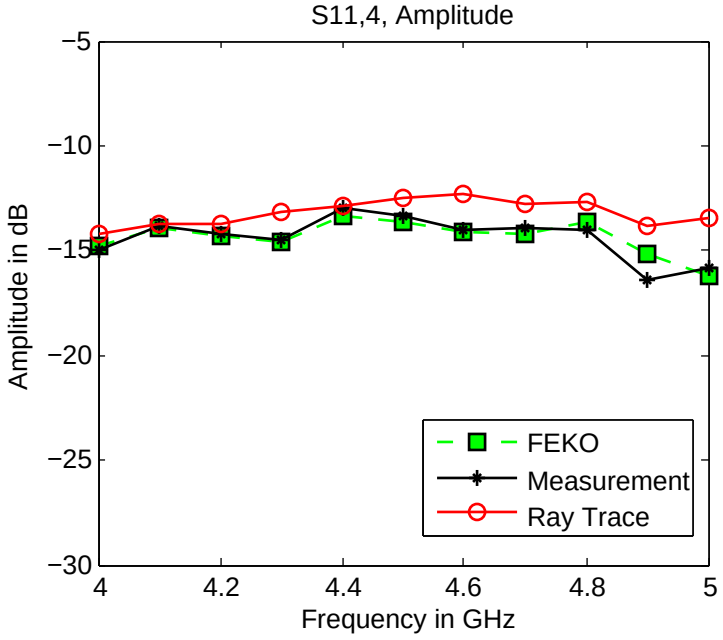

Figure A- 67. Amplitude Coupling between Port 4 and Port 11

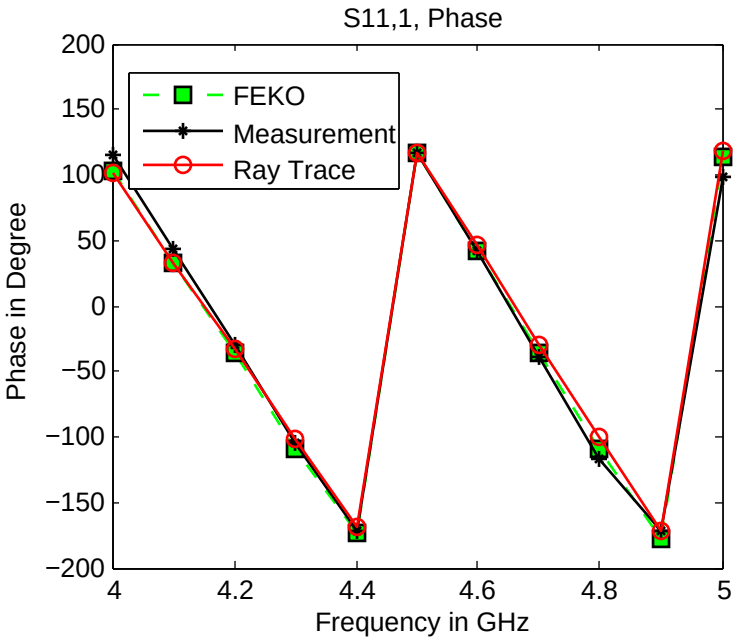

Figure A- 68. Phase Coupling between Port 1 and Port 11

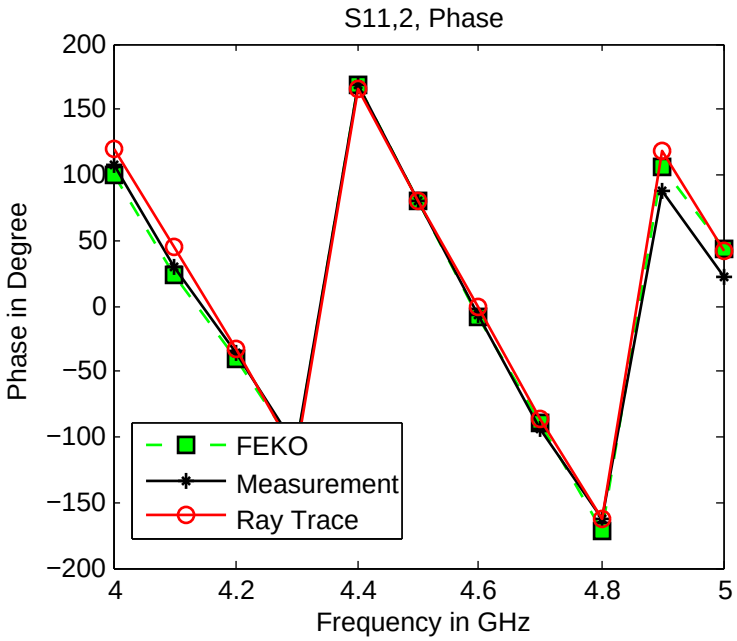

Figure A- 69. Phase Coupling between Port 2 and Port 11

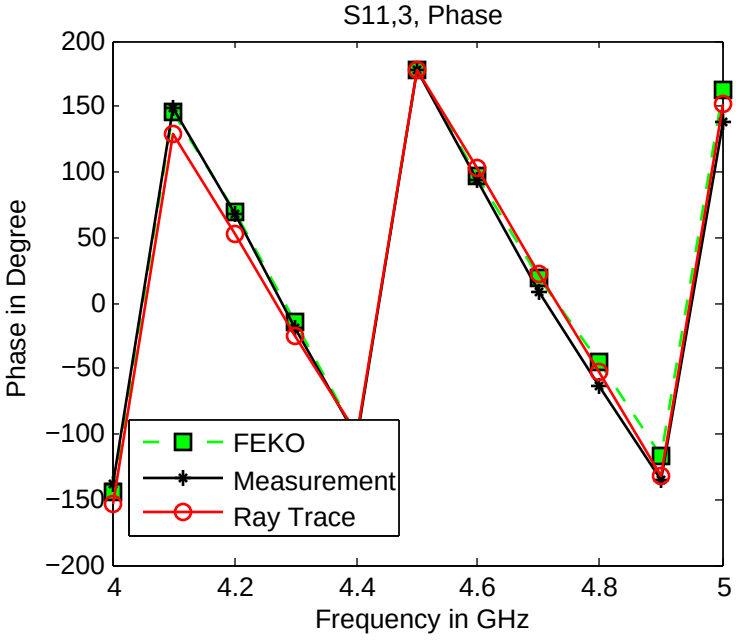

Figure A- 70. Phase Coupling between Port 3 and Port 11

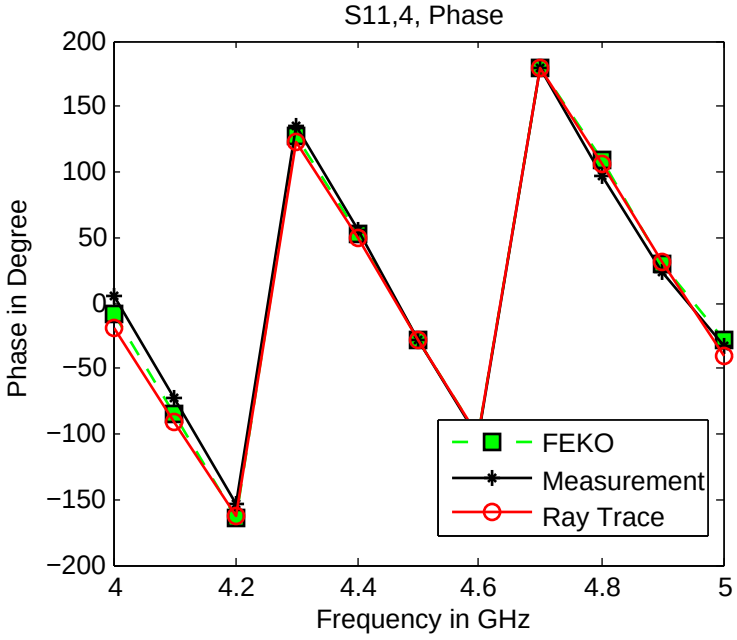

Figure A- 71. Phase Coupling between Port 4 and Port 11

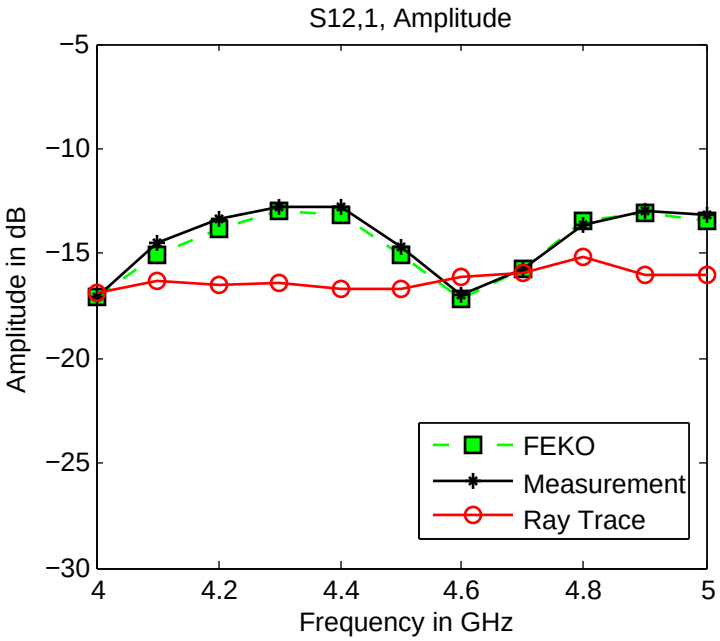

Figure A- 72. Amplitude Coupling between Port 1 and Port 12

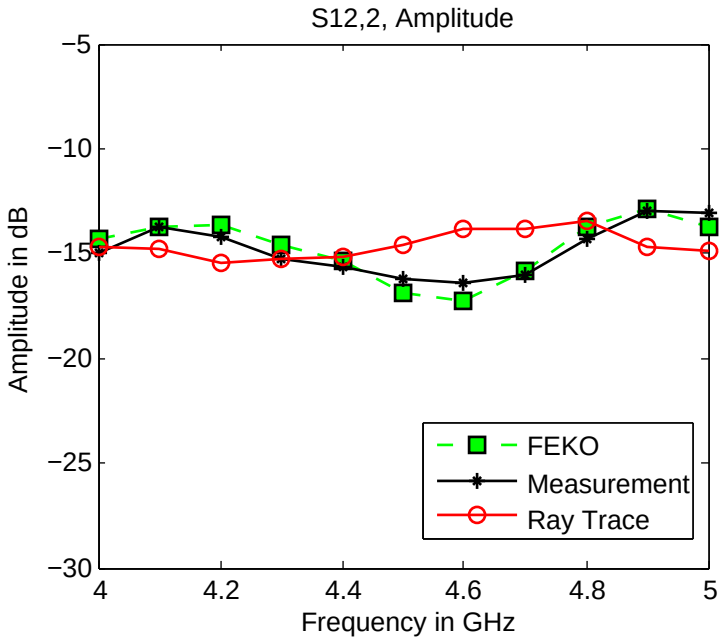

Figure A- 73. Amplitude Coupling between Port 2 and Port 12

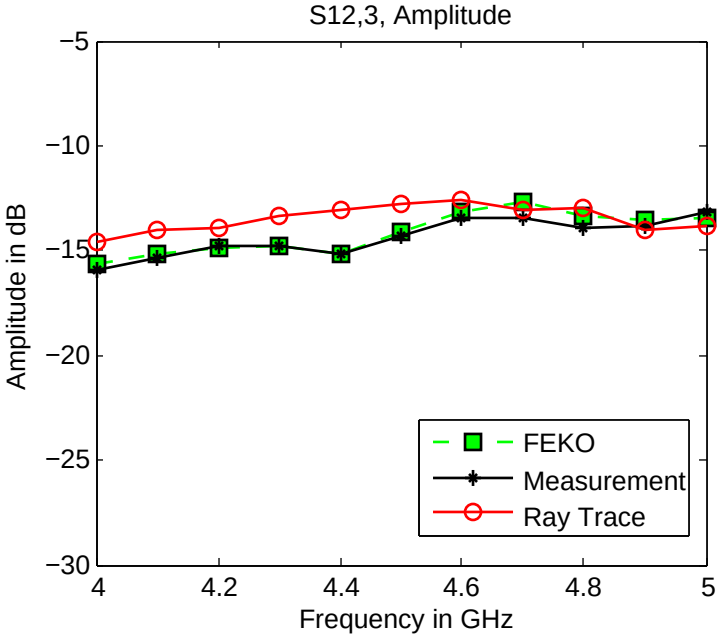

Figure A- 74. Amplitude Coupling between Port 3 and Port 12

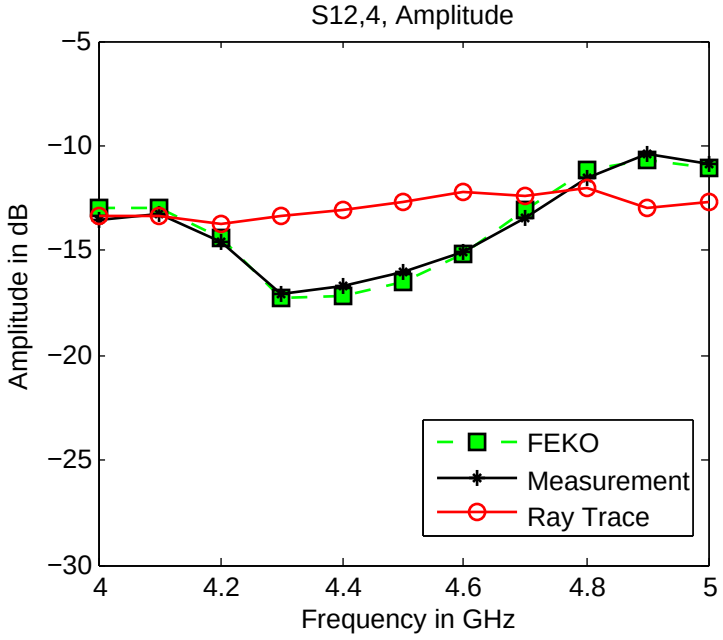

Figure A- 75. Amplitude Coupling between Port 4 and Port 12

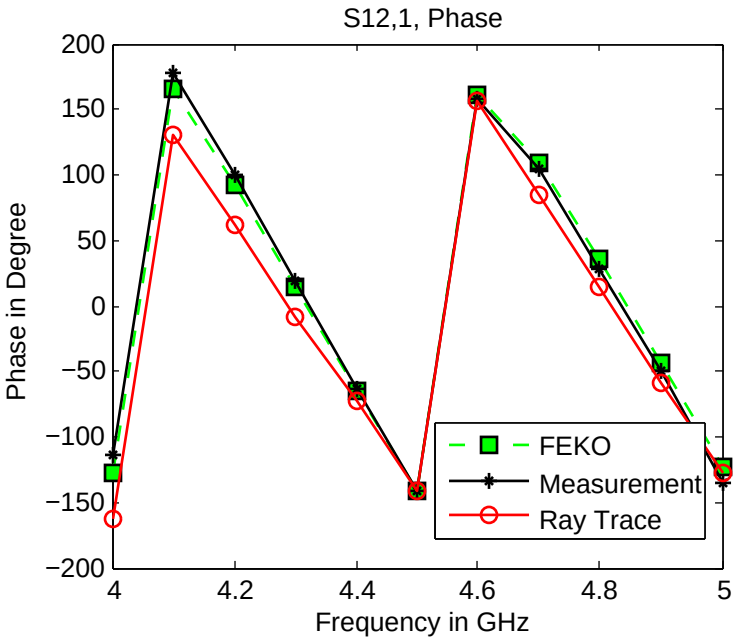

Figure A- 76. Phase Coupling between Port 1 and Port 12

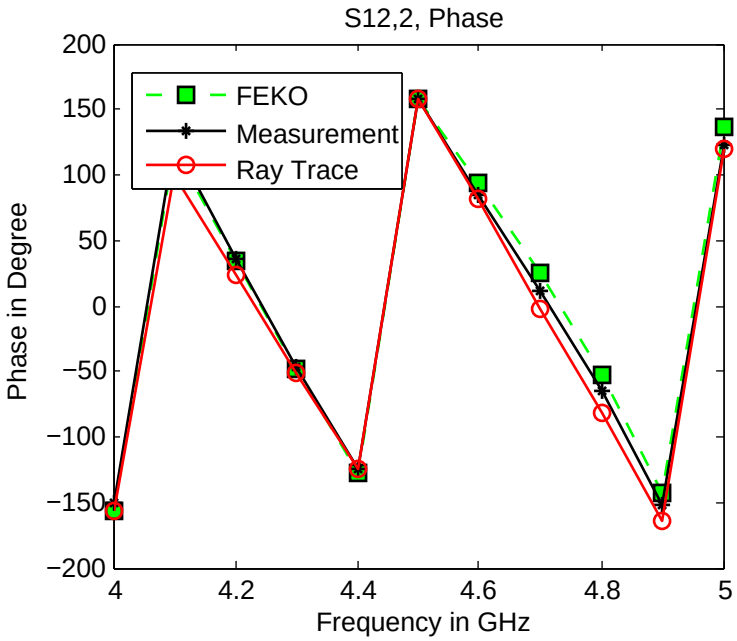

Figure A- 77. Phase Coupling between Port 2 and Port 12

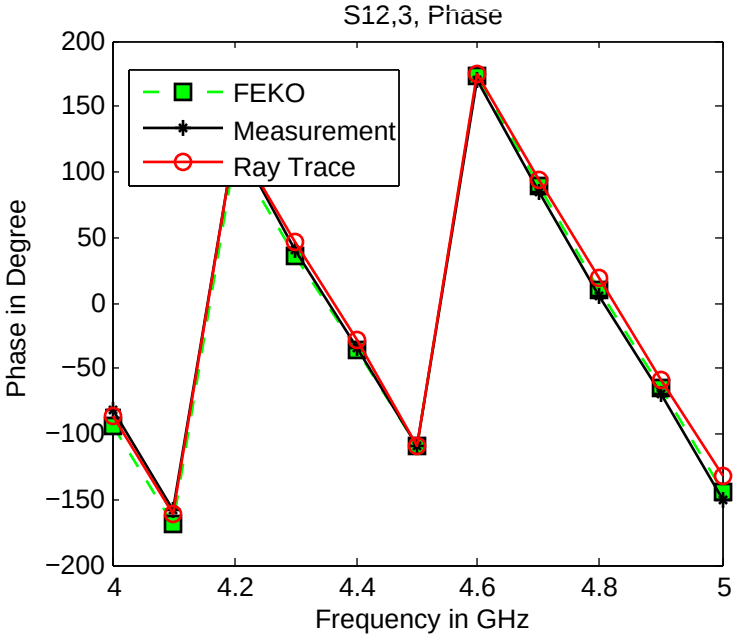

Figure A- 78. Phase Coupling between Port 3 and Port 12

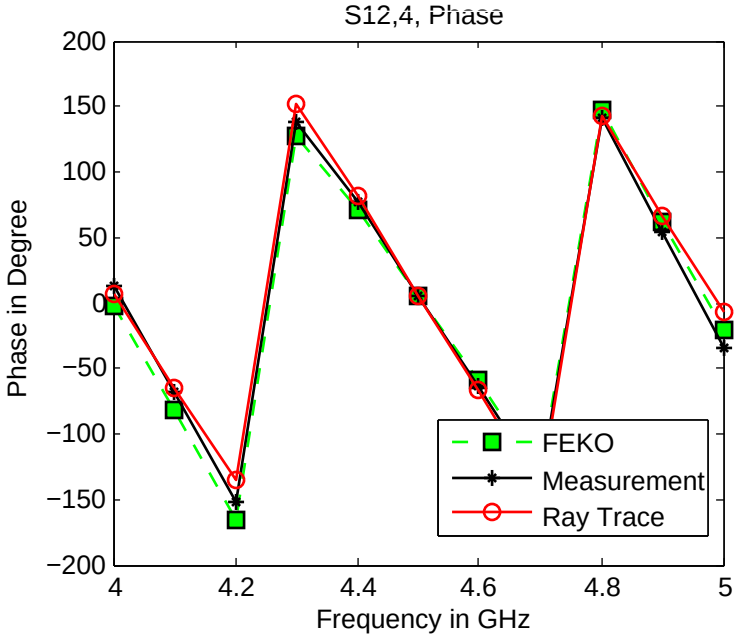

Figure A- 79. Phase Coupling between Port 4 and Port 12

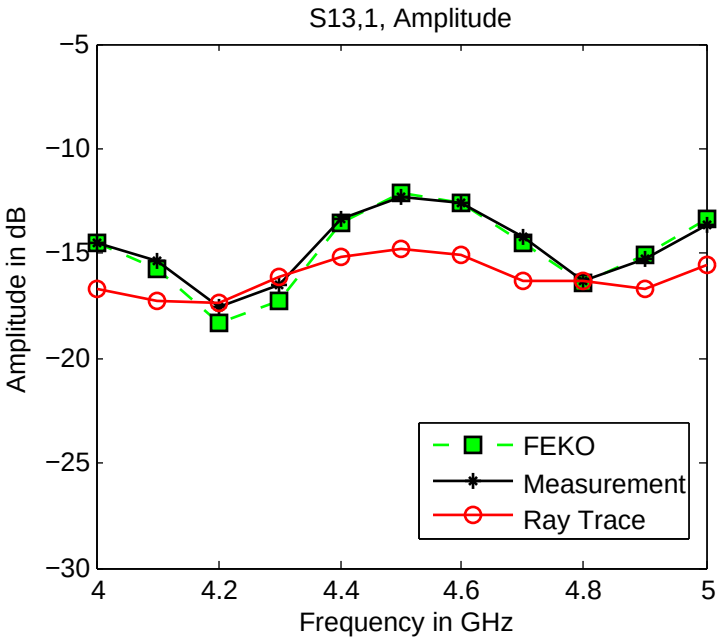

Figure A- 80. Amplitude Coupling between Port 1 and Port 13

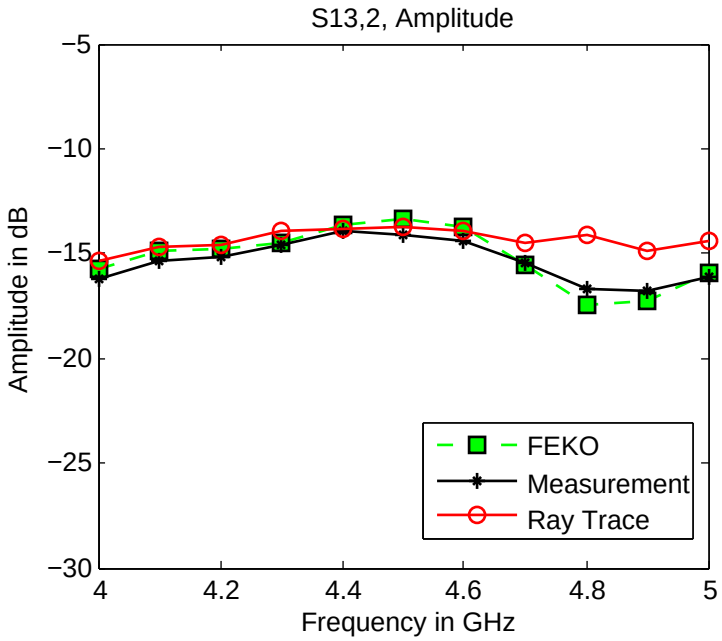

Figure A- 81. Amplitude Coupling between Port 2 and Port 13

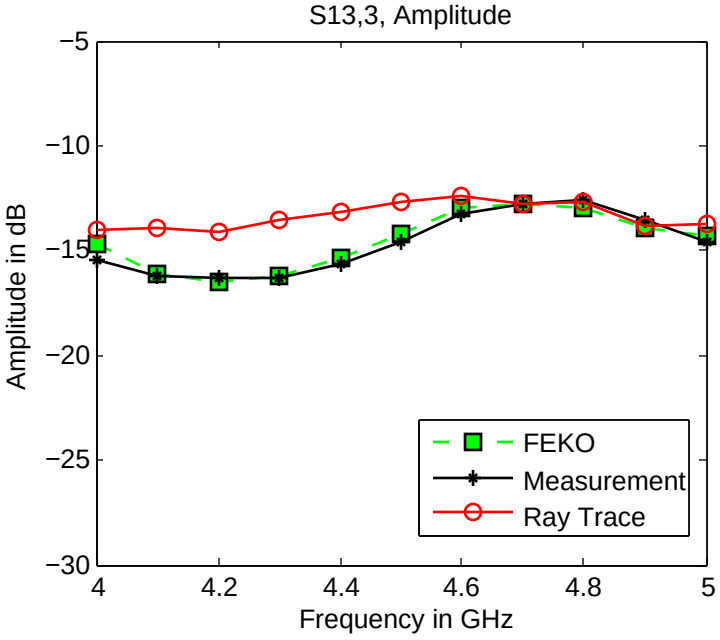

Figure A- 82. Amplitude Coupling between Port 3 and Port 13

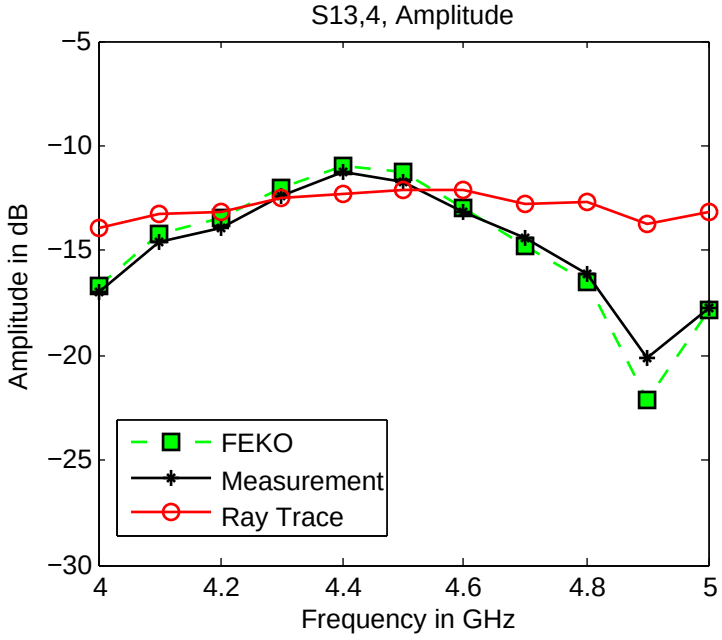

Figure A- 83. Amplitude Coupling between Port 4 and Port 13

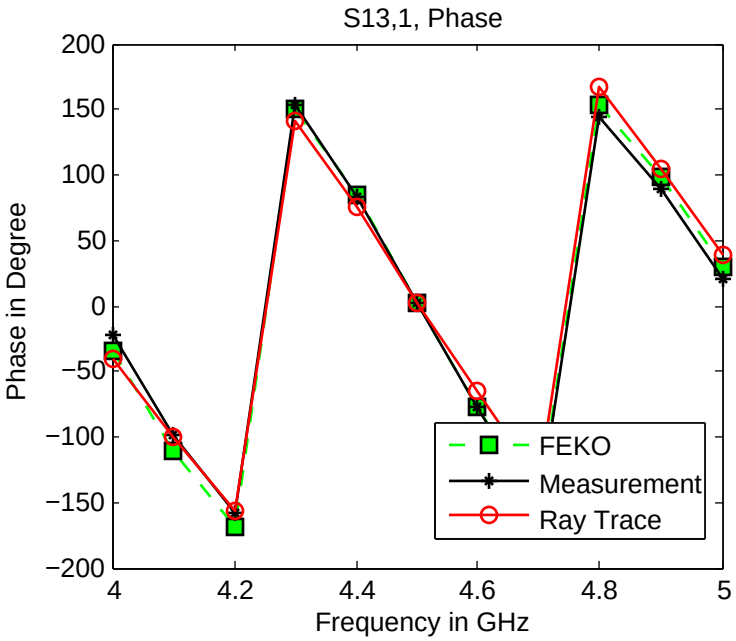

Figure A- 84. Phase Coupling between Port 1 and Port 13

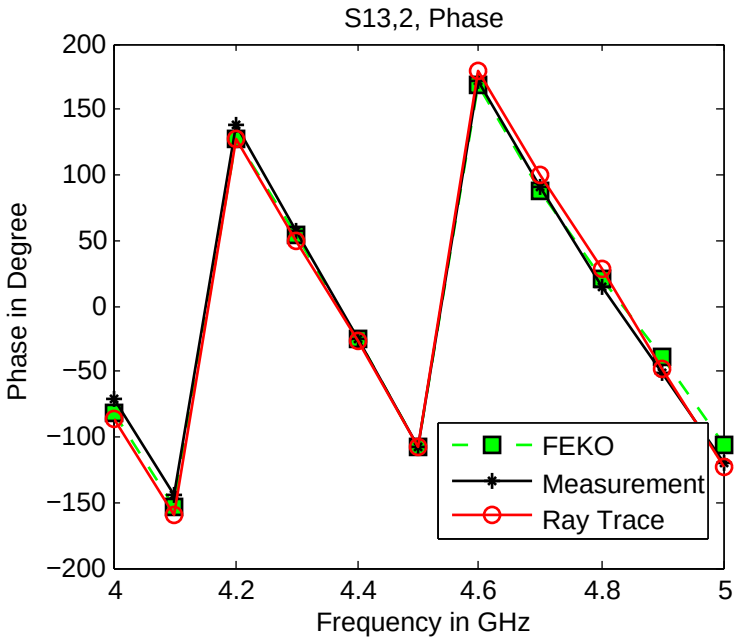

Figure A- 85. Phase Coupling between Port 2 and Port 13

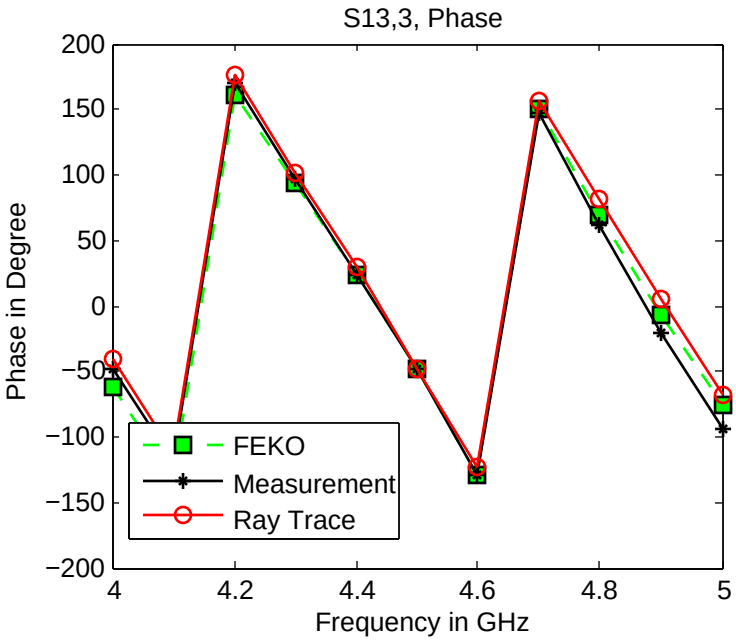

Figure A- 86. Phase Coupling between Port 3 and Port 13

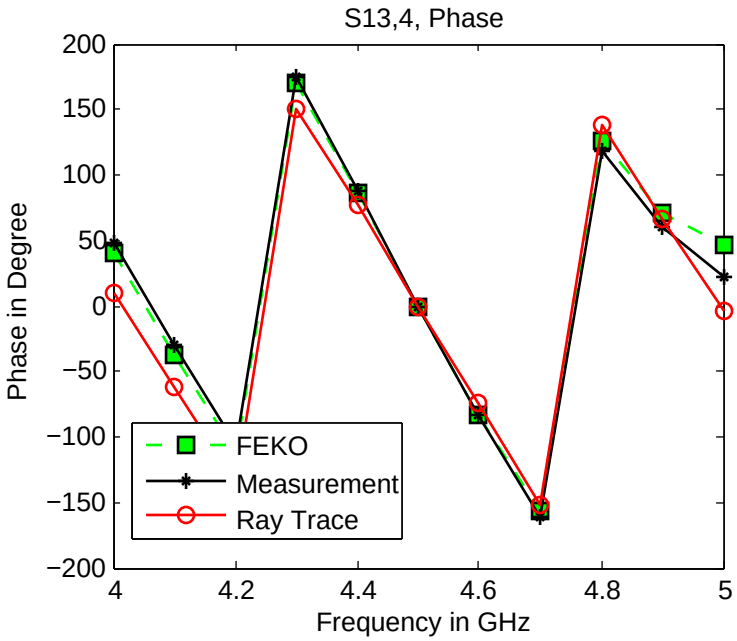

Figure A- 87. Phase Coupling between Port 4 and Port 13

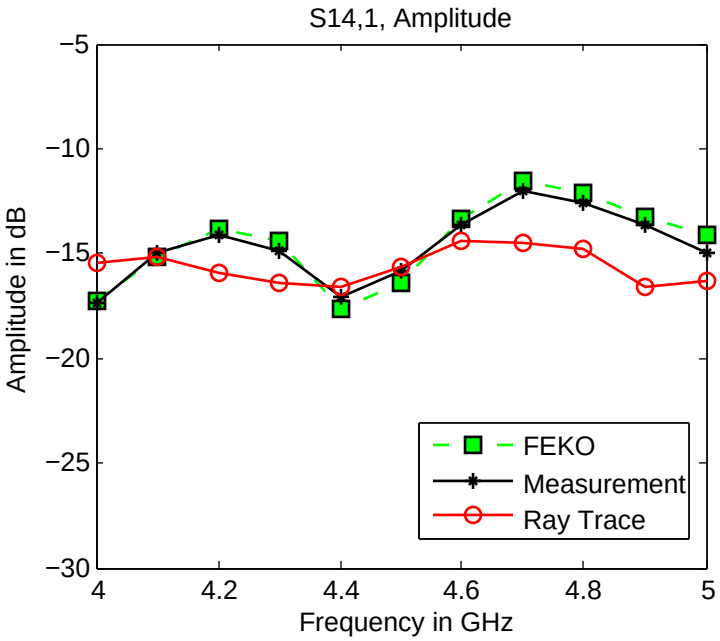

Figure A- 88. Amplitude Coupling between Port 1 and Port 14

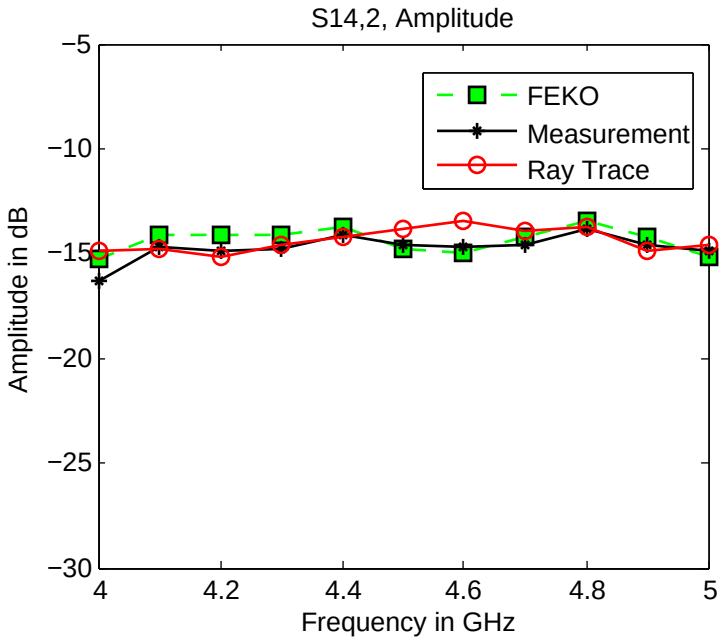

Figure A- 89. Amplitude Coupling between Port 2 and Port 14

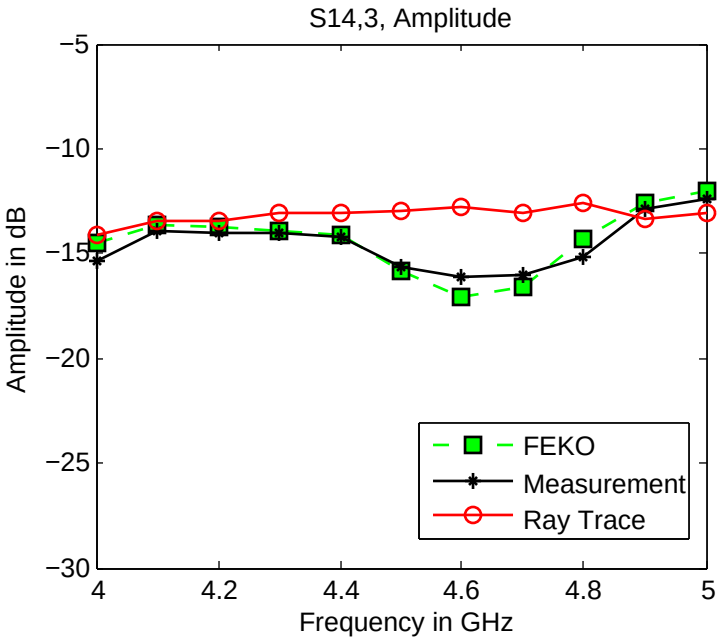

Figure A- 90. Amplitude Coupling between Port 3 and Port 14

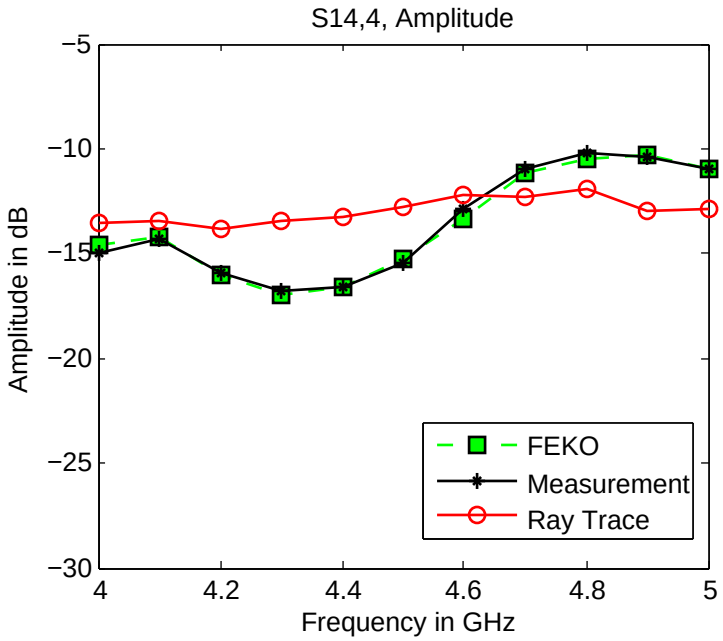

Figure A- 91. Amplitude Coupling between Port 4 and Port 14

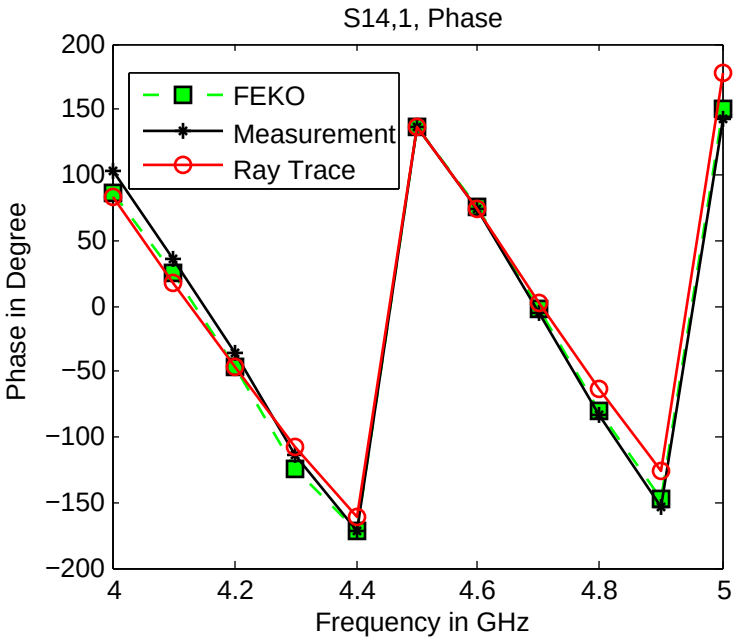

Figure A- 92. Phase Coupling between Port 1 and Port 14

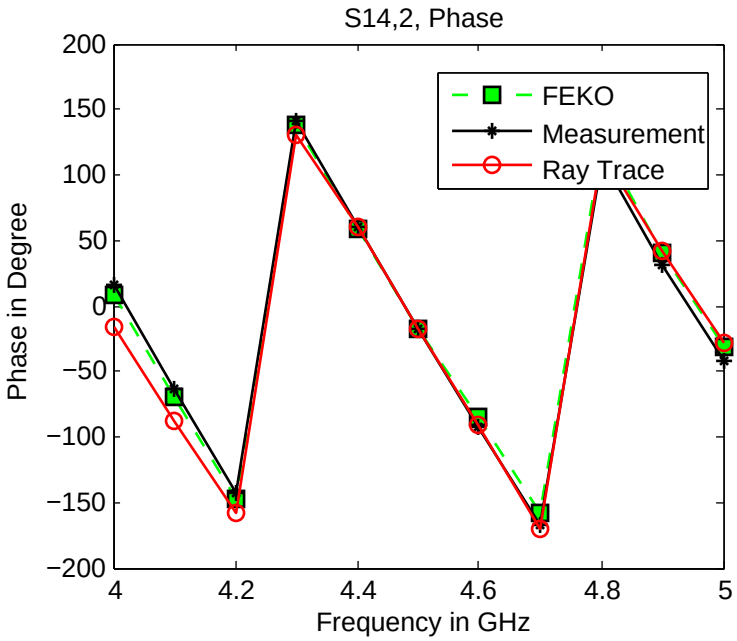

Figure A- 93. Phase Coupling between Port 2 and Port 14

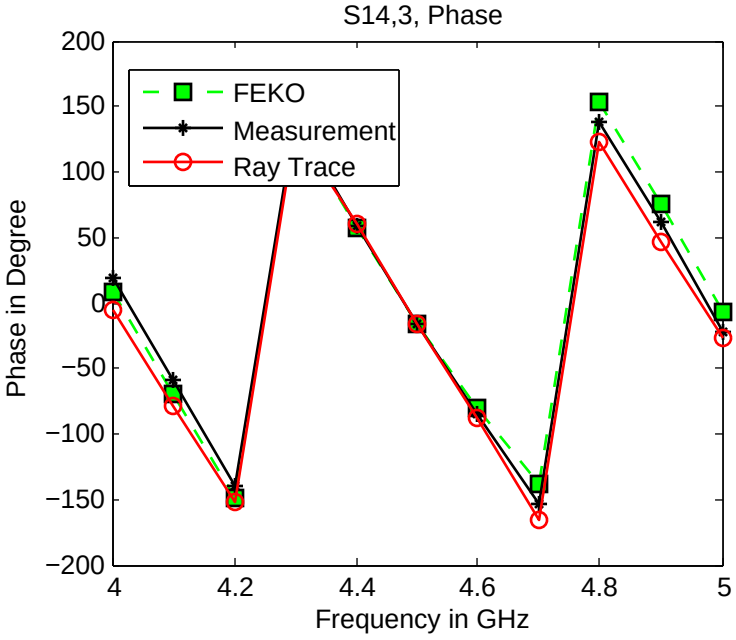

Figure A- 94. Phase Coupling between Port 3 and Port 14

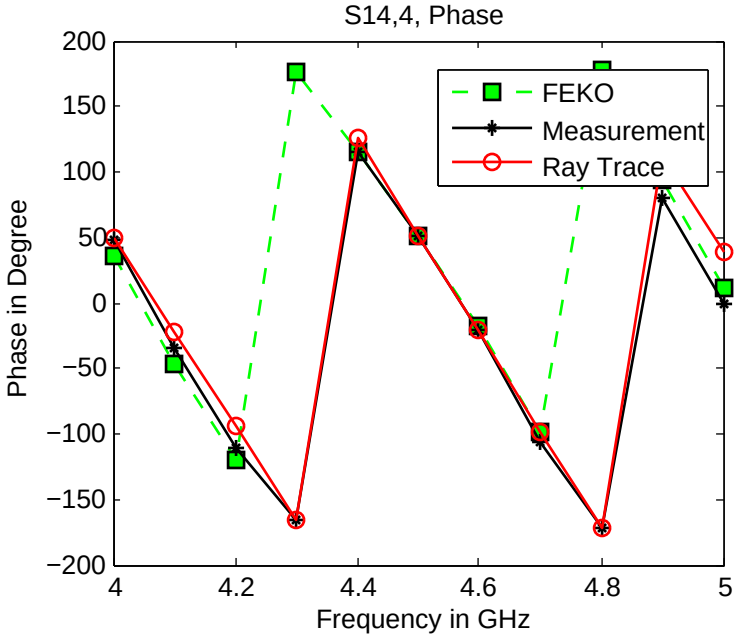

Figure A- 95. Phase Coupling between Port 4 and Port 14

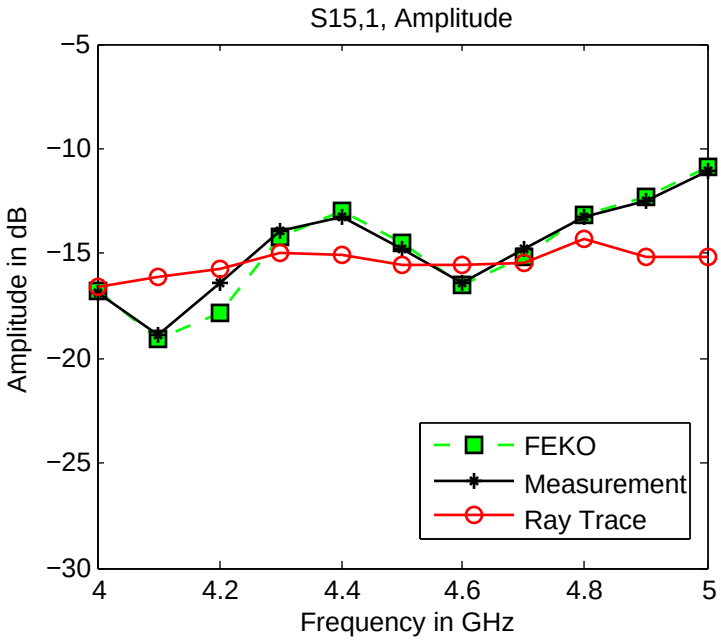

Figure A- 96. Amplitude Coupling between Port 1 and Port 15

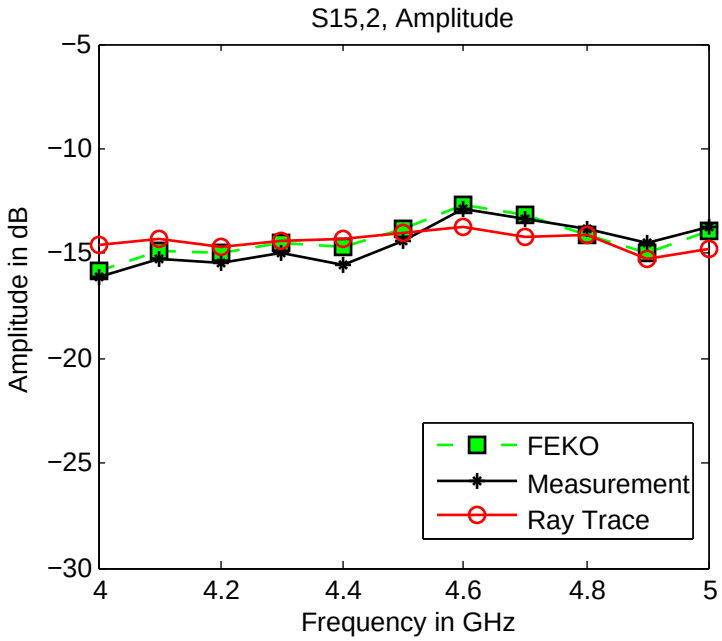

Figure A- 97. Amplitude Coupling between Port 2 and Port 15

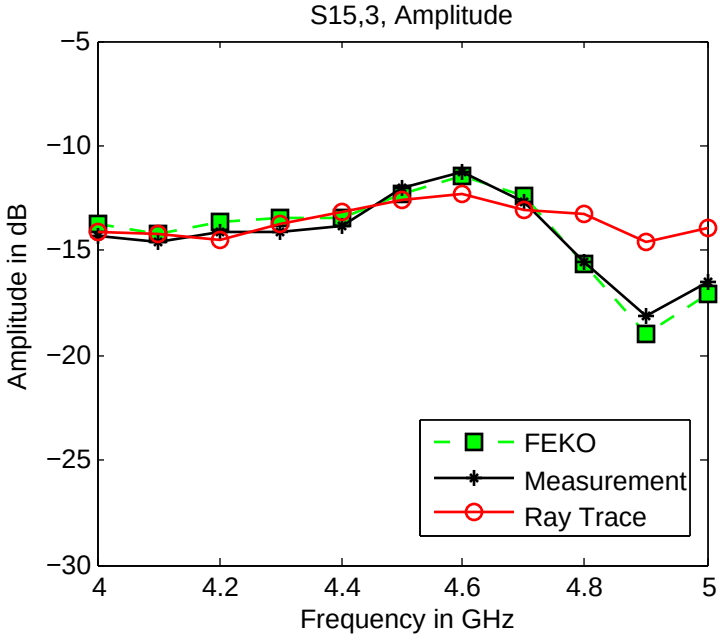

Figure A- 98. Amplitude Coupling between Port 3 and Port 15

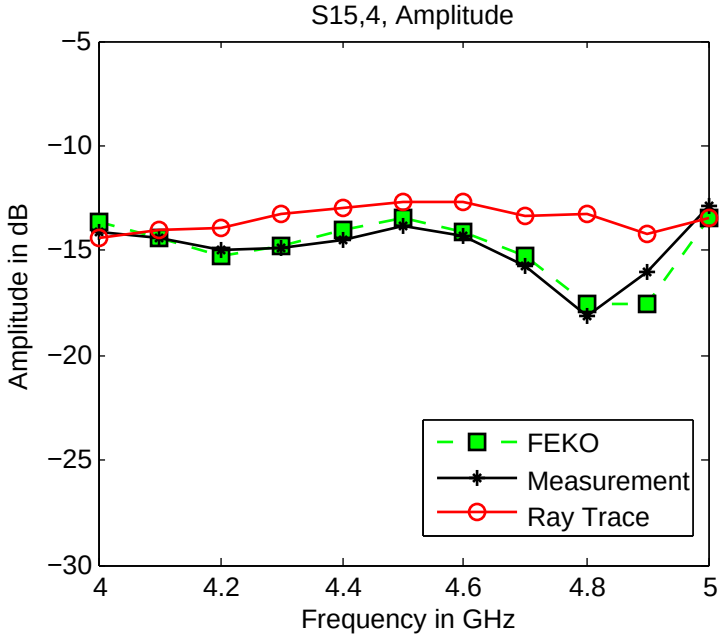

Figure A- 99. Amplitude Coupling between Port 4 and Port 15

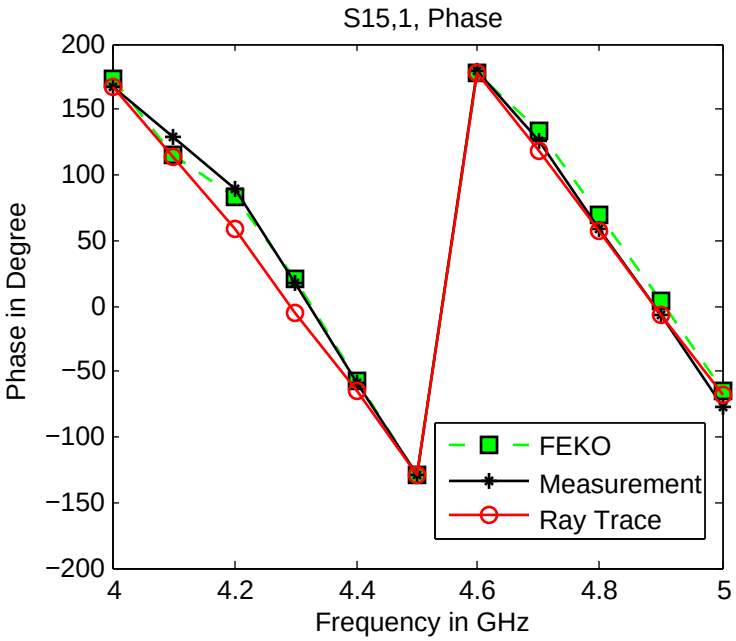

Figure A- 100. Phase Coupling between Port 1 and Port 15

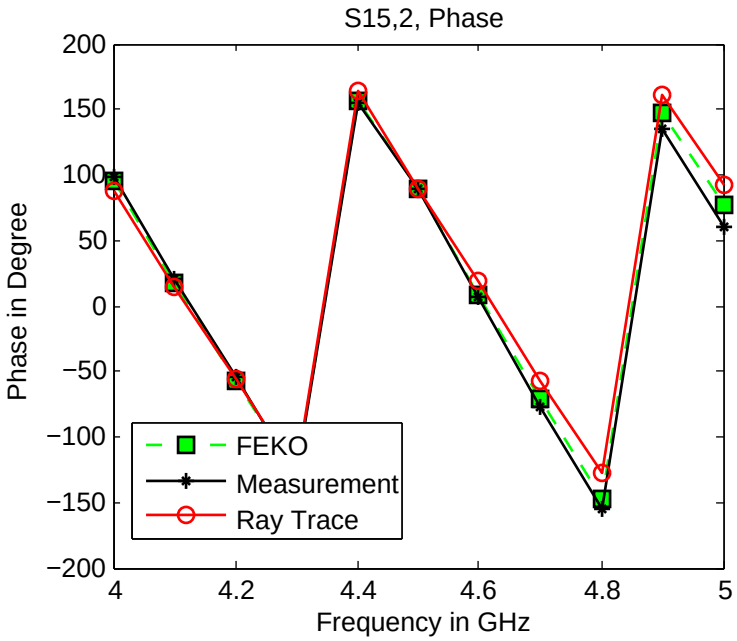

Figure A- 101. Phase Coupling between Port 2 and Port 15

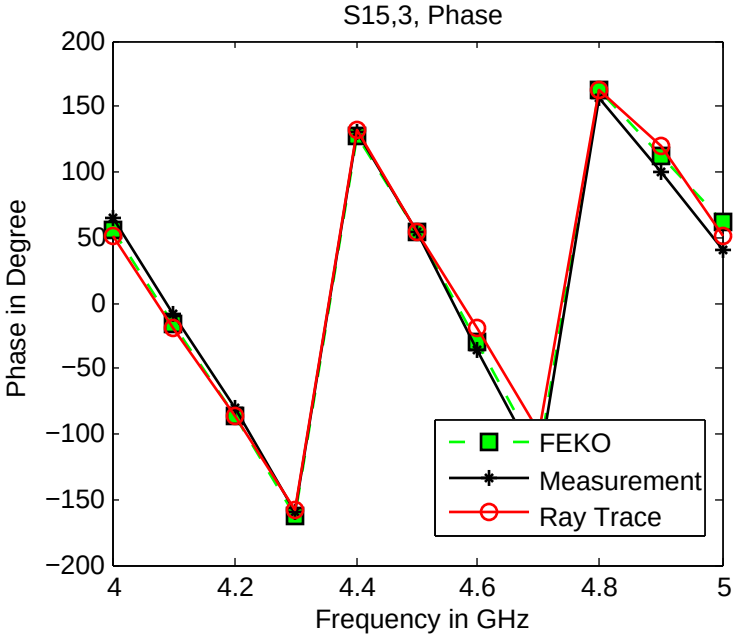

Figure A- 102. Phase Coupling between Port 3 and Port 15

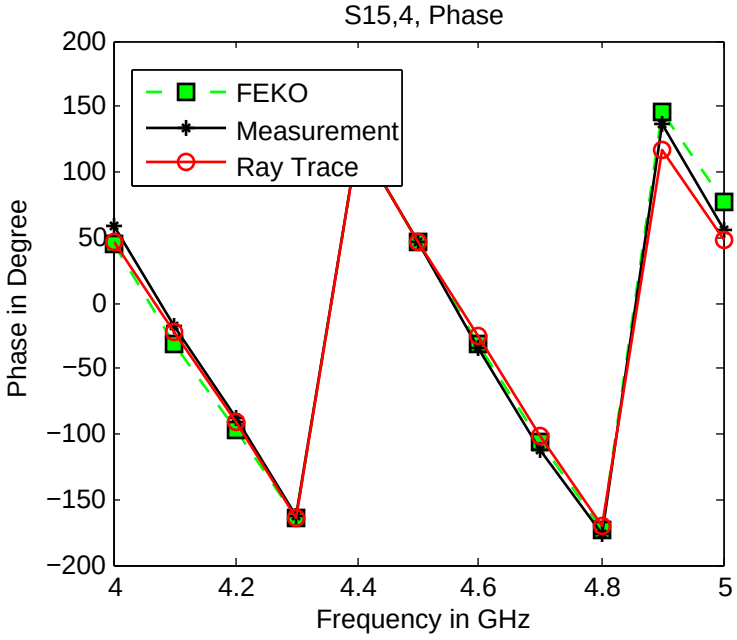

Figure A- 103. Phase Coupling between Port 4 and Port 15

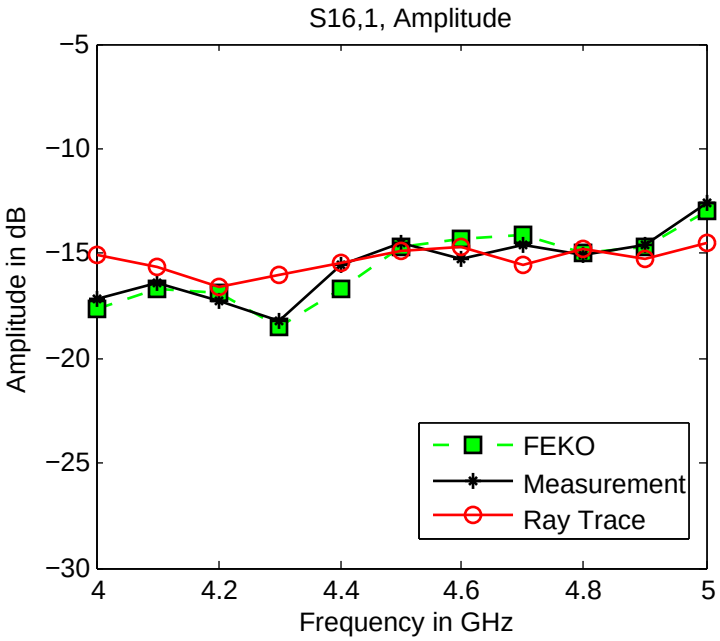

Figure A- 104. Amplitude Coupling between Port 1 and Port 16

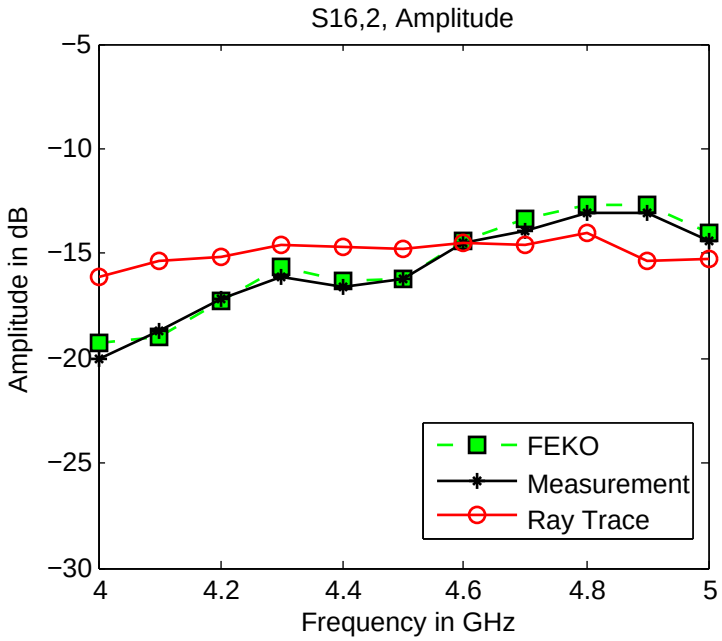

Figure A- 105. Amplitude Coupling between Port 2 and Port 16

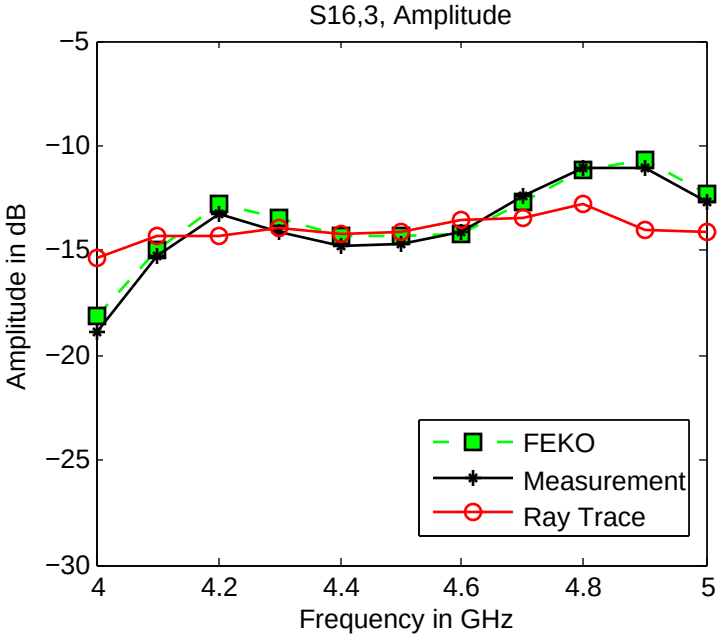

Figure A- 106. Amplitude Coupling between Port 3 and Port 16

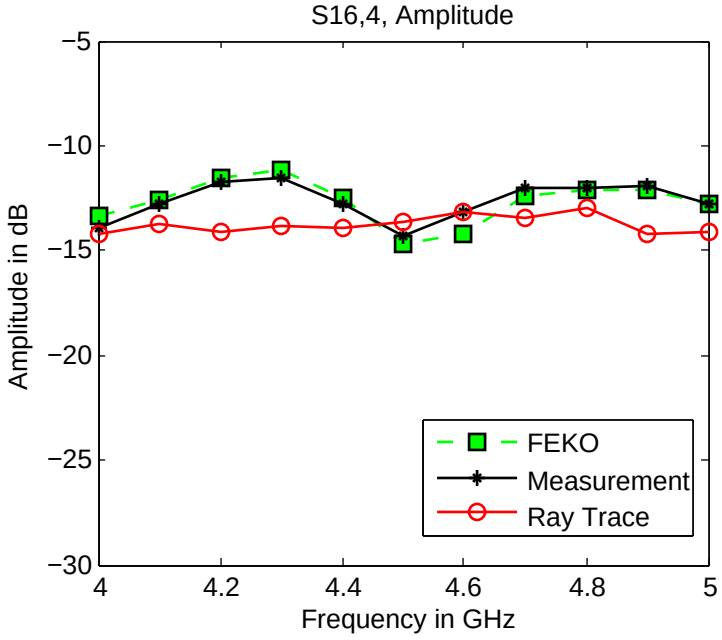

Figure A- 107. Amplitude Coupling between Port 4 and Port 16

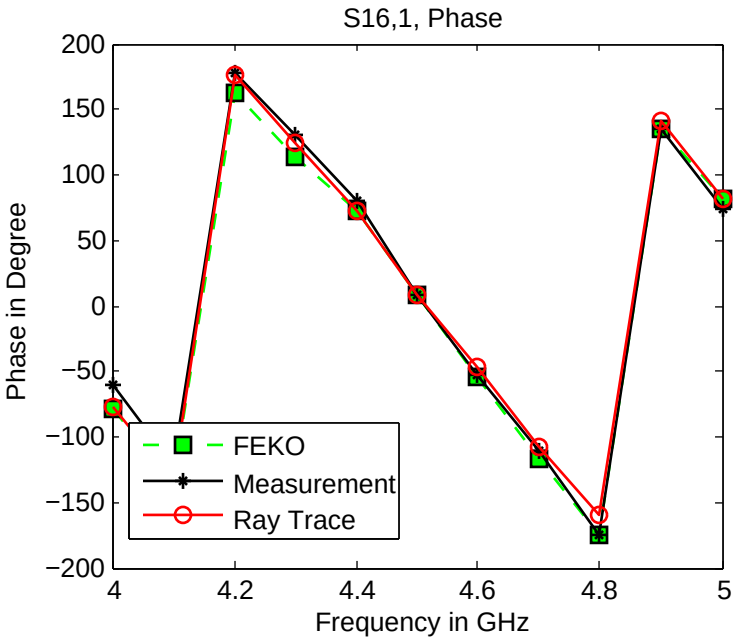

Figure A- 108. Phase Coupling between Port 1 and Port 16

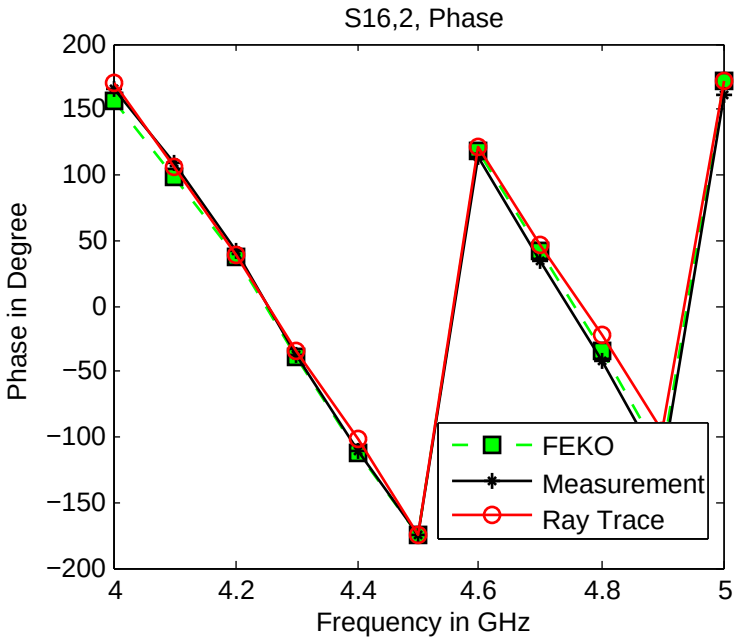

Figure A- 109. Phase Coupling between Port 2 and Port 16

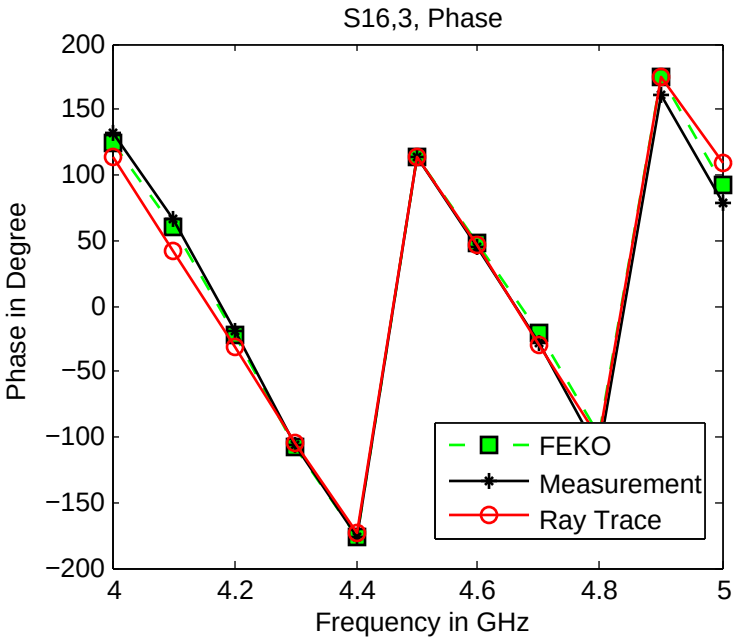

Figure A- 110. Phase Coupling between Port 3 and Port 16

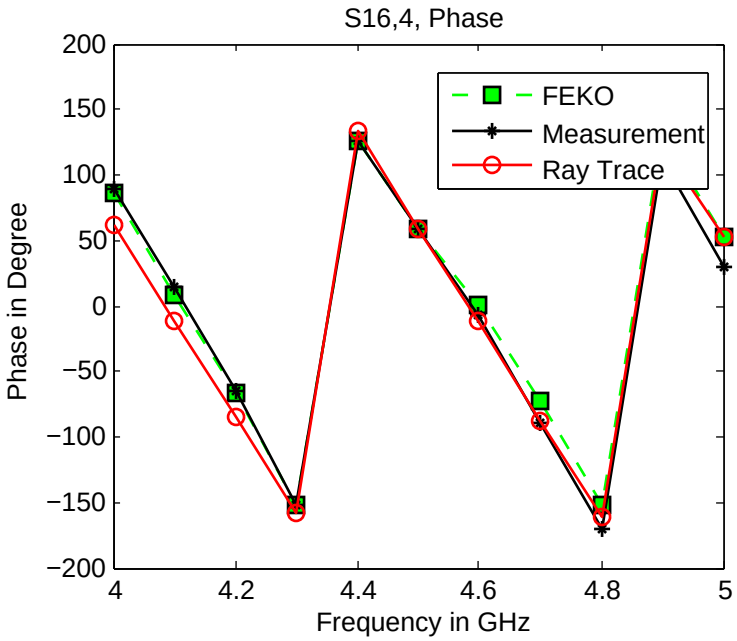

Figure A- 111. Phase Coupling between Port 4 and Port 16

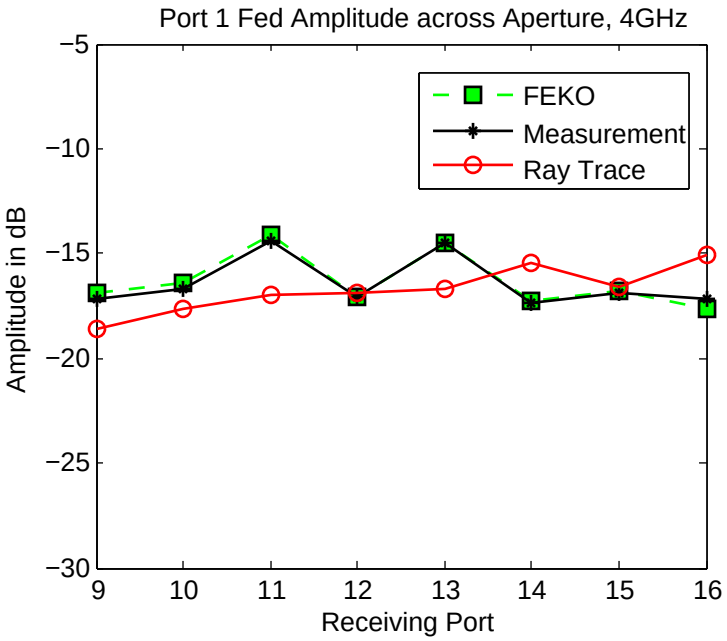

Figure A- 112. Amplitude across Aperture for Port 1 (4GHz)

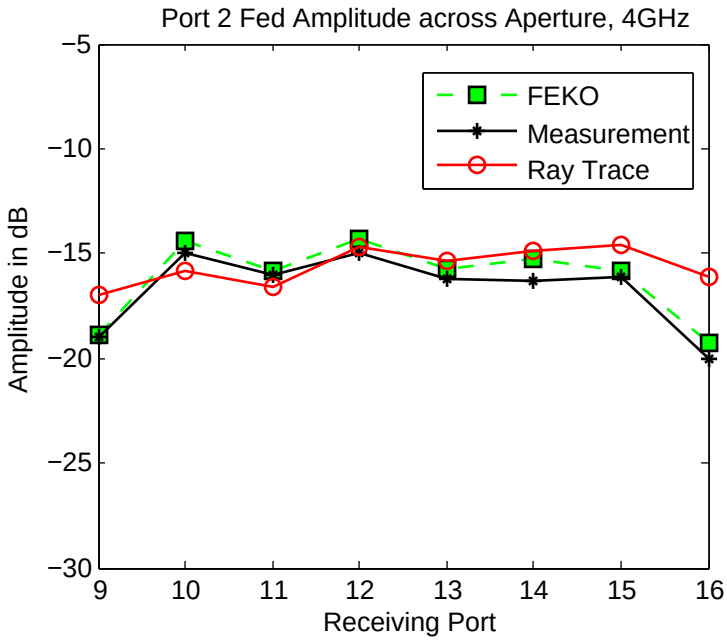

Figure A- 113. Amplitude across Aperture for Port 2 (4GHz)

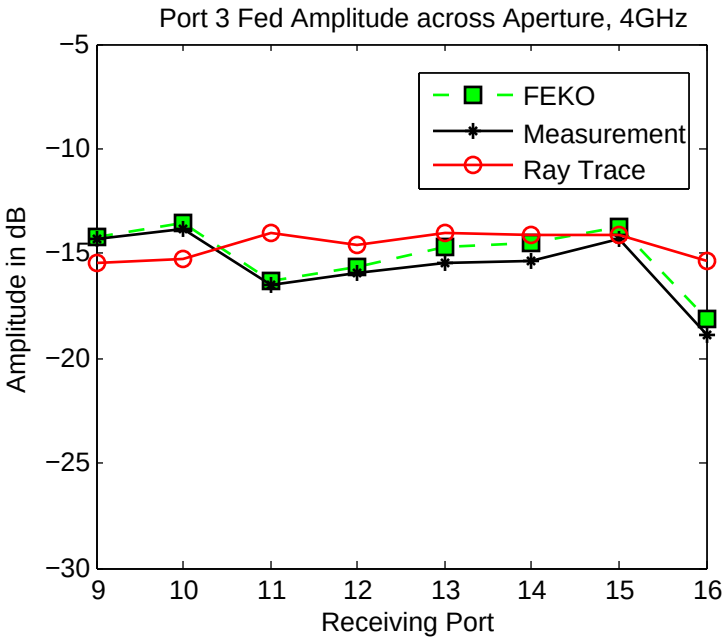

Figure A- 114. Amplitude across Aperture for Port 3 (4GHz)

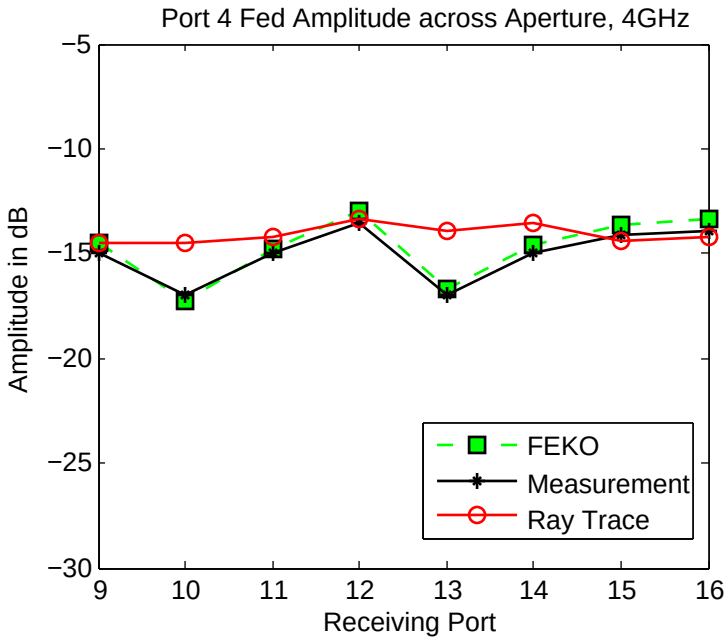

Figure A- 115. Amplitude across Aperture for Port 4 (4GHz)

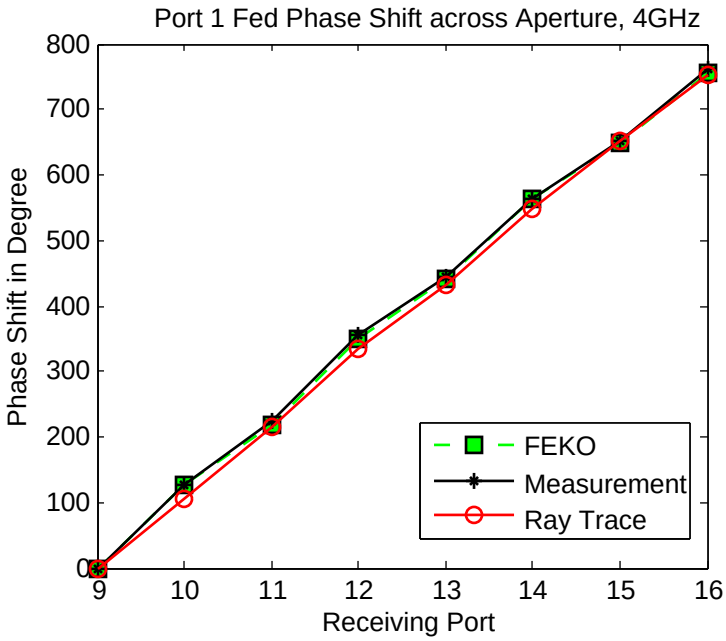

Figure A- 116. Phase Shift across Aperture for Port 1 (4GHz)

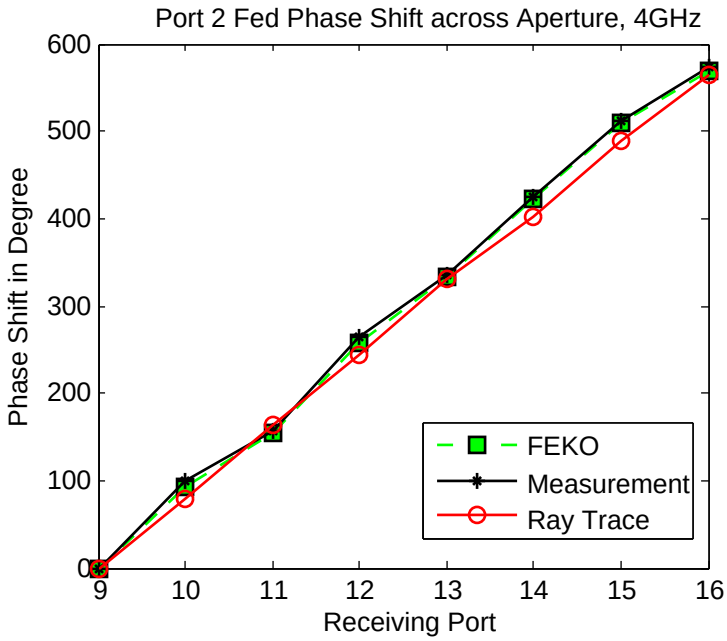

Figure A- 117. Phase Shift across Aperture for Port 2 (4GHz)

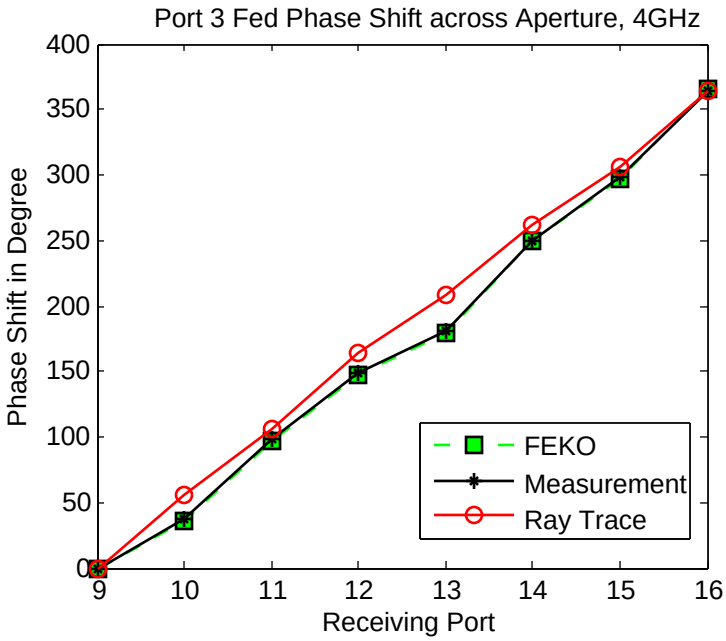

Figure A- 118. Phase Shift across Aperture for Port 3 (4GHz)

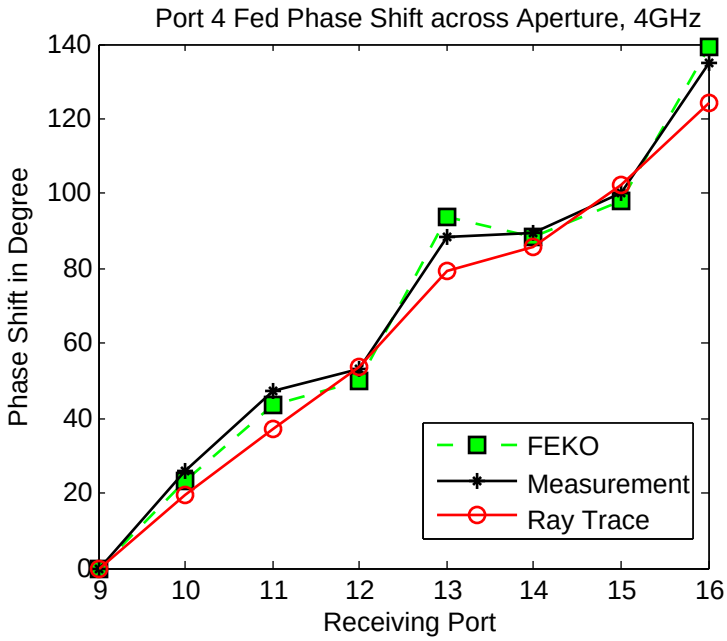

Figure A- 119. Phase Shift across Aperture for Port 4 (4GHz)

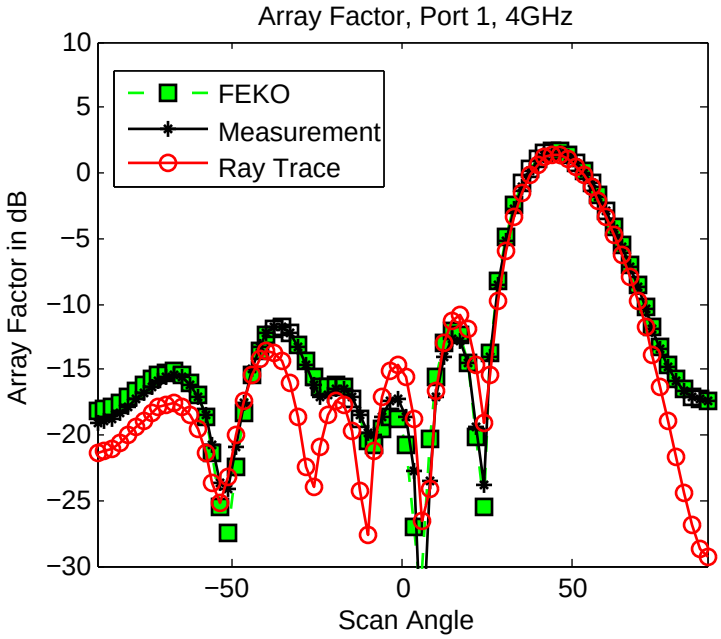

Figure A- 120. Array Factor for Ports 1 excitation (4GHz)

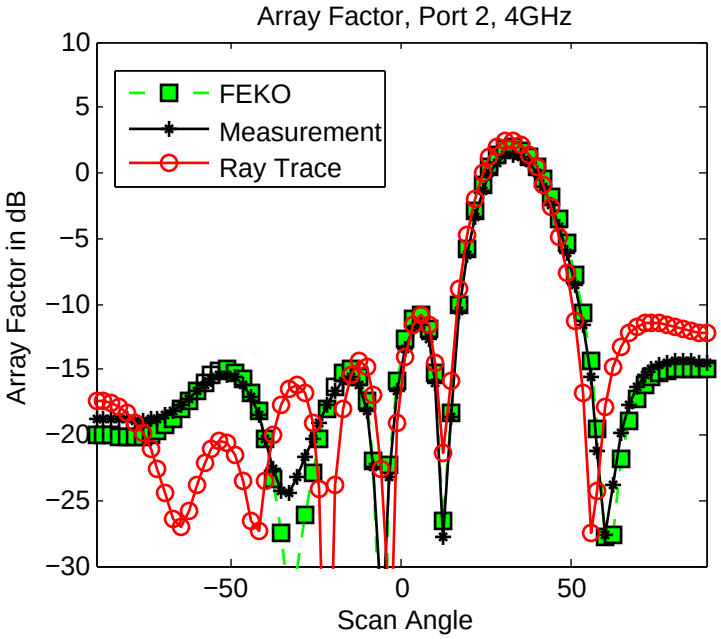

Figure A- 121. Array Factor for Ports 2 excitation (4GHz)

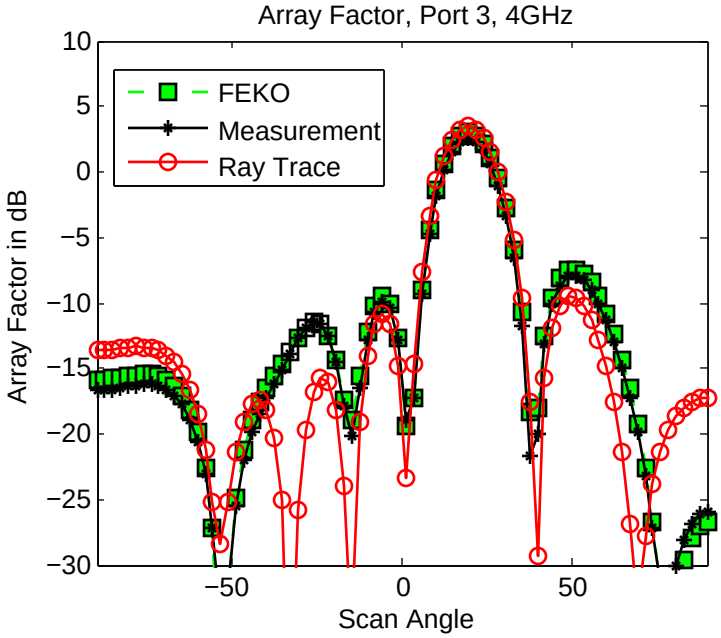

Figure A- 122. Array Factor for Ports 3 excitation (4GHz)

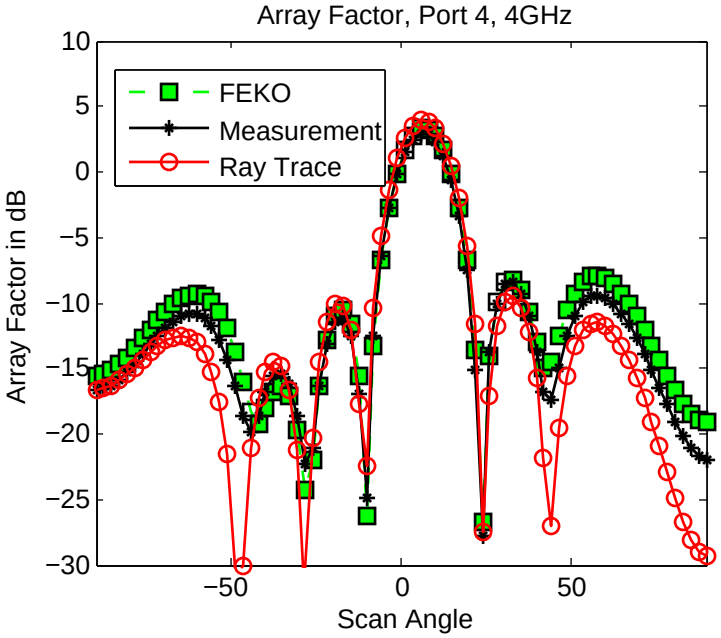

Figure A- 123. Array Factor for Ports 4 excitation (4GHz)

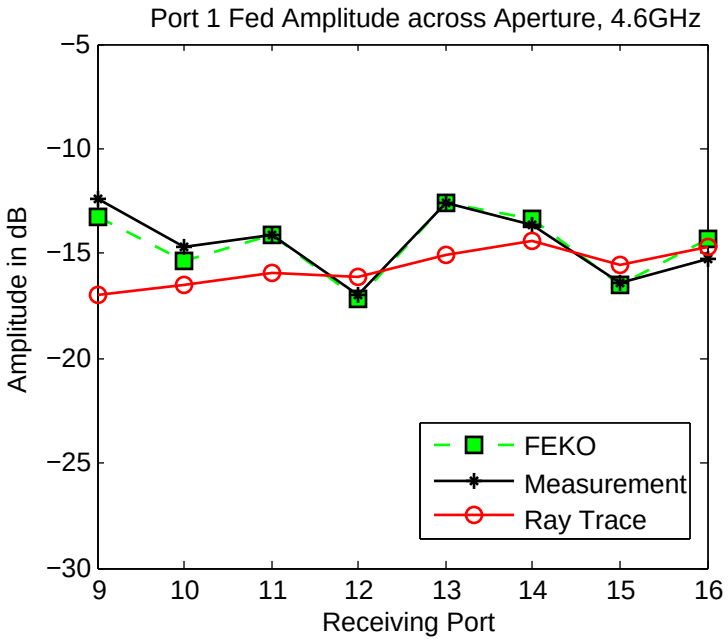

Figure A- 124. Amplitude across Aperture for Port 1 (4.6GHz)

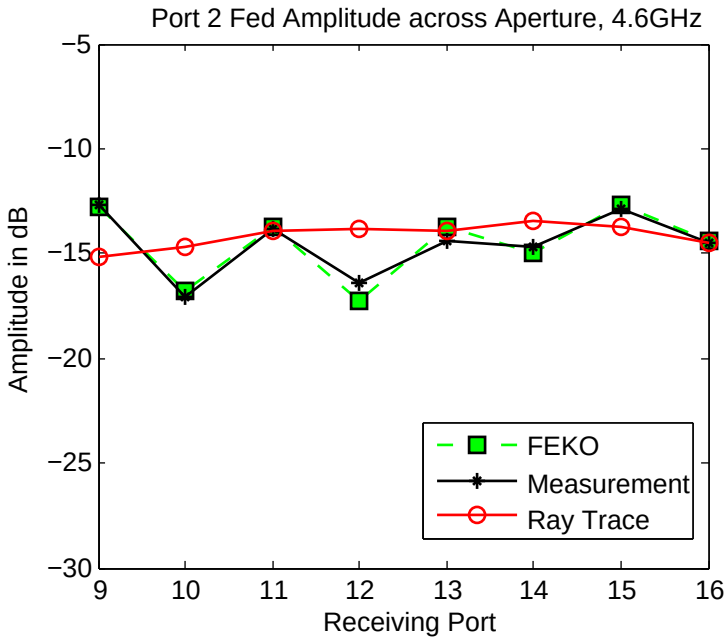

Figure A- 125. Amplitude across Aperture for Port 2 (4.6GHz)

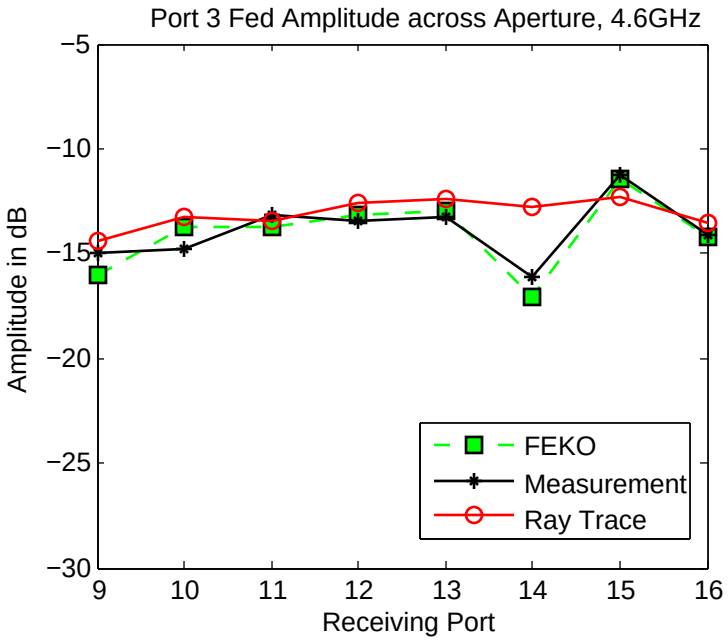

Figure A- 126. Amplitude across Aperture for Port 3 (4.6GHz)

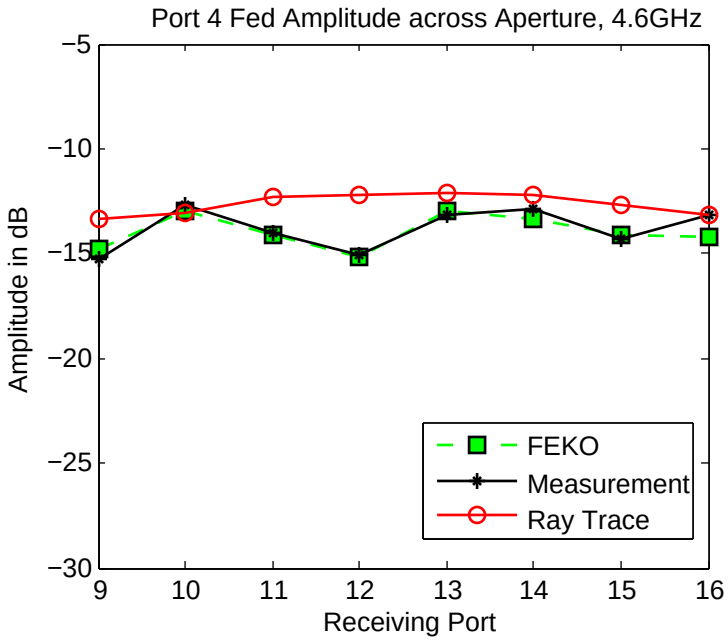

Figure A- 127. Amplitude across Aperture for Port 4 (4.6GHz)

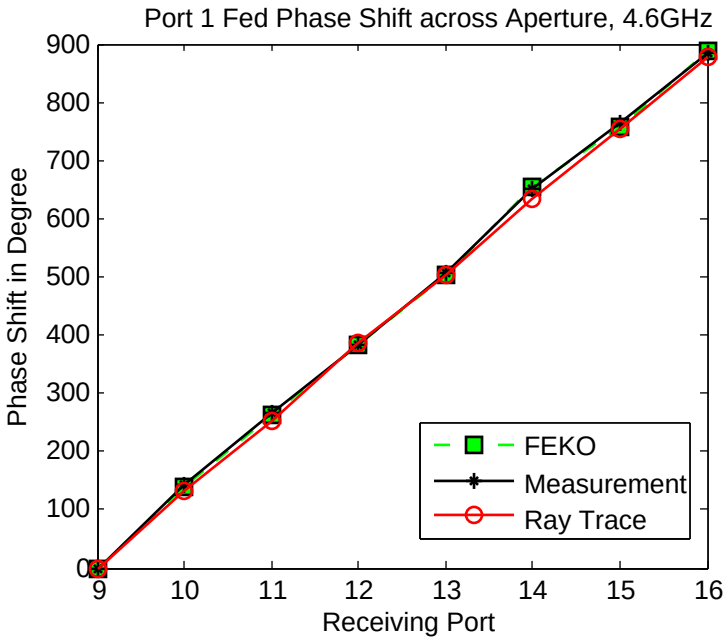

Figure A- 128. Phase Shift across Aperture for Port 1 (4.6GHz)

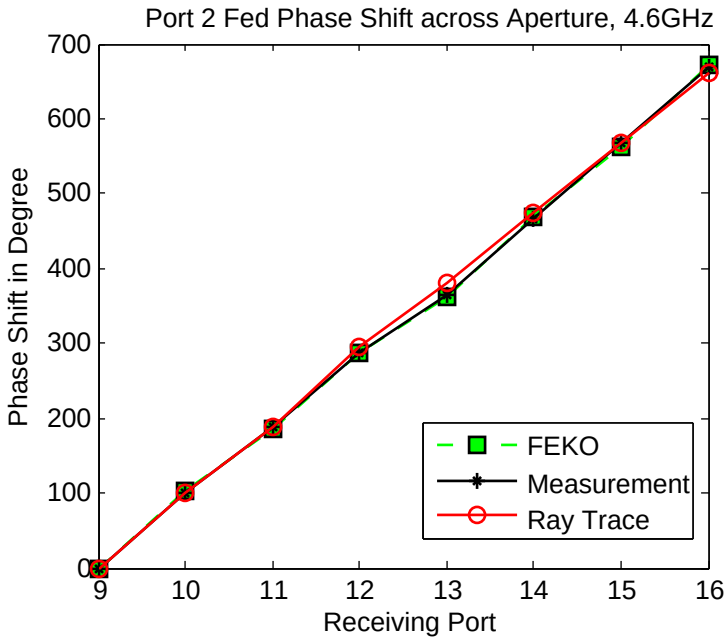

Figure A- 129. Phase Shift across Aperture for Port 2 (4.6GHz)

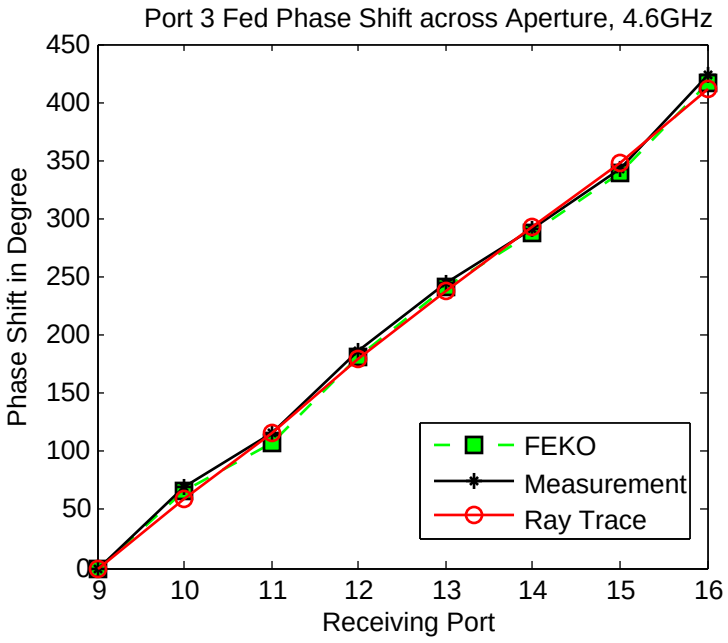

Figure A- 130. Phase Shift across Aperture for Port 3 (4.6GHz)

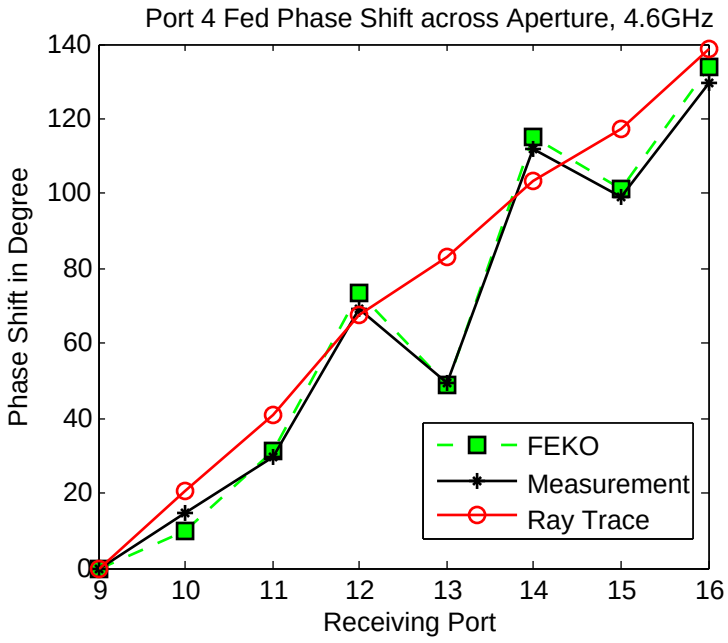

Figure A- 131. Phase Shift across Aperture for Port 4 (4.6GHz)

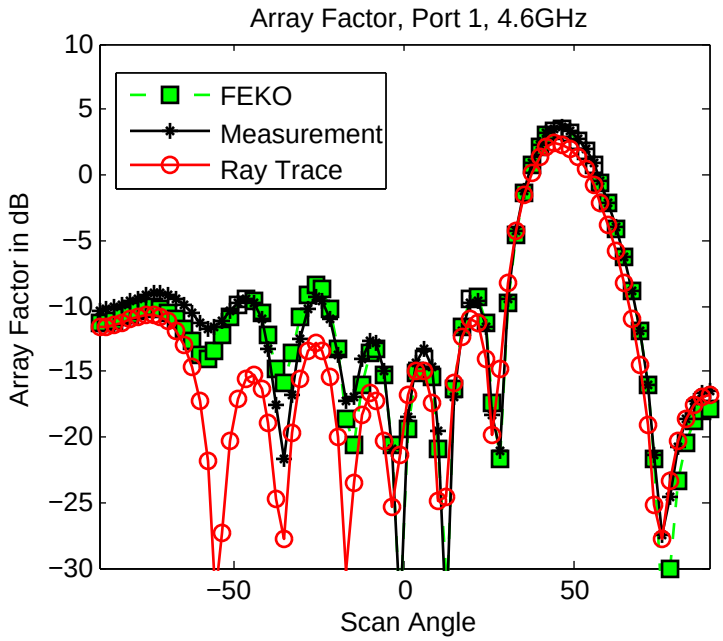

Figure A- 132. Array Factor for Ports 1 excitation (4.6GHz)

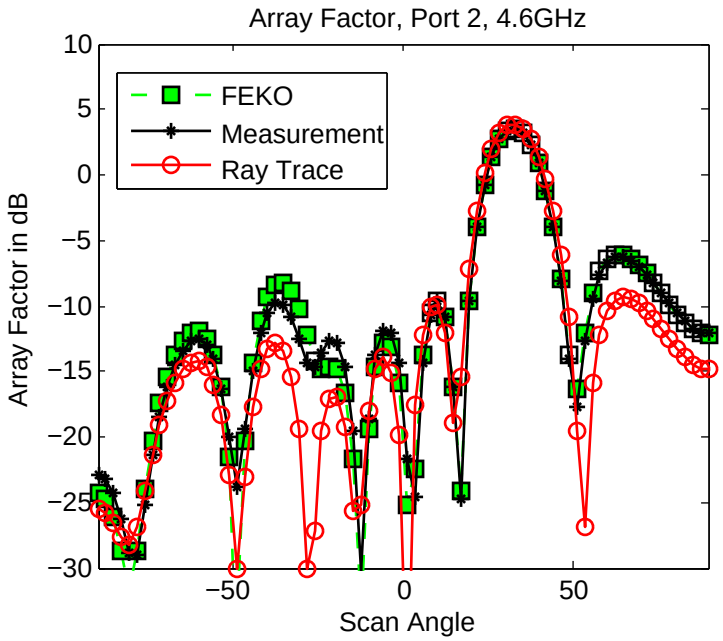

Figure A- 133. Array Factor for Ports 2 excitation (4.6GHz)

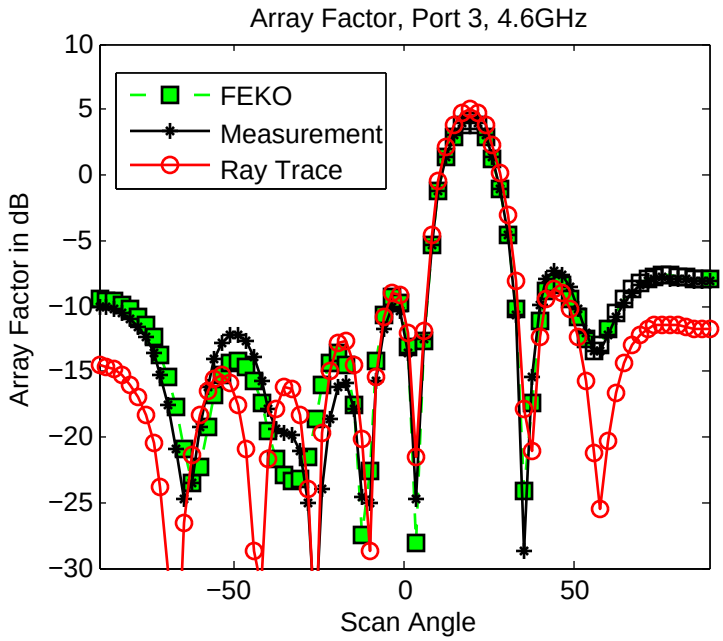

Figure A- 134. Array Factor for Ports 3 excitation (4.6GHz)

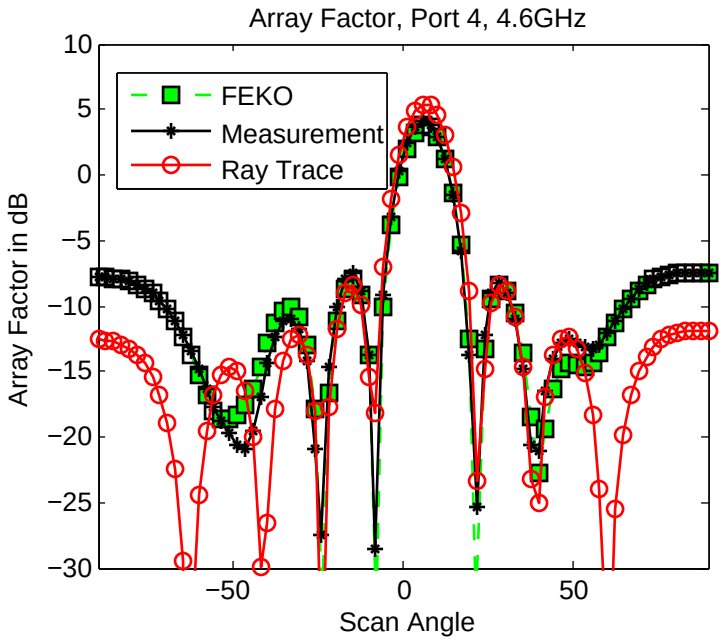

Figure A- 135. Array Factor for Ports 4 excitation (4.6GHz)

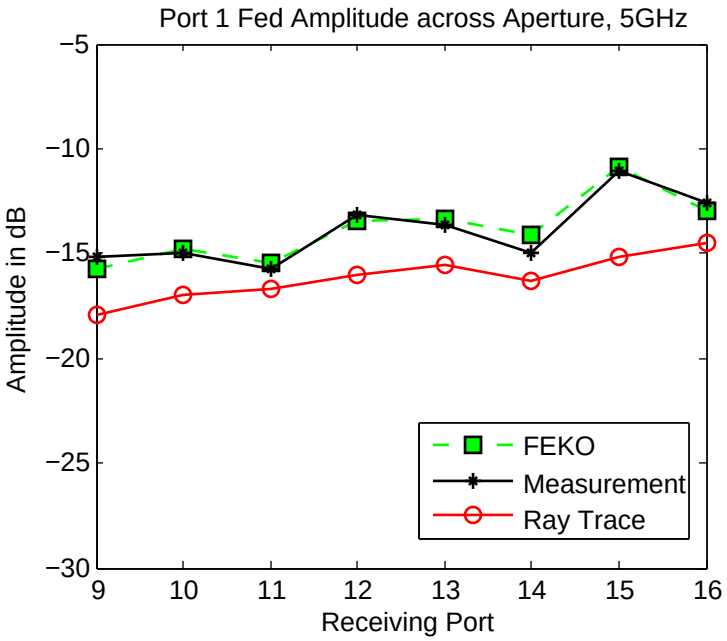

Figure A- 136. Amplitude across Aperture for Port 1 (5GHz)

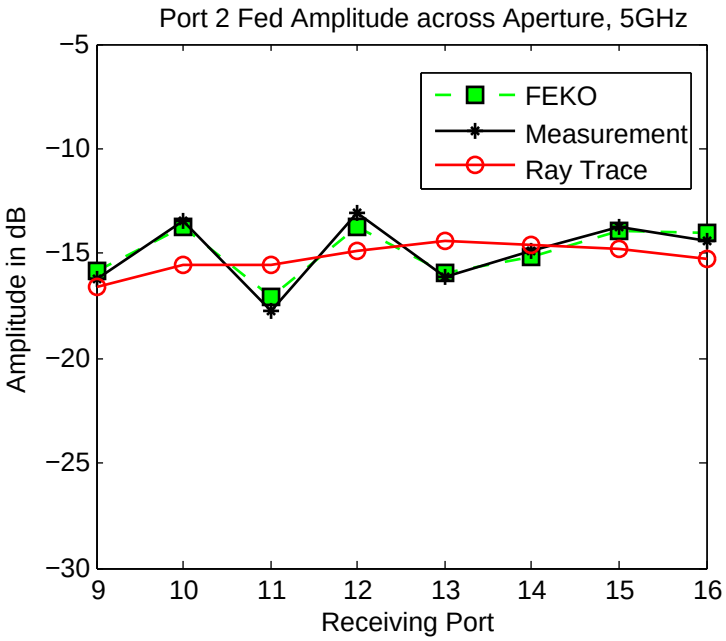

Figure A- 137. Amplitude across Aperture for Port 2 (5GHz)

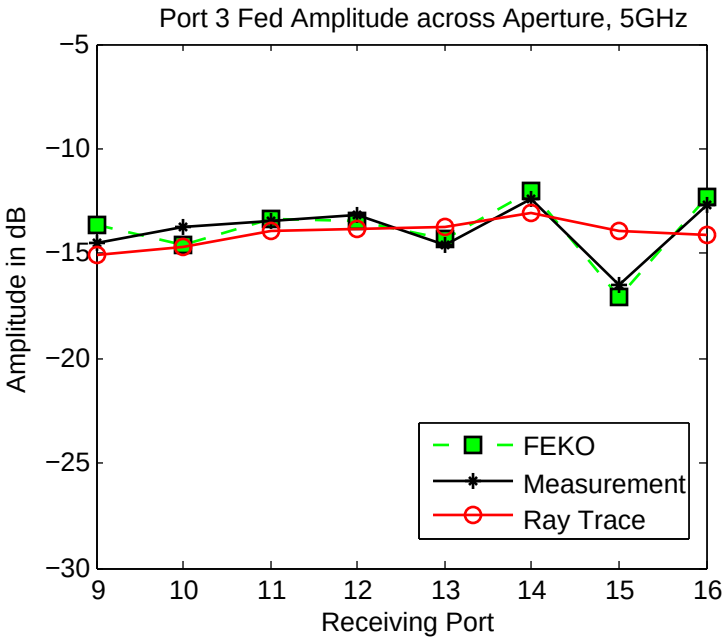

Figure A- 138. Amplitude across Aperture for Port 3 (5GHz)

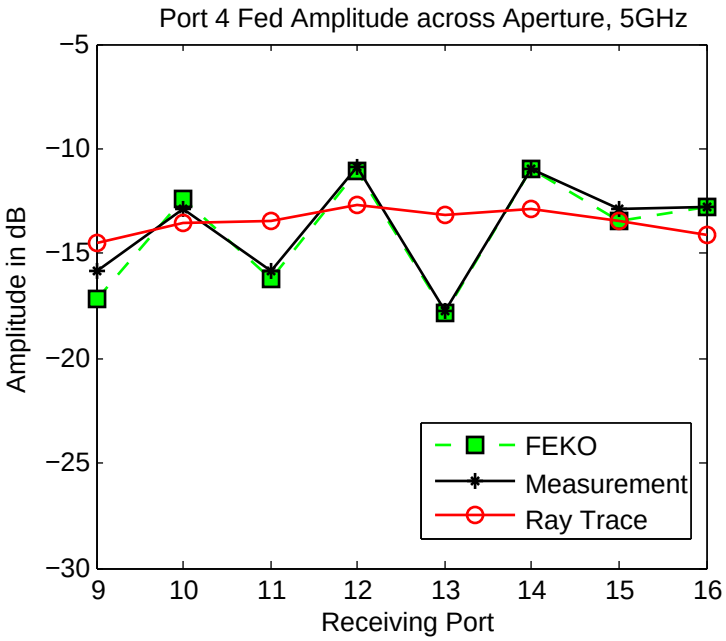

Figure A- 139. Amplitude across Aperture for Port 4 (5GHz)

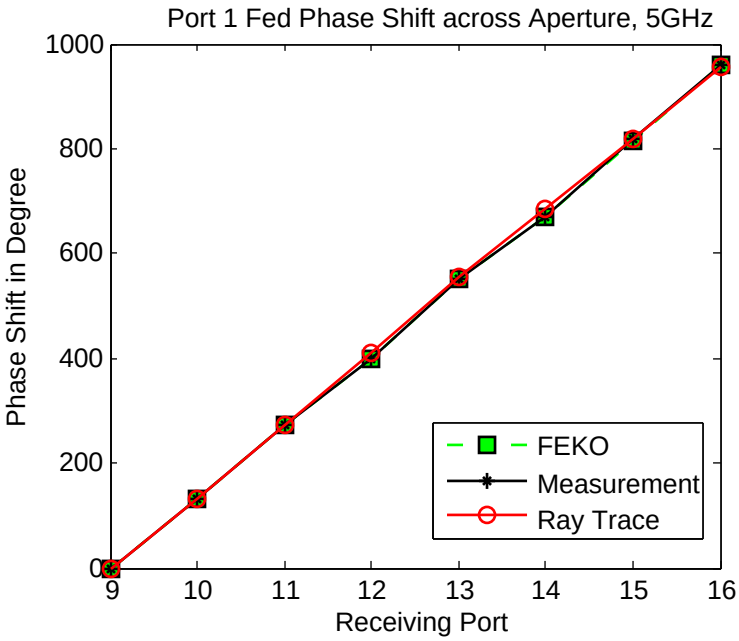

Figure A- 140. Phase Shift across Aperture for Port 1 (5GHz)

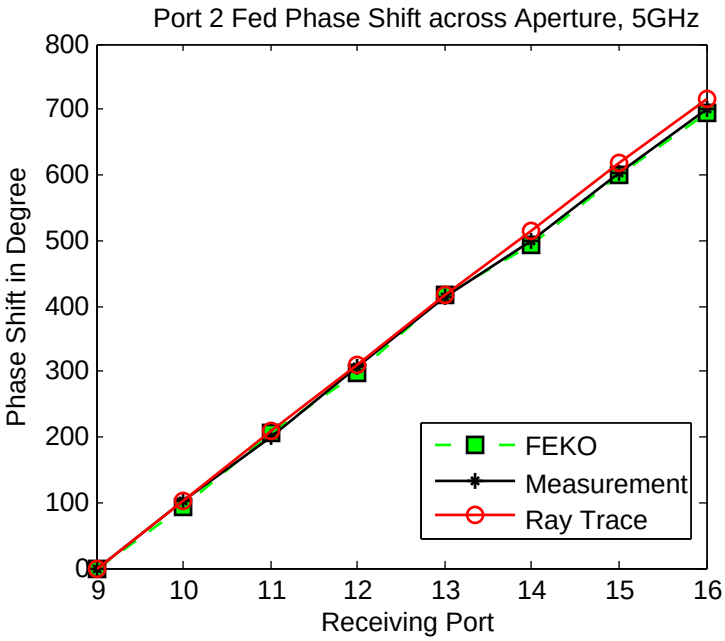

Figure A- 141. Phase Shift across Aperture for Port 2 (5GHz)

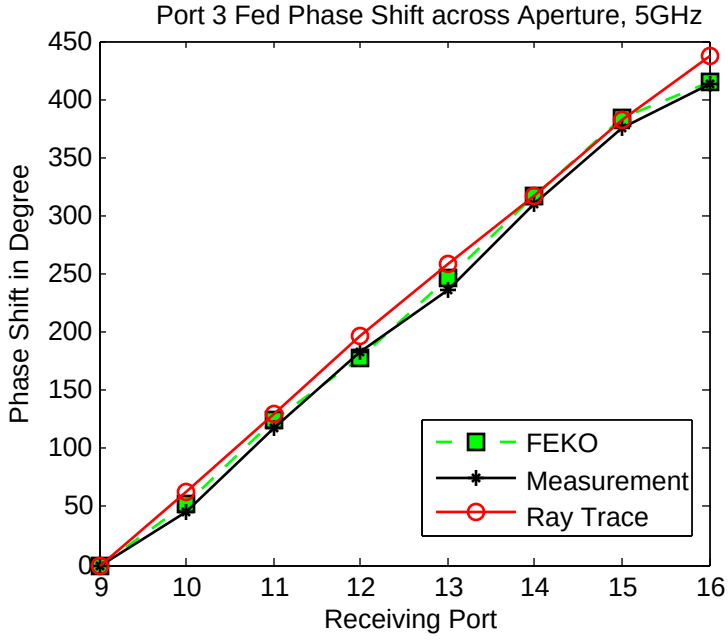

Figure A- 142. Phase Shift across Aperture for Port 3 (5GHz)

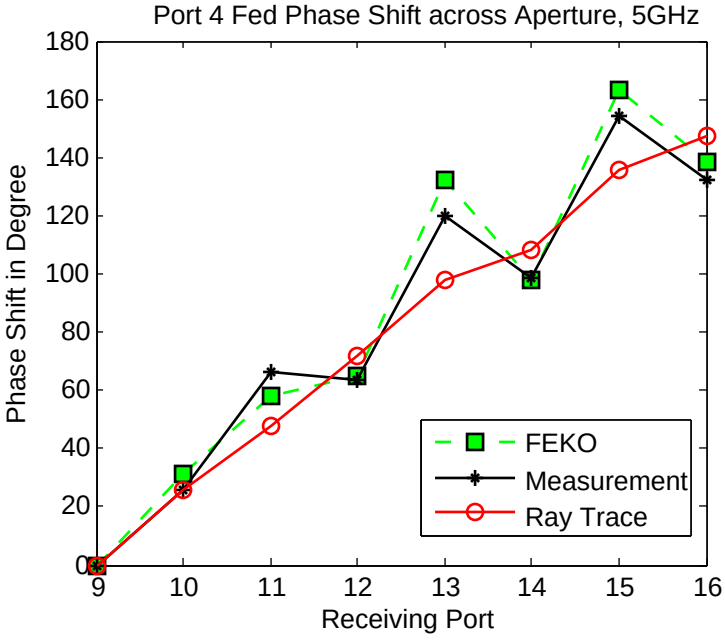

Figure A- 143. Phase Shift across Aperture for Port 4 (5GHz)

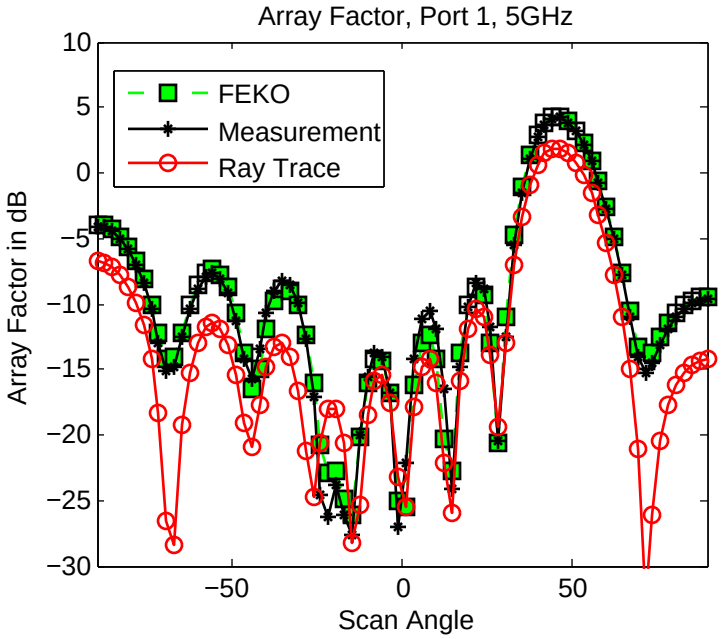

Figure A- 144. Array Factor for Ports 1 excitation (5GHz)

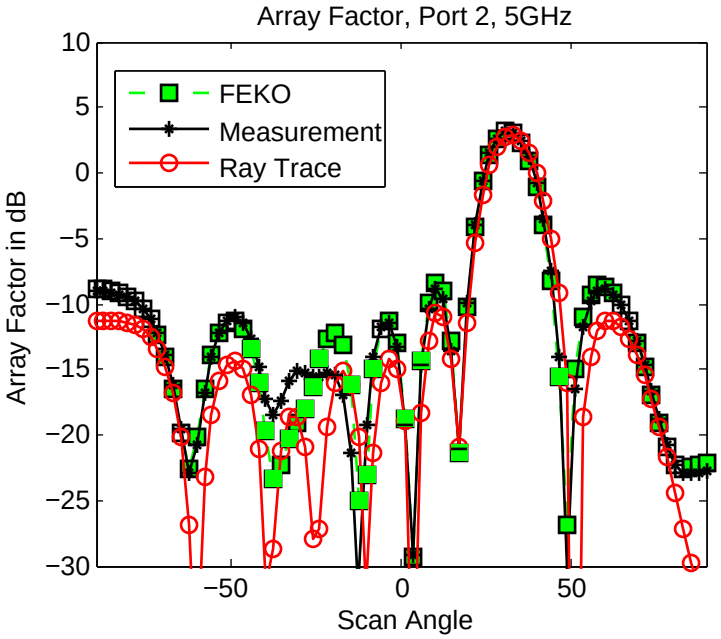

Figure A- 145. Array Factor for Ports 2 excitation (5GHz)

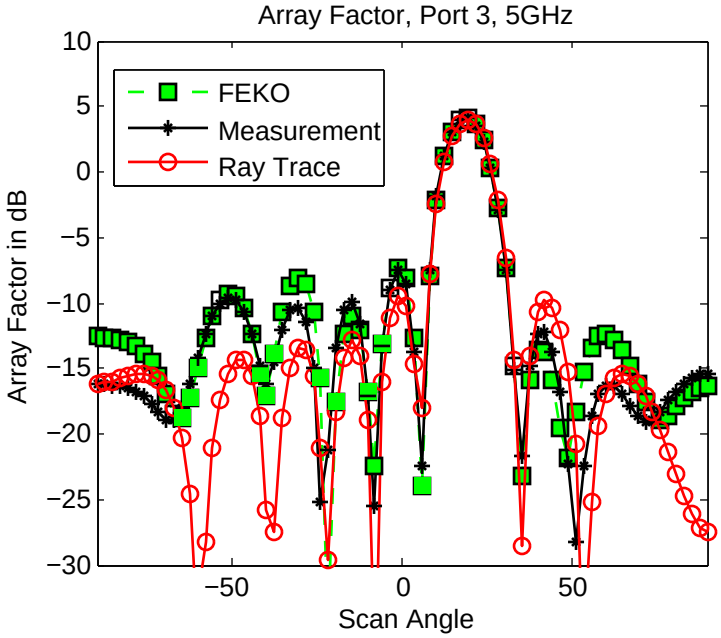

Figure A- 146. Array Factor for Ports 3 excitation (5GHz)

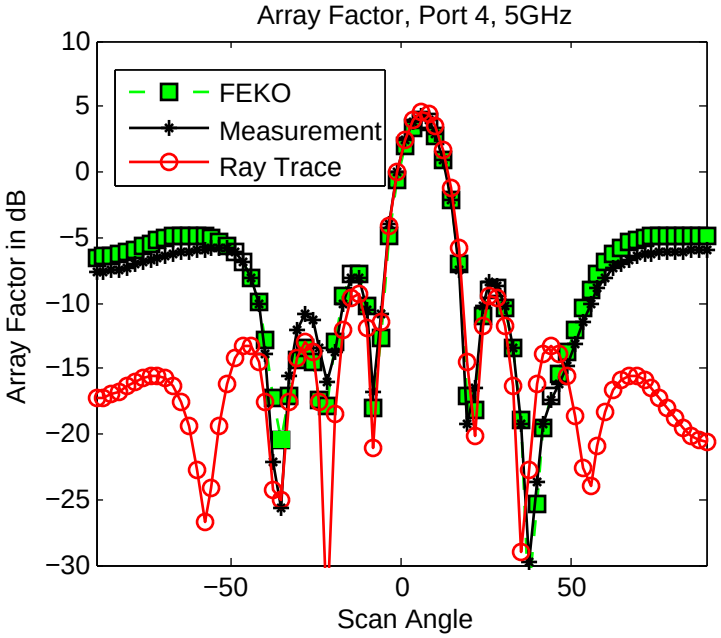

Figure A- 147. Array Factor for Ports 4 excitation (5GHz)

APPENDIX G: Microwave Lens Fabrications Procedures

This appendix graphically documents the fabrication procedures of the printed microwave lens. It assumes that the lens is designed using the software described in previous appendix, and fabricated by etching.

1) Produce initial lens contour geometry

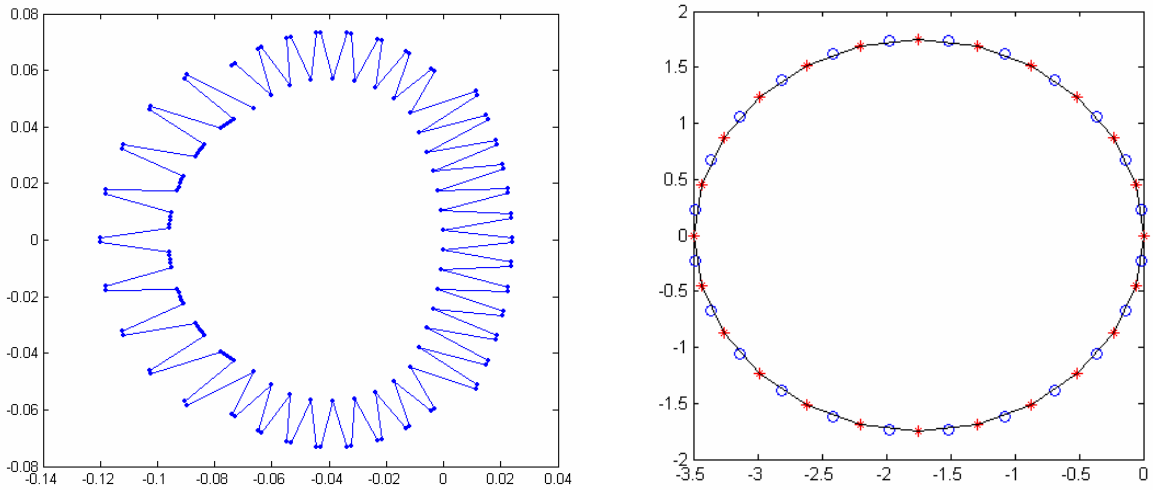

Figure A- 148. Initial Lens Contour Geometry

2) Design transmission lines for given lengths

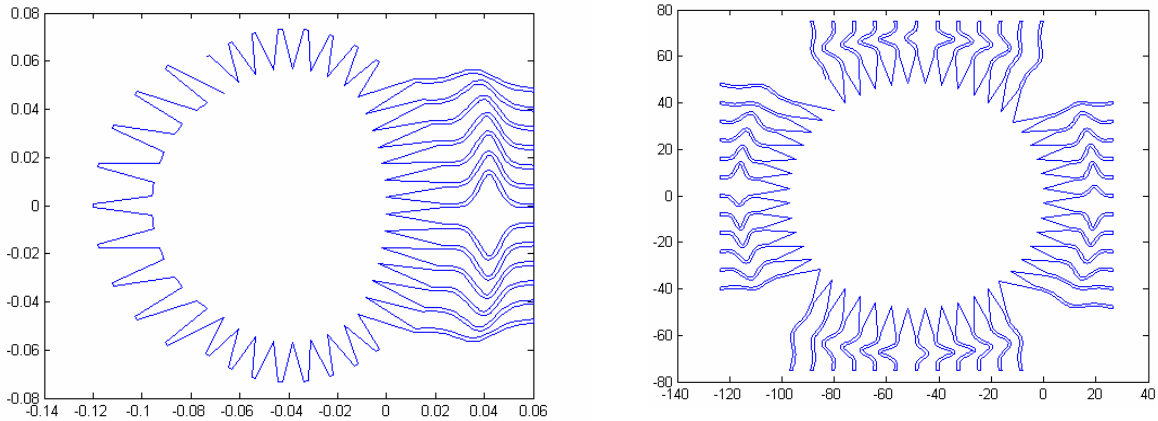

Figure A- 149. Design Transmission Line for Given Lengths

3) Create CAD models in FEKO by importing the contour coordinates

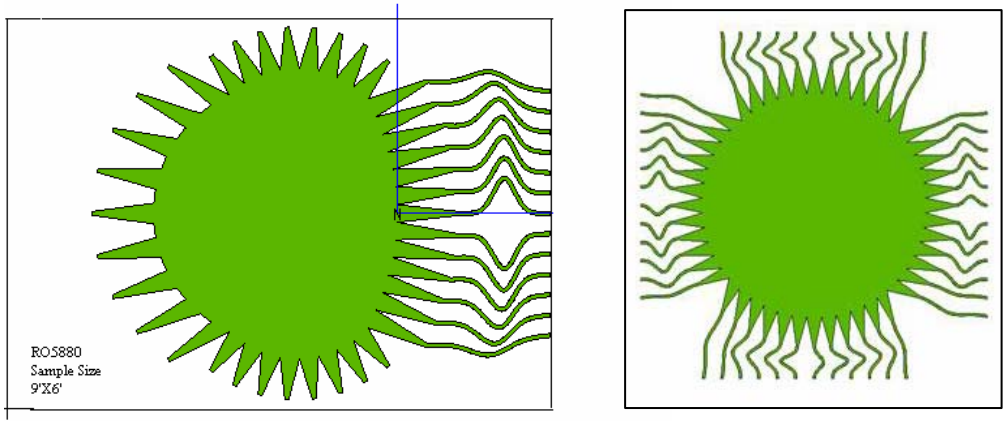

Figure A- 150. Create Microwave Lens CAD Models

3) File Format Manipulations (into *.dxf)

If exporting license allows, use FEKO to export the geometry as *.sat file first, and then read in AutoCAD or HFSS to export the *.dxf. If current version does support *.sat export, then export as *.parasolid file. Use third party software such as SolidWorks to read *.parasolid file and convert into *.sat file.

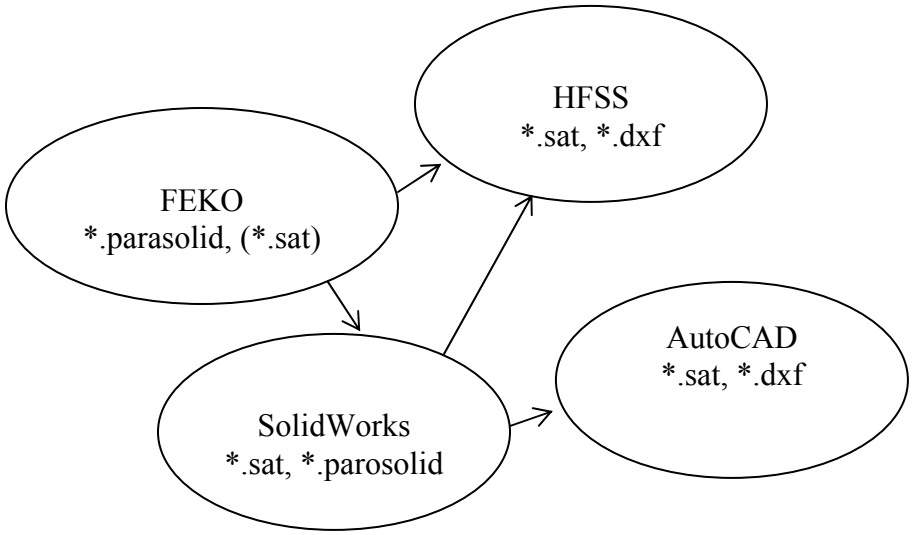

Figure A- 151. File Format Manipulation into *.dxf

3) Creating Gerber file

Gerber file can be created in CAM350. This is typical format for making the PCB board. Upon reading the *.dxf into CAM 350, the negative film/picture can be created. In our case, typical 1:1 ratio .pdf file has been generated.

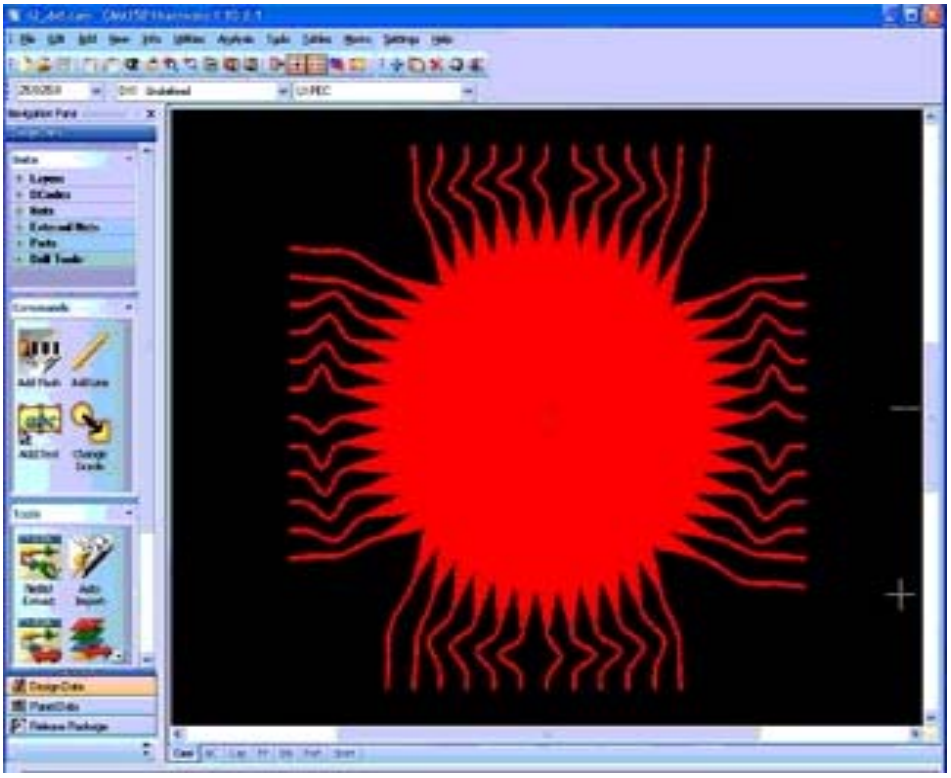

Figure A- 152. Example of Creating Gerber File in CAM350

4) Tuner Transfer with Permanent Ink Enhancement

After having the 1:1 ratio pictures, set the printer to the darkest extent and print the picture on glossy paper. Then use iron to transfer the toner on the PCB board. After washing the paper away, if toner does not stick well, use permanent ink pen to cover the trace accordingly.

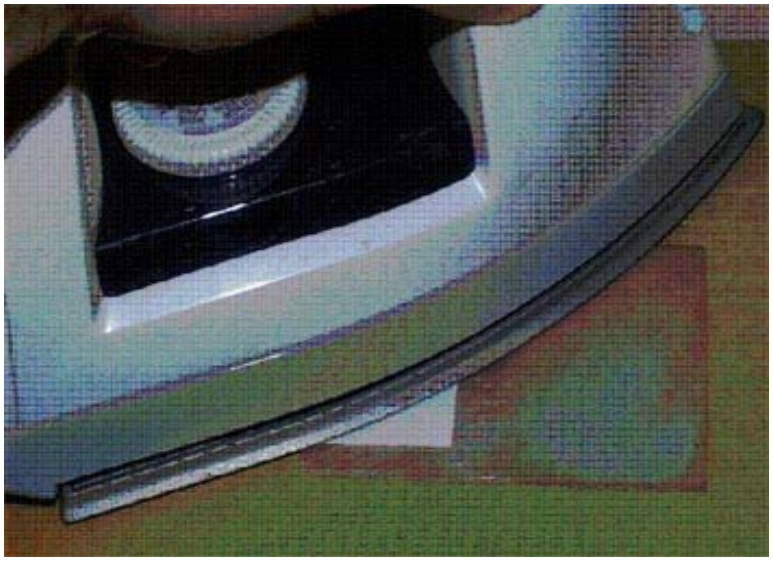

Figure A- 153. Illustration of Tuner Transfer using Iron

Figure A- 154. Alternative Ink Transfer Method for using Permanent Ink Pen

4) Etching

Etching was conducted using the mixture of hydrochloric (HCl) and hydrogen peroxide (H_2O_2). This helps control the etching process as such etchant is more transparent than the classical ferric chloride ($FeCl_3$) liquid.

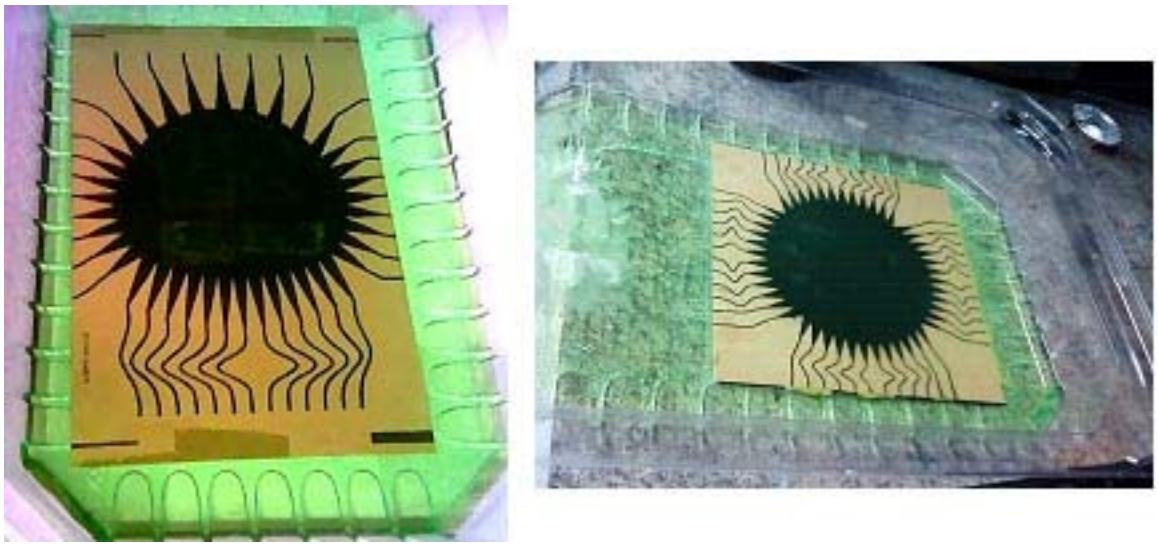

Figure A- 155. Etching Process

4) Soldering and connect coaxial terminations

The toner and inks can be wiped away easily using Acetone. After having clear etched board, the coaxial connectors are soldered on the board. The complete lenses are achieved below.

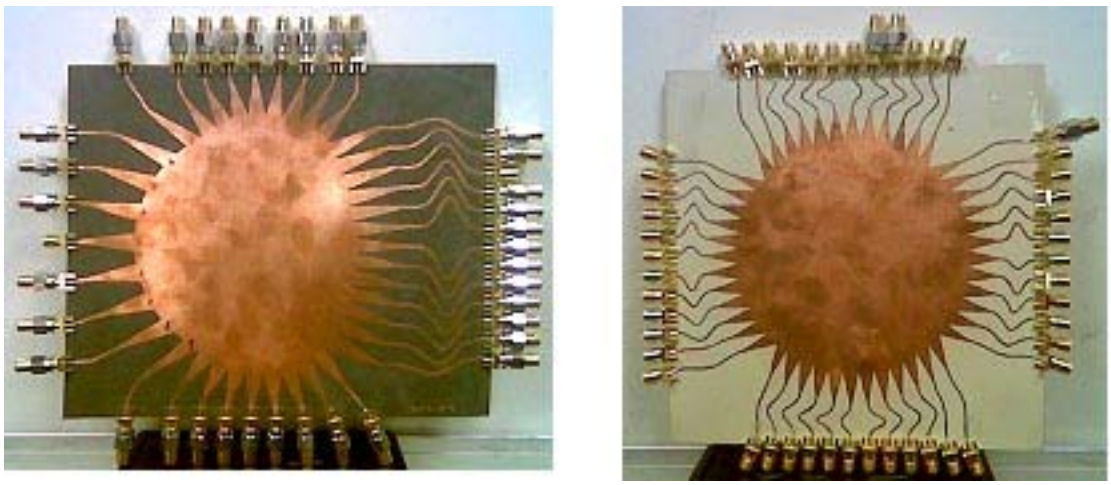

Figure A- 156. Fabricated Lenses

REFERENCES

[1] F. C. Commission, "Commission's Rules Regarding Ultra-Wideband Transmission Systems." vol. FCC-0248, FCC, Ed., 2002.

[2] J. Wells, "Multigigabit wireless technology at 70 GHz, 80 GHz and 90 GHz," RFDESIGN,www.rfdesign.com 2006.

[3] R. F. Harrington, *Time-Harmonic Electromagnetic Fields*, 1st ed. New York: McGraw-Hill Book Company, INC., 1961.

[4] R. C. Hansen, *Phased Array Antennas*. New York: John Wiley& Sons, Inc., 1998.

[5] C. M. S. U. Manual, "http://www.cst.com/," 2008.

[6] http://www.remcom.com/xf7, "XFDTD User Guide Version 6.4," 2008.

[7] http://www.2comu.com/, "GEMS User Guide," 2009.

[8] N. Gershenfeld, *Fab: the coming revolution on your desktop- from personal computers to personal fabrication*. New York: Perseus Books Group, 2005.

[9] J.Ruze, "Wide-angle metal-plate optics," *Proc. IRE,* vol. 38, p. 6, January 1950.

[10] J. Brown, *Microwave Lens*: Methuen, 1953.

[11] J. Brown, "Lens Antennas " in *Antenna Theory*. vol. Part 2: McGraw-Hill, 1969

[12] J. Brown, Jones, S.S., "Microwave Lenses," *Electronic Engineering,* vol. 22, p. 6, Apr-Oct 1950.

[13] H. Gent, "The bootlace aerial," *Royal Radar Establishment J.,* p. 11, Oct. 1957.

[14] J. Shelton, "Focusing characteristics of symmetrically configured bootlace lenses," *Antennas and Propagation, IEEE Transactions on [legacy, pre - 1988],* vol. 26, pp. 513-518, 1978.

[15] R.M.Cox and J.R.Sebring, "MLS-A practical application of microwave technology," *IEEE Transactions on Microwave Theory and Techniques,* vol. MTT-24, p. 8, Dec. 1976.

[16] G. J. Monser, "Advances in Lens-Fed Multibeam Technology," *NTIS,* p. 22, Feb 1992.

[17] W. Rotman and R. Turner, "Wide-angle Microwave Lens for Line Source Applications," *IEEE Transactions on Antennas and Propagation,* vol. 11, pp. 623-632, 1963.

[18] D. H. Archer and M. J. Maybell, "Rotman lens development history at Raytheon Electronic Warfare Systems 1967-1995," 2005, pp. 31-34 vol. 2B.

[19] D. H. Archer, "Lens-Fed Multiple-Beam Arrays," *Microwave J.,* vol. 18, p. 6, Oct 1975.

[20] D. H. Archer, "Lens-Fed Multiple Beams Arrays," *Microwave J.,* vol. 27, p. 6, 1984.

[21] A. Al-Zayed, L. Schulwitz, and A. Mortazawi, "A dual polarized millimetre-wave multibeam phased array," 2004, pp. 87-90 Vol.1.

[22] L. T. Hall, D. Abbott, and H. J. Hansen, "Design and simulation of a high efficiency Rotman lens for MM-wave sensing applications," 2000, pp. 1419-1422.

[23] J. Herd and D. Pozar, "Design of a microstrip antenna array fed by a rotman lens," 1984, pp. 729-732.

[24] C. Metz, J. Grubert, J. Heyen, A. F. Jacob, S. Janot, E. Lissel, G. Oberschmidt, and L. C. Stange, "Fully integrated automotive radar sensor with versatile resolution," *Microwave Theory and Techniques, IEEE Transactions on,* vol. 49, pp. 2560-2566, 2001.

[25] Y. M. Tao and G. Y. Delisle, "Lens-fed multiple beam array for millimeter wave indoor communications," 1997, pp. 2206-2209 vol.4.

[26] T. Katagi, S. Mano, and S. Sato, "An Improved Design Method of Rotman Lens Antennas," *IEEE Transactions on Antennas and Propagation,* vol. 32, pp. 524-527, 1984.

[27] T. Katagi, S. Mano, S. Sato, S. Tahara, and E. Tomimatsu, "An Improved Design Method of Rotman Lens Antennas," *IEEE Transactions on Antennas and Propagation,* vol. 20, pp. 136-139, 1982.

[28] M. S. Smith, "Design Considerations for Ruze and Rotman Lens," *The Radio and Electronic Engineer,* vol. 52, pp. 181-187, 1982.

[29] R. C. Hansen, "Design Trades for Rotman lenses," *IEEE Transactions on Antennas and Propagation,* vol. 39, pp. 464-472, 1991.

[30] C. Rappaport and A. Zaghloul, "Optimized Three-dimensional Lenses for Wide-angle Scanning," *IEEE Transactions on Antennas and Propagation,* vol. 33, pp. 1227-1236, 1985.

[31] J. Dong, A. I. Zaghloul, and R. Rotman, "Non-Focal Minimum-Phase-Error Planar Rotman Lens," in *URSI National Radio Science Meeting* Colorado, 2008.

[32] Y. T. L. a. S. W. Lee, *Antenna Handbook: Theory, Applications and Design* vol. 2: Van Nostrand Reinhoud, 1988.

[33] K. Jaeheung, "Developments of Rotman Lenses at Micro/Millimeter-wave Frequencies," in *Electrical Engineering*. vol. Ph.D. Boulder: University of Colorado, 2003.

[34] M. S. Smith, "Amplitude Performance of Ruze and Rotman Lenses," *Radio Electron,* vol. 53, pp. 329-336, 1983.

[35] J. Rao, "Correction to "Multifocal three-dimensional bootlace lenses"," *Antennas and Propagation, IEEE Transactions on [legacy, pre - 1988],* vol. 31, pp. 541-541, 1983.

[36] J. Rao, "Multifocal Three-dimensional Bootlace Lenses," *IEEE Transactions on Antennas and Propagation,* vol. 30, pp. 1050-1056, 1982.

[37] J. Dong and A. I. Zaghloul, "Method and Computer-Aided Investigation of Microwave Lens for 360-Degree Scanning," in *IEEE International Symposium on Antennas Propagation* Charleston, South Carolina, 2009.

[38] J. Dong and A. I. Zaghloul, "Implementation of Microwave Lens for 360-Degree Scanning," in *IEEE International Symposium on Antennas Propagation* Charleston, South Carolina, 2009.

[39] A. I. Zaghloul and J. Dong, "A Concept for a Lens Configuration for 360-Degree Scanning," *IEEE Letters on Antennas and Wireless Propagation,* 2009 (Accepted).

[40] R. P. O. Resource, "http://www.raytheon.com/."

[41] M. J. Maybell, K. K. Chan, and P. S. Simon, "Rotman lens recent developments 1994-2005," 2005, pp. 27-30 vol. 2B.

[42] P. S. Simon, "Analysis and synthesis of Rotman Lenses," *22nd AIAA International Communications Satellite Systems Conference &Exhibit 2004,* May 2004 2004.

[43] O. Kilic and R. Dahlstrom, "Rotman Lens Beam Formers for Army Multifunction RF Antenna Applications," in *IEEE Antennas and Propagation Society International Symposium*, 2005, pp. 43-46 vol. 2B.

[44] S. Weiss and R. Dahlstrom, "Rotman Lens Development at the Army Research Lab," in *IEEE Aerospace Conference*, 2006, p. 7.

[45] J. Toon, "Rotman Lens Offers Inexpensive, Electronically Scanned Antenna, http://gtresearchnews.gatech.edu/reshor/rh-sf96/rotman.htm."

[46] D. L. a. R. Courtesy Detrick, T.J., "A phased-array radiowave imager for studies of cosmic noise absorption," *Radio Sci.,* vol. 25, p. 4, July-Aug 1990.

[47] K. K. Chan, "A feed network for multibeam triangular grid and hexagonal shape planar array antennas," 1999, pp. 80-83 vol.1.

[48] H. Steyskal, C. Cox, and E. Ackerman, "Digital and optical beamforming techniques," 2003, p. 616.

[49] R. Rotman, "Considerations for a Photonic Beamformer using an LFM Waveform in Transmit," in *Antennas and Propagation Society International Symposium,IEEE*, 2004.

[50] S. Clark, C. Martin, V. Kolinko, J. Lovberg, and P. J. Costianes, "A Real-time Wide Field of View Passive Millimeter-wave Imaging Camera," in *Proceedings of the 32nd Applied Imagery Pattern Recognition Workshop*, Washington DC, 2003, pp. 250-254.

[51] J. Dong, A. I. Zaghloul, R. Sun, and C. J. Reddy, "EHF Rotman Lens for Electronic Scanning Antennas," in *Asia Pacific Microwave Conference (APMC)* Hong Kong, 2008.

[52] J. Dong and A. I. Zaghloul, "EHF Electrically Steerable Lens-Fed Antenna for Vehicular Sensor Applications," *IET Microwaves, Antennas & Propagation,* 2009 (under review).

[53] J. Dong, A. I. Zaghloul, and C. J. Reddy, "Quaduple Bandwidth True Time Delay Printed Microwave Lens Beam Former for Ultra Wideband Multifunctional Phased Array Applications," in *IEEE International Symposium on Antennas and Propagation*, North Charleston, South Carolina, 2009.

[54] J. Dong, A. I. Zaghloul, and R. Rotman, "A Fast Ray Tracing Method for Microstrip Rotman Lens Analysis," in *XXIXth URSI General Assembly* Chicago, 2008.

[55] J. Dong, A. I. Zaghloul, R. Sun, C. J. Reddy, and S. Weiss, "Accurate Simulation of Rotman Lens Using FEKO," in *Applied Computational Electromagnetics Society (ACES) Conference* Monterey, California 2009

[56] J. Dong, H.-C. Ou, A. I. Zaghloul, "Measurement Investigation of Microstrip Lens Sidewall's Termination," in *USNC/URSI National Radio Science Meeting* South Carolina, 2009.

[57] "Eccentricity," *http://en.wikipedia.org/wiki/Eccentricity_%28mathematics%29*, 2006.

[58] J. Dong, A. I. Zaghloul, and R. Rotman, "Non-focal 2D Rotman Lens Design," in *IEEE Transactions on Antennas and Propagation*, 2008, under Review.

[59] D. E. Goldberg, *Genetic Algorithms in Search, Optimization and Machine Learning*. Boston, MA: Kluwer Academic Publishers, 1989.

[60] Dongcai Su, Junwei Dong, and Z. Zheng, "A Stochastic Algorithm for Function Minimization," *Optimization online,* July 2008.

[61] R. Rotman, S. Rotman, W. Rotman, O. Raz, and M. Tur, "Wideband RF Beamforming: the Rotman lens vs. Photonic Beamforming," in *IEEE Antennas and Propagation Society International Symposium*, 2005, pp. 23-26 vol. 2B.

[62] C. W. Penney, R. J. Luebbers, and E. Lenzing, "Broad band Rotman lens simulations in FDTD," 2005, pp. 51-54 vol. 2B.

[63] M. C. Longtin, S. Din-Kow, J. Silvestro, and Z. Cendes, "Domain Decomposition and Distributed Analysis for Large Microwave Structures," 2006, pp. 1053-1056.

[64] S. Weiss, S. Keller, and C. Ly, "Development of Simple Affordable Beamformers for Army Platforms," in *Proceedings of GOMACTech-07 Conference* Lake Buena Vista, FL, 2006.

[65] M. Maybell, "Ray Structure Method for Coupling Coefficient Analysis of the Two Dimensional Rotman Lens," in *Antennas and Propagation Society International Symposium*, 1981, pp. 144-147.

[66] N. Yuan, J. S. Kot, and A. J. Parfitt, "Analysis of Rotman lenses using a hybrid least squares FEM/transfinite element method," *Microwaves, Antennas and Propagation, IEE Proceedings -,* vol. 148, pp. 193-198, 2001.

[67] D. M. Pozer, "Microwave Engineering," *John Wiley&Sons,* 1998 1998.

[68] K. K. G. Avneesh Mittal, G.P.Srivastava, P.K. Singhal, R.D. Gupta and P.C. Sharma, "Contour Integral Analysis of Planar Components," *Journal of Microwaves and Optoelectronics,* vol. 3, p. 15, 2003.

[69] G.Razmafrouz, G.R. Branner, B.P.Kumar, "Formulation of the Klopfenstein tapered line analysis from generalized nonuniform line theory," 1997.

[70] D. M. Pozar, "Microwave Engineering," *John Wiley&Sons,* 1998.

[71] R. H. Clarke, *Diffraction theory and antennas*: E. Horwood ; Halsted Press 1980.

[72] B. G. J.L.Cruz, E.A. Navarro, and V.Such, "The Phase Center Position of a Microstrip Horn Radiating in an Infinite Parallel-Plate Waveguide," *IEEE Transactions on Antennas and Propagation,* vol. 42, p. 4, 1994.

[73] M. L. Skolnik and K. G. Meads, "Senrad: an advanced wideband air-surveillance radar," *IEEE Transactions on Antennas and Propagation,* vol. 37, pp. 1163-1175, 2001.

[74] D. G. Bodnar and J. W. Cofer, "360-degree Scanning Antenna With Cylindrical Array of Slotted Waveguides." vol. 4,458,250, U. S. Patent, Ed. United States: The United States of America as Represented by the Secretary of the Navy, 1984, p. 8.

[75] R. E. Clapp, "Extending the R-2R Lens to 360 degree," *IEEE Transactions on Antennas and Propagation,* vol. 32, pp. 661-671, 1984.

[76] R. K. Luneberg, "Mathematical Theory of Optics," pp. pp. 189-212, 1944.

[77] J. Brown, "Microwave Lenses," *Methuen's Monographs on Physical Subjects,* pp. 83-89, 1953.

[78] J. J. Liang, P. N. Suganthan, and K. Deb, "Novel Composition Test Functions for Numerical Global Optimization," *IEEE Swarm Intelligence Symposium,* pp. 68-75, June 2005.

[79] Z. Michalewicz and G. Nazhiyath, "Genocop III: a co-evolutionary algorithm for numerical optimizationproblems with nonlinear constraints," in *IEEE International Conference on Evolutionary Computation*, 1995.

[80] S. Venkatraman and G. Yen, "A Generic Framework for Constrained Optimization Using Genetic Algorithms," *IEEE Transactions on Evolutionary Computation,* vol. 9, pp. 424-435, 2005.

[81] W. L. Stutzman and G. A. Thiele, *Antenna Theory and Design, 2nd*: John Wiley & Sons, 1998.

[82] "FEKO Suite 5.4," EM Software and Systems, www.feko.info 2008.

INDEX

PAPERS PRODUCED during PH.D. STUDY

Journal Articles

1. J. Dong, A. I. Zaghloul, "EHF Electrically Steerable Lens-Fed Antenna for Vehicular Sensor Applications," accepted to IET Microwaves, Antennas & Propagation
2. A. I. Zaghloul, J. Dong, " A Concept for a Lens Configuration for 360-Degree Scanning," Published in IEEE Letters on Antennas and Wireless Propagation
3. J. Dong, A. I. Zaghloul, R. Sun, C. J. Reddy, S. Weiss, "Rotman Lens Amplitude, Phase, Pattern Evaluation by Full-wave Simulation and Measurement," accepted to Journal of Applied Computational Electromagnetics Society
4. D. Su, J. Dong and Z. Zheng, "A Stochastic Algorithm for Function Minimization," Published in Journal of Optimization Online
5. J. Dong, A. I. Zaghloul, and R. Rotman, "Non-focal 2D Rotman Lens Design," submitted to IEEE Transactions on Antennas and Propagation
6. J. Dong, A. I. Zaghloul, and R. Rotman, "Fast Ray Tracing Method for 2D Microwave Lens Simulation," submitted to IEEE Transactions on Antennas and Propagation
7. J. Dong, A. I. Zaghloul, "Microwave Lens Design for 360-degree Scanning", submitting to IEEE Transactions on Antennas and Propagation

Refereed Conference Papers

1. J. Dong, A. I. Zaghloul, and R. Rotman, "Non-Focal Minimum-Phase-Error Planar Rotman Lens," in URSI National Radio Science Meeting, Colorado, January 2008
2. J. Dong, A. I. Zaghloul, and R. Rotman, "A Fast Ray Tracing Method for Microstrip Rotman Lens Analysis," in URSI General Assembly, Chicago, August 2008
3. J. Dong, A. I. Zaghloul, R. Sun, C. J. Reddy, "EHF Rotman Lens for Electronic Scanning Antennas," in Asia Pacific Microwave Conference (APMC), Hong Kong, December 2008

4. J. Dong, A. I. Zaghloul, R. Sun, C. J. Reddy, S. Weiss, "Accurate Simulation of Rotman Lens Using FEKO," in Applied Computational Electromagnetics Society Conference, Monterey, California, March 2009
5. D. Su, J. Dong and Z. Zheng, "Shrinking Neighborhood Evolution - A Novel Stochastic Algorithm for Numerical Optimization," in IEEE Congress on Evolutionary Computation, Trondheim, Norway, May 2009
6. J. Dong, A. I. Zaghloul, C. J. Reddy, "Quaduple Bandwidth True Time Delay Printed Microwave Lens Beam Former for Ultra Wideband Multifunctional Phased Array Applications," in IEEE International Symposium on Antennas and Propagation, North Charleston, South Carolina, June 2009
7. J. Dong, Hsu-Cheng Ou, A. I. Zaghloul, "Measurement Investigation of Microstrip Lens Sidewall's Termination", USNC/URSI National Radio Science Meeting, South Carolina, June 2009
8. J. Dong, A. I. Zaghloul, "Method and Computer-Aided Investigation of Microwave Lens for 360-Degree Scanning" in IEEE International Symposium on Antennas and Propagation, North Charleston, South Carolina, June 2009
9. J. Dong, A. I. Zaghloul, " Implementation of Microwave Lens for 360-Degree Scanning" in IEEE International Symposium on Antennas and Propagation, North Charleston, South Carolina, June 2009
10. J. Dong, A. I. Zaghloul, " A Review of Radar Techniques for Ornithological Observations" in IEEE International Symposium on Antennas and Propagation, North Charleston, South Carolina, June 2009